



TUM School of Computation, Information and Technology

Investigations on a Fiber-Optic Pressure Measurement System for Aerodynamic Applications

Sascha Ulrich Kienitz

Vollständiger Abdruck der von der TUM School of Computation, Information and
Technology der Technischen Universität München zur Erlangung eines

Doktors der Ingenieurwissenschaften

genehmigten Dissertation.

Vorsitz: Prof. Dr.-Ing. Jia Chen
Prüfer der Dissertation: 1. Prof. Dr.-Ing. habil. Dr. h.c. Alexander W. Koch
2. Prof. Dr.-Ing. Julien Weiss

Die Dissertation wurde am 27.04.2023 bei der Technischen Universität München
eingereicht und durch die TUM School of Computation, Information and
Technology am 06.10.2023 angenommen.

Abstract

The main goal of today's civil aviation industry is to reduce CO₂ emissions, improve fuel consumption to lower cost and moderate noise emissions of next-generation aircraft. Optimized aerodynamics contribute to a more ecological and economical aircraft generation. Nevertheless, the challenging integration of ultra-high bypass ratio engines, flaps, slats, and winglets results in an imperfect and inhomogeneous airfoil design. Furthermore, any discontinuity along the airfoil can result in flow separation in specific flight situations. Thereby, measurements of the local dynamic flow separation, complex vortex flows, and lift coefficients of real-sized aircraft are required to better understand the dominant aerodynamic and aeroacoustic effects better.

The wind industry faces a similar challenge. The growing demand for energy and the need for renewable and environmentally friendly energy sources has led to a steady demand for wind energy. While wind turbine blades have become larger and larger, aerodynamic blade design models have changed little over 20 years.

A central research focus is to validate aerodynamics at high Reynolds number for large wind turbines. This will optimize design models and make turbines more cost-effective in the future. High temporal resolution aerostatic, aerodynamic, and acoustic measurements are required to measure the rotor blades' inflow, lift, and acoustic emissions. However, strict lightning protection requirements hinder instrumentation on wind turbine rotor blades using conventional electrically wired sensors.

Consequently, a fundamental challenge in testing innovative and noise-reduced rotor blades on modern wind turbines and next-generation transport aircraft aerodynamics is to generate validation data on full-scale structures under realistic environmental conditions in long-term measurement campaigns. Moreover, robust sensing technology is required as input for following generation control strategies of more efficient wind turbines.

Conventional electrical pressure sensors strongly degrade in performance in harsh environments during flight or wind turbine monitoring applications. Their low overload protection, susceptibility to electromagnetic influences, and corrosion limit their lifetime for continuous aerodynamic measurement applications. A fundamental advantage of fiber-optic pressure sensors is their inherent immunity to parasitic electromagnetic fields as electromagnetic coupling. The influences of cable length and triboelectric charging caused by colliding dust particles in the air will not affect the fiber-optic sensor reading. In addition, the absence of corrosive materials and the inherent all-glass structure allow a lasting sensor design, which features low fatigue and, most importantly, excellent overload stability.

This work aims to design, develop, and qualify a fiber-optic pressure sensing system in the lab and harsh field testing environments. The proposed system consists of either a cylindrical or a flat passive fiber-optic Fabry–Pérot pressure sensor combined with an edge filter interrogator and shall allow aerodynamic evaluations of real-sized structures in-flight tests and wind tunnel tests in relevant environmental conditions. Therefore, in addition to theoretical validation in the lab, experimen-

tal measurement campaigns in wind tunnel tests, flight tests, and wind turbines characterize the sensor's performance.

As a result, the developed measurement setup has demonstrated its capability to measure steady and unsteady pressure fluctuations for aerodynamic applications on small aircraft, winglet models, and a multi-megawatt wind energy converter. Additionally, the measurements of unsteady pressure phenomena demonstrate the system's benefit in providing new insight into understanding complex flow fluctuations and allowing investigation of complex active flow controls.

Zusammenfassung

Das Hauptziel der heutigen Zivilluftfahrtindustrie ist die Verringerung der Emissionen, die Verbesserung des Treibstoffverbrauchs und die Minderung der Lärmemissionen von Flugzeugen der nächsten Generation. Eine optimierte Aerodynamik trägt zu einer ökologischeren und wirtschaftlicheren Flugzeuggeneration bei. Die schwierige Integration von Triebwerken mit ultrahohem Nebenstromverhältnis, Klappen, Vorflügeln und Winglets führt jedoch zu einem unvollkommenen und inhomogenen Tragflächendesign. Jede Unstetigkeit entlang der Tragfläche kann in kritischen Flugsituationen zu einer Strömungsablösung führen. Um die vorherrschenden aerodynamischen und aeroakustischen Effekte besser zu verstehen, sind daher Messungen der lokalen dynamischen Strömungsablösung, der komplexen Wirbelströmungen und der Auftriebskoeffizienten an realen Flugzeugen erforderlich.

Die Windindustrie steht vor einer ähnlichen Herausforderung. Die wachsende Nachfrage nach Energie und der Bedarf an erneuerbaren und umweltfreundlichen Energiequellen hat zu einer stetigen Nachfrage nach Windenergie geführt. Während die Rotorblätter von Windkraftanlagen immer größer geworden sind, haben sich die aerodynamischen Modelle für Rotorblätter in den letzten Jahren kaum verändert. Mit dem Ziel, die Konstruktionsmodelle zu optimieren, steht die Validierung der Aerodynamik bei hohen Reynoldszahlen für große Windturbinen wieder im Mittelpunkt der Forschung, um die Turbinen in Zukunft robuster und kostengünstiger zu machen. Aerostatische, aerodynamische und akustische Messungen mit hoher zeitlicher Auflösung sind erforderlich, um die Anströmung, den Auftrieb und die Schallemissionen der Rotorblätter zu messen. Darüber hinaus erschweren strenge Blitzschutzanforderungen die Instrumentierung der Rotorblätter von Windkraftanlagen mit herkömmlichen elektrisch verdrahteten Sensoren.

Eine grundlegende Herausforderung bei der Erprobung innovativer und lärmreduzierter Rotorblätter an modernen Windkraftanlagen und der Aerodynamik von Verkehrsflugzeugen der nächsten Generation besteht daher darin, Validierungsdaten an Strukturen in Originalgröße unter realistischen Umweltbedingungen über einen langen Messzeitraum zu generieren. Darüber hinaus sind eine robuste Sensortechnologie als Eingang von neuartigen und effizienteren Regelungsstrategien für effizientere Windturbinen der nächsten Generation erforderlich.

Herkömmliche elektrische Drucksensoren verlieren aber in rauen Umgebungsbedingungen, wie während eines Testflugs oder bei der Überwachung von Windturbinen ihre hohe Sensoreigenschaften. Der geringe Überlastschutz, ihre Anfälligkeit für elektromagnetische Einflüsse und Korrosion schränken ihre Lebensdauer für kontinuierliche aerodynamische Messanwendungen erheblich ein. Ein grundlegender Vorteil faseroptischer Drucksensoren ist ihre inhärente Unempfindlichkeit gegenüber parasitären elektromagnetischen Feldern als elektromagnetische Kopplung. Die Einflüsse der Kabellänge und der triboelektrischen Aufladung durch kollidierende Staubpartikel in der Luft haben keinen Einfluss auf den Messwert des faseroptischen Sensors. Darüber hinaus ermöglicht der Verzicht auf korrosive Materialien mehr Lastzyklen, eine längere Lebensdauer und vor allem eine ausgezeichnete Überlaststabilität.

Ziel dieser Arbeit ist es, ein faseroptisches Drucksensorsystem zu entwerfen, zu entwickeln und dessen Qualität im Labor und unter Feldbedingungen zu testen. Das vorgeschlagene System besteht entweder aus einem zylindrischen oder flachen passiven faseroptischen Fabry–Pérot-Drucksensor in Kombination mit einem Kantenfilter-Abfragesystem und soll die aerodynamische Evaluierung von Strukturen realer Größe in Flugtests und Windkanaltests unter relevanten Umweltbedingungen ermöglichen. Neben der theoretischen Validierung im Labor charakterisieren daher experimentelle Messkampagnen in Windkanaltests, Flugtests und Windkraftanlagen die Leistungsfähigkeit des Sensors.

Im Ergebnis hat der entwickelte Messaufbau seine Fähigkeit zur Messung stationärer und instationärer Druckschwankungen für aerodynamische Anwendungen an Objekten realer Größe bewiesen. Darüber hinaus zeigen die Messungen instationärer Druckphänomene, dass das System neue Erkenntnisse zum Verständnis komplexer Strömungsschwankungen liefert und die Untersuchung komplexer aktiver Strömungssteuerungen ermöglicht.

Contents

1. Introduction	1
1.1. Motivation	1
1.1.1. Pressure Sensing in Aviation	1
1.1.2. Pressure Sensing in the Wind Industry	3
1.1.2.1. Control Input	3
1.1.2.2. Aerodynamic Validation	6
1.1.3. Requirements for novel Aerodynamic Pressure Sensing	7
1.2. Solution: Fiber-Optic Pressure Sensing	11
1.2.1. Derived Research Questions	12
2. State of the Art and Fundamental Principles	14
2.1. Aerodynamic Principles	14
2.1.1. Reynolds Number	14
2.1.2. Aerodynamic Lift and Drag	14
2.1.3. Boundary Layer	16
2.1.4. Dynamic Pressure Fluctuations and Turbulent Flow	17
2.1.4.1. Power Spectral Density	17
2.1.4.2. Cross-Correlation	18
2.1.4.3. Coherence	19
2.2. Optical Principles	20
2.2.1. Light as an Electromagnetic Wave	20
2.2.2. Reflection, Transmission, and Absorption	21
2.2.3. Optical Fibers	24
2.2.4. Fabry–Pérot Interferometer	27
2.2.4.1. Spectrum in Direction of Transmission	27
2.2.4.2. Spectrum in Direction of Reflection	29
2.2.4.3. Resonator Condition	30
2.2.4.4. Finesse	31
2.2.4.5. Free Spectral Range	32
2.2.4.6. Full-Width-Half-Maximum	32
2.2.5. Edge-Filter Interrogation Principle for Fabry-Pérot Sensors	32
2.3. Mechanical Principles	36
2.3.1. Gauge, Differential, Sealed and Absolute Sensor Types	36
2.3.2. Membrane Design	37
2.3.2.1. Displacement Sensitivity of the Membrane	37
2.3.2.2. Dynamic Transfer Characteristic of the Transducer	40
2.3.2.3. Natural Frequency of the Membrane	41

Contents

3. Pressure Sensor Transducer	44
3.1. Concept	44
3.2. Manufacturing	46
3.3. Finalized Sensors	47
4. Qualification and Verification of the Measurement System	49
4.1. Calibration Methods	49
4.1.1. Static Pressure Calibration	49
4.1.2. Dynamic Pressure Calibration	50
4.2. Evaluation of the Sensor Transducer	51
4.2.1. Spectral Characteristics	52
4.2.2. Temperature Rating and Cross Sensitivity of the Pressure Transducer	55
4.2.3. Environmental Stability	61
4.2.4. Shock and Acceleration Cross Sensitivity	63
4.2.5. Burst Pressure of the Fiber-Optic Transducer	63
4.3. Measurement Performance in Combination with the Edge-Filter In- terrogator	64
4.3.1. Linearity and Measurement Range	64
4.3.2. Reproducibility and Other Measurement Deviations	66
4.3.3. Noise Floor, Resolution, Dynamic and Frequency Range	68
5. Experimental Aerodynamic Validation of the Measurement System	70
5.1. Wind-Tunnel Evaluation: Fiber-optic Pressure Sensors in Low and High-speed Wind-Tunnel Tests	71
5.1.1. Description of Experiment	71
5.1.1.1. Low-Speed - Experimental Setup	71
5.1.1.2. High-Speed - Experimental Setup	72
5.1.2. Experimental Results	72
5.1.2.1. Low-Speed Wind-Tunnel Test	72
5.1.2.2. High-Speed Wind-Tunnel Test	77
5.1.3. Summary of the Results	80
5.2. Fiber-Optic Pressure Measurement on a Winglet Model	82
5.2.1. Description of Experiment	84
5.2.1.1. Experiment Setup	84
5.2.1.2. Active Flow Controls in Winglet Model	86
5.2.2. Experimental Results	87
5.2.2.1. Static Pressure Measurements	87
5.2.2.2. Dynamic Pressure Measurements	92
5.2.3. Summary of the Results	98
5.3. Static and Dynamic Pressure Measurement in Flight Test Application	99
5.3.1. Description of the Flight Test	99
5.3.2. Experimental Results	103
5.3.2.1. Static Pressure Measurements	103

Contents

5.3.2.2. Dynamic Pressure Measurements	105
5.3.2.3. Fiber-Optic Boundary Layer Rake	114
5.3.3. Summary of the Results	118
5.4. Integration of Fiber-Optic Pressure Sensors into a Multi-hole Pressure Probe to Monitor Unsteady Inflow	120
5.4.1. Description of Experiment	122
5.4.2. Experimental Results - Spatial Calibration of a Fiber-Optic Pressure Probe	123
5.5. Measurement of Aerodynamics of a Wind Turbine with Fiber-Optic Sensors	126
5.5.1. Description of Experiment	126
5.5.2. Experimental Results	127
6. Conclusion and Outlook	131
Appendix	133
List of Figures	143
List of Tables	147
List of Abbreviations	148
List of Symbols	149
A. Bibliography	154
A.1. Bibliography	154
A.2. Own Publications	171
A.3. Patents	172
A.4. Supervised Student-based Seminar Papers and Theses	173

1. Introduction

1.1. Motivation

This chapter discusses current sensing-related challenges in aerodynamic field testing. This chapter is split into two main applications: aviation in section 1.1.1 and the wind industry in section 1.1.2. After deriving consolidated qualitative requirements on the sensing system for both applications in section 1.1.3, a fiber optic Fabry–Pérot sensor system is outlined as a possible sensing solution in section 1.2. Finally, the chapter closes with the phrased research objectives to be answered within this work in section 1.2.1.

1.1.1. Pressure Sensing in Aviation

The main goal of today’s civil aviation industry is to reduce CO₂ emissions, improve fuel consumption to lower cost, and moderate noise emissions of next-generation aircraft [28].

On the one side, there are revolutionary approaches to replace conventional aircraft with electric aviation in the long term. On the other side, evolutionary trends to develop more fuel-efficient conventional aircraft in the midterm. The trend towards electrical aviation also influences the requirements of sensors for electric powertrain components.

When using electrical sensors, some disadvantages have to be accepted. A qualified electrician must carry out both the instrumentation and the handling. The electrical insulation of conventional sensor cables and their diameter might influence the properties of the test object in an inadmissible way due to installation, for example, by drilling holes. Despite their insulation, the signal quality of conventional sensors can be influenced by electromagnetic interference, electrostatic discharges, and high electrical potentials such as those prevailing in the power electronics environment. The measurement technology used in the lab, in the flight test, and for serial integration must be adapted as the powerful electrical currents and high voltage levels demand intense electrical isolation of low-voltage precision sensing technology.

Besides the electrification of the powertrain, continuous effort is invested in upgrading the aerodynamics of the state-of-the-art systems. In addition to optimized airfoils and winglets, ultra-high bypass ratio engines will contribute to a more ecological and economical aircraft generation [120, 121]. These ultra-high bypass ratio engines have a higher propulsion efficiency than current models but are associated with a larger nacelle size. The aerodynamics of the wing-pylon section of a transport airplane is optimized for cruise flight at high altitudes and at subsonic speed by minimizing drag. Nevertheless, additional mechanical high-lift devices, such as

1. Introduction

slats and flaps, modify the blade profile during slow flight maneuvers such as take-off and landing. Therefore, higher angles of attack and lift coefficients are allowed and postpone the onset of flow separations at slower airspeed [119–121]. To avoid the penalty of longer and heavier landing gears and still provide enough clearance between the nacelle and the runway, the nacelles must be integrated closer and placed in front of the wing. In consequence, no high lift device as conventional slats are integrated near the wing/pylon section [154]. Also, on the outer wing tip, where the sharket’s bent shape and curvature inhibit the installation of a mechanical leading edge device, the risk of flow separation increases, especially in the take-off and landing phases when the aircraft is close to the critical stall condition [119, 122, 195].

A fundamental challenge is to validate the understanding of aerodynamics during flight testing. It is driven by the necessity to get a clear picture of a very complex three-dimensional flow field close to the critical aircraft stall. Moreover, the aviation industry intends to evaluate and optimize the aircraft’s entire flight envelope and include testing in critical flight situations.

In addition to flow separations, acoustic pressure fluctuations excite aircraft’s surface panels and are either caused by turbulent boundary layers or noise-induced vibrations [187]. In order to better understand the characteristics of these pressure fluctuations under realistic conditions, flight tests of true-sized aircraft instead of ground-based tests are also necessary because equal airflow conditions are required to obtain appropriate experimental data [186, 187, 197].

Therefore, aerostatic, aerodynamic, and aeroacoustic measurements of the local dynamic flow separation, complex vortex flows, and lift coefficients of real-sized aircraft in operation are required to understand the dominant aerodynamic and acoustic effects better. The general purpose of flight testing is to evaluate the aircraft’s performance in flight settings and situations, which are as similar as possible to reality, including surface imperfections, manufacturing tolerances, and deviations of serial products from the initial design [219].

Flight testing faces many instrumentation challenges, including the number of sensors, regulatory requirements, and the harsh environment, such as icing conditions, rain, and the moisture of clouds [145, 185, 186]. The flight test engineer’s challenge is that the harsh environments, the installation, and the handling might degrade and alter conventional sensor characteristics. Additionally, the fulfillment of electromagnetic compatibility requirements according to certification standards has also been problematic due to the intrinsic electromagnetic sensing principles or cable lengths [43, 46, 145, 185].

In order to provide the next generation of aerodynamic optimization, industry and research institutions worldwide have identified the need for an upgraded measurement platform. Such novel sensing devices might reveal new aerodynamic insights in lab or flight test environments and potentially become a novel standard in pressure sensing.

1.1.2. Pressure Sensing in the Wind Industry

Worldwide challenges such as climate change, air pollution, energy security, and cost and access to energy ask for alternative, low-carbon technology options such as renewables [35, 86]. A popular and industrialized option for renewable and environmentally friendly energy sources has led to the constant growth of wind energy [86]. In the last decade, wind turbines have become more efficient, optimized, and cost-effective and have become one of the fastest-growing renewable energy technologies [35, 86].

Although the pandemic and the associated supply chain issues challenged the wind industry worldwide, 2020 was the best year in history for year-to-year growth. With almost 94 GW capacity increase worldwide, the year 2021 falls only short by -1,8 % [100], despite a drop in onshore installations in China and the USA, and strict permitting and regulation-associated challenges in Europe. Nevertheless, mainly the offshore wind market has grown significantly in 2021. With 21,1 GW commissioned, the added capacity tripled three times more than the year 2020 [100]. The market growth will continue, as the market forecast predicts over 557 GW of added capacity in new onshore and offshore wind projects to be commissioned in the next five years [100].

An ongoing trend, especially in the offshore segment, is the increased swept area of the rotor blades, which is proportional to the maximum possible annual energy production of a wind energy converter. As wind turbine blades become taller and heavier, the rules of classical mechanical engineering and turbine construction are reaching their limits [165], as an increasing blade length by only 3 % typically increases mass exponentially by 8 % [92]. Additionally, considering a blade growth of 50 %, manufacturing challenges accompany industrialization because, simply due to higher mass, cycle times will be half even if blade factories are doubled in size [92].

To enable larger blades without increasing mass exponentially, a trend towards fully carbon fiber blades has started despite strenuous sourcing efforts and more complicated material handling in the blade design and manufacturing [92].

To decrease the cost of energy further, minimize downtime, and extend the lifetime of turbines in the future, different novel technology strategies have to mitigate loads. Finally, upgrading those more expensive and complex rotor blades with sensors forcing their digitization will drive the next wave of successful turbines [165]. Therefore, new materials, sensors, and control strategies will bend the limit of classical machinery design and therefore enable cost-out and new business cases.

1.1.2.1. Control Input

Any operating wind turbine utilizes a fundamental aerodynamic control concept to avoid overly high loads and ensure optimal energy production. However, in practice, only two aerodynamic design controls can be distinguished: Stall and pitch regulated [16].

In the case of a simplified passive stall concept, the turbine operated at a fixed

1. Introduction

pitch angle regardless of the inflow wind speed. Suppose the nominal wind speed exceeds the design limits. In that case, the angles of attack and airfoil shapes at different radii and the blade increase beyond their respective critical angles of attack, and stall is induced, which reduces overall lift. Therefore, the power production is controlled due to a drop in the limited aerodynamic lift resulting from the intentional stall by design. In the case of an active stall control variant, the blade's angle of attack is adjusted, and the stall is caused, which reduces the aerodynamic load. Especially in the early beginning of the wind industry, stall-controlled wind turbines have been the standard for regulating power on the rotor of a wind turbine. However, with growing blades, the forces acting on the wind turbine increase as well, which leads to a higher possibility of fatigue failures of the rotor blades of wind turbines [113]. The levelized cost of energy is reduced by mitigating those fatigue loads and ensuring the integrity of each blade, and additionally, imperfect operating points lower power.

Stall-regulated wind turbines still have their uses, but with more complex turbines, control has moved towards blade pitch control concepts. Pitch control concepts adjust the blade's angles of attack depending on the inflow speed, desired power output, and loads. To limit the aerodynamic force on blades and, therefore, the mechanical rotor torque to the design limits of the electrical generator and the overall turbine, the turbine controls the blade pitch. By pitching the blade, the turbine can reduce lift and, therefore, the overall torque and loads at higher wind speeds. Pitch adjustment allows for a lightweight and optimized blade design compared to the stall concept. The three blades have an independent pitch mechanism in a pitch-regulated wind turbine. The three blades are always adjusted synchronously by a uniform pitch angle and in specific operating conditions individually.

An active stall or pitch-regulated turbine needs sophisticated sensing input. A prominent and industrialized method to feed individual pitch control systems is to utilize structural measurement in the wind turbine blade. The primary structural loads on rotor blades in the flapwise direction are caused by the asymmetric inflow flow conditions and the gravitational load components. The structural loads propagate through the complete wind turbine, including the rotor, hub, drive train, gearbox, generator, and tower. With the help of simplified blade models, higher-value information, such as root bending moments, is derived from the merged sensing information of multiple sensors. The blades' edge and flapwise deflection information are derived typically from a series of strain gauges inside the blade [130]. The load information of these structural sensor measurements is fed into an individual pitch controller, which then optimizes the loads on the wind turbine blades individually. Peak loads, aerodynamic loads, blade flutter, and imbalances are reduced by individual pitch control of the rotor blades, and this reduction technique achieves consequently up to 20...30% load reduction [165]. In addition, load regulation minimizes significant aging and further increases the turbine's service life without exceeding the safe limit [113, 165].

Different advanced control strategies [106, 130] might be implemented in next-generation turbine designs to accomplish further load reduction in the future. While

1. Introduction

industrialized strain sensing systems detect blade states accurately, state-of-the-art systems cannot predict loads to alleviate load effects on the blade beforehand. In contrast, aerodynamic sensors provide information about the incoming wind field, which affects the structural loads. The aerodynamic sensor information occurs before the aerodynamics affect the blade, and the load reaches the load sensors [165]. Therefore, an advanced active control system and its actuators, which seek to mitigate the projected loads, have more time to react and optimize blade states, even before the loads occur. Consequently, the load reduction potential can exceed today's mentioned structural-based load reduction achievements [14].

Future active control strategies such as aerodynamic load control [4, 36], stall detection [190], and acoustic pitch control [135, 215] require sophisticated and robust sensing input and will drive either the pitch control system or active flow controls as flaps to reduce fatigue loads [4, 31, 106, 130]. Consequently, pressure-based control algorithms have been a research focus recently, and different aerodynamic sensing inputs are considered.

Ongoing research discussions have demonstrated that static pressure-based control algorithms are suitable for controlling a wind turbine. A pressure difference between an airfoil's pressure and suction side, measured at only a single chordwise position retrospectively, as a control input results in a good load reduction potential [3, 53]. Thereby, the controller seeks to keep the lift constant, and the optimal position for such differential surface pressure measurements has been simulated to be at 12,5 % from the chord [4, 53]. In addition to measuring the pressure difference as a control input, the local angle of attack is valuable. In this case, a controller reacts primarily to changes in the incidence and relative velocity, but torsional deflections of the blade need to be considered. The drawback is that the blade profile needs to be well known and a sophisticated and more complicated blade model needs to be implemented because measured aerodynamic quantities and the projected structural loads are not directly correlated [165]. Moreover, high sensing accuracy and model requirements are applied to secure control system effectiveness and avoid potential instabilities [53, 165, 188].

Next, a permanent measurement of flow and continuous adjustment of the blade state concerning the direction and speed of the airflow could enable particularly quiet turbines [7, 21]. Acoustic control algorithms have been recently discussed in research and experimentally validated [7, 20–22]. However, acoustic measurements are undertaken with ideal blade and inflow conditions during qualification and tests. Nevertheless, turbulence is created by mechanical imperfections such as erosion and dirt or poor inflow conditions due to various weather and terrain conditions. Acoustic pitch control by measuring the acoustic emission or the transition of the boundary layer from laminar to turbulent flow allows to control and reduce noise emission to respect noise regulation, especially close to residential areas [135, 141].

These applications are of high commercial interest as they require a serial sensing solution. Although the required lifetime of such a sensing system would be very long, the expected quantity could drive the industrialization and maturation of the sensing mean in the long term.

1. Introduction

1.1.2.2. Aerodynamic Validation

Next to control strategies, even in the short term, validation of aerodynamics of next-generation turbines becomes an uprising challenge. To offer a higher energy yield, the design of turbines must become more powerful and cost-effective. As a consequence, this industrial-economic intention requires an optimized blade design. However, there is a significant knowledge gap between the aerodynamic design and analysis of wind turbines and their operation [93].

In order to design better turbines, new advanced design and simulation tools are needed, but today's underlying models have evolved only a little over 20 years [74, 93]. Conventionally, experimental investigations of wind turbine airfoils have usually been carried out with scaled models in wind tunnels. Firstly, the essential disadvantage of this practice is that the rotational motion of a wind turbine is neglected. Secondly, the blade model is shrunk, so scaling effects for the fluid behavior must be considered. Furthermore, thirdly, the natural turbulence of atmospheric inflow cannot be realistically reproduced in wind tunnels [33, 182]. Consequently, the resulting models and simulations, based on the blade's experimental investigation, are described as two-dimensional models in a controlled environment. At the same time, realistically, the wind turbine faces unsteady three-dimensional flow conditions [33, 56, 62]. For the conventional blade element momentum method, this deviation creates a reasonable uncertainty in the modeling of turbines. Therefore, only simplified models or empirical methods are typically utilized for the performance prediction of next-generation wind turbines and their blade designs [182].

The lift measurement of a rotor blade depends heavily on the inflow properties of the blade. The lightweight structure of modern rotor blades affects flapwise and edgewise bending moments. Also, the torsional stiffness of blades due to bending-torsion coupling mechanisms, which are caused by the anisotropic composite material [69, 147], is a particular concern in design. With growing blade lengths, the torsion of a blade alters the blade's angle of attack locally compared to the root section of the blade. Therefore, additional measurements with pitot tubes to estimate the local inflow conditions, such as the angle of attack and velocity at different blade radii are the focus of validation [33, 56, 62, 152, 173]. Moreover, the dynamic measurement of undesired aeroelastic instability becomes increasingly crucial for validation purposes [133].

A wind turbine operates most of the time under some yaw loads. Because of deviating anemometer data at the turbine nacelle, horizontal or vertical wind shear might occur, or the turbine could misalign with the wind because it does not continuously follow the varying wind direction [62]. In the case of these yaw loads, during the rotation of the blade, it passes a non-uniform flow field in velocity and direction. These induced wind shear and turbulence on state-of-the-art multi-megawatt wind energy converters with rotor diameters beyond 150 m cause another fundamental challenge. As the swept area increases, the induced dynamic loads become more significant. Therefore, the increased aerodynamic lift and drag variations along longer blades must be addressed in the design and quantified in practice. Otherwise, if the

1. Introduction

aerodynamic load variations are neglected in the design phase, adequate structural safety parameters must be adopted.

Additionally, the dynamically changing inflow characteristics are suspected of determining the transition from the laminar to the turbulent boundary layer at the rotating blade [62, 93]. Actual flow conditions in a three-dimensional rotating boundary layer have yet to be fully understood. A fundamental understanding or measurement of the undisturbed incoming inflow field close to the blade helps to optimize blade design, so that boundary layers have an extended laminar zone, which offers less aerodynamic drag and, therefore, higher efficiency [182].

Any object moving through air generates sound emission because of unsteady pressures interacting with the object [22, 96, 189]. For large and modern wind turbines located close to residential areas, noise emission can be a decisive acceptance criterion. Therefore, reducing noise emissions is also of fundamental interest in the design phase. Furthermore, local measurement and optimization of the blade's noise sources could enable particularly quiet turbines [63, 163].

In order to upgrade design tools, experimental validation of the aerodynamics at high Reynolds numbers of large wind turbines is continuously a general research focus [33, 62, 182]. Therefore, high temporal resolution static and dynamic measurements of the actual rotor blades' inflow, the drag and lift coefficients, pressure distributions, boundary layer conditions, and acoustic emissions, especially during qualification, are highly interesting.

1.1.3. Requirements for novel Aerodynamic Pressure Sensing

The following section summarizes the consolidated qualitative requirements of both previously described motivations. Several research projects and publications have formulated generic objectives to ensure the next generation of sensing devices is future-proven for aviation. [79, 127, 169, 170]. Additionally, previous measurement campaigns in the context of wind energy have been a true challenge with varying degrees of success [33, 56, 62, 152, 173]. Based on the literature, the following objectives for a future-proven measurement concept can be derived:

Miniature sensor footprint: A common goal of all measurements is to measure the actual situation and the ideal object (within the physical limits) without influencing it. For the use case pressure measurement in aviation and wind, the sensor should be as small as possible to avoid influences on the aerodynamic structure. Any alteration of the aerodynamic structure results in possible flow-induced self-noise and pressure deviations. Furthermore, the minimum distance between sensors limits spatial resolution, which challenges capturing high-pressure field gradients accordingly. Additionally, conventional flat condenser microphones are large, and the integration of these bulky sensors is, at least in flight testing, limited to the fuselage, mainly on a passenger window, which is replaced by dummy windows [187]. Whereas miniature pressure sensors are usually integrated into the so-called pressure belt to establish

1. Introduction

an interesting measurement location and smooth surface with minimal alteration of the original shape [170].

Ease of installation: Conventional pressure transducers are stored in separate spaces inside the aircraft or wind turbine’s hub. A common practice has been to utilize pressure taps and route these tubes to a centralized data acquisition system inside the blade [24, 56, 152]. Routing pressure tabs from the actual measurement location to the protected sensor limits the response time and is only suited for quasi-static measurement. Due to bandwidth considerations, pressure tubes need to be limited in length. Additionally, the pressure taps have been reported to be challenging to install robustly on turbines [56]. The commonly used pressure scanners are based on a differential pressure sensing method, but ensuring a stable reference pressure reservoir is challenging to provide within a blade. The frequency transfer function needs to be calibrated beforehand. The complex calibration makes it challenging to directly study noise and turbulent flow characteristics. In practice, channels are frequently either blocked by particles or not air-tight because of cuts and bends, making the installation more complicated and error-prone [46, 199, 217]

Reduce cabling: Even if the conventional sensor is instrumented close to remote measurement locations of interest, electrical pressure transducers are connected with multiple copper wires. Length and routing might be subject to electrical interference and alter the sensor reading by picking up more electromagnetic noise. Additionally, considering the necessary shielding, the copper wiring adds disadvantageous weight [46, 145, 169, 199].

Safety: Altering the airfoil’s surface by drilling holes to route cables or pressure taps alters the structural integrity. Moreover, most additional routing of conducting wires from outside into the aircraft’s interior provokes air leakages in the aircraft’s pressure chamber and requires additional considerations and approvals. The possibility of short circuits, which might cause sparks or heating in a hazardous environment near fuel tanks, hinders freedom of placement of sensors or requires additional safety measures, such as shielding [43, 46, 52, 185, 199]. Added installations on the fuselage might require safety considerations as well [43, 145, 185]. Purely passive and electrically non-conducting components offer the potential to ease flight safety approvals [169].

Static and dynamic sensing capabilities: Utilizing a single sensor for static and dynamic measurements avoids doubled instrumentation of a test object with microphones and pressure sensors and reduces testing time. Here, increasing the dynamic range of the maximal signal-to-noise ratio sensors is one big challenge because the hydrodynamic excitation within a turbulent boundary layer can already exceed moderate flow speeds and overload the commercial microphones [187]. In addition, while

1. Introduction

a high sensitivity is better suited in environments with low and medium sound pressure levels, lower sensitivities are better suited for high noise environments, such as flight tests, to avoid clipping and distortion [186].

For a wind turbine, a barometric sensor with a bandwidth from static excitation to 100 Hz is to be preferred to monitor the rotational altitude-induced barometric changes, pitching effects up to 1 Hz and dynamic stall from 2 Hz to 12 Hz [24, 173].

According to the literature [173], the dynamic sensing capabilities shall be capable of detecting turbulence from 100 Hz to 1000 Hz and trailing edge emitting noise from 100 Hz to 5000 Hz.

Synchronicity: In order to validate high-frequency fluctuating pressure fields and evaluate phase differences of multiple sensor locations, high synchronicity between sensor channels has to be ensured.

Durability: Conventional sensors fail in harsh environments. Therefore, higher robustness of the sensing products is expected to ensure successful measurement campaigns in non-optimal weather conditions. The overload robustness also includes the durability of sensor handling and the exposure to overloads [186].

Additionally, a non-corrosive material is favorable, as it does not degrade when exposed to humidity and water and offers low fatigue.

Cost: The costs of the test instrumentation system are directly related to the requirements imposed. High-performance sensors are typically considered rather expensive [187]. The discovery of new insights into aerodynamics and structural loads requires more data points. Otherwise, further knowledge gains are plateauing [169]. The desire to instrument more sensors also inherently asks for a better price-performance per measurement point [185, 186].

Furthermore, for potential industrial series applications of pressure sensors, the cost constraints are forwarded to sensor suppliers in aviation and the energy sector. For commercial success, the sensor unit cost shall be less than the state-of-the-art for conventional applications. Otherwise, high pay-off applications have to be established first in test instrumentation [207].

Sensor Shape: The blades are difficult to access for installation and maintenance. There have been only two integration methods of pressure sensors to rotor blades reported: Utilization of aerodynamic gloves and embedding sensors.

Especially in retrofit installation on wind turbines, a common practice is to install additional aerodynamic gloves, which include a sensor and, in some cases, the complete remote acquisition system [192]. The advantage with this is that the installation efforts are less because the aerodynamic glove is usually instrumented on an already commissioned turbine [173]. An optimal aerodynamic glove must be thin and have the same surface roughness and shape. Nevertheless, in practice, the aerodynamic gloves alter the original shape of the airfoil and, in some cases, e.g., if the

1. Introduction

actual data acquisition system must be integrated as well, will disturb the airflow due to a bulky housing [192]. Furthermore, from an integrational point of view, the sensor's thickness needs to be miniature [173].

The installation is time-consuming if the blade's structure can be manipulated by embedding a sensor or drilling holes. Usually, it requires the sensor installation to happen in the blade factory prior to the erection of the turbine. This procedure ensures that the airfoil's original shape is maintained but is the most costly and time-consuming installation method.

Depending on the integration methods, two sensor shapes can be outlined. If the sensor needs to be installed on an aerodynamic shell, the sensor shall be thin. Therefore, a perpendicular sensing direction regarding the cable or main body direction is favorable. On the other hand, cylindrical-shaped sensors have been preferred in case of installation efforts, budgets, and structural considerations that allow drilled holes in the airfoil.

Lightning concerns: Strict lightning protection requirements hinder instrumentation on wind turbine rotor blades using conventional electrically wired sensors far outboard in the rotating frame. According to the recent IEC 61400 standard, additional conductive components in the blade must be carefully coordinated in the design of the lightning protection system [78]. Furthermore, electrically wired systems endanger the rotor blades' integrity in case of lightning. Therefore, they are avoided at remote locations close to the tip, where aerodynamic measurements are most interesting.

Environmental concerns: Next to lightning, other challenging environmental conditions have to be considered for long-term measurement campaigns. These ambient conditions include rain, mist, icing, and erosion due to dust particles. While hail significantly overloads fragile sensing systems, dust particles induce triboelectric effects, which have deviated measurement results in field tests of conventional electrical sensors. Moreover, the leading edge erosion, especially on turbines with high tip speed, hinders the long-term use of instruments at the stagnation point [51, 173].

The rotational accelerations and vibration have impacted the pressure acquisition systems in field experiments on wind turbines. The relevant radial acceleration due to the rotational movement of the blade must be considered, especially for outward sensing locations. A unique challenge in field tests has been the installation direction in combination with high cross-sensitivity towards acceleration of piezoresistive pressure transducers, which altered the reading depending on the rotor speed [33].

In a long-term experiment, the rainy or icing environments challenge the use of pressure taps, which get blocked due to the allocation of fragments and dust in the long term. Therefore, considering the rain, the sensing system is preferred to be water-proven and without tubes.

1.2. Solution: Fiber-Optic Pressure Sensing

In order to overcome the field challenges and provide a sophisticated sensing proposal, this thesis explores two sensor concepts for wind industry and aviation applications.

On the one hand, next to conventional piezoresistive pressure sensors, the promising trend toward Micro-Electro-Mechanical Systems (MEMS) technology presents main advantages: price, size, and comparable good accuracy [186]. Particularly in the wind industry, the currently developed MEMS technology is the scope of research due to its high accuracy and ease of integration [127, 170]. Nevertheless, the electrical MEMS sensors are usually kept from being wired from the root section of the blade to the area of interest for measurement due to lightning concerns on wind turbines. Therefore, these devices are usually bundled and equipped with a long-ranging wireless connection powered by a battery, which restricts the duration of the measurement campaign. This power limitation restricts their usage to short-term validation purposes [173, 187]. On the other hand, the MEMS technology is interesting for flight testing due to its compact size but is usually challenged by its limited dynamic range [65, 137, 148, 186]. Additionally, the shielded but bulky electrical wiring of the sensors is a drawback [52, 199].

On the other hand, fiber-optic measurement technology offers a robust sensing alternative for aerodynamic applications because of fiber-optics' inherent advantages such as no electromagnetic coupling, passive design, no corrosion, and excellent overload stability [38, 79, 98, 145, 169, 199]. The distinct advantages of fiber-optic sensors are their inherent immunity to parasitic electromagnetic fields. Firstly, this avoids rotor blade damage due to susceptibility to the lightning environment. Secondly, with the advantage of fiber cables having low signal damping, remote sensing location far outward from the blade becomes accessible. Thirdly, by utilizing a non-conductive passive sensor design additionally, triboelectric charges will not affect the sensor reading. In addition to these optical benefits, the fiber-optic sensor usually consists of glass, and the absence of corrosive metallic materials allows for more and higher load cycles, a longer lifespan, and, most importantly, excellent overload stability and durability [72, 199]. For all these reasons, the scientific and industrial communities generally rate fiber-optic sensors as the next technology enabler, having the highest potential for continuous complex real-time monitoring for wind turbines and aviation [104, 161].

Generally, fiber-optic measurements can be categorized into three main types: Intensity-Modulated, interferometric, and distributed scattering systems [30, 161]. Within the interferometric category, Fabry–Pérot and grating-based system, Fiber-Bragg-gratings-based systems are the most popular. Scattering-based systems, based on Raman, Rayleigh, and Brillouin scattering effects, suit strain and temperature monitoring applications well [161]. While the sensing principle Fiber-Bragg-gratings has been industrialized and commercialized for structural measurement on rotor blades, the penetration of fiber-optic sensing into aviation is still mostly limited to research. Fiber-optic measurements, utilizing Fiber-Bragg-grating gratings to

1. Introduction

monitor aerodynamic forces acting on airfoils and wing shape measurement, have been of interest and introduced into flight testing applications [71, 145]. The main focus of commercial long-term monitoring applications have been the monitoring of structural loads, the impact control of landings gears and the structural health monitoring of composite structures [9, 80, 104, 115, 155, 161]. A wider industrial acceptance of fiber-optic sensing systems in the aviation industry is mainly hindered by the need for a standardization and certification framework in aviation [161].

For aerodynamic sensing, measurements of the physical property pressure are of interest. In contrast, two fiber-optic measurement principles are dominant: extrinsic Fabry–Pérot and intrinsic Fiber-Bragg-grating systems [30] [41, 153]. Considering the derived objectives, for direct fiber-optic pressure sensing, the Fabry–Pérot effect over the Fiber-Bragg-gratings is preferred in aerodynamic applications due to mainly three advantages. Firstly, Fabry–Pérot-based pressure sensors tend to be smaller than similar Fiber-Bragg-grating-based transducers. While for Fiber-Bragg-grating, the intrinsic optical design requires a larger transducer to overwhelm the fiber’s stiffness, which contains a grating modulation, the extrinsic optical design of Fabry–Pérot sensor allows design regardless of the mechanical fiber properties [161]. Secondly, reported Fabry–Pérot sensors tend to be more sensitive and therefore are suited better for aerodynamic applications, in which the resolution of low-pressure signals in a wide measurement range becomes necessary [72, 161]. Thirdly, in combination with the tiny dimension and the high interferometric sensitivity, the natural frequency of the transducer can be maximized [161]. Therefore, the same sensor allows not only aerostatic, aerodynamic, and acoustic measurements, but also satisfying dynamic measurement applications with high bandwidth. Furthermore, compared to other interferometric methods, the Fabry–Pérot sensors offer a more straightforward implementation than others because they do not require a reference fiber [30, 72, 94].

Therefore, considering the qualitative requirements of both aerodynamic applications on wind turbine monitoring and in aviation, this work intends to investigate and offer a fiber-optic toolkit based on a Fabry–Pérot transducer for research and design aerodynamic field applications in harsh environments.

1.2.1. Derived Research Questions

From the current state of research, the main topic is to investigate fiber-optic sensing means to monitor aerodynamics in harsh environments. In order to address the main objective of the thesis, it is necessary to explore, identify potentials and extend the limits of fiber-optic pressure sensing in aerodynamic applications. Therefore, the main objective is split into research objectives discussed within this thesis. In detail, the following research questions are derived:

What does a fiber-optic aerodynamic sensing system with synchronous barometric and acoustic measurement capability look like? The final combination of the sensor with an industrialized low-cost, and reliable edge-filtering interroga-

1. Introduction

tor, shall result in a flight-ready, fiber-optic measurement solution with low noise, high dynamic range, and high bandwidth. This research's scope is the development and raising of the maturity of a static and dynamic pressure sensor based on a Fabry-Pérot interferometer, which is miniature, airworthy, passive, and durable. In addition, detailed questions will be addressed regarding mechanical and optical sensor design, manufacturing procedures, and compatibility with an edge-filter interrogator system.

How does it perform in controlled lab environments? The developed system requires rigorous testing in controlled lab environments. Static and dynamic pressure calibration methods will be applied and evaluated. The noise floor, resolution, linearity, and measurement range will be characterized. Other critical parameters of the optical sensing system, such as temperature cross-sensitivity, drift stability, overload robustness, and other potential parasitic cross-sensitives, will be characterized.

Which aerodynamic properties can be measured with a fiber-optic aerodynamic sensing system? Based on the lab result, aerodynamic experiments in the wind tunnel will need to be conducted to evaluate which aerodynamic properties can be measured and which challenges need to be considered in future applications. Additionally, potential benefits and shortcomings of the fiber-optic system in comparison with conventional electrical sensors will need to be identified and evaluated.

How does the developed fiber-optic aerodynamic sensing system perform in harsh environments? In order to raise the technical readiness level of the system, field tests on wind turbines will be carried out to validate the system in actual operating conditions. In addition, the fiber-optic system will be instrumented on a flight test aircraft to demonstrate flight readiness. Finally, the recorded data will be analyzed post-process to investigate the system's potential.

2. State of the Art and Fundamental Principles

2.1. Aerodynamic Principles

The following section introduces the fundamental aerodynamics principle of an airfoil. This introduction provides an overview of the acting aerodynamic forces and eases the interpretation of sensing results in consequential chapters. A fundamental tool to analyze aerodynamics is static and dynamic pressure sensing.

2.1.1. Reynolds Number

The flow of air is modeled as fluid in aerodynamics. As one of the most fundamental variables, the Reynolds number represents the ratio of inertial to viscous forces of fluid and defines if the airflow is relatively laminar or turbulent. It is used to ensure comparability of different-sized flow situations due to scaling effects in aerodynamics [96]. The Reynolds number is directly correlated to the fluid's velocity, the airfoil's characteristic length, and the kinematic viscosity and is a dimensionless parameter. The equation 2.1 defines the Reynolds Number, whereas l_c is the characteristic length of an airfoil, ρ_{air} is the density of the air, u_∞ is the free stream velocity, and μ is the dynamic viscosity. Dynamic viscosity is a measure of the internal resistance of the fluid [96].

$$Re = \frac{\rho_{air} u_\infty l_c}{\mu} \quad (2.1)$$

A low Reynolds number generally marks laminar flow, while a high number indicates generally turbulent flow and, therefore, estimates the onset of turbulence.

2.1.2. Aerodynamic Lift and Drag

A conventional airfoil has a pressure and a suction side. The airfoil splits the incoming airflow into two parts at the stagnation point. While the first part flows along the suction side, the second part flows along the pressure side. At the trailing edge, the flow stream recombines. Due to the different chord lengths, the airflow is accelerated on the suction side while the airflow on the pressure side decelerates. On the one hand, the accelerated air flow reduces its static pressure according to Bernoulli's principle. On the other hand, the decelerated air flow on the pressure side increases static pressure. Therefore, the lift is created on the suction side, and pressure pushes on the pressure side. Bernoulli's principle is derived from the conservation of energy, which states that, in a steady flow, the sum of all forms of energy

2. State of the Art and Fundamental Principles

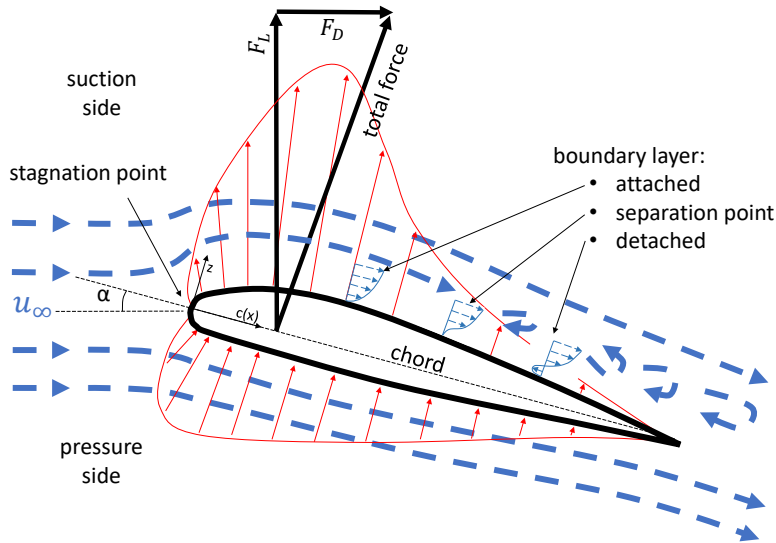


Figure 2.1.: Aerodynamic forces on an airfoil. The flow around the airfoil leads to a pressure gradient. Suction acts on the downwind side, and pressure acts on the upwind side. The resulting total aerodynamic force is the superposition of lift and drag. The boundary layer is the velocity profile of the thin layer of air flowing over the wing’s surface. The boundary layer can either be laminar or turbulent.

in a fluid, kinetic energy, potential energy, and internal energy, along a streamline remains constant. [96].

The following explanation is assuming a two-dimensional flow around the aerodynamic wing. In this simplified case, a force parallel to the inflow direction, the drag force, and the lift force, resulting from the generated total aerodynamic force is generated. The lift force is perpendicular to the inflow. The ratio of lift force to drag force is usually optimized in aerodynamics. Figure 2.1 illustrates the airfoil principle, and the dashed blue line represents the two-dimensional airflow. When increasing the angle of attack (AoA), the airflow velocity has to increase to cover the length difference between the path on the up and downwind sides. The angle of attack α is formed between the inflow direction with velocity u_∞ and the chord or the airfoil. The critical angle of attack α_{max} is the maximal incline at which the airfoil produces the maximum lift coefficient. At such a high angle, the airflow can no longer follow the tilted airfoil’s curvature and starts to separate from it. As illustrated in Figure 2.1, the blue dashed airflow separates at the trailing edge, and flow separation reaches forward towards the leading edge with worsening flow conditions until less lift, but mostly drag is generated. If the airflow is detached completely, the airfoil is stalling.

The red curve illustrates in Figure 2.1 the pressure distribution and emphasizes that most suction forces are generated in the first section of the airfoil and fade out towards the trailing edge. The pressure distribution over an airfoil is a common representation in aerodynamics. It represents the localized forces over the surface area

2. State of the Art and Fundamental Principles

of an airfoil. The dimensionless pressure coefficient C_P , as defined in equation 2.2, is dependent on static barometric pressure p_∞ and the localized measured pressure by p [96].

$$C_P = \frac{p - p_\infty}{q} \quad (2.2)$$

Moreover, the dynamic pressure q relates to the pressure difference between the static barometric pressure and the applied pressure at the stagnation point, which is induced by the kinetic energy of the inflow with the air density ρ_{air} [75].

$$q = \frac{1}{2} \rho_{air} u_\infty^2 \quad (2.3)$$

The lift coefficient C_L and the drag coefficient C_D are defined with the lift F_L and drag force F_D over surface area A and set in relation to the dynamic pressure q [96].

$$C_L = \frac{F_L}{qA} \quad (2.4)$$

$$C_D = \frac{F_D}{qA} \quad (2.5)$$

The best trade-off between lift and drag coefficient in equations 2.4 and 2.5 is usually of interest [96]. For a specific cross-section of an airfoil, the section lift coefficient c_l , the total lift and area of the airfoil is replaced with the lift force per unit span of the wing l and the characteristic length l_c , as shown in equation 2.6 [75, 96].

$$c_l = \frac{l}{ql_c} = \frac{1}{c(x)} \int C_P(x) dx \quad (2.6)$$

Considering a two-dimensional airfoil section, horizontal surfaces, and a negligibly small angle of attack, the aerodynamic coefficient C_L is the integral of the pressure coefficient curve over the chord section $c(x)$.

2.1.3. Boundary Layer

The boundary layer is the thin layer of air flowing over the wing's surface. The boundary layer can either be laminar or turbulent. The layer interacts with the wing's surface. It is subjected to shearing forces, which reduce its flow speed close to the surface. While a laminar boundary layer is relatively thin with limited mass transfer, limited velocity, and low skin friction, a turbulent boundary layer is thicker with more mass transport, higher velocities near the surface, and higher skin friction. According to equation 2.7, the flow velocities at distance y from the surface are quadratic depending on the flow velocity u . The equation includes the boundary layer thickness σ at the distance x downstream from the start of the boundary layer. In literature, the boundary layer is often referred to as δ as well [96].

2. State of the Art and Fundamental Principles

$$u \approx u_\infty \left(1 - \left(1 - \frac{y}{\sigma(x)} \right)^2 \right) \quad (2.7)$$

At the outer boundary layer, the airflow reaches the free-stream velocity, which is the actual speed of the local flow velocity, which depends upon the airfoil's curvature, and the viscosity and compressibility of the air. The boundary layer thickness $\sigma(x)$ can be approximated by equations 2.8 or 2.9, depending if laminar or turbulent flow is expected. As seen in the equations 2.8 and 2.9, the Reynolds number needs to be considered [96].

$$\textit{laminar} : \sigma(x) = 5.00 \frac{x}{Re^{\frac{1}{2}}} \quad (2.8) \quad \textit{turbulent} : \sigma(x) = 0.37 \frac{x}{Re^{\frac{1}{5}}} \quad (2.9)$$

During normal flow conditions, there is low pressure on the suction side and high pressure at the tip, at the pressure side, and at the trailing edge. Near stall conditions, the momentum of flow does not overwhelm the pressure gradient to direct airflow from the high-pressure region at the trailing edge to the low-pressure region of the airfoil so that flow reverses within the boundary layer, which results in flow separation bubbles. Typical boundary layers are illustrated in Figure 2.1 on the suction side for different flow conditions. When the flow is attached, the boundary layer has the described exponential shape. At the separation point of the airfoil, the forward and inverse flow cancel each other out so that the thickness of the boundary layer abruptly increases. With detached flow conditions, the flow direction in the boundary layer even reverses, creating unintended vortexes and increasing drag further.

2.1.4. Dynamic Pressure Fluctuations and Turbulent Flow

Dynamic unsteady pressure fluctuations, turbulence, and acoustics interfere with the previously described static aerodynamic phenomena. In general turbulent flow is a regime where flow velocities and directions vary significantly and determine the acoustic sources [67, 203]. In this case, for analysis of dynamic events, the power spectral density of single pressure signals to analyze noise emissions, the cross-correlation to track turbulence propagation, and coherence functions to characterize the airfoil's turbulent flow phenomena over frequency are of interest.

2.1.4.1. Power Spectral Density

The power spectral density S_{XX} (PSD) of a pressure signal describes the power as a function of frequency and is a prominent tool to analyze the pressure's frequency content and helps to reveal noise sources and classify turbulent flow conditions. As defined in equation 2.10, the time-series $x(t)$ is windowed by a rectangular function $r_T(t)$ of period T and is an ergodic process.

2. State of the Art and Fundamental Principles

$$S_{XX}(f) = \lim_{T \rightarrow \infty} \frac{1}{T} \mathbb{E}\{|X_T(f)|^2\} \quad (2.10)$$

The variable X_T represents the Fourier transform \mathcal{F} of the time function $x(t)$ and is defined in equation 2.11 [17, 45, 81]. While Fourier transforms convert time data to the frequency domain, the power spectral density additionally norms the frequency bin width, which prevents the duration of the analyzed data set from altering the amplitude.

$$X_T(f) = \mathcal{F}\{x(t)r_T(t)\} = \int_{-T/2}^{T/2} x(t)e^{-j2\pi ft} dt \quad (2.11)$$

Generalized to discrete data $x[m]$, if a window with the boundaries $-M < m < M$ is introduced, the power spectral density S_{XX} is defined as equation 2.12, whereas \mathbb{E} is the expectation of the signals [17, 45, 81]. The period T is the multiple of sampling time Δt and the window size M .

$$S_{XX}(f) = \lim_{M \rightarrow \infty} \frac{\Delta t^2}{T} \left| \sum_{m=-M}^M x[m]e^{-i2\pi fm\Delta t} \right|^2 \quad (2.12)$$

2.1.4.2. Cross-Correlation

The cross-correlation of two or more pressure signals reveals the phase delay of two signals. Such information is used to investigate the use of propagation direction, and velocity in separated flow regions [166]. For the sake of explanation, the time series $x(t)$ and $y(t)$ are assumed to be sine functions as given in equation 2.13, whereas symbol ϕ represents an amplitude, f the frequency of the phenomena, t the time and ϕ the phase of the signal.

$$x(t) = \sin(2\pi ft + \phi) \quad (2.13)$$

The phase of the signal ϕ and the discussed phase delay or time difference τ are in relation 2.14.

$$\phi = 2\pi f\tau \quad (2.14)$$

The cross-correlation $R_{xy}(\tau)$ of two time-series $x(t)$ and $y(t + \tau)$ is in the following calculated by equation 2.15, whereas the $x^*(t)$ denotes the complex-conjugated of the signal in period T . [17].

$$R_{xy}(\tau) = \mathbb{E}\{|x(t)y(t + \tau)|^2\} = \lim_{T \rightarrow \infty} \frac{1}{2T} \int_{-T}^T x^*(t)y(t + \tau) dt \quad (2.15)$$

As the measurement data is usually discrete, the cross-correlation is used by the definition 2.16, whereas τ_m represents the delay in samples, m the sample, and M

2. State of the Art and Fundamental Principles

the total amount of samples in the dataset [17].

$$R_{xy}[m] = \lim_{M \rightarrow \infty} \frac{1}{M} \sum_{m=1}^M x[m]^* y[m + \tau_m] \quad (2.16)$$

The cross-correlation 2.16 represents the similarity of the signals at a given shift. Including the layout information and distances between measurement locations, the delay reveals the turbulence field's propagation direction and propagation velocity.

2.1.4.3. Coherence

Identifying the coherent structure of an airfoil helps to understand the formation, evolution, and acoustic properties of turbulent airflow. The following coherence function 2.17 represents the coherence $\gamma_{XY}^2(f)$ over the frequency of the signals and stays between zero and one. It normalizes cross-spectral absolute values by the auto power spectral densities and gives an estimation of causality between the signals $x(t)$ and $y(t)$ at each frequency f [17].

$$\gamma_{XY}^2(f) = \frac{|S_{XY}(f)|^2}{S_{XX}(f)S_{YY}(f)} \quad (2.17)$$

The phase shifts ϕ are derived from the argument of the complex cross-spectral density $S_{XY}(f)$ at the frequency f , where coherence $\gamma_{XY}^2(f)$ maximizes. The argument is the angle between the real and the imaginary part of a complex number [17]. The cross-spectral density $S_{XY}(f)$ is defined by equation 2.18, with the cross correlation R_{xy} of signal $x(t)$ and $y(t + \tau)$ [17, 45].

$$S_{xy}(f) = \int_{-\infty}^{\infty} R_{xy}(\tau) e^{-i2\pi f \tau} d\tau \quad (2.18)$$

For discrete signals as measurement data, the cross-spectral density and the cross-correlation are in a relation, described by equation 2.19 [17].

$$S_{xy}[f] = \sum_{m=-\infty}^{\infty} R_{xy}[\tau_m] e^{-i2\pi f \tau_m} \Delta\tau \quad (2.19)$$

Based on the coherence function, the spanwise coherence length scale of turbulent structures Λ_p characterizes the airfoil's turbulent flow phenomena over frequency. The spanwise coherence length scale includes in equation 2.20 the separation distance between two or more sensors Δz and origins from the averaged coherence function of all sensors γ_{XY} [7, 8, 215]. With an increasing coherence length scale, the airflow persists in form over a longer distance.

$$\Lambda_p(f) = \frac{\Delta z}{-\ln(\gamma_{XY}(f))} \quad (2.20)$$

2.2. Optical Principles

In order to take advantage of the unique capabilities of fiber-optic pressure sensors, a measurement system utilizing Fabry–Pérot pressure transducers is discussed. The fiber-optic measurement setup is separated into a sensor transducer, which modulates a light signal based on pressure differences, and the measurement device, which illuminates the sensor and utilizes a linear demodulation method to convert the received optical information to a digital signal [217, 219]. Both components are discussed in this chapter, which provides an analytic description of the applied optical principles. For a detailed derivation of the Fabry–Pérot effect, other terminology such as light, reflection, transmission, and optical waveguides are discussed beforehand. Next to the Fabry–Pérot terminology, the working principle of an edge-filter interrogator is introduced.

2.2.1. Light as an Electromagnetic Wave

In physics, light is defined as an electromagnetic field. It is typically described as a sinusoidal waveform with an amplitude \hat{E} for the electrical field, respectively \hat{H} for the magnetic field, a constant frequency ω in space z and time t . As illustrated in Figure 2.2, the electric field E and the magnetic field H are perpendicular to each other in the direction of propagation. Therefore, both field types are unambiguously transferable to each other by multiplication with the impedance of free space Z_0 , which equals the ratio of the magnetic μ_0 and electric constant ϵ_0 [40, 178, 196].

$$E(z,t) = Z_0 \cdot H(z,t) = \sqrt{\frac{\mu_0}{\epsilon_0}} \cdot H(z,t) \quad (2.21)$$

Considering dielectric material as media in which the wave travels, the electric and magnetic field relationship derives from the Maxwell equations to the well-known electric wave equation 2.22 [40, 178, 196]. A dielectric material is not electrically conducting, whereas no free charges interfere with the electromagnetic field. Therefore, as a necessary simplification for the following wave equation, the material is described with purely optical properties and is lossless. Therefore the relative magnetic permeability equals $\mu_r = 1$ and the dielectric permittivity ϵ , which relates to the refractive index by $\epsilon = n^2$, is of real value $\epsilon \subseteq \mathbb{R}$. The operator ∇ in the wave equation 2.22 represents the second derivative in time and propagation direction.

$$\nabla^2 \vec{E} + \epsilon k^2 \vec{E} = 0 \quad (2.22)$$

Additionally, the electromagnetic wave equation depends on the wavenumber k , the angular frequency ω , the speed of light c in a vacuum, or the wavelength λ of the light. The wavenumber is defined by equation 2.23 [40, 178, 196].

$$k = \frac{\omega}{c} = \frac{2\pi}{\lambda} \quad (2.23)$$

2. State of the Art and Fundamental Principles

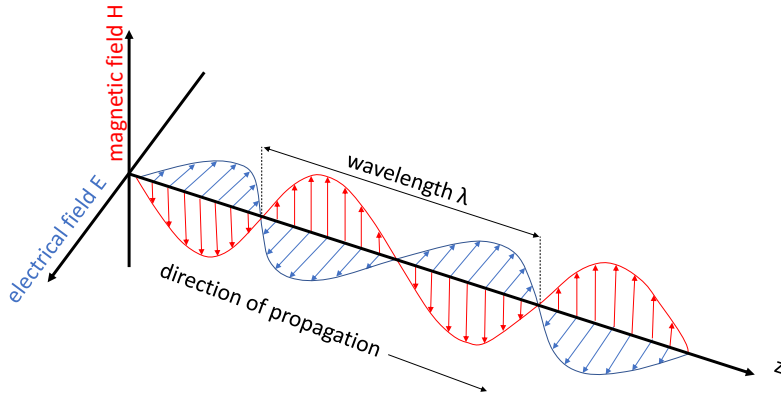


Figure 2.2.: Light as an electromagnetic waveform. Electric and magnetic field vector of a linearly polarized plane electromagnetic wave. Adapted from [40, 178, 196].

2.2.2. Reflection, Transmission, and Absorption

When light strikes the boundary of two materials, a portion of it is either reflected, transmitted, or absorbed. While the reflection \mathcal{R} is the process in which electromagnetic radiation is returned at a boundary, the transmission \mathcal{T} describes the passage of electromagnetic radiation through a medium. The absorption \mathcal{A} is the energy conversion of the radiation to other energy forms. The quantities are defined as ratios, are dimensionless, and their sum equals one due to the light's energy conservation [40, 196].

$$\mathcal{R} + \mathcal{T} + \mathcal{A} = 1 \quad (2.24)$$

The law of reflection 2.25 and Snell's law 2.26 describe the relationship between the angle of incident θ_i and the angle of the transmitting ray θ_t for reflection and transmission [40, 196].

$$\theta_i = \theta_r \quad (2.25)$$

In the case of reflection, the angle of incidence is equal to the angle of reflection. For transmission, Snell's law has to be applied, as light distortion might force a deviation from a straight trajectory. The variable n_1 describes the refractive index of the first medium, and the refractive index n_2 marks the second interacting medium [40, 196, 209].

$$n_1 \sin(\theta_i) = n_2 \sin(\theta_t) \quad (2.26)$$

Moreover, the reflection, transmission, and absorption depend on the wavelength

2. State of the Art and Fundamental Principles

of the affected radiation. The quantities reflection and transmission can be subdivided into regular and diffuse processes. Whereas, r_r describes regular and r_d diffuse reflectance, and regular t_r and diffuse transmission t_d , as shown in equation 2.27. Both processes combined equal the overall amount of reflection or transmission [40, 178, 196].

$$\begin{aligned} r &= r_r + r_d \\ t &= t_r + t_d \end{aligned} \tag{2.27}$$

Optical components have polarization properties when used other than at the incident angle of zero degrees. Therefore, the reflection and transmission coefficients might also depend on the polarization state of the incoming light and the geometric distribution of the incident radiation. There is a set of Fresnel coefficients for two different linear polarization components of the incident wave, named S and P . Polarization directions S and P are defined by their relation to the plane of incidence. The P -polarized light is parallel, and S -polarized, perpendicular to the reflecting surface. Any polarization state can be resolved by combining these orthogonal linear polarizations. Taking polarization effects into account, Fresnel's law of reflection expands to the terms 2.28, in which r_s and r_p are reflectances in the respective polarization directions.

$$\begin{aligned} r_s &= \frac{n_1 \cos(\theta_i) - n_2 \cos(\theta_t)}{n_1 \cos(\theta_i) + n_2 \cos(\theta_t)} \\ r_p &= \frac{n_1 \cos(\theta_t) - n_2 \cos(\theta_i)}{n_1 \cos(\theta_t) + n_2 \cos(\theta_i)} \end{aligned} \tag{2.28}$$

The set of equations 2.29 describes Fresnel's law of transmission coefficients, including polarization effects, in which t_s and t_p are transmissions in the respective polarization directions.

$$\begin{aligned} t_s &= \frac{2 \cdot n_1 \cos(\theta_i)}{n_1 \cos(\theta_i) + n_2 \cos(\theta_t)} \\ t_p &= \frac{2 \cdot n_1 \cos(\theta_t)}{n_1 \cos(\theta_t) + n_2 \cos(\theta_i)} \end{aligned} \tag{2.29}$$

Increasing the incident angle alters the polarization states of refracted and reflected light. At Brewster's angle, unpolarized incoming light gets completely linear S -polarized in reflection [40, 196, 209]. A negative reflection coefficient results in light reflection from an optically thinner to an optically denser medium, i.e., $n_1 < n_2$. Therefore, the reflected wave suffers a phase shift by π . In this case, the wave is multiplied by the expression $r \cdot e^{j\pi} = -r$. While a reflection propagates in the same medium as the incident wave, the reflection \mathcal{R} is the square magnitude of r in trans-

2. State of the Art and Fundamental Principles

mission waves traveling in different directions in the two media. In order to refer to the previously mentioned equation 2.24, the power coefficient has to be obtained by term 2.30 [40, 196, 209].

$$\mathcal{R} = r^2$$

$$\mathcal{T} = \frac{n_2 \cos(\theta_t)}{n_1 \cos(\theta_i)} t \quad (2.30)$$

The total internal reflection is an exceptional optical phenomenon utilized in single-mode fibers and later introduced beam deflection in the sensor design. In case the light ray faces a boundary from optically dense to optically thinner medium, i.e., $n_2 < n_1$, at an angle larger than the critical angle Φ_c , total internal reflection occurs, which reflects reflected the light into the the same medium. This optical phenomenon is used with common optical fibers and in the later introduced sensor design [40, 178, 196, 209].

$$\Phi_c = \arcsin\left(\frac{n_2}{n_1}\right) \quad (2.31)$$

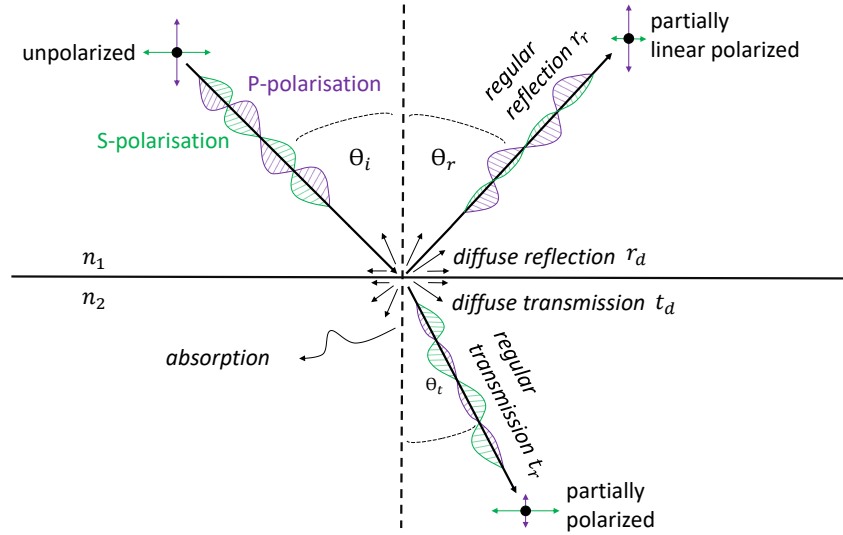


Figure 2.3.: Wave vector of the incident, refracted and reflected wave at the planar interface between two media. in the direction of transmission, the light gets refracted. In the direction of reflection, the angle for regular reflection equals the angle of incident light. When used other than at the incident angle of zero degrees, the light might polarize depending on the incident angle. Adapted from [40, 196, 209]

2.2.3. Optical Fibers

A typical fiber consists of a core, cladding, coating, and a buffer. Such glass fiber with a step-index refractive index profile consists of a homogeneous core with refractive index n_1 and radius a . It is surrounded by a cladding material with the lower refractive index n_2 .

$$n(r) = \begin{cases} n_1, & r \leq a \\ n_2, & r > a \end{cases} \quad (2.32)$$

The ideal fiber is cylindrical, lossless, straight, and free of internal or external stresses. By modeling light as rays, the fiber's core channels the light along the fiber due to total reflection. Nevertheless, modeling light as an electromagnetic wave reveals further insights. Because the difference in the refractive index between core and cladding is typically minimal and is a function of the radius r only, the electromagnetic waves are guided weakly. Assuming a dielectric material, homogeneous cylindrical and constant structure along the fiber axis z , the wave equation can be expressed as equation 2.33. The first exponential term represents the dependency of the field in space, and the second is the time dependency of the oscillating wave [40, 130, 209].

$$\vec{E}(\varphi, z) = \hat{E}(\varphi) e^{\pm j\beta_m z} e^{-i\omega t} \quad (2.33)$$

Each guided mode has a field distribution $\vec{E}(\varphi)$ and a corresponding propagation constant β_m , which depends on the penetration depth of the field into the fiber cladding. The symbol φ represents the polar angle. The sign of the propagation constant in the longitudinal term indicates the direction of propagation of the electromagnetic wave. For example, the effective refractive index of a mode with n_{eff} is related to the wavenumber in vacuum to equation 2.34 [40, 130, 209].

$$n_{\text{eff}} = \frac{\beta_m}{k} \quad (2.34)$$

The total electric field of the guided modes superposes to equation 2.35, in which each field E_m and propagation constant β_m is individual for the modes [40, 130, 209].

$$\vec{E}(\varphi, z) = \sum \hat{E}_m e^{\pm j\beta_m z} e^{\pm i\beta z} \quad (2.35)$$

The electromagnetic wave is guided dominantly in the core of the glass fiber and treated as a weakly guided electromagnetic wave. In contrast to multi-mode fibers, only a single fundamental mode propagates in a single-mode fiber [40, 209]. Therefore, the fiber geometry and optical properties are chosen carefully to achieve that only one mode can propagate with the fiber. The fiber's normalized frequency parameter, so-called V -number, determines the number of guided modes $V^2/2$ in a fiber and is given by equation 2.36. The fiber becomes single-mode for a given

2. State of the Art and Fundamental Principles

wavelength when $V < 2,405$.

$$V = 2\pi \frac{a}{\lambda} \sqrt{n_1^2 - n_2^2} \quad (2.36)$$

The very first primary mode of a cylindrical optical fiber is also called LP_{01} mode (linear polarization). This radial distribution of the field of the fundamental mode is described in good approximation with a Gaussian function as equation 2.37, in which w_G denotes the Gaussian field radius. This electromagnetic field pattern of the radiation is in the plane perpendicular to the propagation direction. The Gaussian field radius marks the point at which the field distribution has dropped to $1/e$ of the maximum field amplitude \hat{E} . This approximation of the field distribution is illustrated in Figure 2.4 for the fundamental mode, and it becomes apparent that the field also reaches into the cladding [40, 114, 123, 178, 209].

$$E(r) = \hat{E} e^{-\frac{r^2}{w_G^2}} \quad (2.37)$$

While in multi-mode fibers, light propagates on different paths, each light mode has an individual path, reaching the end of the optical fiber at different times. This spread is modal dispersion and limits the sampling rate and communication distances. Single-mode fibers' dispersion is lower and allows higher bandwidth signals, which cover a longer distance. The dimension of the core for wavelengths from 1500 nm to 1600 nm for a single mode fiber is equal to the transverse mode field diameter of about 10 μm . The cladding diameter typically has a diameter of 125 μm [29, 123, 209]. In order to achieve different refractive index profiles, the quartz glass is isotropic differently doped [40, 209]. Depending on the application, the quartz glass is usually coated with a coating of acrylate or polyimide to protect the fiber from mechanical damage and other environmental influences, which increases the diameter to typically 160 μm to 245 μm . Other protective plastic buffers surround the fiber with various diameters in industrial applications [29, 114, 130].

As the Gaussian function describes the near field of the fiber, the radiation pattern, i.e., the field distribution at a distance z , can be described as a Gaussian beam [114, 209]. With increasing distance from the fiber end, the mode field diameter of the beam widens. The field's boundary is expressed in equation 2.38. As an approximation, the mode field diameter of a single-mode fiber is roughly six to nine times the operating wavelength [99].

$$w(z) = w_G \sqrt{1 + \left(\frac{z}{Z_R}\right)^2} \quad (2.38)$$

The shape of the field distribution boundary $w(z)$ approaches asymptotically to a straight line, which originates from the fiber's core at the angle θ_D , which is defined in equation 2.39.

$$\theta_D = \arctan\left(\frac{w_G}{Z_R}\right) \quad (2.39)$$

2. State of the Art and Fundamental Principles

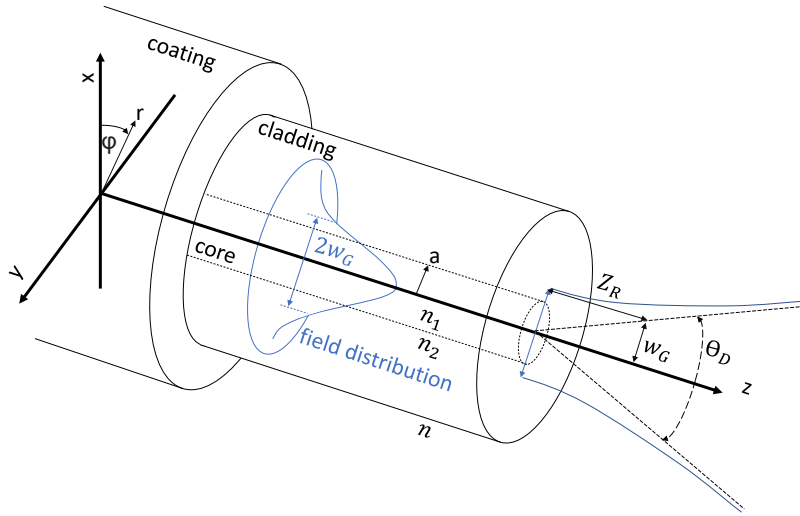


Figure 2.4.: An ideal single-mode glass fiber with step index refractive index profile and its radiation characteristic. The ideal single-mode glass fiber consists of a homogeneous fiber core with refractive index n_1 and radius a . It is surrounded by a cladding material with a lower refractive index n_2 . The coordinate system is the z -axis parallel to the fiber axis. The near-field distribution at the end of the fiber is described as a Gaussian function. The far field is expressed with the Gaussian beam. Adapted from [114, 209].

The distance Z_R to which the beam is mainly collimated is referred to as Rayleigh distance, defined in equation 2.40 [40, 209].

$$Z_R = \frac{1}{2}k \cdot n \cdot w_G^2 = \frac{\pi}{\lambda} \cdot n \cdot w_G^2 \quad (2.40)$$

The radiation characteristics of the fiber are illustrated in Figure 2.4. An important parameter for such fiber is the numerical aperture NA , described by the two refractive indexes of core and cladding as in equation 2.41. The numerical aperture measures the fiber's acceptance angle θ_D and determines how strongly a fiber guides the field and radiation characteristics [40].

$$NA = \sqrt{n_1^2 - n_2^2} = n \sin(\theta_D) \quad (2.41)$$

A particular challenge is additionally to couple light back into the fiber. Especially considering single-mode fibers, the fiber coupling efficiency η is limited by the wavefront mode-matching issues, geometrical losses, Fresnel losses, and angular losses. For extrinsic fiber-optic interferometric applications, in which light is coupled out and into a fiber, the weak fiber coupling efficiency is a challenge in the design phase to obtain the maximum signal-to-noise ratio [205].

2.2.4. Fabry–Pérot Interferometer

This research discusses an optical transducer based on an extrinsic Fabry–Pérot interferometer. In order to understand the functionality of the transducer, the Fabry–Pérot interferometer principle needs to be introduced. The fundamental derivation of important equations is described by utilizing electromagnetic waves to ensure a deep understanding of the filtering characteristics of the Fabry–Pérot interferometer in this sensing application.

Generally, an interferometer is based on the superposition of optical waves. Here, a Fabry–Pérot interferometer consists of two mirrors in the distance L_0 from each other. The mirrors form an optical resonator and are described by a reflection or transmission coefficient. If the resonator is not placed in a vacuum with the refractive index $n = 1$, the optical path length $\Lambda_0 = nL_0$ varies from the geometrical length. Each wavelength λ of the light, which is a multiple N of the doubled optical length $2\Lambda_0$, interferes destructively in the direction of reflection. In the direction of transmission, the light interferes constructively. In order to obtain the interference by the superposition of optical waves, the light must be coherent with each other. The optical waves originate from the same light source [40, 50, 123, 178, 196, 209].

2.2.4.1. Spectrum in Direction of Transmission

With the given set of variables and considerations from chapter 2.2.1, the interference of the electromagnetic field describes an interferometer. If an electromagnetic wave with amplitude \hat{E}_0 is coupled into the resonator at the angle ϕ , a reflecting field \hat{E}_R and transmitting field \hat{E}_T resonate within the resonator L_0 as multiple reflections occur. After each revolution, the electromagnetic field is delayed by a phase factor, described with the exponential term. Figure 2.5 illustrates the following analytical model. In most applications, the incident angle of the wave is $\phi = 0$, which simplifies the phase shift to $e^{-i2k\Lambda}$ [5, 50, 178].

Although the reflection and transmission coefficients for interactions of light at an optically thinner to the optically denser medium are not the same as the coefficients from the optically denser to the optically thinner medium, it is assumed that these are identical in order to simplify the following equations. The resulting electromagnetic field is obtained in the transmission direction by summing up all waves. The term in parentheses in the set of equation 2.42 is substituted by the geometric series $\sum_{m=0}^{\infty} q^m = \frac{1}{1-q}$ [178].

2. State of the Art and Fundamental Principles

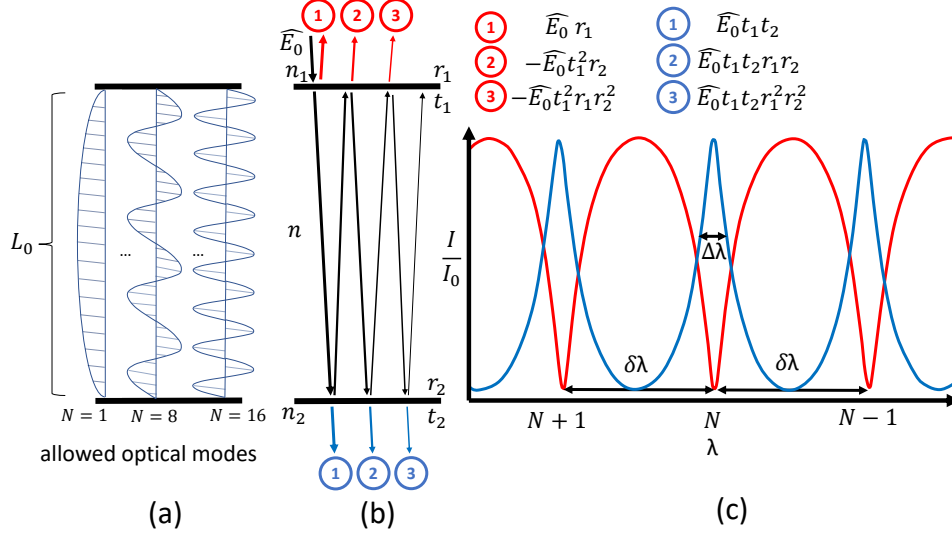


Figure 2.5.: Illustration for the description of the Fabry-Pérot resonator. An electromagnetic wave is partially coupled into the resonator. The resonator is optically thinner than the surrounding medium ($n_1 > n$ and $n_2 > n$). The optical boundary layers form a mirror. Figure (a) illustrates that only standing waves, whose lengths are an integer multiple of the optical length, are allowed optical modes. Figure (b) displays that the electromagnetic wave oscillates in the resonator and is partially coupled. The reflected and transmitted fields result from the superposition of the fields. Figure (c) shows the exemplar relation of intensity and wavelength of a spectrum for various modes. The blue curve displays the logarithmic spectrum in transmission. The red curve illustrates the spectrum in the direction of reflection.

$$\hat{E}_T = \hat{E}_0 t_1 t_2 e^{-ik\Lambda} + \hat{E}_0 t_1 t_2 r_1 r_2 e^{-3ik\Lambda} + \hat{E}_0 t_1 t_2 r_1^2 r_2^2 e^{-5ik\Lambda} + \dots \quad (2.42)$$

$$= \hat{E}_0 t_1 t_2 e^{-ik\Lambda} \left(1 + r_1 r_2 e^{-2ik\Lambda} + r_1^2 r_2^2 e^{-4ik\Lambda} + \dots \right) \quad (2.43)$$

$$= \hat{E}_0 t_1 t_2 e^{-ik\Lambda} \sum_{m=0}^{\infty} \left(r_1 r_2 e^{-2ik\Lambda} \right)^m \quad (2.44)$$

$$= \hat{E}_0 \frac{t_1 t_2 e^{-ik\Lambda}}{1 - r_1 r_2 e^{-2ik\Lambda}} \quad (2.45)$$

Utilizing Euler's formula $2 \cdot \cos(x) = e^{ix} + e^{-ix}$, the exponential terms convert into an angular relation so that the equation needs no longer to be treated in a complex manner. The equations are further simplified by converting the cosine term to a squared sine function using the trigonometric formula $\sin^2(x) = \frac{1}{2}(1 - \cos(2x))$. Additionally, considering that $t_1^2 + r_1^2 \approx 1$ and that the intensity I_T of the electric waves is proportional to the field energy squared $I_T \approx |E_T|^2$, the relative intensity simplifies to the dependence in equation 2.46 [5, 50, 178].

2. State of the Art and Fundamental Principles

$$\frac{I_T}{I_0} = \mathcal{F}_{FP} = \frac{\hat{E}_T \cdot \hat{E}_T^*}{\hat{E}_0^2} \quad (2.46)$$

$$= \frac{t_1^2 t_2^2}{1 + r_1^2 r_2^2 - r_1 r_2 (e^{2ik\Lambda} + e^{-2ik\Lambda})} \quad (2.47)$$

$$= \frac{t_1^2 t_2^2}{1 + r_1^2 r_2^2 - 2r_1 r_2 \cos(2k\Lambda)} = \frac{t_1^2 t_2^2}{1 + r_1^2 r_2^2 - 2r_1 r_2 (1 - 2\sin^2(k\Lambda))} \quad (2.48)$$

$$= \frac{t_1^2 t_2^2}{(1 - r_1 r_2)^2} \frac{1}{\left(1 + \frac{4r_1 r_2}{(1 - r_1 r_2)^2} \sin^2(k\Lambda)\right)} \quad (2.49)$$

$$= \frac{t_1^2 t_2^2}{(1 - r_1 r_2)^2} \frac{1}{(1 + F \sin^2(k\Lambda))} \quad (2.50)$$

If the two mirrors are identical, then the equation simplifies further to the term 2.51, because $t_1^2 = t_2^2 \approx \mathcal{T}$ and $\mathcal{R} = r_1 r_2$. Losses of the light due to coupling into the resonator are neglected [178]. The finesse coefficient F is introduced and discussed in section 2.2.4.4.

$$\frac{I_T}{I_0} = \frac{1}{(1 + F \sin^2(k\Lambda))} \quad (2.51)$$

2.2.4.2. Spectrum in Direction of Reflection

In contrast to the light spectrum in the transmission direction, a minima for the specific interfering wavelengths occur for the reflection. For simplicity, it is assumed that $t_1^2 + r_1^2 \approx 1$. The reflected field is the sum of the direct reflection at the entrance and the light interfering in the resonator [5, 50, 178].

$$\hat{E}_R = \hat{E}_0 r_1 - \hat{E}_0 r_2 t_1^2 e^{-2ik\Lambda} - \hat{E}_0 r_1 r_2^2 t_1^2 e^{-4ik\Lambda} - \hat{E}_0 r_1^2 r_2^3 t_1^2 e^{-6ik\Lambda} - \dots \quad (2.52)$$

$$= \hat{E}_0 r_1 - \hat{E}_0 t_1^2 r_2 e^{-2ik\Lambda} \left(1 + r_1 r_2 e^{-2ik\Lambda} + r_1^2 r_2^2 e^{-4ik\Lambda} + \dots\right) \quad (2.53)$$

$$= \hat{E}_0 r_1 - \hat{E}_0 t_1^2 r_2 e^{-2ik\Lambda} \sum_{m=0}^{\infty} \left(r_1 r_2 e^{-2ik\Lambda}\right)^m \quad (2.54)$$

$$= \hat{E}_0 r_1 - \hat{E}_0 \frac{t_1^2 r_2 e^{-2ik\Lambda}}{1 - r_1 r_2 e^{-2ik\Lambda}} = \hat{E}_0 \frac{r_1 - r_2 (t_1^2 + r_1^2) e^{-2ik\Lambda}}{1 - r_1 r_2 e^{-2ik\Lambda}} \quad (2.55)$$

$$= \hat{E}_0 \frac{r_1 - r_2 e^{-2ik\Lambda}}{1 - r_1 r_2 e^{-2ik\Lambda}} \quad (2.56)$$

The set of equation 2.57 derives the relative intensity of the reflected field. Since mathematically, the reflected field E_R differs from the transmitted field E_T only in the numerator, the calculation simplifies to the transformation of the numerator [5, 50, 178].

2. State of the Art and Fundamental Principles

$$\frac{I_R}{I_0} = \mathcal{R}_{FP} = \frac{\hat{E}_R \cdot \hat{E}_R^2}{\hat{E}_0^2} = \frac{1}{(1 - r_1 r_2)^2} \frac{r_1^2 + r_2^2 - 2r_1 r_2 \cos(2k\Lambda)}{(1 + F \sin^2(k\Lambda))} \quad (2.57)$$

$$= \frac{1}{(1 - r_1 r_2)^2} \frac{(r_1 - r_2)^2 + 4r_1 r_2 \sin^2(k\Lambda)}{(1 + F \sin^2(k\Lambda))} \quad (2.58)$$

$$= \frac{\frac{(r_1 - r_2)^2}{(1 - r_1 r_2)^2} + \frac{4r_1 r_2}{(1 - r_1 r_2)^2} \sin^2(k\Lambda)}{1 + F \sin^2(k\Lambda)} \quad (2.59)$$

$$= \frac{M_{FP} + F \sin^2(k\Lambda)}{1 + F \sin^2(k\Lambda)} \quad (2.60)$$

The equations include the finesse coefficient F , which is discussed in a separate section. Additionally, the factor M_{FP} describes the difference in the reflection coefficients of the two mirrors. If the two mirrors are identical, the result is $M_{FP} = 0$, which would minimize the offset of the spectrum in a lossless resonator. For all other combinations of mirrors, the result is an offset of the spectrum. The mismatch value M_{FP} attenuates the interference modulation in an ideal resonator. In real lossy applications, the second mirror is highly reflective to counteract losses due to diffuse reflections, diverging lens effects, and absorption [5, 50, 178].

2.2.4.3. Resonator Condition

The maximum interference is reached in the formula only if the sine term $\sin^2(k\Lambda)$ vanishes. For this, the argument of the sine must be a multiple N of π . The resonator condition can be derived in equation 2.61 [178].

$$\sin^2(k\Lambda) \stackrel{!}{=} 0 \rightarrow k\Lambda = \frac{2\pi}{\lambda} \cdot nL \stackrel{!}{=} N \cdot \pi \quad (2.61)$$

$$2nL = N\lambda$$

Each wavelength λ of the light, which is a multiple N of the doubled optical length $2\Lambda_0$, interferes. If the coupling of the light is tilted by the angle ϕ , the resonator condition expands by a cosine term $\cos(\phi)$ [178].

$$N \cdot \lambda = 2nL \cdot \cos(\phi) \quad (2.62)$$

By equalizing the interference condition $N\lambda_1 = 2nL\cos(\phi)$ with the interference condition of the following order $(N + 1)\lambda_2 = 2nL\cos(\phi)$ the formula 2.63 is derived. Consequently, the order N can also be determined from the spectrum by calculating $\lambda_2/(\lambda_1 - \lambda_2)$. With those parameters, the length of the resonator can be derived from the spectrum [178].

2. State of the Art and Fundamental Principles

$$L = \frac{1}{2n \cos(\phi)} \frac{\lambda_1 \lambda_2}{\lambda_1 - \lambda_2} \quad (2.63)$$

In the particular interest of extrinsic Fabry–Pérot sensors, in which the reflection \mathcal{R} of the mirrors are usually similar but low, it follows that the set of the equation can be further simplified to a cosine representation 2.64 with good approximation [171, 181]. The symbol \mathcal{R}_{FP} represents the filter in reflection and \mathcal{T}_{FP} in the direction of transmission.

$$\begin{aligned} \mathcal{R}_{FP} &\approx 2R(1 + \cos(2k\Lambda)) \\ \mathcal{T}_{FP} &\approx 1 - 2R(1 + \cos(2k\Lambda)) \end{aligned} \quad (2.64)$$

2.2.4.4. Finesse

The finesse F characterizes the resonator in quality and depends solely on the mirrors but not on the length of the resonator. A larger finesse F means a high selectivity in the spectrum. At high finesse values, the constructively interfering wavelengths are more distinguishable from the destructively interfering wavelengths. The transmission function would resemble Dirac distributions if the finesse were infinitely large. Therefore, the finesse is the ratio of the width of the peak $\Delta\lambda$ to the distance $\delta\lambda$ between the intensity maxima. Assuming two mirrors of high-reflectance $\mathcal{R} = r_1 r_2$, the finesse is strongly coupled to the reflection properties of the mirrors, as shown in the equation 2.65 [5, 40, 181, 196].

$$F = \frac{\pi\sqrt{\mathcal{R}}}{1 - \mathcal{R}} \quad (2.65)$$

Nevertheless, the discussed derivation of the Fabry–Pérot interferometer includes the finesse coefficient F , which is related to the finesse F of the resonator in term 2.66.

$$F = \frac{\pi}{2 \arcsin\left(\frac{1}{\sqrt{F}}\right)} \quad (2.66)$$

In the particular interest of fiber-optic Fabry–Pérot sensors, it should be noted that the concept of finesse is only applicable for Fabry–Pérot interferometers with high reflection [171, 181]. Due to manufacturing challenges, the technically feasible finesse for resonators with parallel plane mirrors is limited. First and foremost, mechanical imperfections, such as the surface roughness and flatness of the mirrors, limit the finesse [39]. Next to that, any spherical error of the mirrors worsens the finesse. In this case, the light is divergent, and the fields are reflected at different spatial angles, so the phase relationships to each other become blurred [174].

2. State of the Art and Fundamental Principles

2.2.4.5. Free Spectral Range

Besides the modulation value M_{FP} and the finesse coefficient, the parameter Free Spectral Range FSR is decisive for the characterization of the Fabry–Pérot resonator. The FSR value, introduced here as $\Delta\lambda$, describes the distance between two adjacent wavelength pairs satisfying the resonator condition. Nevertheless, this distance depends on the order of interference and thus on the wavelength λ_0 . Moreover, the free spectral range also depends on the optical path length of the resonator [40, 196].

$$\Delta\lambda = \frac{\lambda^2}{2\Lambda \cdot \cos(\phi) + \lambda_0} \quad (2.67)$$

2.2.4.6. Full-Width-Half-Maximum

The $FWHM$ term, the Full-Width-Half-Maximum abbreviation, describes the peak's bandwidth at half maximum intensity. The $FWHM$ term, denoted $\delta\lambda$ in the following, is inversely proportional to the finesse F [40, 196].

$$\delta\lambda = \frac{\Delta\lambda}{F} \quad (2.68)$$

2.2.5. Edge-Filter Interrogation Principle for Fabry-Pérot Sensors

One of the most promising approaches in terms of price-performance ratio to read out a limited number of sensors is a single-channel edge filter measurement system [10, 90]. Although this interrogation principle has the drawback of allowing only one sensor per channel and not providing full-spectrum information, it allows a cost-effective, robust design, anti-aliasing, and fast sampling [114, 130, 171, 184].

An edge filter measurement device consists of a broadband light source, illuminating a single fiber-optic sensor, beam splitters, a 3-dB coupler, and at least one edge filter and two separate photodetectors. In contrast, both photodetectors have a sensitivity $E_i(\lambda)$. The optical edge filter possesses a wavelength-dependent transmittance. The filter transmission is described as $\mathcal{T}(\lambda)$ and preferably has a wide linear range over the bandwidth, which corresponds to the full-scale measurement range [184]. After the sensor's light spectrum $\mathcal{R}_{FP}(\lambda)$ is back-reflected into the measurement device, it is split into two channels by a beam splitter. The splitting ratio should have neglectable wavelength dependence [184]. At least one of the two optical paths contains the edge filter element. Usually, the first channel illuminates a photodiode directly and acts as a reference for the total amount of illumination. The second path is filtered by an optical bandpass filter and illuminates the second photodetector [114, 130, 184].

While the intensity of illumination relates to the total light power for the first photodiode Φ_R , the illumination level for the second photodiode Φ_F depends additionally on the phase shift of the sensor's spectrum with respect to the optical filter. The measured ratio ρ reveals the phase shift information of the reflected light [160, 204, 206]. Ideally, the ratiometric principle of both intensities ρ cancels

2. State of the Art and Fundamental Principles

out the parasitic power dependencies and directly depends on the Fabry–Pérot interferometer’s phase information λ_0 . Fluctuations of light power, which might be introduced by fiber bending or transmission loss by connectors, are mostly canceled out [58, 108, 160].

$$\rho(\lambda_0) = \frac{\Phi_F(\lambda_0)}{\Phi_R(\lambda_0)} = \frac{\int \mathcal{R}_{FP}(\lambda, \lambda_0) \mathcal{T}(\lambda) I_0(\lambda) E_F(\lambda) d\lambda}{\int \mathcal{R}_{FP}(\lambda, \lambda_0) I_0(\lambda) E_R(\lambda) d\lambda} \quad (2.69)$$

The equation 2.69 describes the relationship of the reflecting Fabry–Pérot spectrum $\mathcal{R}(\lambda, \lambda_0)$, the edge filter $\mathcal{T}(\lambda)$, the spectral power density of the light source $I_0(\lambda)$ and the resulting scalar value ρ , whereas the illuminating light spectrum defines the boundaries for integral.

After signal amplification and conditioning, the sensor’s wavelength is computed in a data processing layer. Therefore, the continuous and analog photocurrents are amplified accordingly and analog filtered via an electronic low-pass filter. Next, the amplified currents are value- and time-discretized sampled by an analog-to-digital converter and further processed by a digital signal processing unit. Figure 2.6 illustrates the schematic of the edge-filter interrogator.

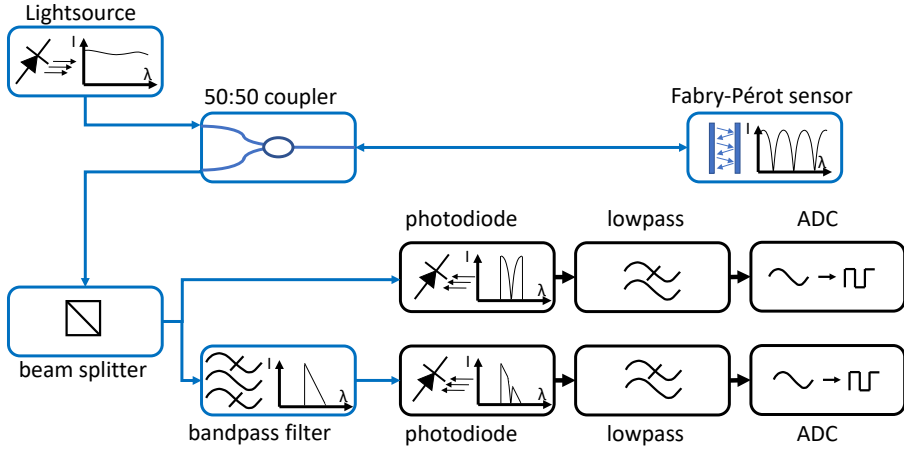


Figure 2.6.: Schematic structure of an edge-filter based fiber-optic measurement device for Fabry–Pérot sensors. The fiber-optic measurement device reads each sensor’s phase condition and converts the optical signal to a digital signal. The edge-filter principle prevents aliasing effects, increases durability, and ensures high sampling frequencies. Due to the continuous analog signal acquisition, it is possible to realize a true low pass filtering, which is essential for stability during dynamic measurement and possible subsequent control applications [130].

The Fabry–Pérot interferometer’s operating point must match the quadrature point of the measurement device’s bandpass filter for a linear response. The Q -Point is defined as the spot of maximal sensitivity, or steepest slope of the relation of ρ

2. State of the Art and Fundamental Principles

and is quasi-linear for the applied physical displacement of the interferometer [160]. Such calibration function must fulfill the necessary condition of bijectivity over the entire measurement range to allow an unambiguous wavelength determination [18]. Nevertheless, at the borders of the measurement range, the signal becomes nonlinear due to the bandwidth limitation, distortion of the edge filter, and finally due to the periodicity of the sensor signal spectrum.

For narrowband Fiber-Bragg-grating sensors, the output signal of the photodetector is directly proportional to the transmission value of the optical filter element at the Bragg wavelength because the transmission function $\mathcal{T}(\lambda)$ is convolved with a Dirac-like Fiber-Bragg-grating spectrum. The signal output for more broadband Fabry–Pérot sensors includes the convolution of the transmission function $\mathcal{T}(\lambda)$ with the sinusoidal-like Fabry–Pérot spectrum $\mathcal{R}_{FP}(\lambda)$, which is more difficult to describe analytically [18]. The best practice is using fit regression of the calibration curve, regardless of the underlying filter form. The Fabry–Pérot transducer’s operating point λ_0 is, therefore, the multiplication of a sensitivity factor k of the measured ratio ρ after subtraction of its offset ρ_0 .

$$\lambda_0 = \rho^{-1}(\Phi_F, \Phi_R) = \sum_{x=1}^n k_x \cdot (\rho - \rho_0)^x \quad (2.70)$$

Figure 2.7 illustrates the calibration curve of the Fabry–Pérot sensor’s phase shift λ_0 and the resulting measurement output of the sensing system ρ . The measurement value is rescaled in this illustration to the $[0;1]$ range. The transfer curve of Fabry–Pérot sensor in combination with an edge filter interrogator equals a sinusoidal-like shape, in which the Q -point marks the operating point of highest sensitivity. The measurement range is limited by the predefined maximal deviation of the fit from the regression [219].

The interrogator’s accuracy, resolution, noise, and reproducibility in the system are subject to various systematic and statistical sources of uncertainties. Regardless of a qualitative consideration, the most prominent influencing factors are explained as follows:

Spectral characteristics of Fabry–Pérot spectrum and its match with respect to the transmission filter define the transfer curve systematically. Changes in the sensor design and manufacturing tolerances alter the spectral characteristics of the sensor. For a Fabry–Pérot spectrum with a lower order, the measurement range becomes smaller, but sensitivity increases. Moreover, the Q -point is an individual result of a channel depending match of transmission filter $\mathcal{T}(\lambda)$ and sensor spectrum $\mathcal{R}_{FP}(\lambda)$. Therefore the calibration curve 2.70 is only valid for a specific sensor channel combination.

The polarization-dependent loss may introduce systematic fluctuations, and hence the measured ratio also deviates from a completely depolarized state. The broadband light source illuminates some degree of polarization. Individual components,

2. State of the Art and Fundamental Principles

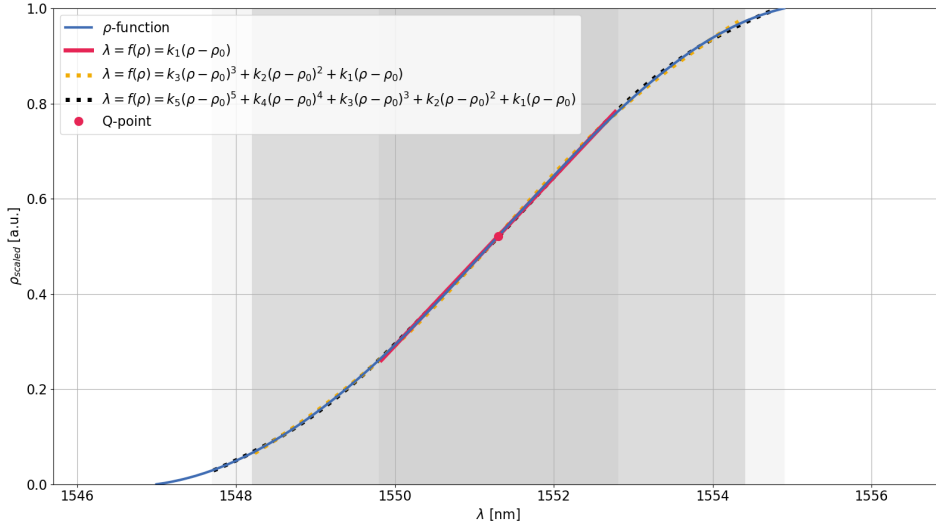


Figure 2.7.: Transfer curve of Fabry–Pérot sensor in combination with an edge filter interrogator. The transfer curve of Fabry–Pérot sensor, sampled by an edge filter interrogator, results in a sinusoidal-like shape. The Q-point marks the operating point of the highest sensitivity. Although a linear regression fit limits the measurement bandwidth of the sensing system, it ensures a minor harmonic distortion of the signal. Furthermore, the measurement range can be expanded with polynomial regressions if sensitivity deviations are expected at the measurement boundaries [108, 116, 130, 178].

such as optical filter elements, photodiodes, and the sensor itself, alter the polarization state in the optical path due to various parameters. For example, a simple torsion of an optical fiber leads to a rotation of the polarization vector of the light guided in the fiber [18, 55].

The optical signal-to-noise ratio between sensor spectrum strength and parasitic reflections systematically impacts the accuracy of a ratiometric wavelength measurement system. In case of parasitic reflections with the optical path originating from fiber connectors or bad termination of the sensor, the assumed regression of the calibration curve 2.70 becomes insufficient, as an additional optical offset needs to be considered. Moreover, colored parasitic offsets correspond to different effective discrimination characteristics of the system [18, 54].

The spectral characteristic of the light source might vary systematically depending on the power setting. The non-uniform power change of the spectral radiation characteristics $I_0(\lambda)$ across the light source’s bandwidth in combination with varying sensitivities of the photodiodes $E_i(\lambda)$ affects the measured intensities unequally, which alters the sensing output in equation 2.69 [18].

2. State of the Art and Fundamental Principles

The shot noise of the photodiodes adds the dominant noise statistically to the measurement signal. The photodiode is usually operated with a trans-impedance amplifier in a quasi-short-circuit mode to offer linear relation between current and intensity. The shot noise adds to the current and describes that light and electrical current consist of the movement of discrete photons and electrons. It is defined as $\sigma_{short} = \sqrt{2\epsilon i_c B}$, whereas ϵ is the elementary charge, i_c is the photocurrent and B represents the frequency bandwidth [18, 130].

2.3. Mechanical Principles

A Fabry–Pérot interferometer converts a mechanical displacement to an optical phase shift. The layout of the transducer’s dimensions is another fundamental design challenge. In order to design a Fabry–Pérot pressure transducer, the optical resonator length must depend on the applied pressure. Based on equation 2.62, there are only two ways to adjust the sensitivity. Either the applied pressure alters the refractive index n inside the resonator, or the resonator length L_0 needs to vary with pressure. Although both concepts of Fabry–Pérot pressure transducer have been introduced to research and design applications for pressure, gas concentration, and sound sensing [50, 57, 102, 108, 129, 164], the majority of the aerodynamic transducers are based on a deflecting mechanical membrane [23, 72, 91, 105, 176]. The mechanics transduce changes in pressure to mechanical deflection and, in turn, in optical length changes [23, 30, 72, 194, 210].

2.3.1. Gauge, Differential, Sealed and Absolute Sensor Types

Mainly four different types of pressure transducers are prominent. These sensor types are grouped in the aimed application: gauge, differential, sealed, and absolute system. Those types aim for different applications, as different full-scale measurements and frequency ranges are achievable [162].

A gauge pressure sensor measures the pressure with reference to the variable atmospheric pressure in the cavity. Therefore, such a sensor usually consists of an additional pressure port. The cavity is not closed but ventilates through this additional port. The sensor type can measure static barometric pressure changes only to a limited extent because the pressure reservoirs will equilibrate over time. Nevertheless, it is well suited for monitoring dynamic events. The main advantage is that the membrane can be designed to be more sensitive, which allows for measuring tiny pressure fluctuations as sounds.

A differential pressure sensor is another kind of gauge sensor. It measures the differential pressure with reference to the variable second pressure port. In case, the second pressure sensor port is not the fluctuating atmospheric pressure but a known reference pressure reservoir.

2. State of the Art and Fundamental Principles

A sealed pressure sensor measures pressure with reference to the atmospheric pressure encapsulated in the cavity. Unlike gauge and differential pressure, the sealed and absolute sensors measure barometric static pressure changes.

An evacuated pressure sensor provides a pressure measurement relative to a reference of almost zero pressure inside a cavity. Here, the cavity usually captures a vacuum, which requires advanced chip packaging manufacturing methods. Therefore, this sensor type is mainly used to measure static pressure levels as barometric pressure.

2.3.2. Membrane Design

The design of the membrane faces a trade-off of two contrary requirements. On the one side, displacement sensitivity must be adopted so that the finalized sensing system covers the full-scale measurement range with high resolution. On the other side, the membrane's natural frequency shall be high enough for the sensing system to be applicable in dynamic applications, particularly for monitoring sounds.

2.3.2.1. Displacement Sensitivity of the Membrane

A change in pressure shall influence the resonator length of the Fabry–Pérot interferometer. Therefore, any membrane deflection ΔL shall linearly depend on the applied pressure difference Δp so that the changes in the cavity length L_0 modulate into a wavelength shift of the interferometer. The displacement sensitivity $\Delta L/\Delta p$ of the membrane thus significantly influences the characteristics of a Fabry–Pérot pressure sensor.

The most straightforward membrane model is a circular plate [47, 146]. The Kirchhoff plate theory, a further development of the common two-dimensional beam theory, models the deflection of such a three-dimensional problem analytically. Nevertheless, the following assumption must be considered [47, 64, 146]:

- the thickness of the plate h is much smaller than the diameter $2 \cdot r_a$ of the membrane, and the membrane is round
- the thickness of the plate h of the membrane is uniform
- the membrane consists of a single isotropic material
- the applied load on the membrane is orthogonal
- Hooke's law is valid, the membrane deforms elastically
- the membrane loads are determined when the system is non-deformed
- the edges of the plate are completely supported
- the applied load is static

2. State of the Art and Fundamental Principles

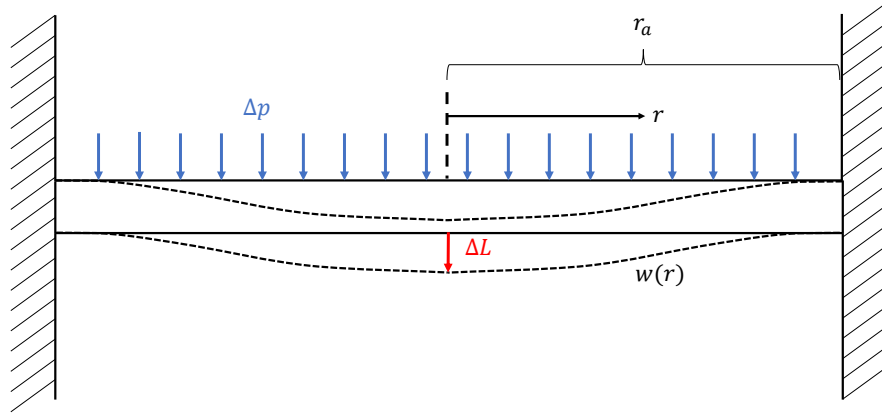


Figure 2.8.: Section drawing of a membrane. The difference between internal and external pressure loads the membrane. The membrane is circularly clamped. The model is treated in a cylindrical coordinate system that exhibits circular symmetry. The distance r_a is the radius of the membrane. The function $w(r)$ describes the bending line of the membrane in cylindrical coordinates. The pressure Δp describes the force applied to the membrane [47, 178].

The model is treated as a symmetric rotational problem in a cylindrical coordinate system by exploiting geometric symmetry. The free section of such circular membrane is shown in Figure 2.8. In order to analytically describe the membrane, the stiffness parameter K is introduced. The plate stiffness K of the round plate is defined in equation 2.71 and models the rigidity of the membrane. It includes the material parameters as Poisson number ν , and Young's module E [47, 64, 146, 177].

$$K = \frac{Eh^3}{12(1-\nu^2)} \quad (2.71)$$

Based on the free section drawing 2.8 and the previously mentioned assumption, similar to the conventional beam theory, an inhomogeneous differential equation 2.72 is derived. The differential equation 2.72 contains the delta operator $\Delta = \nabla \cdot \nabla$, which is the scalar multiplication of two Nabla operations. The parameter p describes the surface pressure load. The solution of the differential equation is the superposition of the homogeneous and particulate solution of the differential equation [47, 60, 177, 178].

$$\Delta\Delta w(r) = \frac{p(r)}{K} = w''''(r) + \frac{2}{r}w'''(r) - \frac{1}{r^2}w''(r) + \frac{1}{r^3}w'(r) \quad (2.72)$$

While the homogeneous equation denotes a solution of the differential equation without any application of force and no boundary conditions, the particu-

2. State of the Art and Fundamental Principles

late equation denotes a solution with force application [107]. Considering the term $w_h(r) = r^\alpha$ as ansatz, a homogeneous term with four unknown constants $C_{1...4}$ is obtained [47, 60, 107]. Two constants are set to zero by deriving the bending moments $m_{rr,h}$, the bending moment $m_{\phi\phi,h}$ and the shear force q_r and considering that freedom from moments and freedom from shear forces must vanish in the center of the membrane at radius $r = 0$ [47, 60, 177]. This simplifies the homogeneous solution to the term 2.73, whereas C_1 and C_2 are still unknowns [47, 60, 177, 178].

$$w_h(r) = C_1 + C_2 \frac{r^2}{r_a} \quad (2.73)$$

The particulate solution 2.74 for such circular membrane under the uniform load Δp is obtained by direct integration [47, 64, 178].

$$w_p(r) = \frac{1}{64} \frac{\Delta p r^4}{K} \quad (2.74)$$

The sum of the homogeneous and particulate solution gives the complete solution 2.75 for the differential equation [47, 64, 178].

$$w(r) = w_h(r) + w_p(r) = C_1 + C_2 \frac{r^2}{r_a^2} + \frac{1}{64} \frac{\Delta p r^4}{K} \quad (2.75)$$

Considering the boundary conditions, in which the circular membrane is clamped $w(r/r_a = 1) = 0$ and in which there is a moment equilibrium at the center of the circle $w'(r/r_a = 0) = 0$, the unknown constants C_1 and C_2 are determined. The bending curve $w(r)$ is then obtained as equation 2.76 [47, 64]. The equation for the bending line can be used to analyze the shape of the membrane bending under different loads. The deformation is linearly dependent on the pressure [47, 64, 116, 178].

$$w(r) = \frac{1}{64} \frac{\Delta p r_a^4}{K} \left(1 - \frac{r^2}{r_a^2}\right)^2 \quad (2.76)$$

The mechanical displacement sensitivity $\Delta L / \Delta p$ in equation 2.77 is converted from the bending line 2.76 by evaluating the bending line $w(r)$ at $r = 0$, converting the plate stiffness K and replacing the maximal deflection at the middle of the membrane $w(0)$ with ΔL . In contrast, the deflection sensitivity of the membrane 2.77 is reciprocally dependent on the thickness of the membrane $\Delta L \propto \frac{1}{h^3}$, the radius $\Delta L \propto r_a^4$ influences the sensitivity quadratic. The modulus of elasticity affects the mechanical displacement sensitivity linearly.

$$\frac{\Delta L}{\Delta p} = \frac{3r^4(1 - \nu^2)}{16Eh^3} \quad (2.77)$$

Therefore, the transducer's sensitivity is tunable by adjusting design and material parameters in the initial design phase. Any mechanical changes in the thickness h and radius of the membrane r_a , and choice of appropriate material, as well as integration of additional stiffness features, such as, for example, mesa structures,

2. State of the Art and Fundamental Principles

modify the mechanical displacement sensitivity. Besides the analytic solution, the issue can be solved numerically using the finite element methods. These simulation tools are essential if the membrane's shape has more features than a flat membrane. The finite element simulation decomposes a structure into finitely many smaller parts whose properties and behavior are known. Although this work included simulation tools utilizing the finite element, their fundamental principle is excluded from this work.

2.3.2.2. Dynamic Transfer Characteristic of the Transducer

The system monitors dynamic events if the membrane is excited by an oscillating external force, such as a sound wave [26, 68, 108]. In order to be able to understand and optimize the dynamic performance of the sensor, the frequency characteristics of the membrane, mainly its natural frequency, need to be addressed in the design. The natural frequency of the transducer shall be designed by a magnitude larger than the most significant exciting frequency to avoid any resonance effect. The mechanical system acts in a quasi-static operation. Staying far below the natural frequency also avoids undesired distortions and a non-linear transient response in the dynamic application.

Each membrane has an intrinsic restoring force when deflected. Additionally, the material is afflicted with mass and internal friction. Therefore, this mechanical element is described as a spring-mass-damping system to explore the dynamic behavior of the mechanics. The mass m_a of the membrane oscillates around its neutral position with the deflection ΔL . If the equation of motion is derived at this neutral point, a differential equation with constant coefficients of the second order 2.78 is obtained. The differential equation is the sum of the forces proportional to the acceleration $\ddot{\Delta L}$, damping forces proportional to the speed $\dot{\Delta L}$ and restoring forces proportional to the deflection, whereas m_a represents the mass, ζ the damping and k_s the spring constant. The time-variant pressure $p(t)$ describes the external excitation on the mechanics [25, 107, 193, 200].

$$p(t) = m_a \ddot{\Delta L} + \zeta \dot{\Delta L} + k_s \Delta L \quad (2.78)$$

In a weakly damped system, the movement of the membrane after a single forced displacement equals a sine function with a damped natural frequency f_ζ and a dropping amplitude \hat{A} . Therefore an ansatz for the differential equation is expressed as term 2.79, in which the decay rate constant δ and the phase difference $0 \leq \phi \leq 2\pi$ are introduced [25, 193, 200].

$$\begin{aligned} \Delta L &= \hat{A} \cdot e^{-\delta \cdot t} \sin(2\pi f_\zeta \cdot t + \phi) \\ f_\zeta &= \sqrt{f_0^2 - \delta^2} \\ \delta &= \frac{\zeta}{2m_a} \end{aligned} \quad (2.79)$$

2. State of the Art and Fundamental Principles

In order to derive the transfer function for the differential equation, the Laplace transformation has to be taken into account. The differential equation is divided by mass m_a , and the undamped angular frequency is introduced based on the relationship $\omega_0^2 = k_s/m_a$ [70, 107, 118, 136].

$$\ddot{\Delta L} + 2\delta\dot{\Delta L} + \omega_0^2\Delta L = \frac{u(t)}{m_a} \quad \circ\text{---}\bullet \quad (s^2 + 2\delta s + \omega_0^2)X(s) = \frac{P(s)}{m_a} \quad (2.80)$$

Thus the transfer function $G(s)$ results in the equation 2.81, which is the division of the sensor's response $X(s)$ with the excitation $P(s)$ [70, 118].

$$G(s) = \frac{X(s)}{P(s)} = \frac{1}{m_a \cdot (s^2 + 2\delta s + \omega_0^2)} \quad (2.81)$$

The dynamic behavior describes as a linear time-invariant PT_2 element, which is proportional and has a transmission delay response of second order. The dynamic response is, therefore, solely dependent on the natural frequency, the membrane mass, and its damping factor due to internal friction of the material and viscous shearing and compression of encapsulated air inside the cavity. According to the so-called squeeze-film, damping is the more dominant damping mechanism and describes air resistance between two planar structures moving normally to each other [32, 59, 143]. However, modeling the exact damping constant with a thin film damping model is complex, and experimental characterization requires a very wide frequency bandwidth of the interrogator; therefore, the following explanations describe the typical exacted dynamic behavior with an assumed damping coefficient. The Bode-Diagram contains a raise of amplitude at the natural frequency with a typical damping factor $0 < \delta < \omega_0$ [70]. Any high-frequency measurements close to the natural frequency are strongly distorted in amplitude and phase because such a system has an intrinsic low-pass characteristic. Therefore, the relevant measuring range of the sensor is limited to frequencies lower than the resonance increase, $f \ll f_0$. The phase difference of the system at f_0 is exactly 90° . Figure 2.9 illustrates the typical simulated Bode diagram of the pressure transducer. As marked in the graph, the actual damped resonance frequency f_ζ is slightly smaller than the natural frequency f_0 of a system in a vacuum [32, 59, 70, 143].

2.3.2.3. Natural Frequency of the Membrane

The natural frequency f_0 of the undamped system defines the dominant lowest oscillation frequency without permanent external force after a single excitation.

Considering that the mechanical sensitivity of the membrane is already known due to equation 2.77, another straightforward approach to calculate the undamped natural frequency f_0 is to take advantage of Hooke's law. Hooke's law describes that the displacement ΔL and the spring constant k_{spring} are in linear relation to a restoring force F_S of a spring. The restoring force F_S is a result of this substituted by the applied pressure Δp over the membrane's area. The multiplication of the force

2. State of the Art and Fundamental Principles

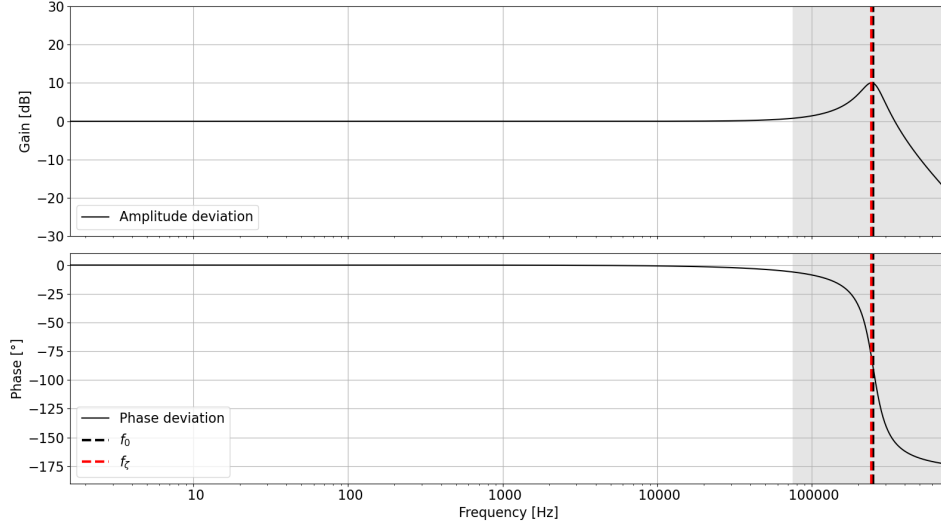


Figure 2.9.: Typical simulated Bode-Diagram of the membrane. The phase and gain of the transducer are constant over a wide frequency range. Near the resonance frequency, the gain increases significantly. The phase deviation increases near the resonance frequency as well. Therefore the frequency measurement range is limited to a bandwidth much lower than the resonance frequency. For this simulation, while the mass and the dimension of the membrane are well, the damping factor is assumed so that the gain does not exceed 10 dB

with reciprocal of mechanical sensitivity $\frac{\Delta L}{\Delta p}$ equals the spring constant k_S as seen in equation 2.82 [70, 109].

$$k_S = \frac{F_S}{\Delta L} = \frac{2\pi r^2 \Delta p}{\Delta L} \quad (2.82)$$

Taking into account the conventional formula 2.83 for the natural frequency of a spring mass system and neglecting the system's damping, the ansatz 2.79 simplifies to a non-exponential shape with steady amplitude and no decay rate constant $\delta = 0$. Whereby the natural frequency of a spring mass system and the system's damping are the non-trivial solution of differential equation 2.78 of the undamped spring oscillator with $\zeta = 0$. By derivation and insertion of the ansatz into the differential equation, the undamped natural frequency is derived in equation 2.83, whereas the mass m_a equals the multiplication of membrane volume and material's density is ρ_D .

$$f_0 = \frac{1}{2\pi} \sqrt{\frac{k_S}{m_a}} = \frac{1}{2\pi} \sqrt{\frac{\Delta p}{\Delta L h \rho_D}} \quad (2.83)$$

Another approach, referred to as the Bernoulli approach, to determine the natural frequency is to describe the system as a clamped circular membrane with the differential equation 2.72. For an unloaded membrane $\Delta p = 0$, the ansatz 2.84 is used. This ansatz also corresponds to the oscillation equation of a periodically excited

2. State of the Art and Fundamental Principles

membrane. The membrane oscillates with the angular frequency ω and a specific phase displacement κ to its excitation [37, 200].

$$w(r, t) = R(r) \cos(\omega t - \kappa) \quad (2.84)$$

The Bernoulli approach is transformed with the Laplace transform to equation 2.85, whereas λ_x describes the eigenvalues of the problem [37, 200].

$$\Delta \Delta R(r) - \frac{\rho_D h}{K} \omega^2 R(r) = 0 \quad (2.85)$$

Considering the boundary conditions that there is no deflection $w(r = r_a) = 0$ without bending $w'(r = r_a) = 0$ at the edge of the membrane, it results in a Bessel function. The eigenvalues thus result from the zeros of this frequency equation. Therefore, the natural frequency f_0 of the first zero is of particular interest. The lowest natural frequency derives as equation 2.86 and limits the frequency range of the transducer [25]. All frequencies f_x larger than the first natural frequency are other eigenshapes of the membrane. Tables 2.1 refers to the eigenvalues, which are required for the equation 2.86 [37, 144, 200].

$$f_x = \frac{1}{2\pi} \lambda_x^2 \frac{K}{h\rho_D} \quad (2.86)$$

Table 2.1.: Eigenvalues of the frequency equation 2.86 [37, 144, 200].

x	0	1	2	3	4
$\lambda_x r_a$	3,196	6,306	9,439	12,577	15,716

The mechanical system is weakly damped due to internal friction of the diaphragm material and air friction, which slows down the motion of the membrane. Unfortunately, estimating the damping constant based on aerodynamic effects and internal friction is not trivial. As a result, the natural frequency in a weakly damped system is slightly less than the undamped natural frequency $f_\zeta < f_0$.

3. Pressure Sensor Transducer

Within the scope of this thesis, two sensor shapes have been designed, manufactured, qualified, and industrialized. Based on the introduced fundamentals of Fabry–Pérot interferometers, pressure transducer mechanics, and the interrogator principle, the following chapter summarizes the conceptual approach and manufacturing of the transducer.

3.1. Concept

The sensor transducers include a pressure-sensitive membrane, a cavity, two glass-air mirrors with low reflectivity, and a glass body with an adhered single-mode fiber.

If the pressure between the cavity and the outside increases, the membrane bends inwards. The incoming light resonates at a shorter cavity length, and the transducer’s phase condition will shift to the smaller wavelengths. If the applied pressure decreases, the diaphragm relaxes, so the resonator lengthens. With dropping pressure, the phase condition in the spectrum shifts to a larger wavelength.

The cavity micro-machined chip is either sealed, vented, or evacuated. While a cylindrical-shaped sensor with a front-facing membrane is well suited for tight intrinsic integration, the flat pressure sensor with respect to the fiber direction perpendicular facing membrane targets retrofit installation. Figure 3.1 and 3.2 illustrate the schematics of the sensors [40, 72]. In both designs, single-mode fiber is bonded to a chip, and the end surface forms the optical resonator with the membrane. A diffusor replaces conventional high-reflecting coating and is added to avoid parasitic back reflections in the cylindrical design. For a perpendicular sensing direction, the fiber end face is 45° laser cleaved and used for light beam deflection, so that a flat sensor design is possible, which is illustrated in Figure 3.2. Utilizing total reflection, as introduced in equation 2.31, the beam reflects on the fiber’s front surface, and the light interferes between the membrane and the fiber’s cladding.

Prior to this work, it has been identified that managing the drift tendency of fiber-optic pressure sensors induced by adhesive aging is crucial for long-term monitoring applications [178]. The former work elaborated that any adhesive used to bond optical components such as lens and prism along the fiber’s optical path, alter parasitic resonators, and misplace fiber. As the fiber alignment is suspected of tilting over temperature, a longer resonator length might occur. As a result of this work, a design recommendation has been defined. The adhesive shall be avoided along the optical path [178] with the fiber alignment, and only a minimal amount of adhesive shall be used. These design considerations have been considered in the design of the flat and cylindrical sensors. The fiber end does not contain either lens elements or

3. Pressure Sensor Transducer

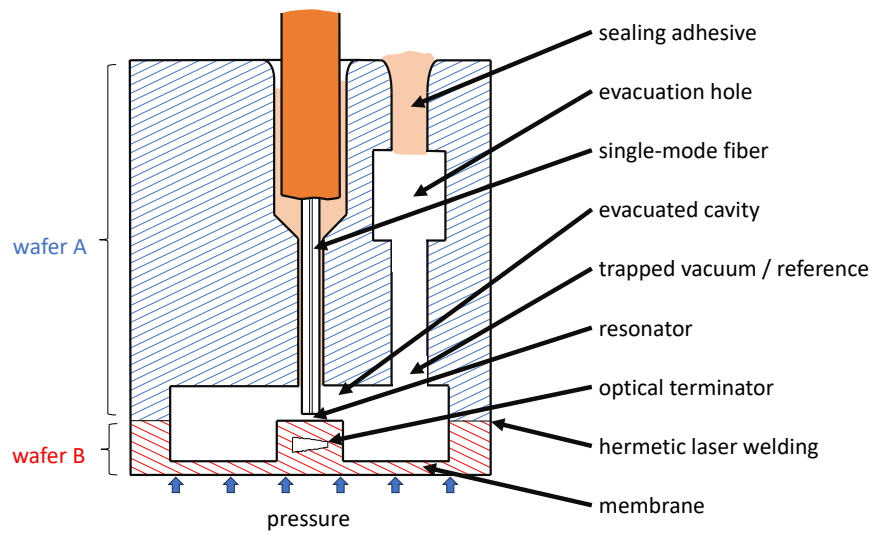


Figure 3.1.: Schematic drawing of the cylindrical fiber-optic pressure sensor. The sensor consists of a membrane, which forms an optical resonator inside a cavity with single-mode fiber. Additionally, the sensor has a ventilation hole for packaging purposes. For hermetic sealing, two wafers are laser welded together during manufacturing. The mesa-shaped membrane allows the utilization of thicker wafers. The finalized sensor head is of glass material only. To avoid parasitic back reflection, it includes an optical terminator, which scatters parasitic lights.

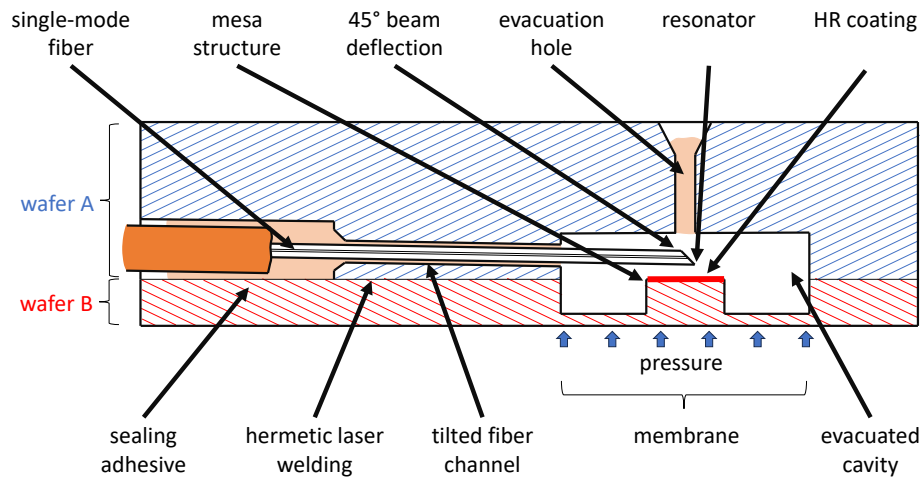


Figure 3.2.: Schematic drawing of the flat fiber-optic pressure sensor. The flat pressure sensor also includes a beam deflection at the fiber tip so that the sensing direction is almost orthogonal to the fiber inlet. Further, the membrane has a high-reflecting coating to compensate for the light loss due to the slightly tilted fiber inlet.

3. Pressure Sensor Transducer

bonded beam deflections but is laser processed. By integrating the fiber's end into the cavity, the requirement for collimation of light has also dropped.

3.2. Manufacturing

The sensing structures are micro-machined in Fused Silica wafers, which minimizes temperature cross-sensitivity because the material features a very low coefficient of thermal expansion. In addition, each wafer is micro-machined in a selective etching laser process, offering tight tolerances and batch processing capabilities [95, 128, 220].

In the initial step, all geometric features of the transducer are locally light-exposed with femtosecond laser pulses, altering the material's local etchability in the focal point. In the second step, a wet-chemical etching solvent reacts to processed areas with higher selectivity. This manufacturing process allows complicated three-dimensional designs at low quantities with high aspect ratios [95, 128, 220].

Due to the high surface requirement of the mirroring surface, a second polished wafer must be laser-welded on the carrier structure. Therefore, the upper wafer of 2 mm thickness, which contains the sensor's cavity, a fiber channel, a ventilation hole, and a bottom wafer of 300 μm thickness, which contains the membrane and diffusor are machined completely and the wafers later laser welded together. In the last step, the sensors are etched or diced to shape and separated from the wafer structure.

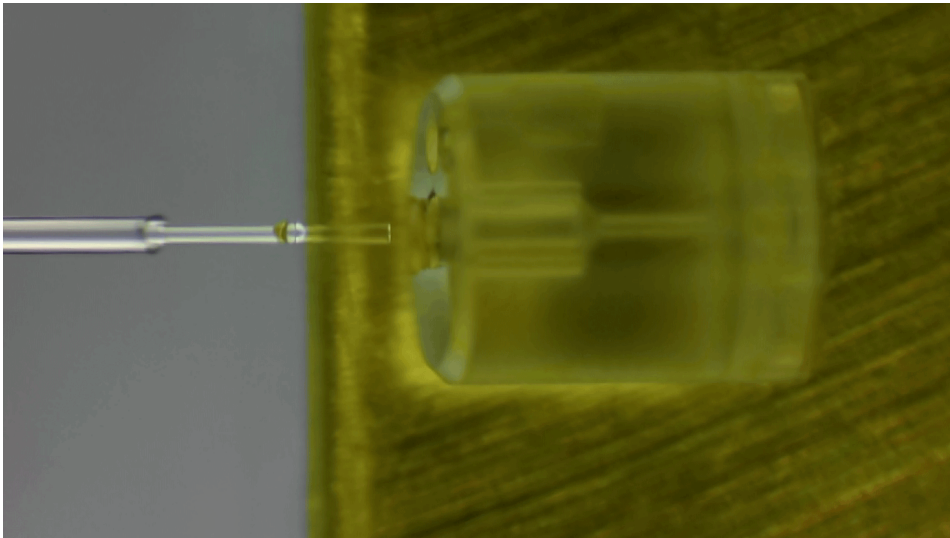


Figure 3.3.: Cylindrical sensor head with single-mode fiber before bonding. After trail alignment, a minimal amount of epoxy adhesive is added, and the fiber is inserted into the chip. After optimal alignment, heating cures the adhesive while an operator monitors and keeps the alignment in place.

Up to this point, the manufacturing process is a batch process and still has the

3. Pressure Sensor Transducer

advantage of not relying on traditional lithographic processes for micromachining. Therefore, this manufacturing process becomes more flexible for design updates but offers easy production scalability. The main challenge in production is that the sensor's operating point must match the quadrature point of the measurement device's filter for a linear response. In the following manual step, a single-mode fiber with a cleaved end is bonded inside the chip's cavity.

In the case of the cylindrical sensor, the fiber is cleaved perpendicular to the fiber. The flat pressure sensor also includes a beam deflection at the fiber tip so that the sensing direction is almost orthogonal to the fiber inlet. In this case, the fiber is laser cut with a 45° angle. In addition, the concept utilizes total reflection to avoid any reflecting coating at the tip of the fiber.

The prepared single-mode fiber is aligned to the sensing head so that the destructive phase condition matches the operating point of the interrogator. Figure 3.3 displays the manual alignment process. In the illustration, the fiber is not yet inserted into the fiber channel, but the adhesive is already applied. Then, with the help of two precise adjustment tables, a heating unit, a microscope, and a spectrometer, each sensor is bonded in serial consequence. Afterward, depending on the application, the sensor is finalized as a differential sensor, sealed, or hermetically packaged in a vacuum chamber to ensure static measurement. For hermetic vacuum packaging, the transducer is placed in a vacuum chamber, and the second inlet is closed with low-outgassing adhesives after evacuation. By reducing the tolerances of the fiber inlet to its minimum, most effects of shrinkage or expansion of the epoxy are diminished.

As one of the last steps before calibration, the epoxy-based adhesive is tempered with an extended thermal treatment process at elevated temperatures at 150°C up to 24 h to ensure a high cross-linking level of the duromer adhesive.

3.3. Finalized Sensors

Based on the models, simulations of the proposed concepts have been realized. Both sensors feature miniature size and a high natural frequency of over 250 kHz, allowing measurements of steady and unsteady pressures as barometric, aerodynamics, and acoustic effects. The cylindrical transducer is illustrated in Figure 3.4. The illustrated fiber-optic cable is protected with a 0.9 mm polyamide buffer. The cylindrical transducer has a diameter of 2 mm. Figure 3.5 illustrates the flat fiber-optic pressure sensor. Its sensor shape is characterized by sensing direction perpendicular to the fiber inlet. The outer dimensions of the chip are 3 mm x 5 mm with a thickness of 1.3 mm.

3. Pressure Sensor Transducer

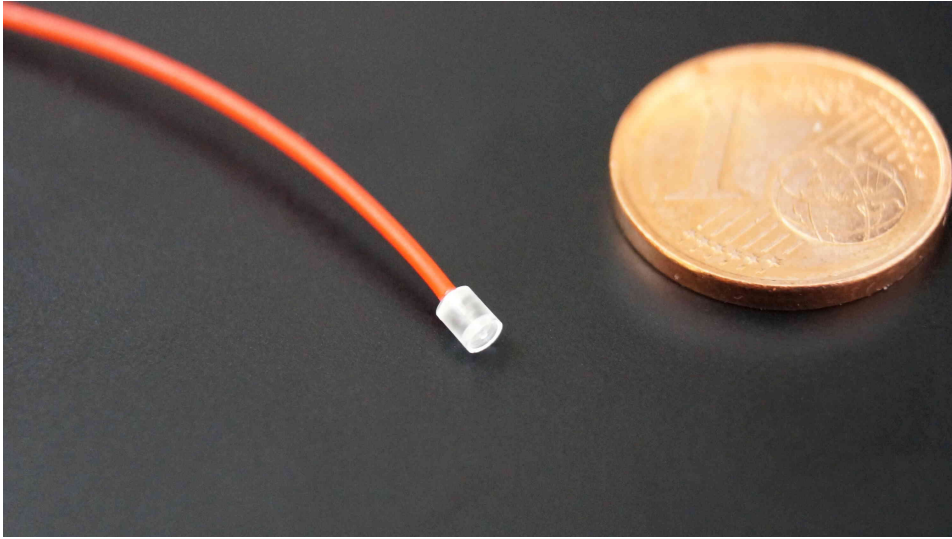


Figure 3.4.: Cylindrical-shaped fiber-optic pressure sensor. The pressure sensor true-surface membrane is front-faced. The fiber-optic cable is protected with a 0.9 mm PVC buffer, and the sensor head has a diameter of 2 mm. The sensor is minimized to be integrated into tight applications where size matters.

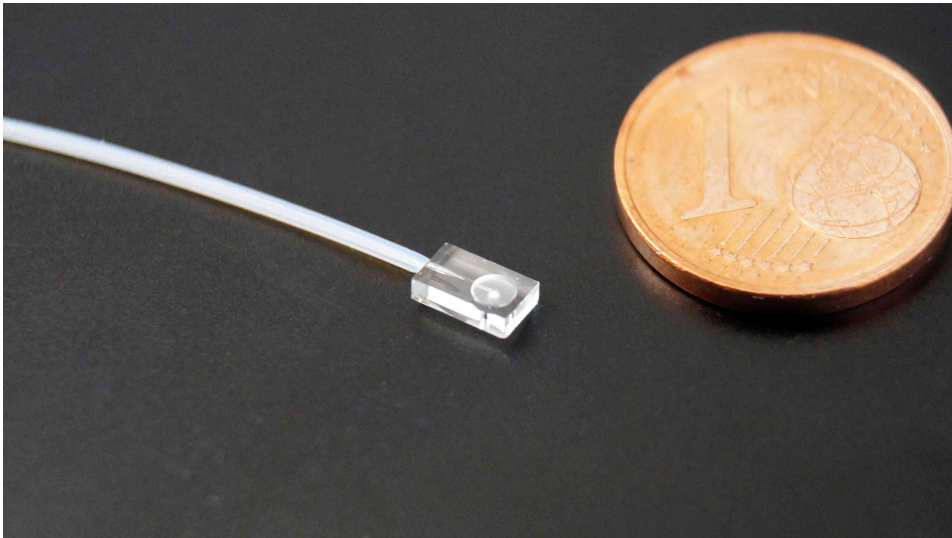


Figure 3.5.: Flat fiber-optic pressure sensor. The dimensions of the flat pressure sensor are 3 mm in width, 5 mm in length and 1.3 mm in thickness. The pressure-sensitive membrane is in a perpendicular direction with respect to the fiber inlet. This version is equipped with PTFE tubing with 0.9 mm thickness.

4. Qualification and Verification of the Measurement System

This chapter summarizes the main findings of the lab evaluation of the presented measurement system. Therefore, each section highlights the typical sensing behavior of an exemplary sensor. The measurement systems have been optimized in several iterations based on these lab evaluations to achieve the best performance in the subsequent field tests.

4.1. Calibration Methods

A fundamental challenge of the sensing system is the calibration process. The primary need for such calibration is derived from the sensor chip's manufacturing challenges and the interrogator's edge filter. Each combination of sensor and interrogator channel needs a unique calibration. The calibration aims to map raw data to the reference pressure reading with the correct conversion factors. There are two fundamental concepts to calibrate the sensing system: static calibration and dynamic calibration principles. Both calibration routines use standard industrial calibration equipment, and both routines are traceable back to normalized industrial calibration standards.

4.1.1. Static Pressure Calibration

A professional calibration of the pressure sensor is essential to ensure the quality of the measurement results. As described previously, an obvious method to calibrate the sensors is a static calibration tool to apply static pressure changes on the sensor. For static calibration, a high-precision measurement and calibration device, Halstrup-Walcher KAL100, is utilized [76]. Nevertheless, the complete sensing channel in combination is subject to calibration this time. After the commissioning of the sensing system, the calibrator acts on each sensor port individually. Firstly, pressure and suction on the fiber-optic sensors are applied in a decreasing or increasing step function. Next, the recorded fiber-optic measurement reading is compared to the calibration device reading. Secondly, each pressure threshold is identified by computing a histogram of recorded fiber-optic data, and raw readings are recorded. Thirdly, the fiber-optic sensor reading is mapped with the reading of the calibration device, fitted with a polynomial regression, and the sensitivity and offset of each sensor are derived [219, 235]. Figure 4.1 illustrates the data processing for the static calibration routine. The main benefit of this calibration routine is that the pressure calibrator traverses the entire measurement range. Therefore, this ensures that each

4. Qualification and Verification of the Measurement System

sensor is tested for its full-scale measurement range. The measurement range is expandable with nonlinear transfer functions, but the calibration procedure stays the same.

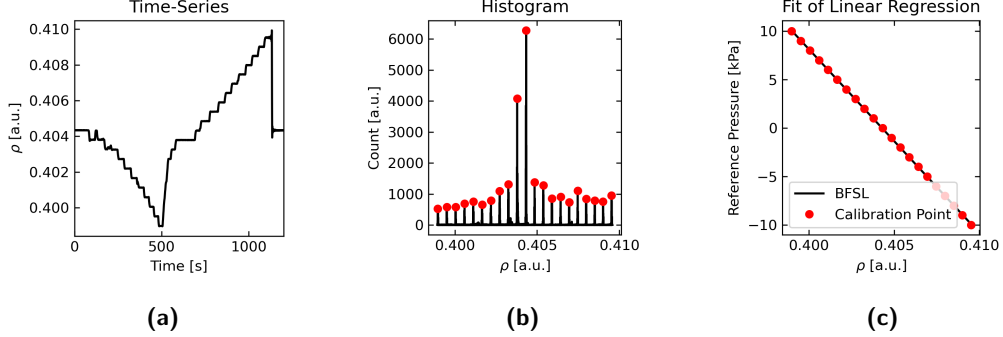


Figure 4.1.: Calibration procedure of the fiber-optic sensors. At first, pressure and suction on the pressure sensors are applied to decrease and increase step function, as seen in Figure a. In the second step, each calibration step is identified in measurement by calculating a histogram, which is displayed in Figure b. Figure c compares the reading of the fiber-optic sensor with the reading of the calibration device and fits a linear regression into the data [219].

4.1.2. Dynamic Pressure Calibration

While static calibration devices are preferred for conventional static pressure sensors, a pistonphone is conventionally used to calibrate microphones. A microphone emits dynamic pressure fluctuations, or pressure waves, which are perceived as a sound. Therefore, a straightforward approach to calibrate a sensing channel in the field is to utilize a GRAS 42AG pistonphone, IEC 60942 class 1, as a sound emitter [61]. Such pistonphone emits a pressure wave at a specific amplitude and frequency. In order to derive the sensitivity factor k_1 with such a dynamic sensing approach, the power spectral density $S_{XX}(f)$ of a recorded pistonphone in a defined distance must be computed. Conventionally, the integral of the power spectral density $S_{XX}(f)$ over the entire frequency range equals the variance σ_X in equation 4.1. This variance represents the mean power of the signal [17].

$$\sigma_X^2 = \int_{-\infty}^{\infty} S_{XX}(f) df \quad (4.1)$$

Most of the emitted power is within a narrow frequency band around the pistonphone's unsteady oscillation frequency. The raw signal's root-mean-square ρ_{RMS} of the sensor within the narrow frequency band corresponds to the mean power σ_X described in the term 4.2.

4. Qualification and Verification of the Measurement System

$$\rho_{RMS} = \sqrt{\int_{f_{lower}}^{f_{upper}} S_{XX}(f) df} \quad (4.2)$$

Dividing the ratio of the applied pressure reference level p_{cal} and the root-mean-square reveals equation 4.3.

$$k_1 = \frac{p_{cal}}{\rho_{RMS}} \quad (4.3)$$

The routine computes the linear calibration factor k_1 . According to chapter 2.3.2.2, the sensor's transfer function is constant over a wide frequency range so that the obtained calibration factor can be applied to static measurement as long as linear regression is assumed. Figure 4.2 illustrates the system's power spectral density of such dynamic calibration. For example, the signal's power spectral density at 1.0 kHz with 114.0 dB SPL is shown in equation 4.2.

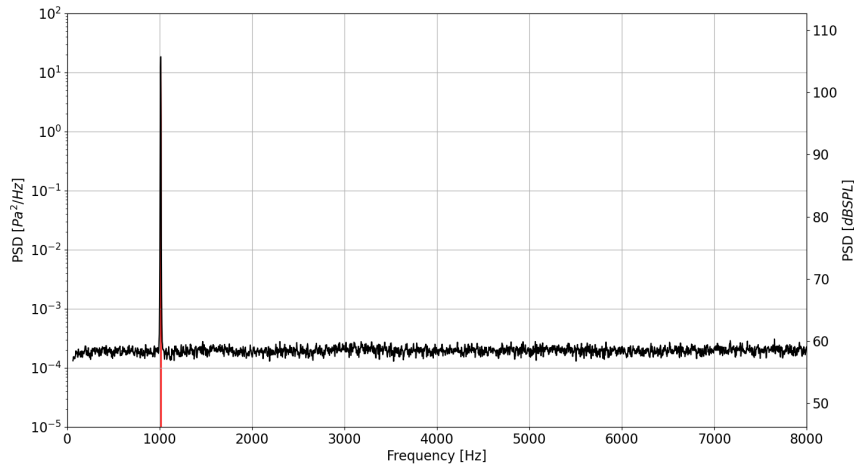


Figure 4.2.: Dynamic calibration of a pressure sensor with a pistophone. For dynamic calibration, a pistophone outputs at 1 kHz with 114 dB SPL sound pressure. The power spectral density features this source and proves the white noise floor. This specially optimized sensor demonstrates that the system can be utilized as a microphone due to the low noise. The red area marks the integrated power density, referenced to the applied sound pressure level. [178, 217].

4.2. Evaluation of the Sensor Transducer

The following section focuses on isolating the fiber-optic pressure transducer from the edge filter principle to provide fundamental insights into the sensor's capabilities. Then, in the subsequent section, the performance of the complete sensing system,

4. Qualification and Verification of the Measurement System

including the sensor and edge filter interrogator, is discussed and quantified.

4.2.1. Spectral Characteristics

As discussed in chapters 2.2.4 and 2.3, the pressure transducer utilizes the Fabry–Pérot effect to transduce mechanical deflection of the pressure membrane to an optical phase shift of light. The sensor’s optical properties require matching the spectral characteristics of the Fabry–Pérot pressure sensor to the edge filter interrogator principle. Figure 4.3 illustrates a light spectrum of a cylindrical sensor. As a recording measurement instrument, a high-resolution spectrometer, such as the Micron Optics SI155EV, is utilized [85]. The spectrometer contains an internal fiber-coupled gas cell installed as a reference standard, which is filled with Hydrogen Cyanide ($H^{13}C^{14}N$, NIST Standard Reference Material 251). The gas cell enables the sensors to be referenced to a stable standard and exhibits a defined comb of absorption lines in the infrared C-band. The wavelength of the absorption lines is stable, and only their width is influenced by pressure and temperature.

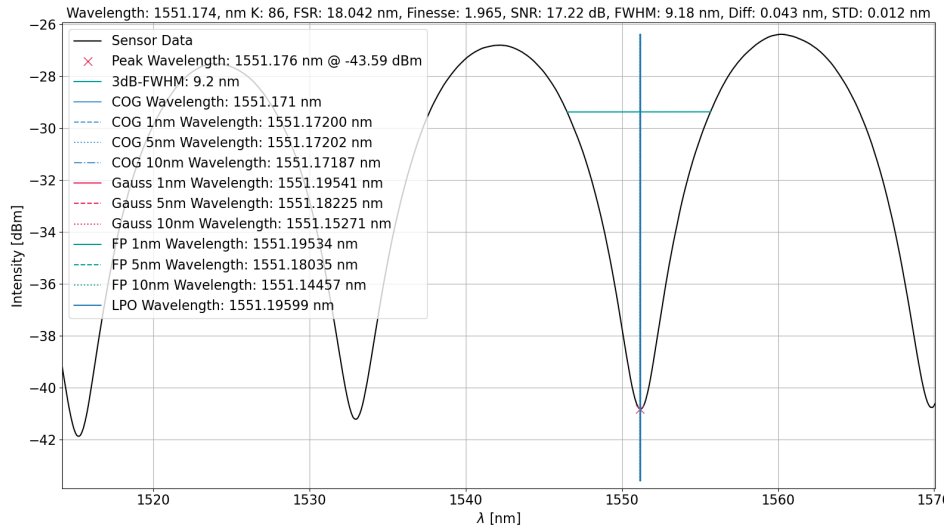


Figure 4.3.: Fabry–Pérot spectrum of a cylindrical pressure transducer. The fiber-optic sensor has various optical properties, which are of interest during design and manufacturing to match the sensor to the edge filter interrogator. The reflection spectrum shows the remarkable destructive interference effect of the light at a certain wavelength, which fulfills the Fabry–Pérot resonance condition. From the shape of the spectrum, different optical parameters as the $\Delta\lambda$, $\delta\lambda$, F and the Q -point, which is nearest to 1550 nm, are derived. Special attention is paid to the symmetry of the spectrum, which is why the operating point is computed via various algorithms and compared to each other.

The destructive interference effect of the light at a particular wavelength, which fulfills the Fabry–Pérot resonance condition, characterizes the reflection spectrum. As elaborated in chapter 2.2.5, the spectral characteristics of Fabry–Pérot spectrum

4. Qualification and Verification of the Measurement System

with respect to the transmission filter systematically affect the measurement performance. Therefore, the shape and symmetry of the Fabry–Pérot spectrum around the Q -point are of particular interest to improve the interchangeability of sensors and provide similar measurement characteristics. As illustrated in Figure 4.3, the derived spectral parameters as FSR $\Delta\lambda$, FWHM $\delta\lambda$, Finesse F , Q -point λ_0 and the modulation intensity are based on the recorded spectrum of the sensor, and the displayed optical values are computed. Comparing these optical parameters provides necessary insights on how repeatable such sensor transducer is manufactured and will ultimately lead to a simplified calibration procedure in a later stage to ease industrialization.

By measuring the center wavelength of the Fabry–Pérot pressure sensor, the cavity length or pressure applied to the sensor can be derived from the sensor spectral response with conventional valley search algorithms. Furthermore, to evaluate and compute the symmetry of the Fabry–Pérot spectrum, the result of various valley search algorithms and window sizes are compared to each other. Notably, the internal inscribed light diffuser and the direct coupling of the fiber’s end facet as a mirror surface with a glass mirroring membrane result in an almost parasitic-free light modulation of the Fabry–Pérot interferometer [219].

Next, the wavelength shift of such Fabry–Pérot pressure sensor at different static pressure levels is depicted in Figure 4.4. The pressure differences are applied with a Halstrup-Walcher KAL100 calibration device [76]. Based on the recorded spectra, the given set of formulas in chapter 2.2.4.3, and the mechanical deflection, the optical transducer sensitivity $\Delta p/\Delta\lambda$ is derived. Figure 4.5 illustrates the calculated cavity length and the correlating change with pressure. The pressure response of the sensor is linear within the applied pressure range.

Within this thesis, multiple versions of pressure sensors have been developed and tested. The table 4.1 summarizes relevant optical and mechanical properties of three different sensor versions, which have been produced sequentially in small batch processes. Concerning the shown data in table 4.1, on the one hand, cylindrical sensors seem to be more reproducible and more straightforward to process than the flat sensor version with respect to their optical properties. However, on the other hand, it can be derived that sensors with a smaller order have higher optical sensitivities even though the mechanical sensitivity is in the same range.

4. Qualification and Verification of the Measurement System

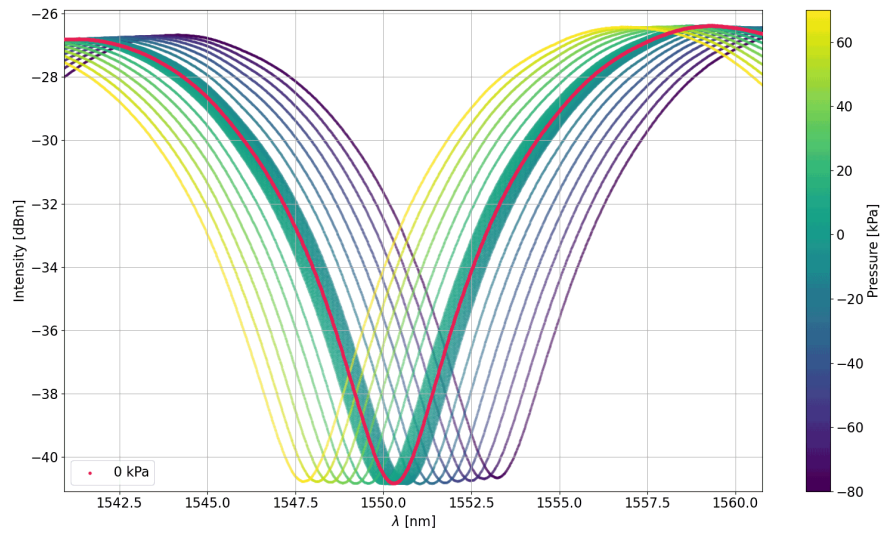


Figure 4.4.: Measured spectral shift of a fiber-optic sensor shifts depending on the applied pressure level. The red curve marks the spectrum at the ambient pressure level. The spectrum shifts to smaller wavelengths with increasing pressure acting on the sensor. With decreasing pressure, it shifts to larger wavelengths.

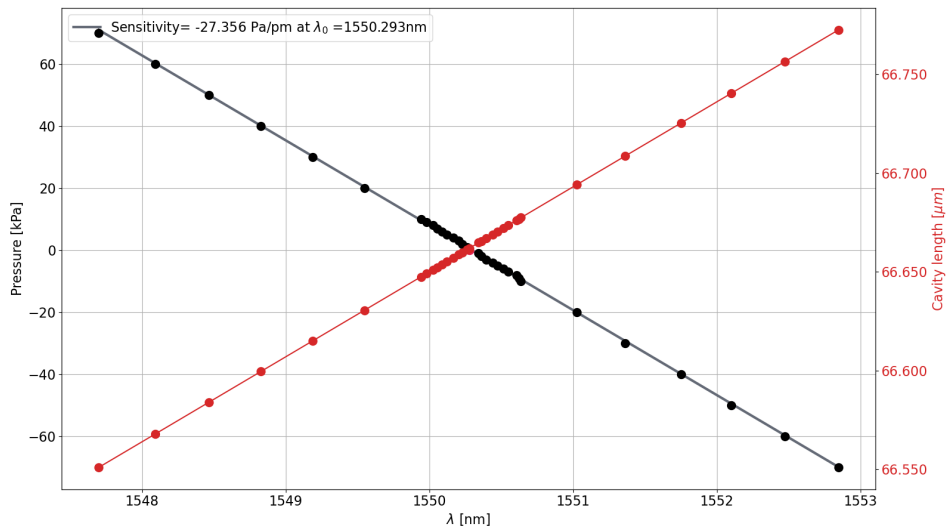
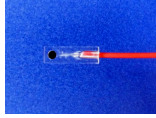


Figure 4.5.: Cavity length in relation to the applied pressure. The cavity length and the relation between the length change and pressure changes are linear. With increasing pressure, the cavity length, as well as the center wavelength, decreases.

4. Qualification and Verification of the Measurement System

Table 4.1.: Specifications of different fiber-optic pressure sensors. The table summarizes the fundamental mechanical and optical properties of each sensor version. Whereas, the variable $\Delta p/\Delta\lambda$ describes the pressure sensitivity of the transducer, $\Delta L/\Delta p$ the cavity length change over pressure, L_0 the cavity length, N the operating order of the Fabry–Pérot interferometer, λ_0 the center wavelength, F the Finesse coefficient, $\Delta\lambda$ the *FSR* and $\delta\lambda$ the *FWHM*.

Version	V2-0-X	V2-1-X	V1-2-X	V2-1-X
picture				
shape	cylindrical	cylindrical	flat	flat
Applied in application	[212, 214, 220]	[1, 88, 219]	[215, 217]	[88]
$\Delta p/\Delta\lambda$ [Pa/pm]	-10.3 ± 1	-23.5 ± 4	-12 ± 5	-36 ± 5
$\Delta L/\Delta p$ [nm/kPa]	-2.9 ± 0.1	-1.83 ± 0.1	2.5 ± 0.1	-1.68 ± 0.1
L_0 [μm]	47.0 ± 2.0	66.6 ± 3.0	46.3 ± 3.0	93.8 ± 5.0
N [a.u.]	60 ± 2	86 ± 3	60 ± 5	121 ± 7
λ_0 [nm]			1551 ± 2	
F [a.u.]	2.1	2.0	2.0	1.9
$\Delta\lambda$ [nm]	27.3 ± 1	18 ± 1	26.3 ± 1	13.0 ± 1
$\delta\lambda$ [nm]	13 ± 0.5	9 ± 0.5	13.3 ± 1	6.5 ± 0.5

4.2.2. Temperature Rating and Cross Sensitivity of the Pressure Transducer

As described in chapter 3.1, different pressure sensor types aim for different applications. Nonetheless, a fundamental challenge of the pressure transducer is the inherent need to measure pressure accurately regardless of temperature changes. Temperature cross sensitivities $\Delta\lambda/\Delta T$ are in general a combination of several residual effects [44, 116, 179, 249]

- gas expansion of enclosed residual air inside the cavity
- thermal expansion due to elongation of the material
- refractive index changes
- thermally induced alignment issues
- mechanical induced stress

In order to measure static pressure differences, this work focus on absolute pressure sensors with an evacuated cavity. An evacuated packaging reduces undesired

4. Qualification and Verification of the Measurement System

temperature cross-dependencies by minimizing the amount of trapped air. The choice of Fused Silica as a material with a low coefficient of thermal expansion and vacuum packaging benefits low-temperature cross-sensitivity. Additionally, internal temperature-induced stress due to a mismatch of thermal expansion coefficients is neglectable because the sensor consists only of a single choice of material [44, 198]. Moreover, tight geometric tolerances for the fiber alignment and the minimal amount of adhesive reduce the effects of organic swelling of the adhesive.

Although these design measures reduce the thermal cross-sensitivity, an elevation of the thermal properties of each sensor is necessary. To evaluate different production batches of a pressure sensor, the setup, illustrated in Figure 4.6, has been developed. The setup contains the high-resolution Hyperion SI155 spectrometer, a Redhawk edge filter interrogator, optical switches, a microcontroller, a reference barometer, and a dry block temperature calibrator, *TP37200E.2* SIKA [85, 158, 183]. A specially manufactured round brass insert allows the insertion of several sensors and a thermoresistance probe. A web interface allows setting the target temperature and reading out the actual temperature. The temperature device itself does the temperature control. A *PT100* temperature probe is utilized as a reference sensor, which is monitored with a measuring amplifier integrated into the device.

Although the spectrometer contains a gas cell for referencing, to create additional redundancy, an external gas cell is connected to one measuring channel of the spectrometer. The added gas cell used in the setup is continuously measured by the spectrometer and held against the standard values determined by NIST. This redundancy ensures stability and reproducibility in the measurement of the sensors.

All components are connected via an ethernet network to control the evaluation process. The process is controlled, and resulting data is processed and stored centrally by a computer. The data contains the spectrum of all sensors at each temperature level.

4. Qualification and Verification of the Measurement System

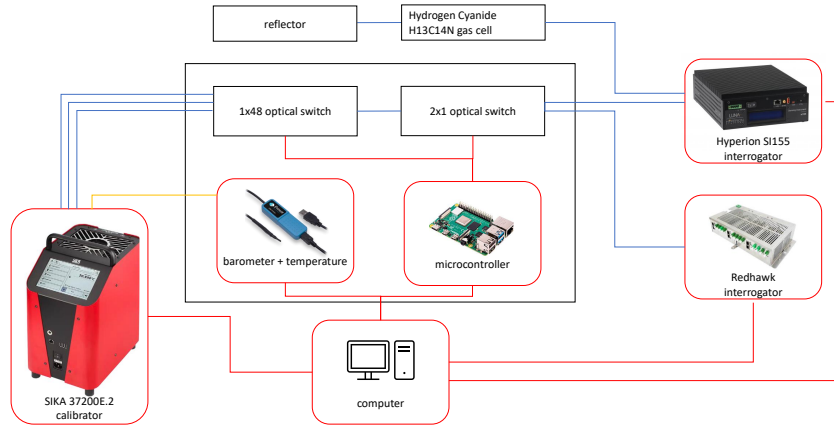


Figure 4.6.: Calibration set up to evaluate temperature cross sensitivities of the fiber-optic pressure sensors. The setup consists of a dry block temperature calibrator, a high-resolution spectrometer, an edge filter interrogator, a reference barometer, a microcontroller, and optical switches. The computer collects the spectrum of all sensors at each temperature level, sets and checks the temperature on the calibrator, and controls the optical switches. As a result, the light spectrum and the edge filter interrogator’s measurement are gathered at each temperature step. While the blue line indicates a fiber-optic connection, the red lines mark an electrically wired connection.

The setup gathers the light spectrum and the measurement of the edge filter interrogator at each temperature step. Figure 4.7 illustrates the light spectrum of a fiber-optic pressure sensor. With an increase in temperature, the optical spectrum shifts to higher wavelengths. Therefore, the cavity length is expanding. Additionally, the light modulation is changing, indicating that the fiber’s alignment with the mirroring membrane is tilting. The spectral properties are evaluated at each temperature step based on the recorded spectrum. Figure 4.8 shows the center wavelength over temperature. Especially at a higher temperature range above $40\text{ }^{\circ}\text{C}$, an exponential relation occurs. Nevertheless, the temperature cross-sensitivity at the targeted temperature range can be fit a linear regression, which results in a temperature cross-sensitivity of $5.4\text{ pm}/^{\circ}\text{C}$. Taking into account the static calibration and results from section 4.2.1, this thermally induced wavelength shift equals a temperature cross-sensitivity of $151.2\text{ Pa}/^{\circ}\text{C}$ in this example.

In addition, Figure 4.8 also illustrates the ρ modulation of the edge-filter interrogator. Here, the ρ modulation follows the center wavelength, which is evaluated by the high-resolution spectrometer.

The setup evaluates various pressure sensors simultaneously. Interestingly, even sensors of the same batch have different temperature cross-sensitivities. Figure 4.9 displays two histograms of cylindrical and flat fiber-optic pressure sensors. Each sensor type is of the same production batch. The cylindrical fiber-optic pressure sensor

4. Qualification and Verification of the Measurement System

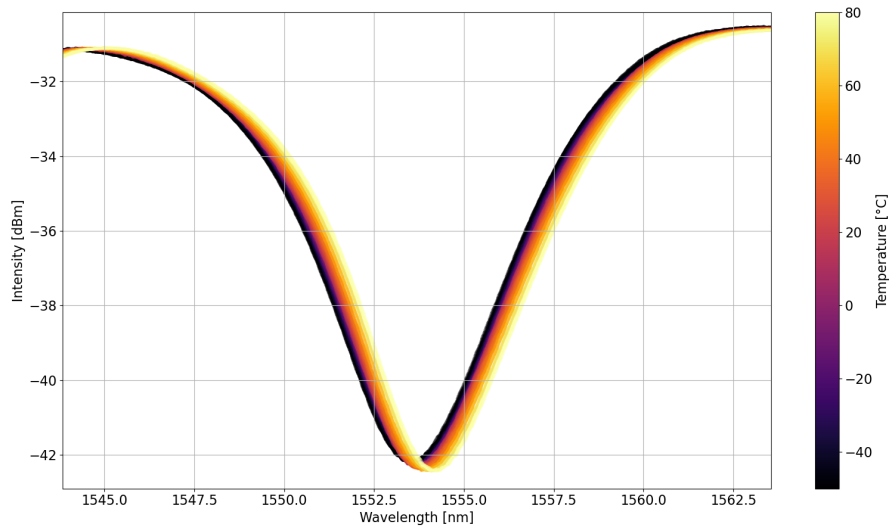


Figure 4.7.: Typical spectral shift of a fiber-optic pressure sensor due to temperature changes. With an increase in temperature, the optical spectrum shifts to higher wavelengths. Therefore, the cavity length is expanding. Additionally, the light modulation is changing, indicating that the fiber's alignment with the mirroring membrane is tilting.

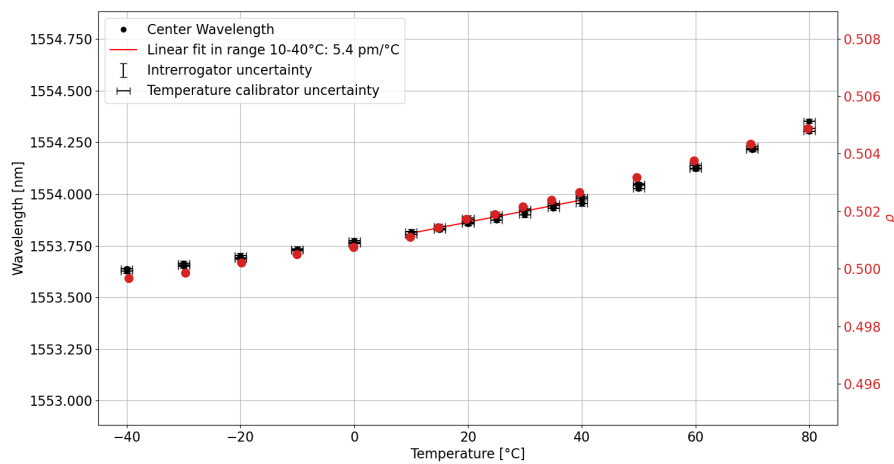


Figure 4.8.: Center wavelength shift of a fiber-optic pressure sensor over temperature. With increasing temperature, the center wavelength typically shifts to higher wavelengths. The resonator length is expanding. Noticeably, the relation between temperature and center wavelength becomes non-linear for elevated temperature, indicating that multiple temperature effects affect the sensor overlap.

4. Qualification and Verification of the Measurement System

is noticeably less affected than the flat fiber-optic pressure sensors. While the variance of the temperature cross-sensitivity is probably the subject of packaging and tolerance issues during manufacturing, the offset in temperature cross-sensitivity between the sensors styles indicates a systematic cause by design. The primary differentiation of the sensor design lies in the fiber alignment. In the cylindrical sensor version, the fiber channel is manufactured with very tight tolerances, and the sensing direction is parallel to the adhesive's preferential direction of thermal elongation and swelling. For the flat sensor version, the fiber bore must be manufactured with high bore tolerances, which allows less organic adhesive in the fiber channel to bond. In combination with the design challenge that the sensing direction is perpendicular and across the thicker adhesive layer, a higher temperature cross-sensitivity results.

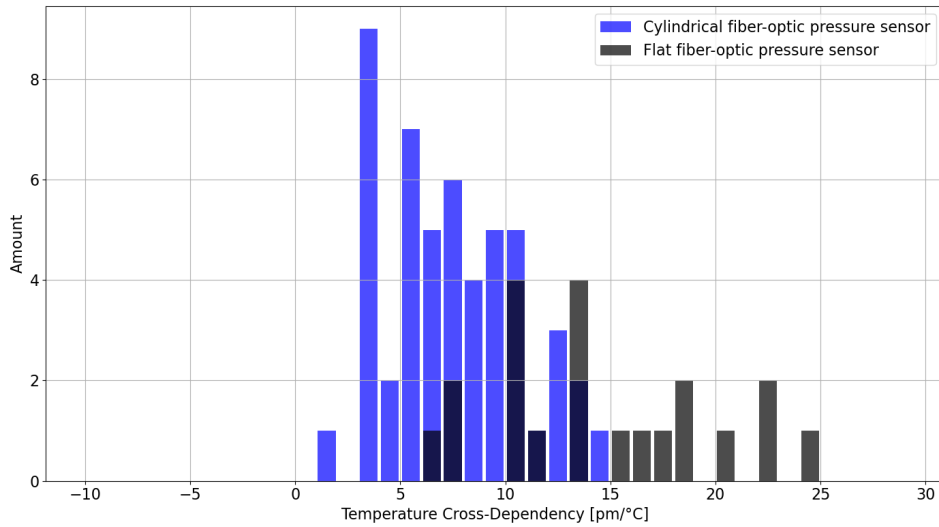


Figure 4.9.: Histogram of the temperature cross-sensitivity of a cylindrical and flat fiber-optic pressure sensor of the same batch each. The histogram reveals that the cylindrical sensor has less temperature cross-sensitivity than the flat fiber-optic pressure sensors. The variance of the temperature cross-sensitivity is due to manufacturing and packaging tolerances.

Notably, if a pressure sensor is not evacuated and used purely as a differential sensor, the temperature cross-sensitivity is reduced significantly. In this case, the unwanted gas expansion as the main driver for temperature cross-sensitivity cancels out, and primarily the thermal expansion of the material and the refractive index changes remain. Figure 4.10 display the temperature response of a differential pressure sensor.

4. Qualification and Verification of the Measurement System

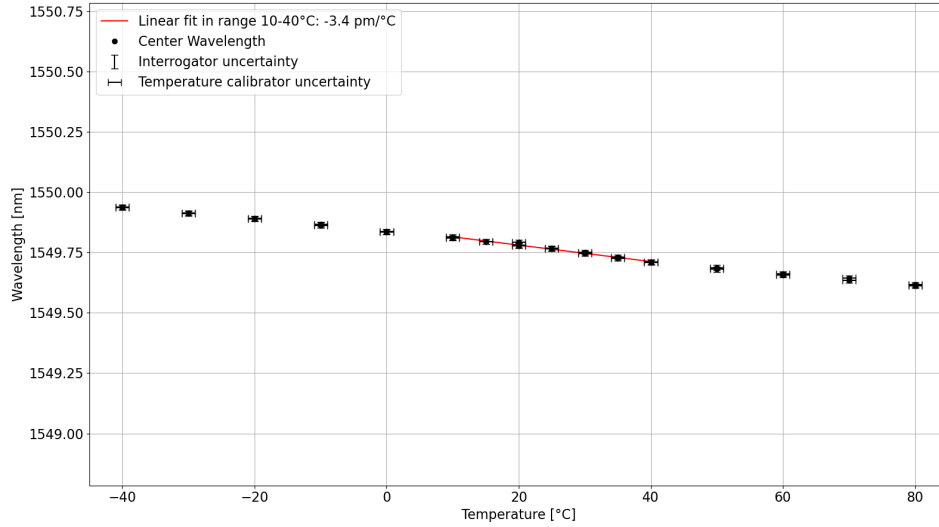


Figure 4.10.: Center wavelength shift of a differential fiber-optic pressure sensor over temperature. With increasing temperature, the center wavelength typically shifts to lower wavelengths. As the cavity is ventilated, gas expansion is not affecting the resonator length. The Fused Silica material's thermal expansion also affects the geometrical resonator length less. However, the refractive index change of the air due to temperature alters the optical path length.

The temperature cross-sensitivity can also be simulated by considering gas expansion, thermal elongation of the material, and refractive index changes. Firstly, in the case of a closed cavity with residual air insight, the trapped air is treated as an ideal gas, and the finite number of air molecules is constant. The ideal gas law applies. Secondly, the volume expansion is dominated by the material's thermal expansion. Thirdly, the refractive index change is approximated with Ciddor's equations [27]. Finally, the model results in the table 4.2, which describes that the sensor's packaging significantly affects temperature cross-sensitivity.

Each sensor contains epoxy adhesive to bond the fiber into the sensing structure and to seal the vacuum inside the cavity. The model does neither include thermally induced tilting effects of the fiber alignment due to epoxy nor the thermal elongation of the epoxy itself. Due to the high thermal coefficient of epoxy adhesive and its organic properties, this process is challenging to model and resembles a random process. Nevertheless, the parasitic organic effects of the epoxy are suspected to be the reason for deviations between the experiment and simulation and scatter the temperature cross-sensitivity dominantly.

After final iterations in the sensor design, improving manufacturing tolerances, identifying and scrapping low-grade sensors, and defining strict guidelines for manufacturing, the thermal cross-sensitivity has been reduced. By the end of this work, the residual temperature cross-sensitivity ranged around $3.5 \pm 2,5 \text{ pm}/^\circ\text{C}$, which equals a temperature cross-sensitivity of $-91 \text{ Pa}/^\circ\text{C}$ typically [156, 157].

4. Qualification and Verification of the Measurement System

Table 4.2.: Model of the residual temperature cross-sensitivity $\Delta\lambda/\Delta T$.

Packaging level	$\Delta\lambda/\Delta T$
not evacuated	11.7 Pa/°C
low vacuum at 50 kPa	6.2 Pa/°C
low vacuum at 20 kPa	2.9 Pa/°C
low vacuum at 10 kPa	1.8 Pa/°C
medium vacuum at 0.1 kPa	0.7 Pa/°C
ventilated	-2.5 Pa/°C

Another temperature-related subject of interest is the maximal temperature rating of the transducer. The previously discussed test proves that the temperature range can be defined from -40 /°C to 80 /°C without remarks. However, considering that during the manufacturing process, the transducer is handled at a much higher temperature and that the transducer design only includes passive components, expanding the temperature range might be easily achievable, considering that the operating temperature of the limiting epoxy is above 350 /°C. Nevertheless, for the targeted applications, a higher temperature rating is currently not needed [42].

4.2.3. Environmental Stability

A fundamental challenge for the long-term monitoring application of fiber-optic pressure sensors is, next to their robustness, the aging behavior of the sensors. The environmental settings, especially considering lasting condition monitoring application on a wind turbine, require the sensing system to be unsusceptible to signal drifts and mechanical degradation. The fiber-optic pressure sensors are mainly dependent on two aging effects. On the one hand, the mechanical displacement of the fiber alters the resonator length randomly. On the other hand, the entrapped vacuum might escape due to undesired gas exchange with the environment. For the introduced fiber-optic pressure sensors, a high-performance, low-outgassing epoxy adhesive bonds the fiber bonding and seals the evacuated cavity. Epoxy adhesives are known to be duromer with a superior cross-linking level. When exposed to changing environmental conditions, the mechanical properties of the adhesive layer, the interfacial bonding properties, and the substrates' mechanical performance might change due to the intrinsic organic behavior of plastics. Any aging of these adhesive joints results from frequent drying and water absorption at cycling temperatures.

Cycle tests at temperature and humidity levels exceeding the specified environmental specification are an accepted means to accelerate aging effects for validation purposes, according to the standard [87]. The effect of cyclic aging on different sensor versions has been investigated. Therefore sensors have been calibrated, and the spectrum measured prior to and after the environmental cycling. The environmental test procedure is defined as follows and has been repeated for 14 times. The duration of the test in a professional climate chamber exceeded 1 week [87]:

4. Qualification and Verification of the Measurement System

- expose for $5 \text{ h} \pm 20 \text{ min}$ at $70 \pm 2^\circ\text{C}$ at a relative humidity not lower than 90 %
- change the temperature, in $60 \pm 20 \text{ min}$, to $-40 \pm 3^\circ\text{C}$ and expose for $5 \text{ h} \pm 20 \text{ min}$
- change the temperature, in $60 \pm 20 \text{ min}$ to $70 \pm 2^\circ\text{C}$

The result of this test reveals the performance improvements in the sensor design. Furthermore, as elaborated in chapter 3.1, the novel sensor design heeded the recommendation to avoid adhesive along the optical path and reduce the adhesive quantity to the absolute minimum by tightening mechanical tolerances.

As a benchmark test, the outdated sensor design and the novel design have been aged, tested, and compared to each other to confirm the design approach of minimizing the usage of adhesives. Figure 4.11 illustrates the representative result. While the older sensor version's spectrum varies so much that a recalibration is impossible, the newly designed sensors survive the aging conditions.

While the drift behavior is consistent across the tested novel pressure sensor samples, it varies significantly with the older version. The spectrum of the novel sensors has shifted to a shorter wavelength, indicating that the sensor contains its vacuum level inside the cavity. However, the bonded fiber might be misplaced slightly so that the resonator length has shortened. In this example, an offset of only -2 kPa has been established. Nevertheless, a recalibration of the sensor is possible, and the sensor can stay in service without any other degradation.

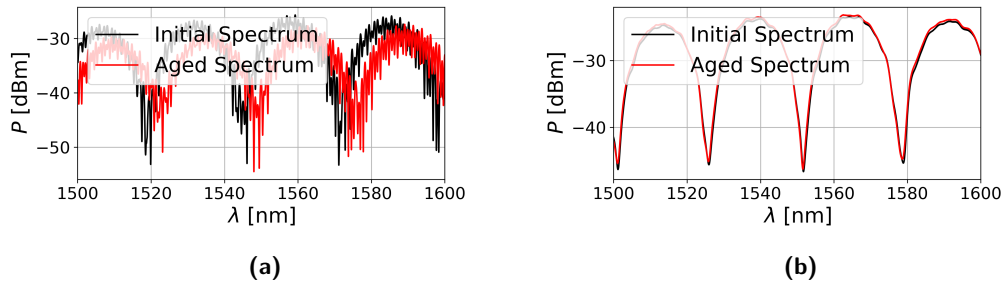


Figure 4.11.: Aged spectrum of fiber-optic pressure sensors. Figure (a) illustrates the spectrum of a flat fiber-optic sensor of the first generation. The sensor version contains an adhesive along the optical path, which is used to bond optical components such as lens and prism and alters parasitic resonators. Additionally, it is suspected of misplacing the fiber's orientation. The Q -point has shifted to larger wavelengths after the aging test. The sensor is not usable anymore as the shift of wavelength would exceed the measurement range. Additionally, the spectrum displays parasitic overlaying resonators. Due to the optical mismatch of adhesives, a lens and a beam splitter parasitic mirrors are added, which result in those effects. Figure (b) represents the spectrum of the novel cylindrical fiber-optic sensor, in which the use of adhesive is minimized. The Q -point has shifted to shorter wavelengths after the aging test, but a recalibration of the sensor is possible, and an offset of -2 kPa would have been established.

4.2.4. Shock and Acceleration Cross Sensitivity

Next to temperature cross sensitivities, acceleration affects the pressure reading in a vibrating environment. Due to acceleration acting on the membrane's mass, the resulting force deflects the membrane. Depending on the membrane's stiffness, the acceleration cross sensitivity correlates with the pressure sensitivity. Therefore, a mechanically sensitive pressure sensor will also be more sensitive regarding accelerations. The analytic model of the membrane calculates the weight m_a , which acts at the center of gravity, via multiplying volume with the material's density ρ_D and relates the force F_{acc} , which is induced by the acceleration a_{acc} to the deflection sensitivity $\Delta L/\Delta p$. With a typical deflection sensitivity of -2.84 nm/kPa, a considerable pressure reading of 1.72 Pa is induced by an acceleration of 1 g. The deflection sensitivity of the membrane is based on equation 2.77 and has been derived in section 2.3.2.1.

For evaluation purposes, sensors have been mounted on an air-cooled vibration test system [84]. Thus the membrane perpendicular is perpendicular to the shaker's movement direction. In order to prove stability and quantify the cross-sensitivity, three different routines have been tested:

- frequency spot with 1 kHz and a peak acceleration of 1 g sine
- shocks at 20 g with half-sine of 11 ms duration and shocks at 50 g half sine of 5 ms duration
- frequency sweep from 20 Hz to 2 kHz at 20 g

The sensors survived the rigorous vibrating environment, but the considerable acceleration cross-sensitivity has been confirmed in magnitude. Moreover, next to acceleration, the air is compressing in front of the sensor due to its movement. Considering the maximal dynamic pressure and multiplied with the drag coefficient of a short cylinder, the resulting pressure, which is acting additionally on the sensor's membrane, is magnitudes smaller and neglectable in this experiment. Considering the measurement range FS , which is defined in section 4.3.1, an acceleration sensitivity FS/g of 0.0024 % is derived. Such acceleration sensitivity is very similar to electrical counterparts [110]. Design measures to reduce the effects further are challenging, but a lightweight material for the membrane design might be preferable.

4.2.5. Burst Pressure of the Fiber-Optic Transducer

A primary intention for developing a fiber-optic pressure sensor is the requirement of increased overload stability, as discussed in the motivation in chapter 1.1.3. In order to prove the burst pressure rating of a fiber-optic pressure sensor, the sensor has been tested destructively after calibration. Here, again the high-resolution spectrometer has been utilized to determine the pressure sensitivity, similar to the procedure in section 4.2.1 in the first step. A flat sensor has been mounted into a screw clamp, raising the pressure stepwise sequence. After recording a spectrum at

4. Qualification and Verification of the Measurement System

the ultimate load level, the fatigue resonator length is calculated by taking equation 2.63 into account. Then, the burst pressure is approximated by dividing the resonator length change by the pressure sensitivity. Table 4.3 summarizes the experiment, in which the sensor's resonator length has shortened by $15.63 \mu m$ and divided by the typical mechanical displacement sensitivity, as shown in table 4.1, a burst pressure p_{max} above 9.3 MPa results. This high rating exceeds the rating of electrical counterparts by two magnitudes [110]. The high overload stability is caused by the intrinsic advantage of the brittle glass material, which, unlike metal, stays under stress elastically until it suddenly ruptures with high elongation.

Table 4.3.: Experimental evaluation of the burst pressure p_{max} .

condition	λ [nm]	$\delta\lambda$ [nm]	N	L_0 [μm]
idle	1555.361	25.497	62	48.216
burst	1551.697	37.846	42	32.585

The erosion due to environmental precipitation on a wind turbine is being considered to bring the burst pressure rating into perspective. The blade is subject to continual wear during a wind turbine's lifetime. At the exposed leading edge, constant collisions with raindrops, dust, hailstones, and insects trouble those remote sensing locations. Meanwhile, wind turbines are designed to take advantage of higher tip speeds up to $v_{tip} = 110 \text{ m/s}$ to be able to capture more energy per turbine [12]. Assuming a very large raindrop with a diameter $d_{drop} = 5 \text{ mm}$ and elevated impact velocity, impacting at the most severe erosion location, applies a pressure similar to $p_{drop} = 8.0 \text{ MPa}$. This force is less than the tested burst pressure p_{max} [134]. Similar sensors have been tested for non-destructive overpressures of 10 MPa with a high-pressure cleaner [132] for additional verification. Nonetheless, the impact of heavier and larger hailstones at the stagnation point may damage the sensor severally [134].

4.3. Measurement Performance in Combination with the Edge-Filter Interrogator

The sensing performance of the setup relies on the interaction of the sensor transducer and edge filter measurement system, as elaborated in chapter 2.2.5. Therefore, the following section examines the completed measurement setup.

4.3.1. Linearity and Measurement Range

Unlike the measurement with a broadband spectrometer, due to the distortion of the edge filter, the signal becomes non-linear at the measurement borders when measuring with the proposed edge filter interrogator. Therefore, the full-scale measurement range FS of the fiber-optic system, including the edge filter interrogator, is limited by

4. Qualification and Verification of the Measurement System

the predefined maximal linearity deviation. Figure 4.12 illustrates a fitted straight line's linear deviation, relative and absolute measurement deviation into the transfer curve. The upper left Figure displays additional calibration measurement data, which matches the simulation, assuming the sensor transducer's sensitivity and the edge filter properties are tuned within their tolerances. In this example, the maximal deviation is limited to 0.5%. Next to non-linearity, the sensitivity decreases towards the measurement boundaries as the ρ relation reduces its slope [116].

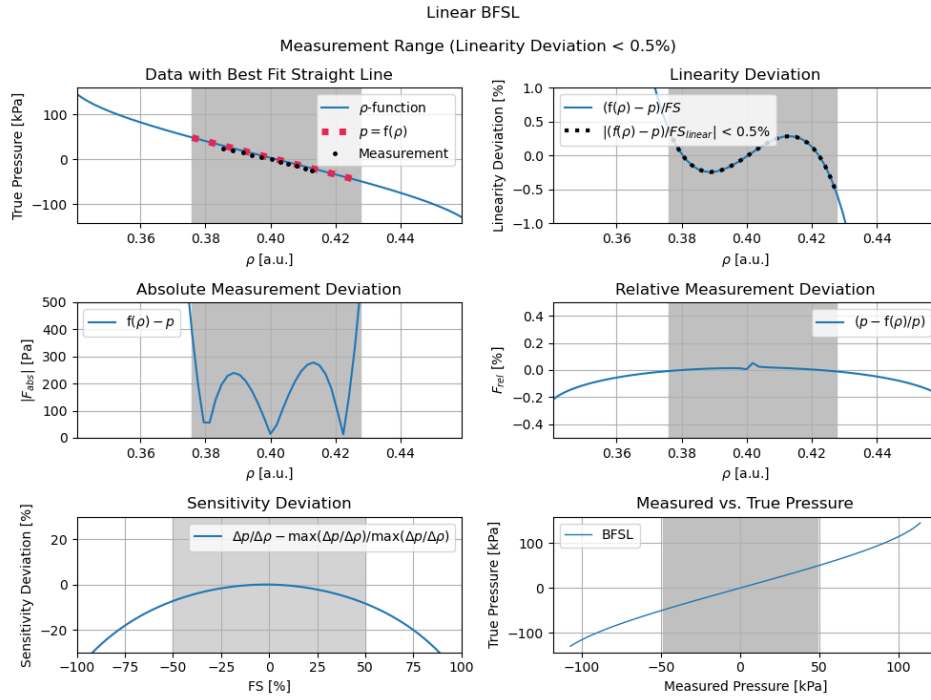


Figure 4.12.: Fit of measurement data with simulation, linear deviation, a relative and absolute measurement deviation of the transfer curve of Fabry–Pérot sensor in the combination of an edge filter interrogator. The transfer curve of Fabry–Pérot sensor, sampled by an edge filter interrogator, results in a sinusoidal shape. The Q-point marks the operating point of the highest sensitivity. The defined maximal deviation of the fit from the regression limits the measurement range. Although a linear fit of the regression limits the measurement bandwidth of the sensing system, it ensures the least distortion. The measurement range can be expanded with polynomial regressions if sensitivity deviation is exceeded at the measurement boundaries [219].

Based on the requirements of the individual application, the measurement range is defined by the maximal allowed linear deviation from a fitted transfer curve. Additionally, the signal quality is subject to a lower signal-to-noise ratio for a fitted straight line due to decreasing sensitivity towards the measurement boundaries, where the ρ function reduces its gain. Such sensitivity deviation must be especially considered in a dynamic sensing application, such as sound monitoring because

4. Qualification and Verification of the Measurement System

the signal-to-noise ratio degrades. A non-linear bandwidth expansion will allow monitoring of large quasi-static pressure changes for almost static measurement. Next to the reduced signal-to-noise ratio, implementing the fitted equations to the signal processing unit requires higher computational power. Table 4.4 summarizes that the measurement range can be expanded by utilizing non-linear functions of higher order, considering a maximal linearity deviation of 0.5 % and an optimally positioned Q -point. Nevertheless, the degradation of sensitivity at the measurement borders must be considered.

Table 4.4.: Measurement ranges of the final cylindrical fiber-optic pressure sensing setup. Assuming an optimally positioned Q -point, the deviation of the fit limits the measurement range and can be expanded with a non-linear fitting function [116, 130, 178]. This table summarizes different mathematical functions which are fitted to the data. The *BFSL* describes the fit of a polynomial of 1st degree. The data is also fitted with polynomials of higher order. Moreover, the data is fitted with a sine function, Gaussian distribution, and the Lorentz shape.

Method	FS [kPa]	F_{abs} [Pa]	FS [nm]	λ_{min} [nm]	λ_{max} [nm]	F_{rel} [%]	Sensitivity [%]
<i>BFSL</i>	47.32	254	2.8	1550.8	1553.6	0.53	-8
Polynomial 3rd	128.44	609	7.6	1548.4	1556	0.47	-48
Polynomial 5th	169	778	10	1547.2	1557.2	0.46	-71
Sine	133.51	761	7.9	1549.3	1556.2	0.56	-50
Lorentz	123.37	1217	7.3	1548.5	1555.8	0.98	-45
Gauss	130.13	676	7.7	1548.3	1556.0	0.51	-49

4.3.2. Reproducibility and Other Measurement Deviations

Every measurement system is subject to measurement deviations. Therefore, an inherent task of sensor design is to analyze and quantify the root cause of measurement deviations. The most prominent systematic effects are grouped into the deviation of the fitted regression of the transfer curve, optical polarization, light fluctuations, temperature, and acceleration influences. The discussed temperature and acceleration cross-sensitivities are neglected in the following because those systematic effects can be compensated for with an appropriate sensor.

Deviation of the fitted regression of the transfer curve is a significant cause of measurement deviation. Depending on the type of fit, the absolute measurement deviation F_{abs} and the relative measurement deviation differ. The table 4.4 summarizes the expected systematic measurement deviations of the final sensor iteration. For a linear fit, the measurement deviation increases with distance regarding the optimal operating Q -point. Nevertheless, the predefined deviation of linearity of 0.5 % adds to the overall uncertainty.

4. Qualification and Verification of the Measurement System

Light source fluctuations of the interrogator alter the pressure reading if the integrated amplified spontaneous emission light source of the interrogator is used in a non-linear power setting. In order to evaluate the dependencies, a pressure sensor has been calibrated multiple times at different power settings. As illustrated in Figure 4.13, a significant measurement deviation occurs at low power settings. The root cause of this measurement deviation is a non-uniform light density increase of the light source at low power settings. Only at mid and high-power settings will the amplified light sources, which illuminate a narrowband light spectrum, increase its light spectrum uniformly across its entire bandwidth. In order to reduce such power-dependent deviation, the interrogator's power setting has persisted at high power settings. Still, excluding polarization effects, which are discussed in the following, the effect adds the uncertainty of additional 0.8 %.

The polarization of an optical system is a crucial parasitic challenge. Although the light source of the interrogator illuminates depolarized light in the C-band to a high degree, each optical component alters the polarization state. Figure 4.13 illustrates the stochastic effects of polarization on the pressure reading. Here, a pressure sensor has been calibrated multiple times, and the polarization state has been altered mechanically by polarization paddles. The minimum and maximal deviation about mean calibration result in a maximal peak-to-peak deviation of 84 Pa in relation to the measurement range equal uncertainty of 0.19 %. In order to confirm the impact of polarization, the experiment was repeated without changing polarization orientation. The resulting maximal deviation indicates reduced repeatability of 66 Pa the system.

4. Qualification and Verification of the Measurement System

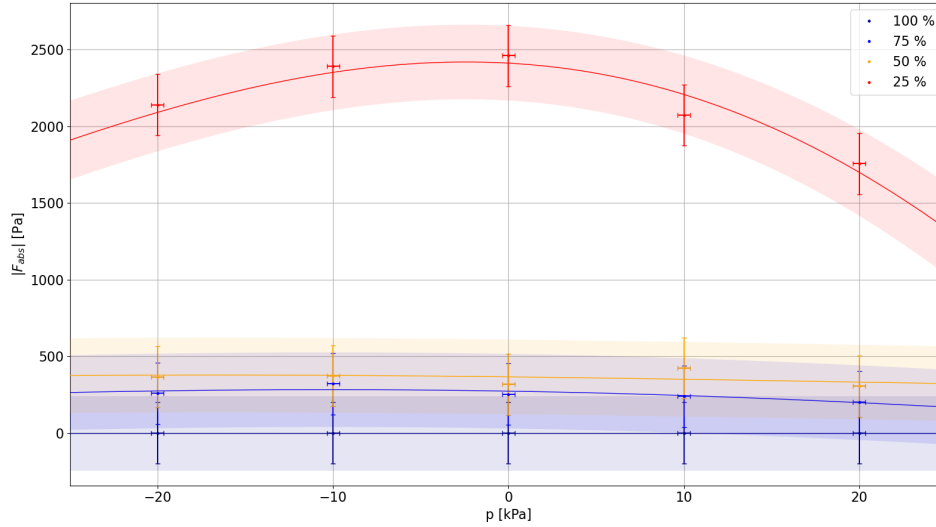


Figure 4.13.: Measurement deviations due to polarization and a non-uniform light density increase. The deviation of the pressure sensor reading at different power settings of illumination results in a non-uniform increase in light intensities over the bandwidth. Additionally, the error bar and colored shadow indicate the stochastic deviation due to polarization effects.

Considering the mentioned stochastic measurement deviations, the system’s reproducibility is better than 1.5 % of the full-scale measurement range. On top of this uncertainty, systematic effects such as temperature and acceleration cross-sensitivity have to be considered.

4.3.3. Noise Floor, Resolution, Dynamic and Frequency Range

The achieved noise floor, resolution, dynamic range, and sampling frequency of the fiber-optic setup depend mainly on the electronics of the edge-filter interrogator.

Noise Floor: Regarding Figure 4.2 on page 51, the noise floor is constant over a frequency bandwidth up to 10 kHz and has been reduced to $0.01 \text{ Pa}/\sqrt{\text{Hz}}$, which equals 60 dB SPL for an optimized sensing system. This noise floor is comparable to the noise of conversational speech in 1 m distance. Nevertheless, systems, which have been suited for large-scale static pressure monitoring, have required a less sensitive design in order to expand the measurement range. In those cases, the evaluated sensor systems have a noise floor around $0.3 \text{ Pa}/\sqrt{\text{Hz}}$, which equals around 80 dB SPL, when sampled at 10 kHz.

Resolution: The signal resolution defines the smallest resolveable incremental signal change. In practice, especially the analog-digital converter dictates the measurement performance. Here, the interrogator has utilized a 16 bit analog-digital converter. Due to the ratio principle, in which two digital data streams are divided,

4. Qualification and Verification of the Measurement System

the dynamic range and resolution are optimized. By dividing two digitizers with each other, the characteristics of 32 bit converter are mimicked. Multiplying the smallest digitizer resolution $\rho_{min} = 1/2^{32}$ with the typical linear sensitivity factor $k_{typ} = 5.0 \cdot 10^6$ results in a typical pressure resolution of 0.136 mPa. This theoretical resolution is subject to data type precision.

Dynamic Range: The dynamic range is the ratio of the loudest undisturbed signal and the signal's noise floor. When assuming that the largest possible sound amplitude is half of the measurement range, a linear regression of the transfer curve and a noise floor $0.3 Pa/\sqrt{Hz}$, the dynamic range equals 103 dB. As elaborated, this high dynamic range is larger than the maximal theoretical dynamic range of a single 16 bit analog-digital converter due to the ratio formation of two converters with each other. Practically, the analog-digital converter provides a lower number of effective bits. Nevertheless, depending on the application, the trade-off between maximal monitoring of large static amplitude and silent monitoring sounds needs to be considered. The dynamic range can be shifted to larger or smaller amplitude ranges. Nevertheless, increasing it to suit large static pressure changes and tiny fluctuations is challenging.

Frequency Bandwidth: The frequency range of the measurement system is determined partly by the sensor's mechanics, as discussed in section 2.3.2.2 on page 40, and the sampling mechanism of the electronics. For the utilized interrogator, the sampling frequency up to 50 kHz is adjustable individually for each sensor channel. Due to the sensor's high natural frequency above 250 kHz, any phase delays for the monitored pressure fluctuations up to the cut-off frequency of 10 kHz can be neglected. The high oversampling combined with low pass filter characteristics ensures that the Nyquist criteria are fulfilled. In addition to the low response times, the synchronicity of the individual channels down to $20 \mu s$ is to be mentioned when pressure signals need to be correlated to each other [158]. After sampling, the digitized data is transferred from the interrogator to a host computer via Ethernet interface [158].

5. Experimental Aerodynamic Validation of the Measurement System

This chapter summarizes the main experimental results in the context of aerodynamic validation with fiber-optic pressure sensors in field tests. The chapter is based on publications made within the scope of this dissertation and partnering research work, which utilizes the developed measurement system to investigate related detailed research questions in the broad field of aerodynamics.

This chapter is divided into the following parts:

Wind-Tunnel Evaluation: Fiber-optic pressure sensors in low and high-speed Wind-tunnel tests [218, 220]

Winglet: Fiber-optic pressure measurement on a complex outer winglet model with active flow control actuators [218, 219]

Flight Test: Static and dynamic pressure measurement in a flight tests [217, 218]

Fiber-optic probe: Monitoring inflow velocity and angle with fiber-optic pressure sensors [212, 214]

Wind Turbine: Measurement of the aerodynamics of a wind turbine with fiber-optic pressure sensors [215, 218]

Several aerodynamic experiments have been instrumented with fiber-optic pressure sensing systems in recent years. Based on these studies, the maturity of the technology is discussed. The following discussion has been published. The field test validation of aerodynamic profiles of wind turbines is very similar to the evaluation of an aircraft's airfoil. Nonetheless, in both applications, the field measurement results are confidential to a large extent, and the manufacturer's intellectual properties must be maintained. Therefore the published results are either relative or normalized, even though the work concentrates on the sensor characterization in the field application. The chapter covers static pressure distribution applications, lift coefficient and dynamic field propagation measurement, acoustic signals, and cross sensitivities.

5.1. Wind-Tunnel Evaluation: Fiber-optic Pressure Sensors in Low and High-speed Wind-Tunnel Tests

5.1.1. Description of Experiment

In order to increase the maturity of the sensor technology, different wind tunnel tests have been conducted. Compared to lab experiments, these wind tunnel tests aim to provide more complex aerodynamic situations, which shall be investigated with fiber-optic means. Two wind tunnel tests have been carried out as part of the Cleansky 2 project SKOPA (Skin friction and fiber optics-based surface pressure measurements for aircraft applications). One of the goals of this project is to design and test a complete, flight-ready fiber-optic sensing system for time-resolved surface pressure measurement. The first test in a wind tunnel shall test the sensor's dynamic capability to monitor complex propagating pressure turbulence. The second wind tunnel test investigates the static measurement performance of sensor [220].

Another objective of the project is to demonstrate and quantify the effect of active flow control oscillators (AFC) on aerodynamic structures close to inhabitable flow conditions with a suitable sensing system. Such device mixes oscillating flow into the turbulent boundary layer and is supposed to delay a stall. In addition to all validation measurements in the wind tunnel, the experiments include validating active flow control concepts. Active flow control has been instrumented in both cases to alter flow conditions. Previous research projects have proven that a highly loaded compressor stator cascade as an active flow control leads to an increase in efficiency of 5% [138, 139, 220]. The following experiments shall demonstrate the beneficial effect of pulsed fluid jets for active flow control and evaluate a robust monitoring solution.

The results have been published in a conference proceeding [220].

5.1.1.1. Low-Speed - Experimental Setup

The first low-speed wind tunnel tests have been performed to investigate the dynamic characteristics of the fiber-optic measurement setup. As this has been the first wind tunnel test utilizing this concept, the main objective is to investigate the feasibility of measuring dynamic pressure with the proposed design and neglecting the evacuated packaging process. Therefore, these sensors have been manufactured as differential sensors. The leading edge of this test setup has been equipped with a fluid actuator system capable of forcing active oscillating air streams inside the boundary layer. Figure 5.1 - a illustrates the complete setup, including a diffuser, which can vary the angle α from 0° to 23° . The eight pressure and three reference sensors are placed in a line in the chordwise direction. The fiber-optic pressure sensors have a distance of 14 mm to each other. In order to control and ensure a constant Reynolds number during the duration of the experiment, a fresh-water cooling system controls the temperature of the flow [138, 220].

5. Experimental Aerodynamic Validation of the Measurement System

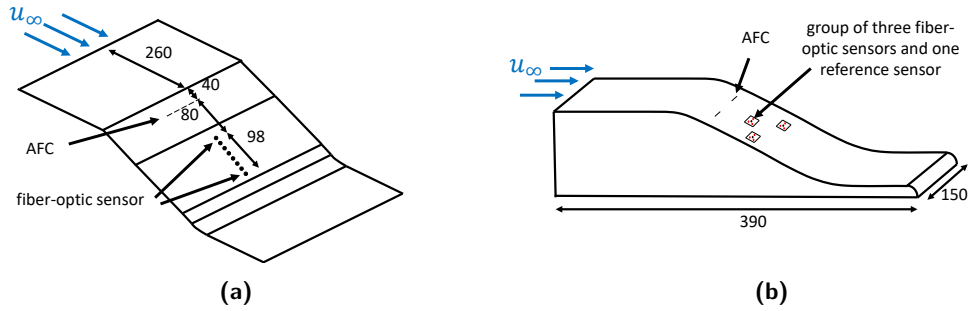


Figure 5.1.: Test setup of the low-speed and high-speed wind tunnel test. The low-speed inflow coming from left to right is influenced by an active flow control oscillator (AFC). The spacing between the fiber-optic pressure sensor is 14 mm in the low-speed wind tunnel test (a) [220]. The high-speed test is shown on the right (b). In both tests, the inflow from left to right is influenced by the active flow control to generate a complex airflow [220].

5.1.1.2. High-Speed - Experimental Setup

In a second high-speed wind tunnel test, the static performance of nine fiber-optic pressure sensors is evaluated up to $M = 0.5$. In order to generate a complex three-dimensional flow, a bump and an active flow oscillator are integrated into this test setup. The right Figure 5.1 illustrates the measurement setup, including the bump and active flow control. Additionally, to benchmark the fiber-optic sensors, three additional reference sensors are located in groups with three fiber-optic sensors each [138, 220].

5.1.2. Experimental Results

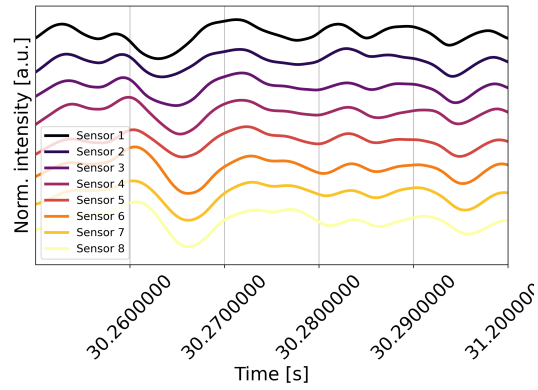
5.1.2.1. Low-Speed Wind-Tunnel Test

A fundamental advantage of the fiber-optic pressure sensor is its surface-neutral membrane, which allows measuring fast pressure phenomena without interference due to pressure taps or covered and retracted membranes [132, 148, 212, 214]. Here, the fiber-optic sensors are supposed to monitor the propagation of a pressure field. Although the pressure field does not travel quickly over the array of eight pressure sensors, the measurement sampling rate is set to 16.0 kHz to ensure a high time-resolved signal. The measurement is performed in two stages. After the inflow settles at 10.0 m/s, the active flow control is enabled additionally. The device interferes with the turbulent flow, and the sensors monitor the turbulent flow propagation with and without active flow modulation. Later, the diffuser is set to a different angle α , and the measurement is repeated. Figure 5.2 demonstrates that the system can resolve high-frequency fluctuations in the pressure field propagation at $\alpha = 0^\circ$.

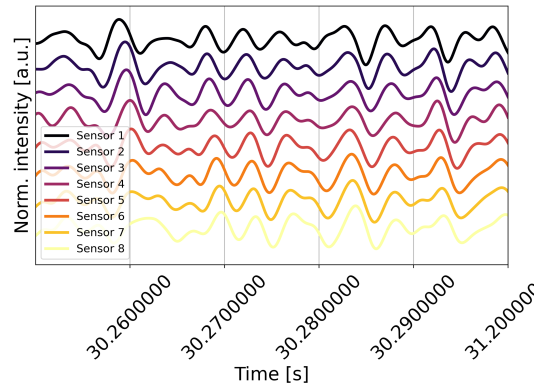
Figure 5.3 illustrates the propagation of the active flow control's airflow, which traverses the fiber-optic pressure sensors.

The following results are based on the methods described in section 2.1.4.2 on

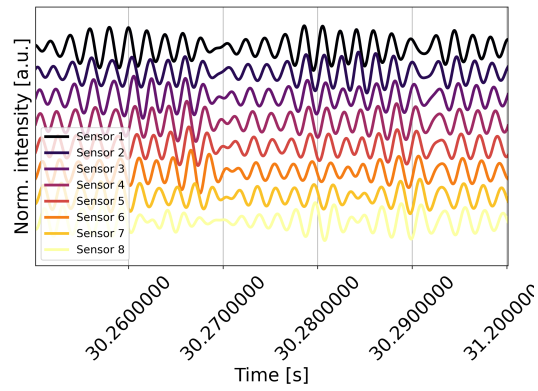
5. Experimental Aerodynamic Validation of the Measurement System



(a) 0 Hz...10 Hz



(b) 10 Hz...30 Hz



(c) 40 Hz...60 Hz

Figure 5.2.: Filtered time-series of eight fiber-optic pressure sensors illustrate the propagation of a pressure field. Depending on the filter characteristic, normalized and band-pass filtered time-series can be computed, which show the pressure field propagation over eight differential pressure sensors. The top signal is measured by the first sensor encountered by inflow [220].

5. Experimental Aerodynamic Validation of the Measurement System

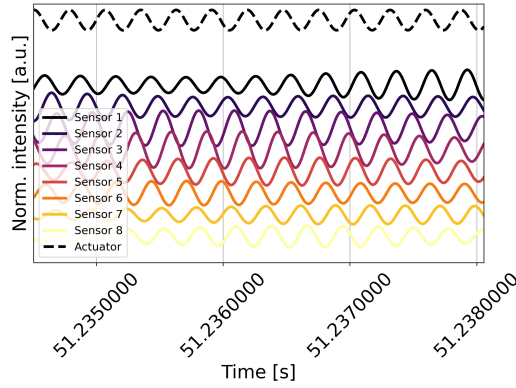


Figure 5.3.: Filtered time-series of eight fiber-optic pressure sensors and an electrical sensor integrated into the AFC illustrate the propagation of the pulsed air stream from the AFC. The top signal is measured by the first sensor encountered by inflow [220].

page 18. By filtering the time-series signal, the propagation speed is traced. In this setup, the sensors are aligned in a row, and the steady turbulent inflow passes each sensor subsequently. The sensor signals in the Figure are normalized and shifted to illustrate the comprehension more clearly. The time-series illustrates the propagation of the pressure fields at a 10 m/s flow rate. The sensor signal, displayed at the top of all graphs, represents the first sensor inline and encounters the inflow first. Each subsequent filtered sensor signal is highly correlated, but a phase-shifted signal of the first sensor signal [220].

Two approaches are considered to evaluate the delay τ or phase shift ϕ of the pressure field. At first, the cross-correlation of the data and, secondly, the coherence are discussed.

If the active flow control is disabled, the mean phase differences between the sensor result to -18.8° , which corresponds to a delay of 14.5 ms at 36 Hz . Considering the spacing of 14 mm between the sensors, the propagation speed of the turbulence equals 9.62 m/s , which is almost similar to the expected inflow speed of 10.0 m/s . When the active flow control is enabled, the correlation approach calculates an average phase difference of -71.5° between the sensors. Here, the algorithm picks up the dominant frequency origin from the flow control at excitation at 352 Hz .

Extracting the time delay information via the coherence function is helpful for larger data sets because the result also provides frequency information. While the direct correlation integrates over all frequencies as shown in equation 2.15, the coherence approach leads to no frequency discrimination [17]. The following results are based on the principles introduced in 2.1.4.3 on 19.

Figure 5.5 displays the measurement results utilizing the coherence approach. Nevertheless, this approach via coherence has the drawback that the resolution of the frequency Δf has to be considered, which is equal to the sampling frequency f_s divided by the window size. This frequency resolution determines the resolution of the time delay. A high-frequency resolution is required to convert angular phase

5. Experimental Aerodynamic Validation of the Measurement System

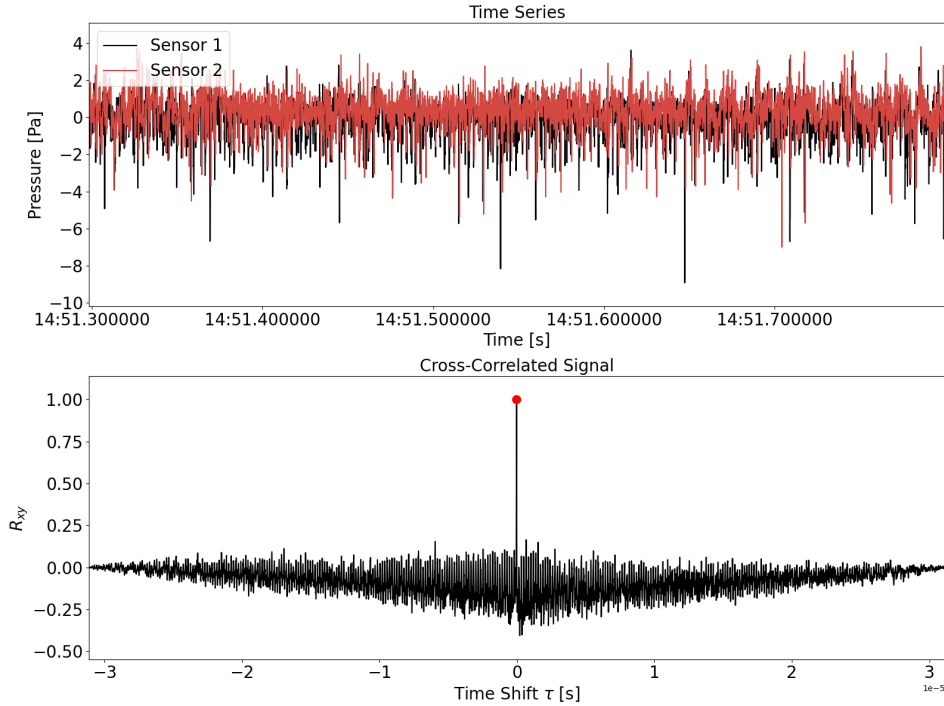


Figure 5.4.: Time-series and cross-correlation of a windowed turbulent flow. The cross correlation of two time-series reveals the time shift between the signals. With such information and considering the distance between the sensor location, the propagation speed of a pressure field can be calculated.

difference to a time delay, as discussed in equation 2.14. In order to increase the frequency resolution, the window size would have to increase while keeping the sampling frequency. Therefore, expanding the windowing function at an equal length of the measurements results in lower numbers of iterations of Fourier transforms but higher frequency resolution. Depending on the windowing function, the frequency resolution might be inadequate [17, 45].

The chordwise coherence length scale of the turbulent structure characterizes the relationship between the airfoil turbulence phenomenon and the frequency. For example, Figure 5.6 illustrates the coherence length of the turbulent airflow on a flat plate, e.g., the diffuser is set to $\alpha = 0^\circ$ for enabled and disabled active flow control. If the active flow is enabled, the coherence length for the characteristic oscillation frequency and its harmonic multiples increase [97]. Next, compared to measurements with disabled flow control, the enabled active flow control also shapes the low-frequency region to larger coherence lengths. This result indicates the beneficial effect of the active flow control, which extends the length of regimes in which the flow stays attached [7, 8, 97].

In conclusion, for the present measurement data, both calculations for phase shift tracking are very much in agreement. To give a numerical example, when the ac-

5. Experimental Aerodynamic Validation of the Measurement System

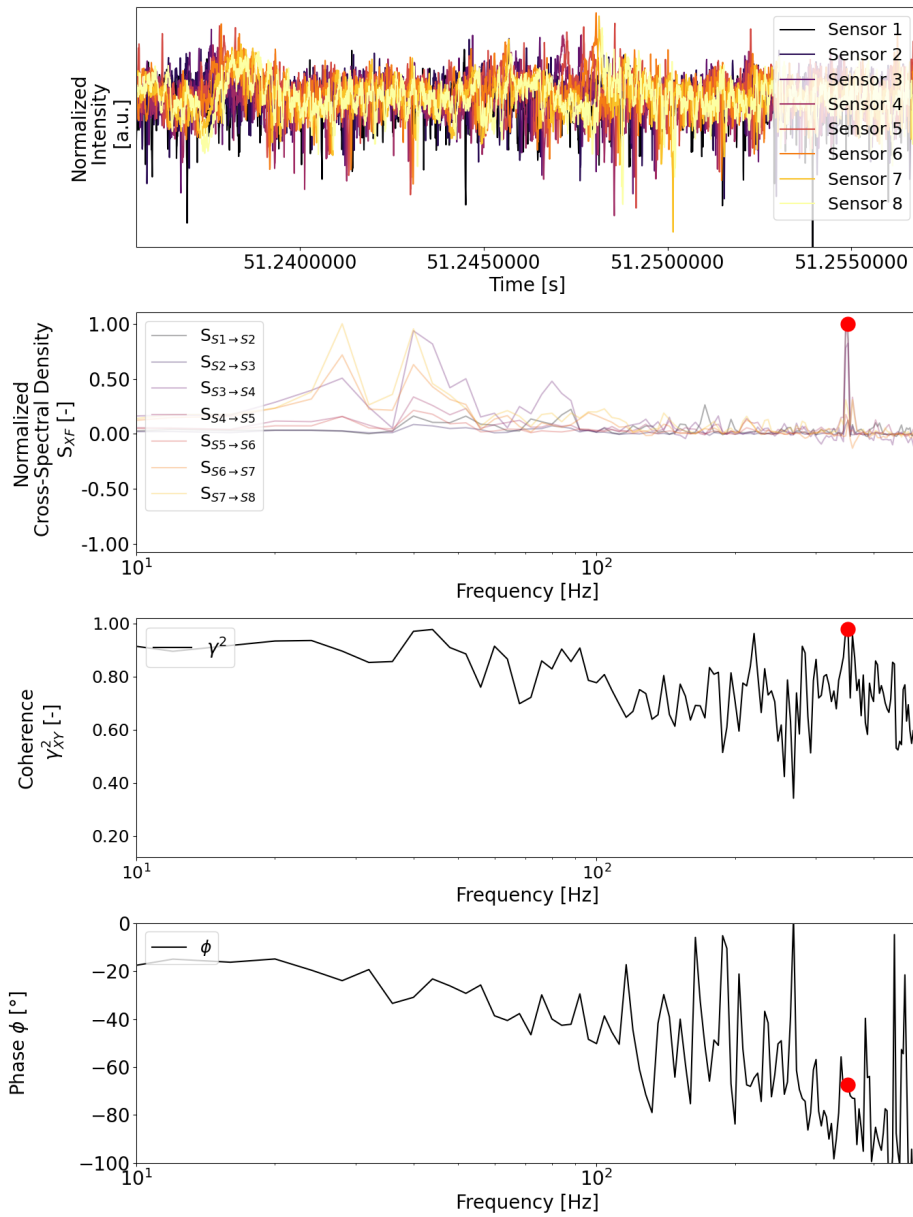


Figure 5.5.: Coherence of the measurement signals. The first illustration shows the time-series of the measurement of eight fiber-optic pressure sensors. The second illustration displays the cross-spectral density of the sensors to each other. Noticeably, the active flow control's frequency is detected and marked with a red dot. The averaged coherence function is derived from the cross-spectral density of the sensors to each other, which also provides phase information in the last illustration.

5. Experimental Aerodynamic Validation of the Measurement System

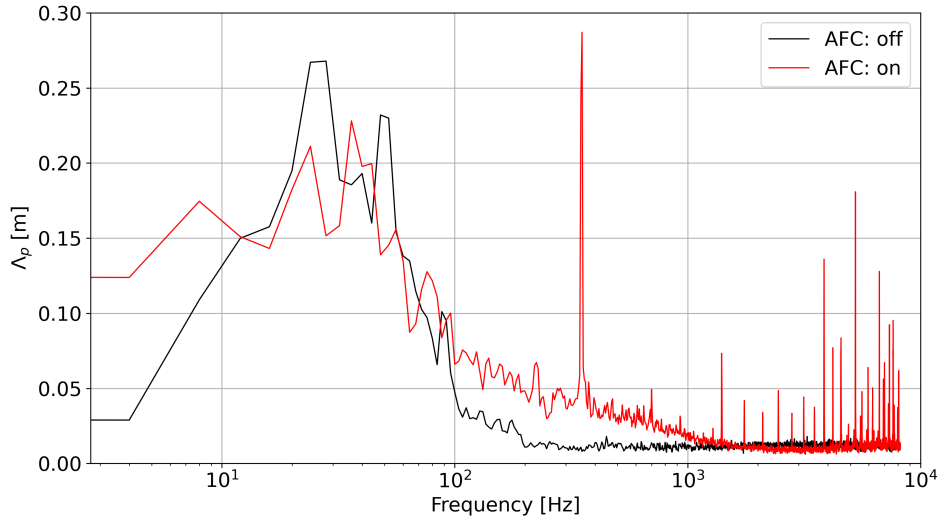


Figure 5.6.: Coherence length of the turbulent airflow on a flat plate. The chordwise coherence length of a turbulent airflow indicates in which frequency range the airflow topology becomes more uniform. Obviously, due to the excitation, the coherence length in the frequency range of the active flow oscillator is dominant. Nevertheless, the active flow control also enlarges the coherence length in the quasi-static frequency region, which indicates a more stable and uniform airflow in a spanwise direction.

tive flow control is enabled, the correlation approach calculates an average phase difference of -71.5° and the calculation via coherence results -67.4° for excitation at 352 Hz. If the active flow control is disabled, the mean phase differences between the sensor result to -14.4° and -15.8° , which equals to a time shift of 16 ms at 24 Hz. By measuring with multiple sensors with true-surface membranes, the coherence length can be monitored in an extensive frequency range which fingerprints the properties of an airfoil.

5.1.2.2. High-Speed Wind-Tunnel Test

While the low wind speed test investigates the sensor's dynamic measurement capabilities, the high wind speed test evaluates the sensor's static measurement capabilities. In order to examine the active flow control and the sensor's performance on static pressure fields, an absolute pressure sensing design has been utilized for a second consecutive high-speed wind tunnel test. Moreover, state-of-the-art reference sensors have been instrumented at a very close distance to the sensor being tested to benchmark the sensor signals. While the fiber-optic sensor measured up to 10 kHz, the reference sensors of type Kulite XT-140M are limited to a sampling rate of 1 kHz due to the electrical imc CANSASflex-UNI8 interrogator [83, 111]. Therefore, the comparison analysis will concentrate on the smaller frequency range. Figure 5.7 illustrates the pressure reading of a fiber-optic sensor compared with a conventional sensor used as a reference [220].

5. Experimental Aerodynamic Validation of the Measurement System

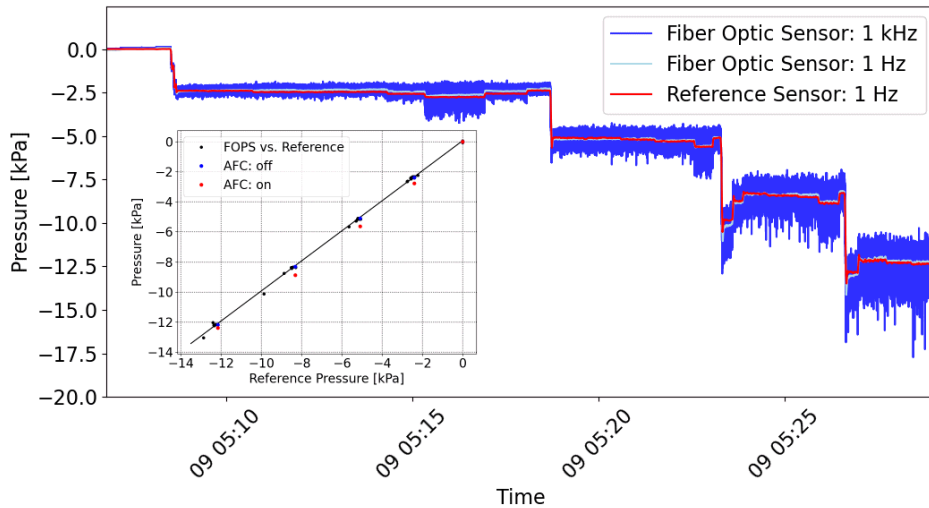


Figure 5.7.: Time-series of the pressure signals in the high-speed wind tunnel test. The pressure signals show a great match between the sensor under test and the reference sensors. More suction has been generated with increasing Mach numbers, which range from 0.2 M up to 0.5 M. Moreover, the active flow control has been triggered at each flow condition to investigate its aerodynamic impact [220]. The sub-picture illustrates the fiber-optic sensor reading versus the reference pressure sensor reading. The fiber-optic pressure sensor matches the reference sensor reading very well. The slope of the polygonal fit of the data equals 0,99. Additionally, the Figure contains data-colored plots, which demonstrate the effect of the active flow control. In this experiment, the active flow control affects the aerodynamics, generating additional suction.

The fiber-optic sensors match the reference signal well in the time-series, as illustrated in Figure 5.7. Moreover, the subfigure in Figure 5.7 displays the relation between the reference sensor and the reading of the fiber-optic sensor. The pressure signal varies with the Mach number. With increasing Mach number from 0.2 M up to 0.5 M, more suction is generated. Eventually, the active flow is enabled at each velocity level. The active flow influences the static lift positively. The added suction varies non-linearly for each flow speed and ranges between 1.8 % for high Mach numbers to 15.0 % for low Mach numbers [220]. Additionally, the power spectral density results of the reference and the fiber-optic pressure sensor in Figure 5.8 match within the expected measurement deviation as elaborated in chapter 4.3.2. The measurement results of the fiber-optic setup are compared to the reading of the reference sensor. The electrical measurement setup equals the results for the low-frequency region. Due to the low cut-off frequency of the electrical interrogator, the measurement of dynamics at a higher frequency cannot be compared. Nevertheless, the fiber-optic measurement system, sampling, and having a cut-off frequency at 10 kHz measures all dynamic effects and the sounds generated by the active flow control. A more comprehensive frequency range of the power spectral density, neglecting the reference sensor, is shown in Figure 5.8 as well [220].

5. Experimental Aerodynamic Validation of the Measurement System

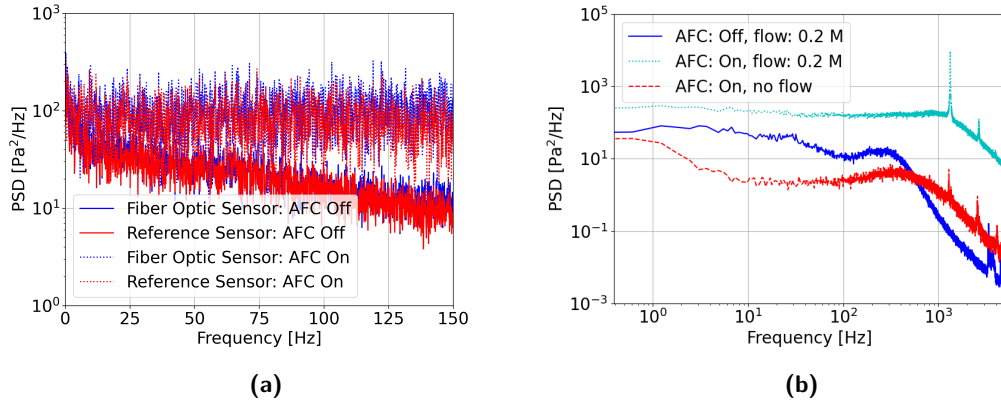


Figure 5.8.: Typical power spectral density of measurement demonstrating the effect of the active flow control in the low and high-frequency region. Figure (a) shows that the low-frequency dynamic measurement results of the reference and the fiber-optic sensor overlap each other [220]. Figure (b) illustrates the high-frequency range without any reference data. If the active flow control is enabled, oscillating flow interferes with the turbulent flow conditions. The oscillation generates the typical switching frequency as a noise source. Next, the flow control generates more dynamic streams at low frequencies and improves the static lift [220].

While sensors at the leading edge have measured suction, sensors located downstream have monitored static down thrust due to the high angle of attack and detached airflow. The power spectral density of the sensors demonstrates their capabilities as dynamic sensors. If the active flow control is enabled, the oscillating mechanism generates a high-frequency noise as sound, which depends on the amplitude of the volume flow. Additionally, the flow control also generates more dynamic streams at low frequencies. Therefore, it improves the static lift for this illustrated sensor [220].

5. Experimental Aerodynamic Validation of the Measurement System

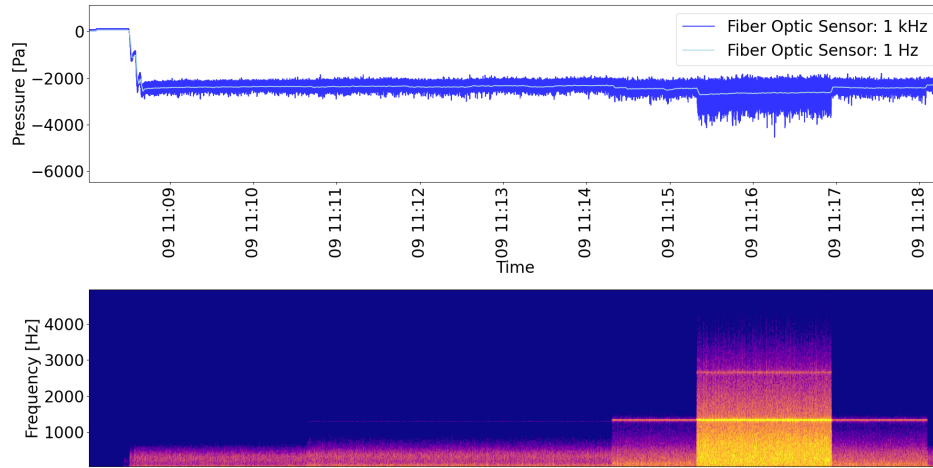


Figure 5.9.: Spectrogram a sensor in the high-speed wind tunnel. The diagram relates the static measurement to the dynamic measurement. The active flow control generates a specific frequency pattern regardless of volume flow. Additionally, the AFC affects the static lift by reattachment of flow. Therefore, monitoring this frequency fingerprint exposes whether the flow control is active or not [220]. The pressure drop is confirmed by reference and fiber optic sensor.

Figure 5.9 relates the static measurement to the dynamic measurement in a spectrogram. On this occasion, the wind tunnel settled at 0.2 M, and the volume flow of the active flow control increases up to 213 l/min. The illustration demonstrates the effect of the active flow control for this sensor position very well. By increasing the volume flow, the triggered dynamic vortex flows influence the static suction on this sensor position, represented by the downsampled sensor signal. The emitted specific frequency pattern is very well observable by the sensor; therefore, monitoring this frequency fingerprint exposes the functionality [220].

5.1.3. Summary of the Results

For validation, seventeen sensors have been mounted in a low-speed, high-speed wind tunnel equipped with active flow controls in two wind tunnel campaigns, and the sensors being tested have been compared to their electrical counterparts. The low wind tunnel test has demonstrated that the sensor's surface-neutral membrane benefits monitoring turbulence pressure field propagation. Furthermore, due to the surface-neutral membrane of the optic sensor, no parasitic acoustic disturbances occur [132]. The second high-speed wind tunnel test focused more on the static pressure measurement performance. Both tests, in conjunction, prove that such measurement systems can resolve complex aerodynamic conditions in the static and dynamic domain and have raised the maturity of the technology [220].

Nevertheless, some complications with the measurements due to the layout of the differential fiber-optic pressure sensor and the reference sensor have been found during the wind tunnel tests. Firstly, in the low wind speed test, the reference

5. Experimental Aerodynamic Validation of the Measurement System

sensors are located too far from the sensors under the test. Secondly, the differential characteristic of the fiber-optic pressure sensors in the test did not allow static comparisons or calibrations. Finally, in the high-speed wind tunnel tests, the sensors have been manufactured with a sealed air reservoir in the sensor's cavity, which results in a higher temperature dependency. However, the high-speed wind tunnel changes its temperature significantly. Additionally, the temperature sensor utilized for active compensation has been mounted too far from the pressure sensor, so a temperature gradient has persisted. Despite the mentioned challenges, the high-speed experiment has proven that the static pressure sensing capability is sufficient to resolve the effects of flow controls on aerodynamic structures [220].

5.2. Fiber-Optic Pressure Measurement on a Winglet Model

Modern aircraft winglets' complex shape is aerodynamically optimized for normal flight configuration at cruising altitude. The low lift-to-drag ratio reduces the climb performance of the entire aircraft at high angles of attack and, therefore, detriment the aircraft's low-speed performance [154]. Consequently, this aerodynamic drawback expands take-off and landing distances and affects commercial and safety-critical aspects. Conventional high-lift devices such as extendable flaps and slaps improve the aerodynamic characteristics at low speeds by decreasing stall speed but are challenging to integrate into the winglet's complex three-dimensional curved geometry [117, 120, 124]. In consequence, the modern winglet must contain cut-outs of slats. These areas are prone to flow separation even at lower angles of attack. In addition to conventional mechanical high-lift devices, active flow control actuators, which periodically blow out compressed air, are evaluated to modify boundary-layer flow near critical areas prone to flow separation. This experiment validates the capability to measure the local flow separations at a winglet with the fiber-optic sensing system and benchmarks it with conventional pressure measurement systems. Additionally, it demonstrates the technical feasibility of evaluating the innovative active flow control system's performance in combination with the measurement setup. A large-scale wind tunnel experiment has been set up with a 1:4.5 scale model of an outer wing of a commercially relevant civil aircraft in the "GroWiKa" at the Technische Universität Berlin. The model features high-lift devices, such as a slat and a flat, in take-off configuration [119, 121, 122, 219]. As a fundamental part of the Cleansky2 project SKOPA, a fiber-optic pressure sensing measurement has been evaluated in wind tunnel tests. The project scope is to evaluate the measurement performance of the pressure sensor in controlled environments [219]. The results have been published in a journal paper [218, 219].

5. Experimental Aerodynamic Validation of the Measurement System



Figure 5.10.: Outer Winglet Model installed in the wind tunnel [219].

5.2.1. Description of Experiment

5.2.1.1. Experiment Setup

The sensors are instrumented downstream closely to the slat's end and near the outlet of an active flow actuator to monitor the slat's vortex, which degrades airflow. In total 25 fiber-optic pressure sensors in a row at spanwise location $y/b = 42\%$ and four fiber-optic temperature sensors for active temperature compensation are integrated into the model. Moreover, the sharklet is mounted on a six-component balance to measure all aerodynamic forces during the experiment. The sensors are distributed on the suction and pressure side to evaluate the pressure distribution with high spatial resolution. Beforehand, the model has been evaluated with an electrical reference pressure sensor [119, 121]. This data is used as comparative results for the evaluation of quasi-static pressure. Figure 5.11 illustrates the experimental setup. The critical parameters of the experiment are summarized in Table 5.1 [219].

Table 5.1.: Aerodynamic key parameters of the experiment [219].

Parameter	Unit	Value
b	m	1.04
l_c	m	0.443
A_{ref}	m^2	0.493
Re	—	1.1 mio
u_∞	$\frac{m}{s}$	38
Ma	—	0.12

5. Experimental Aerodynamic Validation of the Measurement System

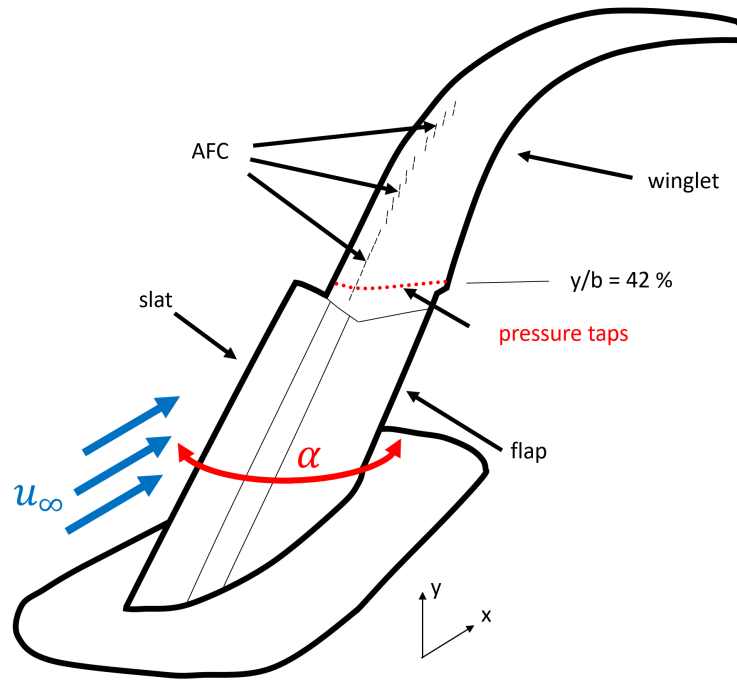


Figure 5.11.: Drawing of outer winglet model. The pressure taps used for the fiber-optic pressure sensors are installed at the relative position $y/b = 42\%$ with respect to the span b . The sensors are distributed on the suction and pressure side to evaluate the pressure distribution with high spatial resolution. Because of the missing slat, this area is prone to flow separation at a high angle of attack. A slat vortex degrades airflow, which originates from the end of the slat. [219].

Due to the tight integration of the active flow control equipment, actuators, their solenoid valves, and sensors in the same model, the pressure taps for sensors and actuators are necessary. In this experiment, the Reynolds number is kept constant at $Re = 1.1$ million, and the wing model's angle of attack α as well as the active flow control parameters vary. Nevertheless, this measurement approach comes with limitations. Firstly, routing long pressure tabs and small diameters limits the response time and allows only quasi-static pressure measurement in a limited frequency range. For dynamic sensing, the frequency transfer function would be needed to be calibrated beforehand [168, 212, 214]. The complex calibration means that it is challenging to study noise and turbulent flow characteristics directly and that each sensing channel's low-pass characteristic is expected. Secondly, in practice, channels are frequently either blocked by particles or not air-tight because of cuts or crushed taps, which complicates the installation [217]. In order to ensure the sensor's compatibility with conventional sensor housing, which has been instrumented to that model beforehand, the evacuated fiber-optic sensors are mounted into a PEEK plastic housing with a compatible shape for more straightforward installation purposes. The housing is shown in Figure 5.12. Additionally, in order to mitigate parasitic

5. Experimental Aerodynamic Validation of the Measurement System

damping due to tight packaging in the model, a bend-insensitive fiber has been utilized. This fiber allows damping-free light transmission down to a 5 mm bending radius and is assembled with a thicker buffer to increase robustness [29, 219].

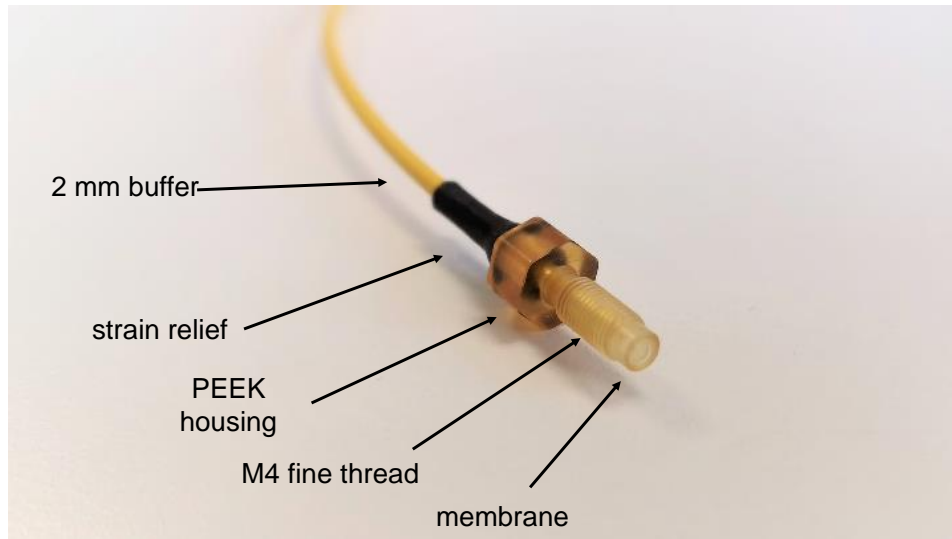


Figure 5.12.: Absolute fiber-optic pressure sensors in a PEEK housing. Non-metal absolute fiber-optic pressure sensors in a PEEK housing with a reinforced bend-insensitive fiber are used in this experiment. The threaded housing eases the integration. The pressure-sensitive membrane is located at the front face of the sensor. [219].

5.2.1.2. Active Flow Controls in Winglet Model

Actual flow separation is particularly undesired from an aerodynamic point of view since it limits both the maximum lift coefficient and the lift-to-drag ratio of the aircraft. These two aerodynamic quantities are safety-critical for landing and take-off, respectively [154]. Ongoing research activities try to tackle this challenge by introducing novel, integrated, active flow-control techniques applied at the wing-pylon interface or near the blended winglets to minimize possible separated-flow zones [117, 124, 195]. In order to increase safety during stall-critical flight maneuvers at high angles of attack, such as during landing and take-off, local active flow-control actuators are the focus of research. Due to their small size, the active flow control provides an alternative for the discussed integrational challenge of slats, and flaps [101, 117, 120, 124, 126]. These innovative lift devices improve the lift-to-drag ratio and therefore enable a better climbing performance by mitigating local flow separation in critical flight situations [121]. Therefore, these devices decrease stall speed but allow minimized integration into complex shapes. The actuators are instrumented close to the inhomogeneous aerodynamic elements as cut-outs of slats, which are prone to local flow separations [119–121, 219, 220].

This experiment features active flow control. Especially with this complex-shaped winglet, integrating conventional slats and flaps is challenging. The investigated

5. Experimental Aerodynamic Validation of the Measurement System

actuator is based on the principle of fluidic amplification [119–121, 180].

Flow separation is delayed to higher angles of attack if turbulent air mixes with the boundary layer. Therefore the actuators emulate the effect of a missing slat due to reduced flow separation with an appropriate choice of actuation parameters. The oscillating characteristics of the actuator depend on the internal layout and its supplied air pressure [119, 139, 140].

Each actuator segment consists of a driving and outlet stage. The driving stage is coupled to a solenoid valve to enable periodic switching. Each outlet stage features at least two chambers, which output flow periodically. Tuning the oscillation frequency and the mass flow affects the actuator’s performance because the induced air interferes with the dynamic flow field. If the active flow control matches the flow separation frequency, its performance optimizes due to a higher mixing rate across the shear layer in the airflow. In this experiment, the maximum switching frequency is limited to 300 Hz. The maximum mass-flow rate through each actuator segment is $\dot{m} = 10.8 \text{ g/s}$ [119, 121, 219]. The model contains three actuator segments, and in total, the excitation system consists of 28 slots, each 11.2 mm long and 0.8 mm wide. The actuator outlet openings align parallel to the leading edge of the wing. Only for the first actuator segment, all slots align parallel to the leading edge because the slat vortex forms locally and shall be influenced [119–121, 219].

5.2.2. Experimental Results

The following section summarizes the test results. This part is divided into two sections, which discuss the static and dynamic measurement characteristics for this wind tunnel test. In each run, the angle of attack α is varied in the same manner from its minimal angle α_{min} to its maximal angle α_{max} with an adequate resolution of 1° . The pressure distribution is evaluated at each angle of attack α . At the critical angle of attack α_{max} , the lift coefficient C_L maximizes, and it is defined at the highest angle between the chord line and the incoming airflow. Here the maximal amount of pressure is generated. Out of 25 fiber-optic sensors installed, 22 fiber-optic sensors have worked properly. Presumably, some pressure taps must have been incorrectly instrumented to the pressure taps, as no damage to sensors was subsequently observed in the lab. The following results exclude those non-functional sensors due to non-tight or blocked pressure taps.

5.2.2.1. Static Pressure Measurements

The pressure distribution over an airfoil is a common and fundamental representation in aerodynamics for an airfoil’s performance. Figure 5.13 shows the pressure distribution of the airfoil for different angles of attack at spanwise $y/b = 42\%$ with disabled active flow control. The pressure distribution represents the localized forces over a surface along the airfoil at the described spanwise position. Here, the dimensionless pressure coefficient C_p is plotted over the relative chordwise wing position x to the chord length l_c of the airfoil at the relative spanwise location $y/b = 42\%$. By

5. Experimental Aerodynamic Validation of the Measurement System

convention, the y-axis is displayed in the inverse direction. For this experiment, the pressure coefficient C_P is normalized to $C_{P,norm}$ by the maximal pressure coefficient $C_{P,max}$ due to confidential reasons as in equation 5.1.

$$C_{P,norm} = \frac{C_P}{\max(C_P)} \quad (5.1)$$

Additionally, for an easier explanation, Figures 5.13 and 5.14 display only the data points of the suction side. With increasing angle of attack α , the suction peak increases until the maximum angle of attack α_{max} is reached. For an angle of attack above α_{max} , the pressure distribution drops significantly because the airflow detaches completely [219].

The fiber-optic measurement setup monitors the active flow control's effectiveness. Figure 5.14 illustrates the pressure distribution with enabled active flow control, which is set to the maximum mass-flow rate \dot{m} of 10.8 g/s and the oscillating frequency of the actuators is kept constant at 90 Hz in this experiment. Especially the comparison of the blue curve reveals that the pressure distribution increases its α_{max} to a higher α . With enabled active flow control, the suction forces rise above their former maximum with disabled active flow control. Therefore, in this experiment, the maximal angle of attack α_{max} increases when the active flow control is enabled. As a result, the stall is delayed by 1° , which is in agreement with the literature [122].

The lift coefficient C_L can be estimated using the extracted pressure distribution at each angle of attack. Figure 5.15 shows the lift coefficient measurement based on the pressure measurement for active flow control enabled and disabled. The graph also includes a measurement of the lift coefficient based on the force balancing system, acting as a reference system. The so-called lift polars represent the lift of the model. Nevertheless, coupled with the outer winglet model and integrating all applied lift, the force sensors systematically blur out detailed local insights of the flow situations. Whereas the pressure sensors measure the flow separation locally, a local flow separation or the slat vortex near the pressure sensor alters the result locally. The lift polars are normalized for confidential reasons, and the pressure sensor-based polars must be scaled to match the force sensor-based curve. The active flow control increases the lift coefficient slightly and delays the maximal angle of attack. Again, this effect is primarily observable when the airfoil is close to stalling conditions. Moreover, Figure 5.15 shows the flow patterns on the winglet model, which are visualized utilizing the tuft visualization technique [122]. Figure 5.15 shows three different angles of attack. For low angles of attack ($\alpha \ll \alpha_{max}$), no separated regions are observable because all tufts line up in the main flow direction. The flow starts to separate on the outer wing at the maximum angle of attack ($\alpha \sim \alpha_{max}$). The intensity of flow separation increases towards the wing tip region. For higher angles of attack ($\alpha > \alpha_{max}$), the outer wing entirely separates [219]. When the airfoil is below the critical angle of attack, the active flow control does not have severe positive effects.

Figure 5.16 compares the pressure distribution derived from the fiber-optic mea-

5. Experimental Aerodynamic Validation of the Measurement System

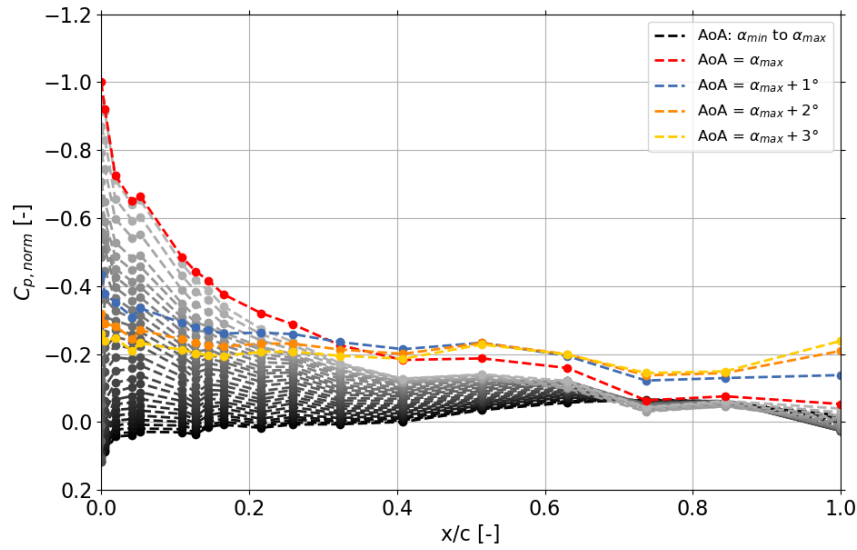


Figure 5.13.: C_p distribution of suction side based on fiber-optic sensors with disabled active flow control. A decreasing pressure coefficient on the suction side corresponds to an increase of the low-pressure zone on the upper surface area and thus increases the lift. For angles of attack above α_{max} , illustrated in blue, orange, and yellow, the airflow separates, and almost no lift is generated, leading to a stalling airfoil. For the test campaign the AoA has been increased from -5° to $\alpha_{max} + 3^\circ$ in 1° steps. [219].

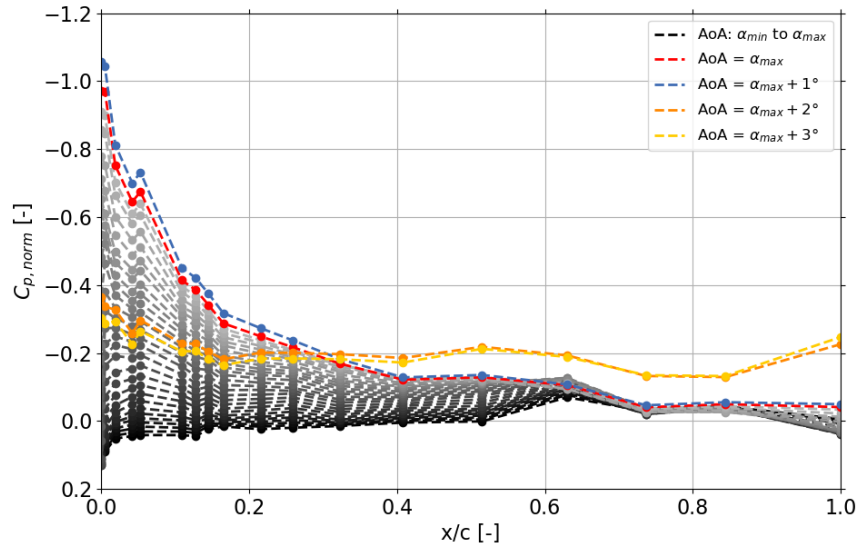


Figure 5.14.: C_p distribution of suction side based on fiber-optic sensors with enabled active flow control. With the activation of the active control mechanism, the stall is delayed by 1° . In contrast to the disabled active flow control results, the blue curve still shows strong suction. For a non-critical angle of attack, the active flow control does not affect the pressure forces significantly [219].

5. Experimental Aerodynamic Validation of the Measurement System

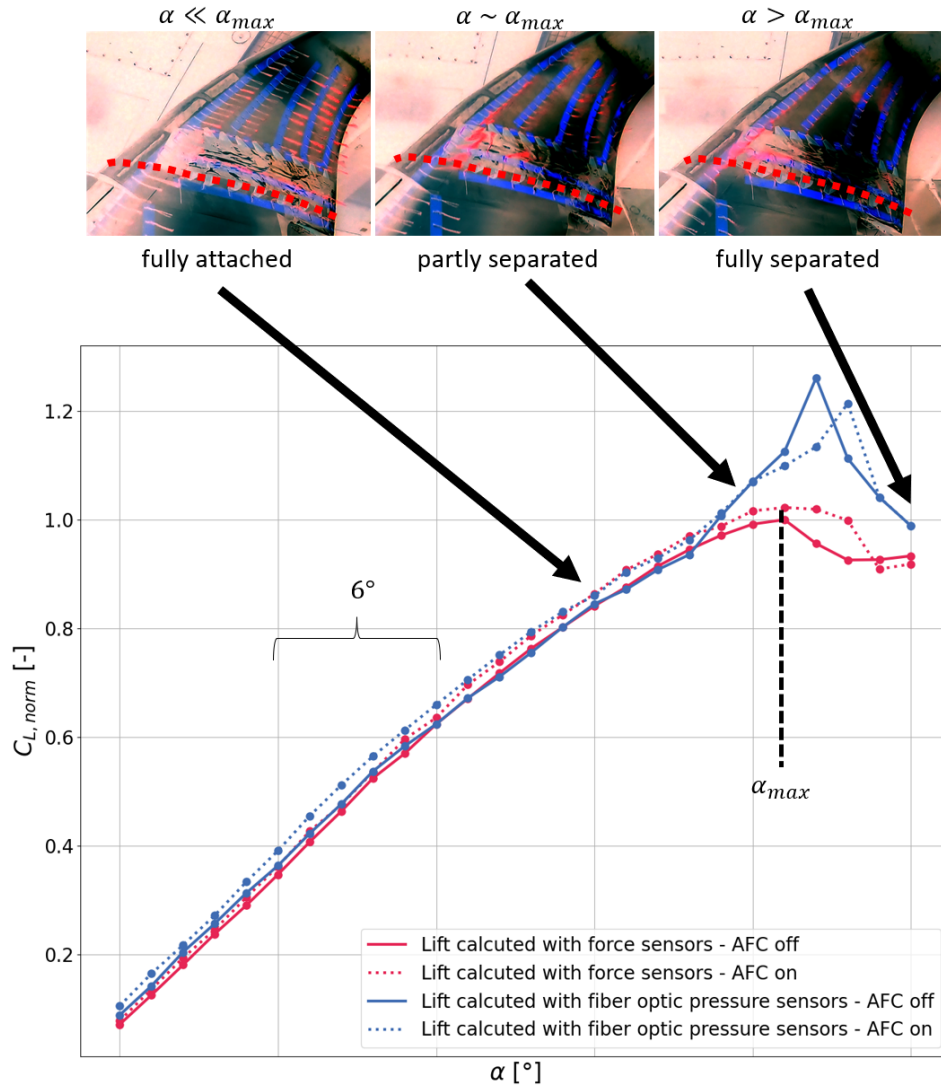


Figure 5.15.: Normalized lift coefficient based on the force sensor and pressure sensor. In this illustration, the results have been normalized by the maximal lift, measured by the force sensors. In addition, the lift coefficient, based on the pressure data, has been scaled to match the force’s sensor lift coefficient [122, 219]. The force sensors integrate the applied lift and systematically blur out detailed local insights into the flow situations. The pressure sensors measure the flow separation locally; therefore, a local flow separation or the slat vortex near the pressure sensor alters the result locally at a high angle of attack. For low angles of attack ($\alpha \ll \alpha_{max}$), no separated regions are observable. The flow starts to separate on the outer wing at the maximum angle of attack ($\alpha \sim \alpha_{max}$). The intensity of flow separation increases towards the wing tip region. For higher angles of attack ($\alpha > \alpha_{max}$), the outer wing entirely separates [219].

5. Experimental Aerodynamic Validation of the Measurement System

measurements with the electrical reference's measurements to evaluate the system's precision. The electrical reference sensing system consists of miniature amplified low-pressure sensors from First Sensor, type HCLA00075B. Such a conventional sensor is a common sensing element in wind tunnel experiments. The sensors are calibrated, temperature compensated and linearized, achieving very high offset stability. However, its very narrow measurement range allows the resolution of marginal pressure fluctuations but is fragile due to low overload robustness [48].

The fiber-optic pressure measurement follows the reference signals, but a constant offset between the measurements is observable, as illustrated in Figure 5.16. Moreover, the relative measurement deviation between the experiments significantly increases at the leading-edge positions. Therefore, the fiber-optic sensing equipment underestimates the applied suction in these sequential experiments. This deviation might originate from inadequate temperature compensation for the offset correction or installation deviations of the reused model [219]. Additionally, surface imperfections due to other sensor installations might have degraded the surface texture and, consequently, aerodynamics.

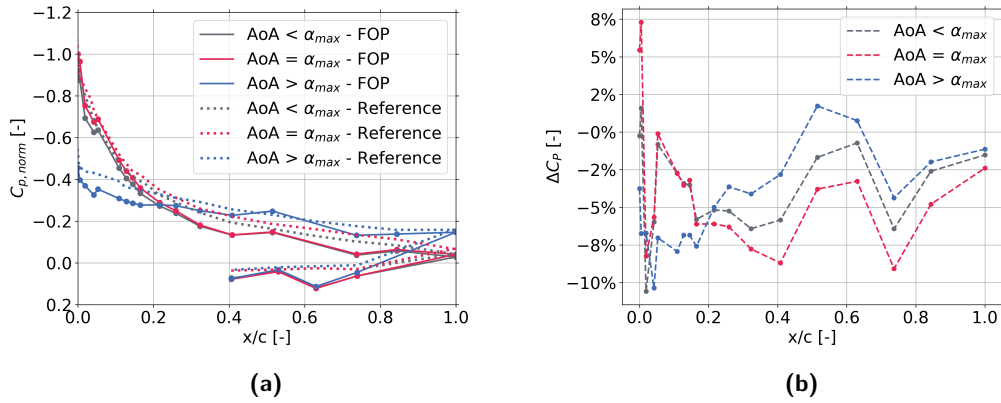


Figure 5.16.: C_p distribution of the outer winglet model recorded with the electrical reference pressure sensor (Reference) and the fiber-optic pressure sensor (FOP). Figure (a) shows the pressure and suction side distribution. The dotted lines represent the measurements with an electrical setup, and the solid line embodies the measurement with the fiber-optic pressure sensors. Figure (b) shows the relative deviation between the experiments conducted with electrical reference and fiber-optic sensors. The fiber-optic sensing equipment underestimates the applied suction in these sequential experiments. This deviation might originate from inadequate temperature compensation for the offset correction or slight installation deviations of the reused model [219].

In order to analyze the temperature cross-sensitivity, the sensors have been recorded and corrected for the barometric pressure change. At the same time, the heated wind tunnel cooled down overnight. Figure 5.17 illustrates the temperature response of the sensors. With the rising temperature, the pressure signal drops for each sensor individually. For this reason, the pressure signals are tared shortly before each iteration. The temperature is tracked and compensated actively in the post-processing.

5. Experimental Aerodynamic Validation of the Measurement System

The wind tunnel heats up to 35 °C. As expected, the temperature sensitivity for all sensors is different. The range of the temperature cross-sensitivity is between 69.4 Pa/°C and -318.9 Pa/°C and might distort the C_P measurement if not considered. The measured pressure signals are in a range of -5 kPa to +5 kPa. The mean temperature cross-sensitivity of the sensors is only about -104.7 Pa/°C, but the standard deviation is about 120.0 Pa/°C. The spread of sensors is so high that each sensor needs to be addressed individually with the active temperature compensation. Moreover, the pressure sensors are distributed randomly in the model and referenced to a single temperature sensor in the experiment. Therefore a thermal gradient along the model might have distorted the relationship between the more embedded temperature sensor and the pressure sensor, warmed by the airflow more directly, as well [219].

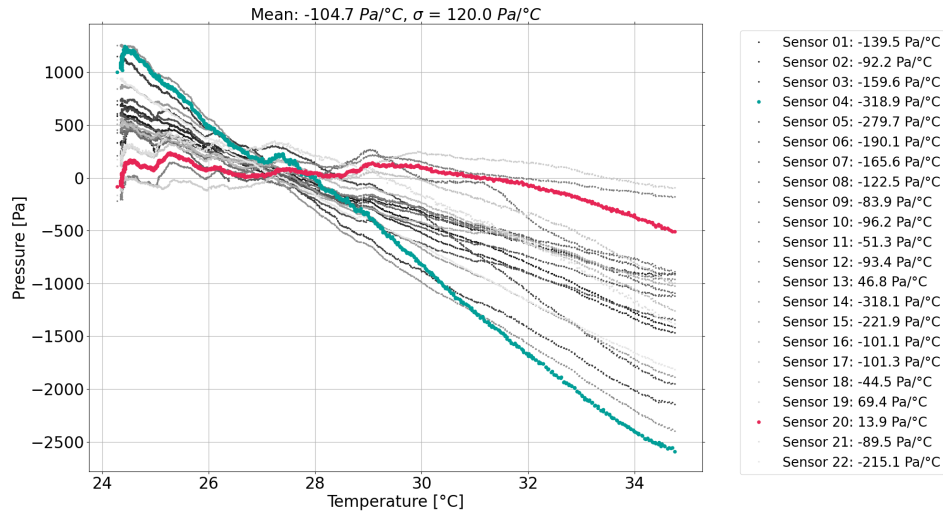


Figure 5.17.: Temperature response of the pressure sensors. The sensors with the highest and smallest temperature cross-sensitivity are marked in green and red. [219]. In this experiment, if not compensated for temperature, the sensor will induce a measurement deviation for the C_P of 2.5 %/°C in average.

5.2.2.2. Dynamic Pressure Measurements

In order to evaluate the actuator’s effectiveness, it is necessary to quantify the complex, unsteady flow field on the sharklet when the actuator is enabled [119, 122]. Steady and unsteady pressure measurements represent the fundamental signature of the flow around the airfoil and are ultimately linked to all aerodynamic forces [219]. Although the pressure taps’ length influences the frequency response of each sensor channel, a relative comparison of attached and separated flow condition reveals interesting insights [217].

Unlike the static electrical reference system, the fiber-optic interrogator can sample dynamically up to 50 kHz. Nevertheless, due to the low-pass characteristics of

5. Experimental Aerodynamic Validation of the Measurement System

the pressure taps, acoustic effects in a higher frequency range than 100 Hz are neglected. Therefore, a lower sampling frequency of 1 kHz has been chosen so that the noise floor is at about $0.1 \text{ Pa}^2/\text{Hz}$. Due to the unknown routing and length of the pressure taps of each sensor, only the difference in the power spectral densities and the qualitative changes are discussed [219]. The color-coding of the following figures relates to Figure 5.13 and Figure 5.14 so that the colors denote the same angle of attack, which eases explanations. Figures 5.18 show the measurements for the sensor position at $x/c = 0.053$. This location is near the leading edge and the active flow control outlet. With increasing angles of attack, the turbulence intensifies.

Moreover, because the fluidic active flow control system works by creating an oscillating fluid injection, the sensor measures the switching frequency of the active flow control of 90 Hz in case the active flow control is enabled. Compared to the Figures 5.18, there are no significant changes in turbulence intensities besides the change of the blue curve. Here, the enabled active flow control fits the power spectral density's shape of the previous measurement, evaluated at a lower angle of attack.

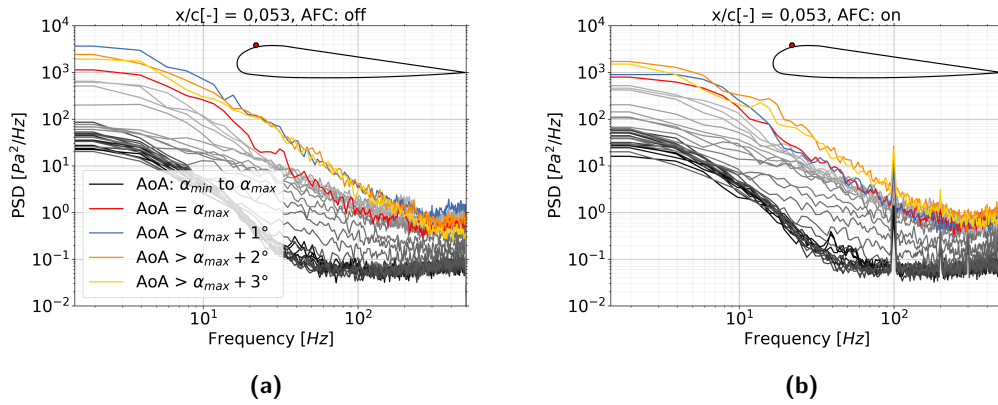


Figure 5.18.: Power spectral densities of a pressure sensor located near the leading edge with disabled (a) and enabled active flow control. The fiber-optic pressure sensor detects the switching frequency of the active flow control if enabled. The enabled active flow control smooths the power spectral density at its maximal angle of attack, shown by the blue line in relation to the maximal angle of attack measurement with disabled active flow control in red. Additionally, the sensor measures the switching frequency of the active flow control at 90 Hz, observable by a peak in the spectrum, in case the active flow control is enabled [219].

Figure 5.19 illustrates additional power spectral densities for exemplary sensor locations across the airfoil in a chordwise direction on the suction side. The active flow control shapes the power spectral density of the evaluated angle of attack to the flow conditions at the former maximum angle of attack α with disabled active flow control in all cases. Thus, the active flow control demonstrates its effectiveness by delaying stall effects to a higher angle of attack and preventing the detached vortex airflow at that specific angle of attack. The sensors, close to the leading edge, as sensor location $x/c = 0.005$, exhibit an attached flow oscillation, which characterizes

5. Experimental Aerodynamic Validation of the Measurement System

in power spectral density at about 200 Hz. If the suction forces detach, the pressure fluctuations, presumably originating from the cut-off of the slat [121], do not follow the curvature of the airfoil, so they are not detectable to the sensors. A sensor near the outlet or in the flow direction in the midsection, as the sensor $x/c = 0.216$, monitors the oscillating frequency of the active flow control in addition. Besides that, the power spectral density pattern matches the flow condition of the attached flow again if active flow control is enabled. The sensor at $x/c = 0.216$ illustrates the typical measurement results of a sensor at a further distance. Here the sensor is already at such a distance and shielded from the characteristic sound, so positive flow effects of the active flow control are observable.

Neglecting the sensor close to the stagnation point, the sensor at location $x/c = 0.530$ on the pressure side is representable for all sensors mounted towards the pressure side. Here, the active flow control does not affect the flow conditions. Even at a higher angle of attack, airflow must follow the airfoil's shape because it always faces the incoming flow. Moreover, the active flow control outlets are only on the suction side of the airfoil, and no switching frequency can be detected. Unlike others, Figure 5.20 illustrates a white noise spectrum of the power density, which indicates that no dynamic inhomogeneous flow separation or vortex flows are generated on the pressure side of the airfoil.

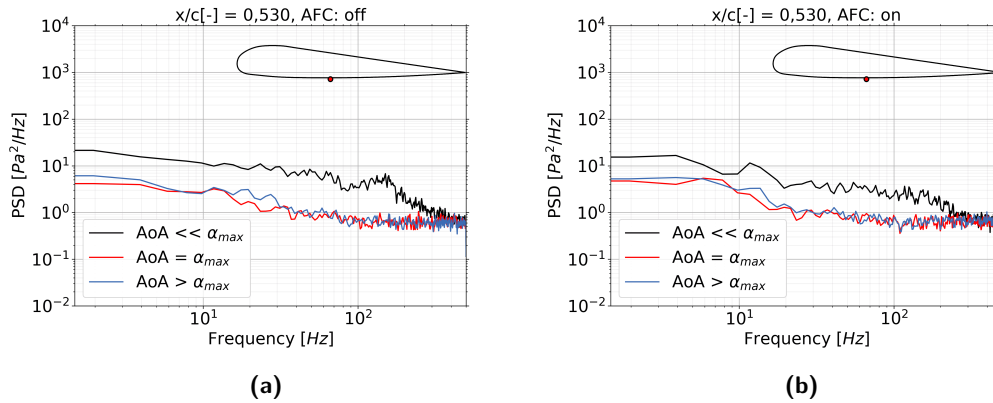


Figure 5.20.: Power spectral densities of pressure sensors located on the pressure side. Because the active flow control outlets are only on the suction side, sensors at the pressure side neither detect the switching frequency nor additional aerodynamic performance.

The most significant influence is observed for the trailing edge sensor in Figure 5.21. The enabled active flow control decreases low-frequency components of the power spectral density by the power of 10. Nevertheless, even at a low angle of attack, the turbulent intensities are so large that the oscillating frequency is shadowed [219]. With enabled active flow control, the measurement, marked in blue, representing the maximal angle of attack with disabled active flow control, imitates the power spectral density spectrum of attached flow conditions. Above the maxi-

5. Experimental Aerodynamic Validation of the Measurement System

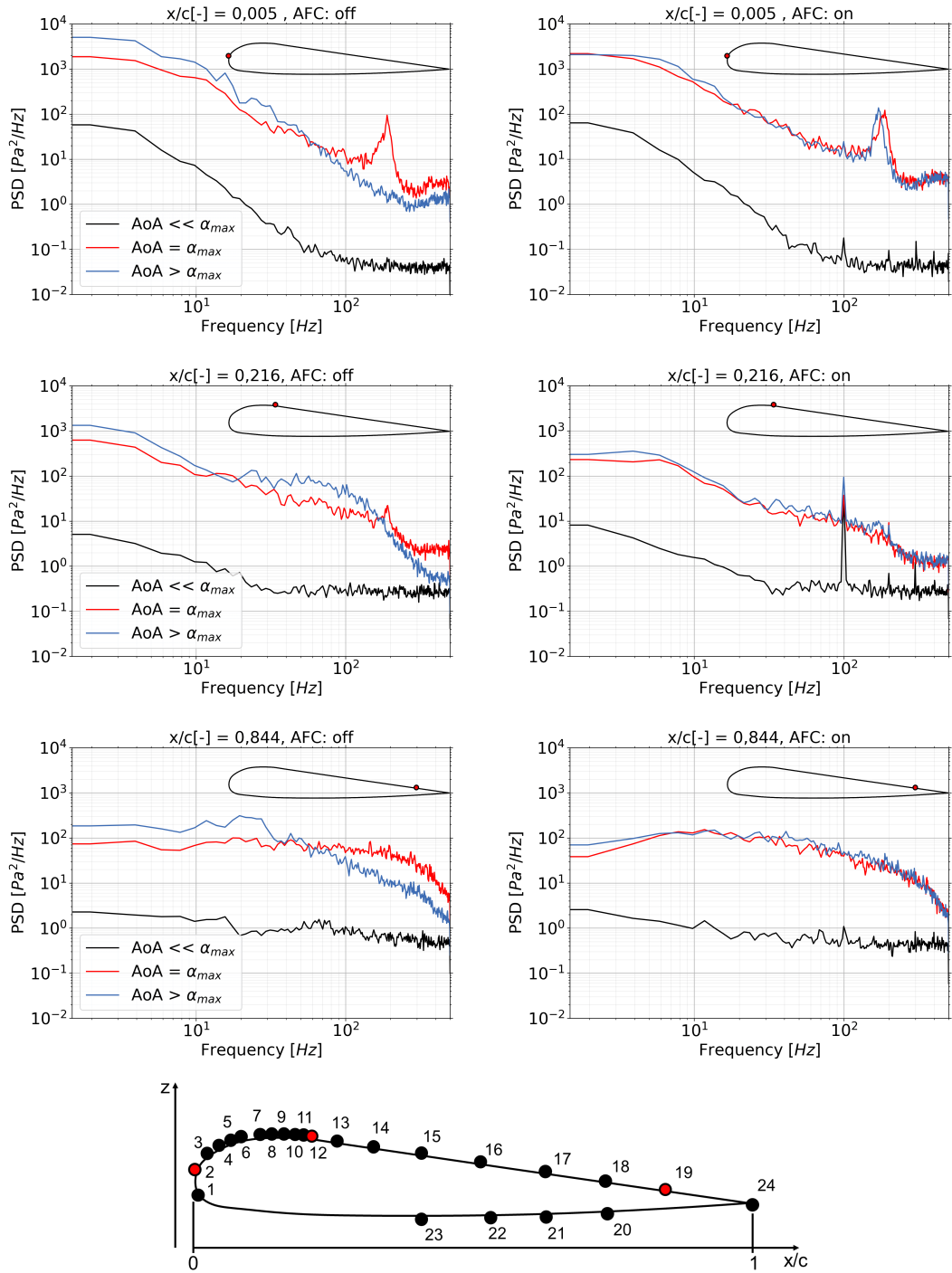


Figure 5.19.: Power spectral densities of pressure sensors on the suction side for sensors across the blade in the chordwise direction. The three representative pressure sensors at different chordwise length positions. The sensors are close to the stagnation point, midsection, and close to trailing edge. The dynamic characteristics of the disabled and enabled active flow control are shown. With activated flow control, the dynamic, turbulent intensities at an angle of attacks above α_{max} match flow characteristics at α_{max} [219].

5. Experimental Aerodynamic Validation of the Measurement System

mal angle of attack in the frequency range of 10 Hz to 50 Hz, pressure fluctuations increase significantly, which indicates separated flow conditions.

In general, unsteady upstream conditions produce more broadband noise in the far-field [15, 215]. However, the turbulent trailing edge fluctuations are the primary source of airfoil self-generating noise because pressure and suction interact. Therefore, these pressure fluctuation measurements provide valuable insights regarding the turbulent boundary layer [137].

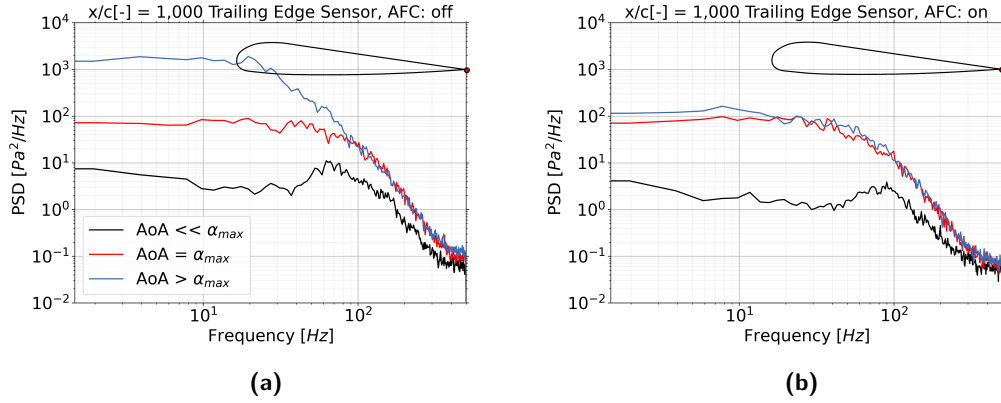


Figure 5.21.: Power spectral densities of the pressure sensors located in the trailing edge. The trailing edge sensors exhibit a clear intensity increase as soon as the airflow detaches, where the active flow control enables higher AoA at similar PSD levels.

As illustrated in Figure 5.22 a single differential sensor provides relevant information about the overall performance of the flow properties. Therefore, such a fiber-optic sensor can act as a stall detection sensor, which is particularly interesting. The methods used are introduced in chapter 4.1.2 on page 50.

As discussed, pressure taps are expected to limit the frequency response. The pressure tap's length in this example is short enough to assume an undisturbed frequency response up to 50 Hz [73]. For the Figure 5.22, the root of the integral of power spectral density for each angle of attack α over the frequency range from $f_{lower} = 1$ Hz to $f_{upper} = 50$ Hz is computed and represented as a pressure fluctuation value p_{RMS} in equation 4.2.

In order to calculate these pressure fluctuations, the power spectral density lower frequency threshold is set to be 1 Hz. This threshold reduces low-frequency parasitic temperature effects. Therefore the computed results are band-filtered signals but highly correlated with the variance of the signal in general. The result is scaled by extracting the root of the integral of the power spectral density. The outcomes in Figure 5.22 illustrate different colored areas and thresholds. In this experiment, if the pressure fluctuations stay below the threshold of less than 50 Pa, no stall at the section is observed. The pressure fluctuation increase by factor 4x to above 200 Pa and the airflow is detached in this experiment. The grey area indicates the angle of attacks, in which the active flow control benefits the flow characteristics. The red

5. Experimental Aerodynamic Validation of the Measurement System

area marks the angle of attacks, in which the airfoil stalled nonetheless.

Nevertheless, in aerodynamics, turbulence intensity $T.I.$ is defined in the following equation 5.2. It is conventionally dimensionless. A steady flow of air has low turbulence, and unsteady flow results in higher turbulence [6, 208].

$$T.I. = \frac{u_{RMS}}{u_{\infty}} = \sqrt{\frac{p_{RMS}}{q}} \quad (5.2)$$

Here, the variable u_{∞} represents the average velocity at the same location over the same period, and the variable u_{RMS} represents the standard deviation or root-mean-square of the turbulent velocity fluctuations. If the standard deviation is larger than the turbulent part of the flow, there will be an increased turbulence intensity factor. The measurement of this experiment is nevertheless presented in pressure units. Therefore, applying the relation 2.3 of page 16 between velocity u and pressure p for the dynamic pressure q to the numerator and denominator of equation 5.2, the expression based on pressure values is derived, which also becomes independent of the density ρ_{air} [96].

The resulting turbulence intensity values range up to 0.25 for attached flow conditions and from 0.50 to 0.60 for detached flow conditions.

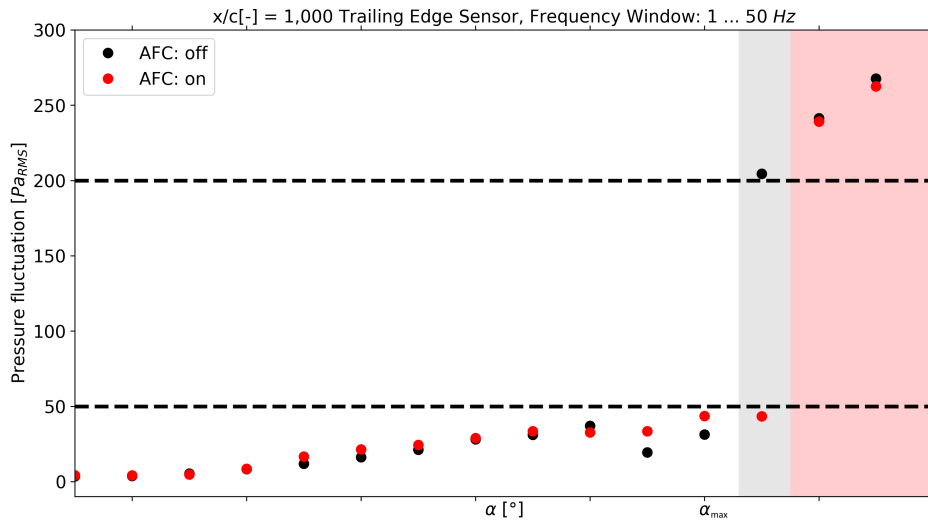


Figure 5.22.: Turbulence intensity of the trailing edge sensors over the angle of attack. The sensors at the trailing edge location can measure a significant increase in turbulence intensity when the airflow is detached. The generated vortex and detached flow create dynamic turbulence whenever the airfoil is in a stall. For this result, the root of the integral of the power spectral density function in a frequency range from 1 Hz to 50 Hz has been considered. The grey area indicates the angle of attacks, in which the active flow control benefits the flow characteristics. The red area marks the angle of attacks, in which the airfoil stalled nonetheless. This result proves that a single differential sensor at the trailing edge provides relevant information about the overall performance of the flow properties.

5.2.3. Summary of the Results

To safely operate an active flow control system in aircraft applications and optimize its performance, it is crucial to provide a robust sensing system to feed the current effectiveness of the active flow control system back into a control system. Closing the feedback loop requires a high-frequency resolving pressure measurement of the aerodynamics. The dynamic measurement results represent a fingerprint of the flow conditions, even though the routing of pressure tabs limits the response time and allows only quasi-static measurement, e.g., pressure distributions or relative measurements. Having the sensors mounted closely to the aerodynamic interacting surfaces provides additional high, frequently resolved insights. Although the sensors are miniature, for such surface-neutral integration without pressure taps, the sensor size would have to shrink even further, which challenges the sensitivity and robustness of the system. This experiment demonstrates that next to the lift measurement, the system could be used to tune the actuator to the specific flight situation by monitoring the oscillation frequency, the pressure distribution, and the turbulence intensity. While static pressure distributions require several distributed sensor locations, monitoring for turbulence intensity and oscillation frequencies require only few. Reducing such a system from a distributed sensing system with multiple sensors to a single sensor could open commercial applications that are more related to serial applications than a test and measurement market. The discussed dynamic stall sensing mechanism of a single sensor integrated into the trailing edge requires only minimal hardware effort and limited computational power. A simple sensing system is feasible by outputting a digital alarm if the turbulence intensity exceeds a predefined threshold. On top of the superior overload stability of the sensor itself, this sensing location at the trailing edge is well protected, considering rain and dust erosion. Nevertheless, such a predefined threshold would have to be set for each airfoil and spanwise location along the airfoil, most likely individually. Additionally, in aerodynamics, the interest is in measuring if the flow condition is stalling and in how close flow properties are to a stall.

5.3. Static and Dynamic Pressure Measurement in Flight Test Application

Another fundamental part of the Cleansky2 project SKOPA (Skin friction and fiber-optics-based surface pressure measurements for aircraft applications, H2020 – 820835) is evaluating a fiber-optic pressure sensing measurement in a flight test [217]. This experiment proves the maturity of the technology by instrumenting fiber-optic sensors for time-resolved surface pressure measurement on a lightweight aircraft, as shown in Figure 5.23. Unlike wind tunnels, where custom models are evaluated in protected lab conditions, flight testing aims to measure actual environmental conditions and witness all challenges related to flight mission-dependent processes. The results have been published in a journal paper [217].



Figure 5.23.: Test aircraft with instrumentation in flight. Test aircraft is instrumented with fiber-optic pressure sensors on its right-wing [217].

5.3.1. Description of the Flight Test

The scope of the flight test is to measure detached flow conditions at airspeeds close to the aircraft's stall with novel fiber-optic sensors. The instrumented light aircraft is an FA01 Peregrine SL with an SM701 airfoil profile [49]. Next to its use in academic teaching, this aircraft is mainly used in research projects as a universal experimental carrier for the Technical University Berlin. The flight program consists of low-speed maneuvers in different flight configurations. In these maneuvers, the aircraft reduces its speed and increases the angle of attack until the stall warning alerts. Therefore, a detached flow at the wing's trailing edge is highly likely in these maneuvers.

5. Experimental Aerodynamic Validation of the Measurement System

For in-flight testing, sensors' integration usually requires a non-intrusive installation on the original airframes. Due to the requirement of a non-intrusive integration of the sensors on the flat airfoil, a flat fiber-optic pressure sensor with a sensing surface perpendicular to the fiber direction is preferred as it is easier to install. Even though the sensor thickness is just about 1.6 mm, the sensors are additionally mounted into aerodynamic gloves to smooth the edges. Nevertheless, even with the flattest installation principle, thickness and imperfections are added after the airfoil's original shape. The location of the fiber-optic pressure and reference sensors are displayed in Figure 5.24. The sensors are distributed on the wing with a local concentration on the trailing edge, where detaching airflow most likely occurs. Therefore, four flat pressure sensors are installed on the flap. The remaining four pressure sensors are instrumented on the main wing to evaluate in-flight static pressure distribution. The three reference sensors have been placed next to neighboring fiber-optic pressure sensors at different chord-wise lengths of the airfoil. Additionally, a fiber-optic temperature sensor for the pressure sensors' active temperature compensation of the fuselage is installed. Figure 5.25 shows the full instrumentation in flight.

5. Experimental Aerodynamic Validation of the Measurement System

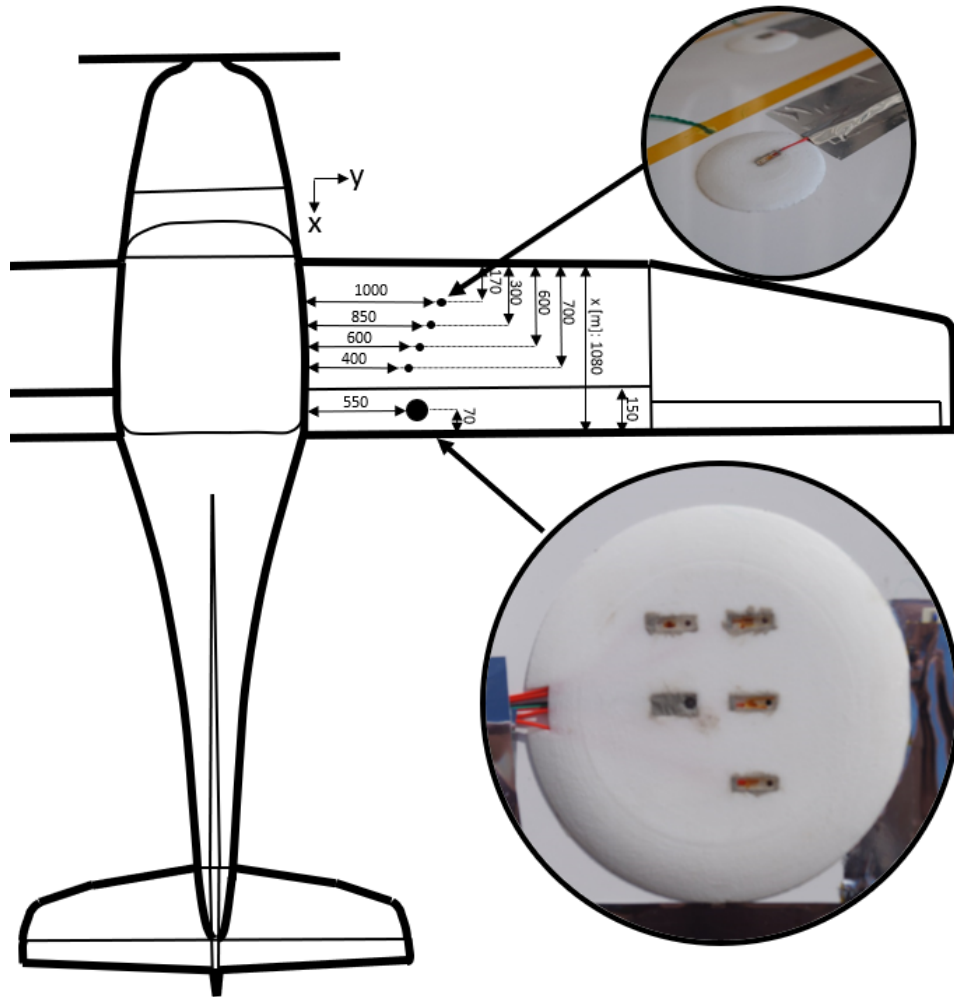


Figure 5.24.: Location of the fiber-optic pressure sensors in-flight tests. The sensors are distributed along the chord-wise length of the airfoil in order to measure a static pressure distribution. Additionally, the sensor distribution concentrates on the flap to measure local detaching turbulent airflow [217].

Three electrical pressure and two temperature sensors are installed on the fuselage additionally for benchmarking purposes. Three Kulite LQ-080-258G sensors are digitized as reference electronics by an HBM Quantum MX1615B interrogator [77, 110]. Next to a recording laptop, an Ethernet switch and a DRPC 100 computer to synchronize the different measurement systems are instrumented and stored in the luggage compartment of the aircraft [82]. Moreover, the aircraft's flight management system tracks and records time, pitch, roll, yaw, airspeed, altitude, turn rate, GPS position, and accelerations. All systems are individually powered with separated LiPo batteries. The LiPo batteries power each electrical component with 24 V and 4000 mAh, which limits the fiber-optic measurement device's recording time to less than 1.5 h. The optical fibers and the electrical wires are routed to the wing and the

5. Experimental Aerodynamic Validation of the Measurement System



Figure 5.25.: Cockpit view on instrumentation. In this picture, the aircraft is airborne and climbing above the Werbellinsee, north of Berlin, Germany. The figure shows the instrumentation. The fiber-optic sensors are installed across the airfoil with a concentration on the flap. The cables are taped to the airfoil. In order to route the cables along the movable flap, the cables have been mounted in a loop near the mainframe. This routing of the fibers allows them to expand. The extra green chords are installed to illustrate the airflow direction and are monitored with a video camera during flight. Other electrical sensors have been installed next to the fiber-optic equipment for other research and benchmark purposes [217].

5. Experimental Aerodynamic Validation of the Measurement System

flap through the airplane's window sealing and bonded with removable airworthy tape. The fiber-optic measurement system under test includes a Redhawk interrogator by fos4X GmbH, cables, and sensors, which weights in total less than 2 kg [158]. Adding the electrical referencing equipment increases the total weight to 8 kg. After installation, the sensors are calibrated with a pistonphone [61]. A second aircraft escorts the test airplane as an additional observer. Therefore, the documentation of the flight testing includes external and internal video footage. The flight path is located over the northern Berlin area. In this flight tests, which is up to 2500 m altitude, the temperature drops from 25 °C to 4 °C. Table 5.2 summarizes the most aerodynamic key parameters for the flight experiment.

Table 5.2.: Aerodynamic key parameters of the flight experiment [217].

Parameter	Unit	Value
l_c	m	1.08
z	m	0.4 ... 1.0
Re	—	1.5 mio ... 5.0 mio
u_∞	$\frac{m}{s}$	<60
Ma	—	<0.17

5.3.2. Experimental Results

The following section summarizes the test results. This part is divided into the measurement, discussing the static measurement characteristics and its dynamic performance for the flight test.

5.3.2.1. Static Pressure Measurements

Figure 5.26 illustrates the pressure reading of a fiber-optic sensor, a barometric sensor, and a reference sensor for the complete flight interval. With increasing altitude, the static pressure reading drops. On top of the barometric pressure changes, aerodynamic lift forces act on the sensors so that the pressure reading of the sensors in the airflow distinguishes from the barometric pressure changes. The challenge in aerodynamic sensing in-flight applications becomes obvious. On the one hand, the application requires a wide pressure measurement range due to barometric changes, but on the other, relatively small pressure differences induced by the aerodynamic forces have to be resolved. Therefore, a large dynamic range of measurement technology is needed. Figure 5.26 includes a zoomed time-series in which the pilot moves flaps from the cruise flight configuration to the fully extended position. In this detailed time-series in Figure 5.26, the pressure measurement on the flap is influenced by the flap movement, and more suction is generated. Additionally, the airflow gets more turbulent, indicating detached airflow conditions.

Figure 5.27 illustrates the fiber-optic pressure reading in relation to the reference sensors for the entire flight interval. While a static offset needs to be addressed

5. Experimental Aerodynamic Validation of the Measurement System

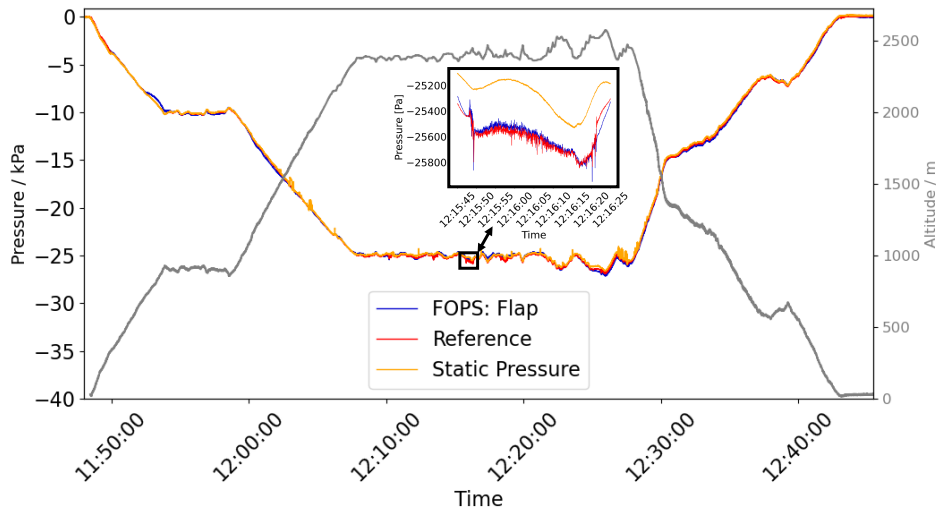


Figure 5.26.: Static pressure reading of a fiber-optic pressure sensor and a reference sensor at the flap in flight tests. The static pressure reading of a fiber-optic pressure sensor and a reference sensor, which are mounted on the flap, match for the full duration of the flight. The barometric pressure and altitude are also measured at the fuselage with an electric sensor. With increasing altitude, the static pressure reading drops. The aerodynamic forces acting on the flap create additional suction. The detailed time-series illustrates a turbulent detached airflow while the flaps are fully extended [217].

by active temperature compensation, the sensor’s sensitivities are not affected by temperature due to the large linear range, as discussed in chapter 4.3.1. In this illustration, the temperature sensitivity has already been corrected. The sensors’ temperature dependency ranges from $-10 \text{ Pa}/^\circ\text{C}$ for the best sensor to $363 \text{ Pa}/^\circ\text{C}$ for the worst sensor. The standard deviation of the measurement deviation between the reference sensor and a fiber-optic sensor next to them equals 283 Pa . In relation to the full-scale operating range from $-40 \text{ kPa} \dots 40 \text{ kPa}$, and a coverage factor of 2, the measurement uncertainty equals 0.70% and is therefore in the expected boundaries as discussed in chapter 4.3.

After addressing the residual temperature effects, the system can measure the pressure distribution of the airfoil SM701, as shown in Figure 5.28. Figure 5.28 illustrates exemplary the pressure distribution for the aircraft’s airfoil at a high angle of attack at different time points during the flight. Based on the temperature and the air density, derived from the airspeed and the airfoil geometry, the Reynolds number of this experiment is about $Re = 2.5$ million. The graph indicates that suction is generated at the leading edge and fades towards the trailing edge. Even though the pressure distribution equals the theory of an SM701 airfoil [34, 150], for better interpretation, more sensors at the leading edge would be required. Moreover, quickly changing uncontrolled environmental parameters, such as temperature, or changing flight configuration, such as unstable airspeed, pitch, and roll rates, vary

5. Experimental Aerodynamic Validation of the Measurement System

the pressure distribution significantly. Therefore, the results in Figure 5.28, especially the fitted curve, are averaged. Due to the temperature cross-sensitivity of the sensors, these pressure distributions, especially after long flight times in changing temperature environments, become more error-prone.

5.3.2.2. Dynamic Pressure Measurements

The dynamic sensor capabilities are discussed in the following section. Monitoring of near stall events of the test aircraft, the correlation of the pressure signals to detect the direction and speed, and turbulent intensities at detached airflow events are discussed.

As a first flight experiment, the measurement setup is supposed to measure the turbulence intensity of a detached airflow. The detached airflow at the trailing edge is due to abnormal flap position at low speeds. This flight experiment is split into three phases. In the first phase, at standard flight configuration, the airspeed is normal, and the flaps are fully retracted. Because of the different path lengths between the suction and pressure side of the airfoil, the airflow accelerates on the suction side and creates lift. Nevertheless, there are high-pressure regions at the stagnation and trailing edges. Therefore, during normal flight conditions, the air momentum overwhelms the pressure forces directing the flow from the trailing edge to the front. However, at low speed, close to stall conditions, the air momentum does not overwhelm the pressure forces so that the airflow close to the boundary layers counters the airflow direction [13].

In the second phase, the lift device creates additional lift when extending the flap. The airflow detaches as soon as the flap moves to an abnormal position beyond the landing position. As a result, the turbulent airflow does not follow the curvature of the airfoil anymore.

Figure 5.29 illustrates the static pressure reading of a fiber-optic pressure sensor during flow separation at the flap. The induced flow separation at the flap decreases lift on the sensor mounted closer to the leading edge.

In the third phase, the aircraft decelerates until the stall warning alarm activates. Then, with an increasing angle of attack and lower airspeed, the transition zone from the turbulent boundary layer to the separated airflow moves further in the direction of the airfoil's leading edge. During this deceleration, less suction is generated, but the overall drag increases. After reaching the minimum airspeed, the pilot retracts the flap, pitches the aircraft forward, and gains airspeed. Figure 5.29 shows sensor signals for these flight situations. The pressure measurements are tared in a moment of stable cruise flight condition at normal airspeed, and the flaps are fully retracted for better illustration purposes.

Next to the time-series of this event, the power spectral density function can be of particular interest. The power spectral density function at normal cruise conditions is shown in Figure 5.30. It is composed of a peak at about 90 Hz originating from the engine noise and contains an equally distributed frequency response shape. This frequency peak shifts with the power settings during the flight. The flat frequency

5. Experimental Aerodynamic Validation of the Measurement System

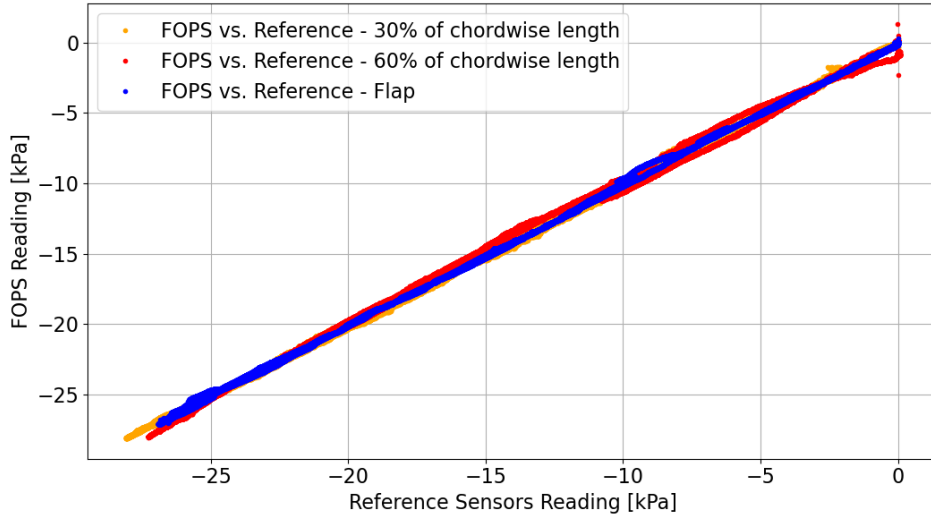


Figure 5.27.: The quasi-static pressure readings of the reference sensor. After temperature compensation, the static pressure readings of the fiber-optic system under test match the reference sensors sufficiently [217]

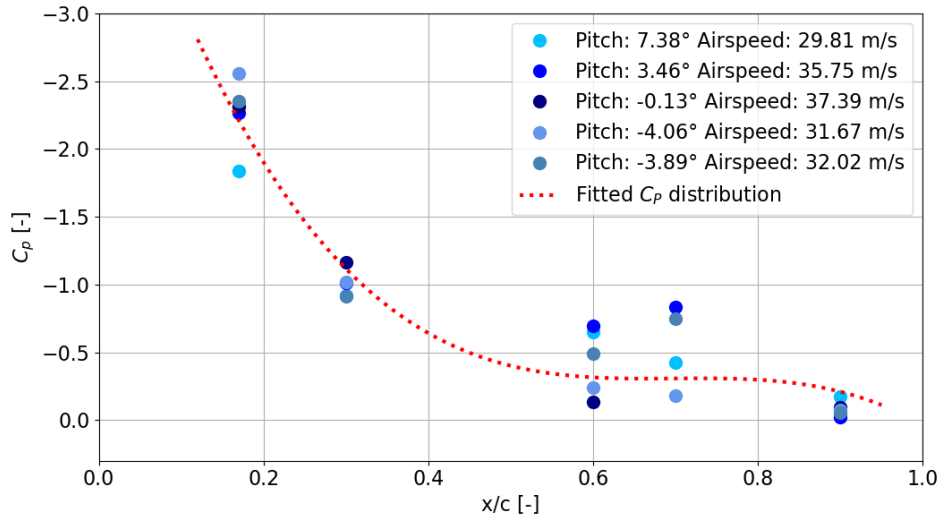


Figure 5.28.: Pressure Coefficient distribution of the airfoil SM701 shortly after take-off. Pressure coefficient distribution of the airfoil illustrated indicates the typical pressure distribution of an SM701 airfoil at a high angle of attack as during the initial climb. The Reynolds number of this experiment is at $Re = 2.5$ [217].

5. Experimental Aerodynamic Validation of the Measurement System

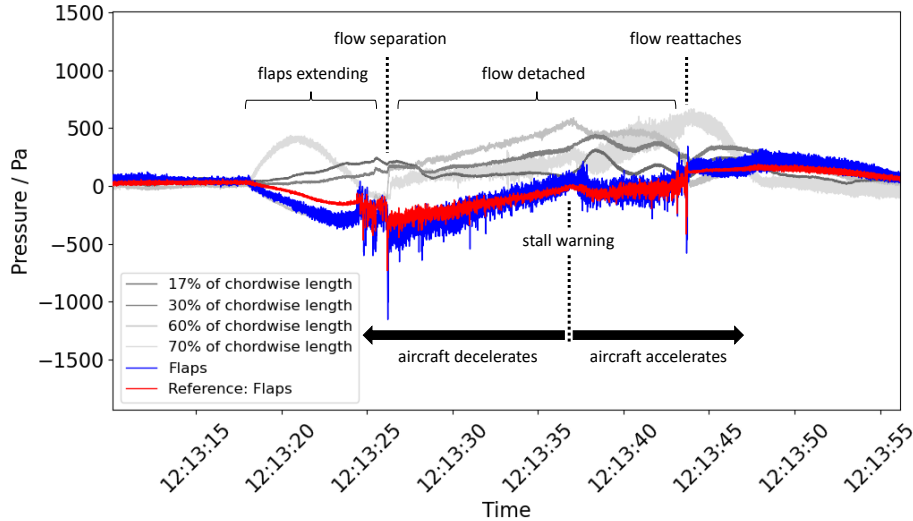


Figure 5.29.: A static pressure reading of a fiber-optic pressure sensor during flow separation at the flap. While the flaps extend, more suction is generated. When the flap is overextending, flow separation occurs. The aircraft is slowing down until the stall warning alerts. The aircraft is recovering, retracting the flap, and flow attaches again [217].

response indicates that no region of recirculating flow occurs immediately near the sensing locations. With a flow separation, the power spectral density function, displayed in Figure 5.31, looks different. Compared to Figure 5.30, the peak at about 90 Hz, which originates from the engine noise, is missing because the engine is idling.

Additionally, the amplitudes at low frequencies increase significantly. Near stall conditions, the momentum of flow does not overwhelm pressure's tendency to direct the turbulent flow from the high-pressure region at the trailing edge to the low-pressure region of the airfoil. The graph in Figure 5.31 illustrates the detachment of the boundary layer from a surface into wake effects during this low-speed maneuver. The detaching wake affects a different broader range in the low-frequency region. Moreover, as shown in the photo, the flap chords indicate a detached turbulent airflow during flow separation. The right Figure 5.32 also depicts the noise floor of the measurement systems prior to the flight. Even though the fiber-optic measurement system is by almost 10 dB noisier, the turbulence intensity, even in less turbulent cruise flight conditions, is measurable. In the case of a detached airflow, the turbulence intensity increases by 30 dB for quasi-static frequency components.

The noise level of the sensing system under test is of higher magnitude, when all parasitic noise sources in the aircraft are switched off, the conclusion is different in the case of an actual performing aircraft. A very illustrative example of the fiber-optic benefits is shown in the left Figure 5.32, which shows the exact moment of shutdown of the anti-collision lights, called strobe lights. The strobe lights are a set

5. Experimental Aerodynamic Validation of the Measurement System

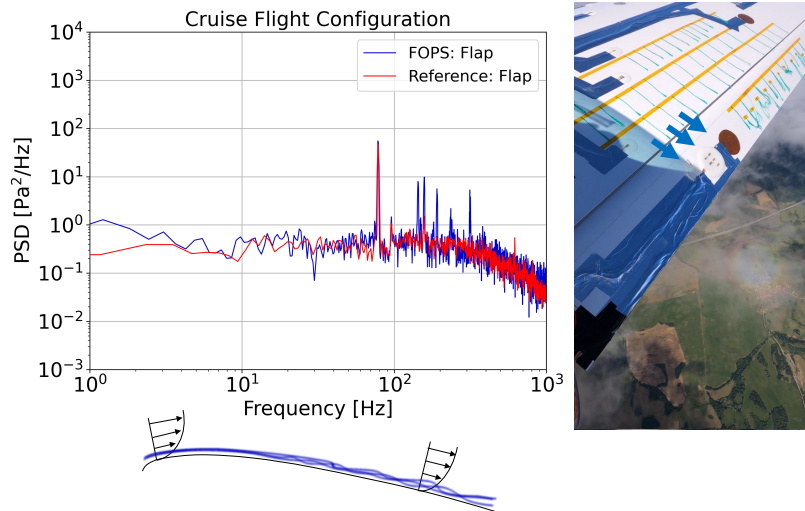


Figure 5.30.: Power spectral density in cruise flight conditions. The power spectral density function shown here has a white shape and peaked at 90 Hz, originating from the engine noise. The turbulent intensity is larger than the fiber-optic system’s noise floor at cruise flight conditions for high frequencies. The video image on the right shows the airfoil instrumented with chords to indicate flow direction and turbulence intensities. The white arrow indicates the sensor positions on the flap. The blue arrows indicate the general flow direction [217].

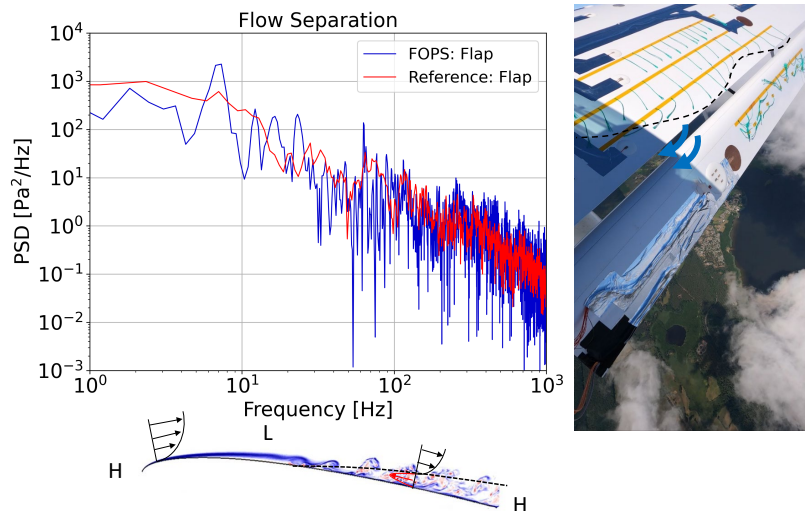


Figure 5.31.: Power spectral density in flight conditions with the separated flow. The power spectral density function is shown to be composed of more low-frequency turbulences. Compared to the cruise flight conditions, the turbulence’s intensity increases by more than 30 dB. Additionally, as the engine is idling, the characteristic sound peak vanishes. The video image shows that the chords are tilted and not in the general direction of the flight path. This observation indicates high turbulence intensities and wake or vortex effects. Moreover, the tear of the line of the attached flow is roughly indicated in the video image [217].

5. Experimental Aerodynamic Validation of the Measurement System

of lights at the wingtip to improve visibility. Because the cabling for electrical reference sensors is unfortunately routed in parallel to powering lines of flaps, motors, and lights, the electrical impulses couple into the electrical sensor's signals. Here the intrinsic fiber-optic benefits, such as inherent immunity to parasitic electromagnetic fields like electromagnetic coupling, no influence of cable length, and no influence of triboelectric charging, are demonstrated illustratively. Although the noise level of the reference sensor is lower than that of the fiber-optic sensing system, the parasitic coupling affects the electrical sensors but not the fiber-optic sensors. The impulses of roughly 100 Pa exceed the noise level of the fiber-optic system. Therefore, unfortunately, the electrical sensor would require more shielding of the cables on one side, which interferes with the airflow even more. On the other side, parasitic electrical cross-sensitivities concerning the electrically driven flap engines and landing lights can not be avoided entirely.

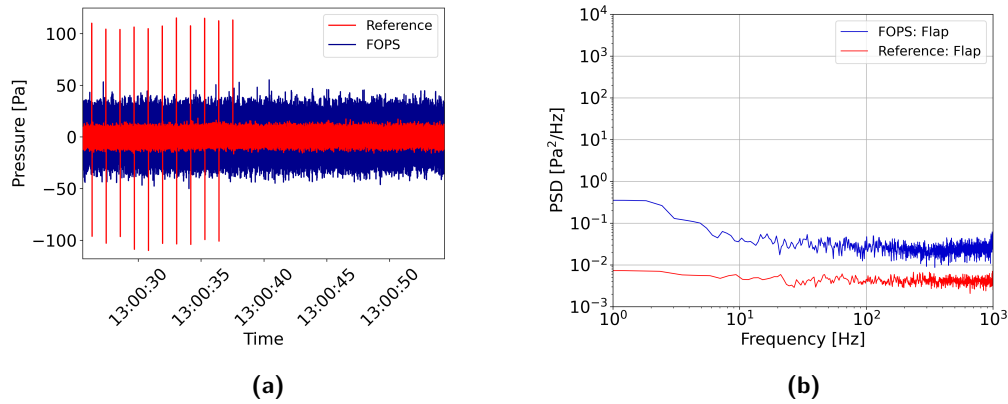


Figure 5.32.: The noise floor measurement of the system under test and the reference system. The time-series of the electrical reference sensor and the fiber-optic sensor demonstrates an electromagnetic coupling of the strobe lights into the electrical reference sensor in Figure (a). When all other electrical systems are switched off, the noise floor of the reference systems is by 10 dB better than the system under test, as illustrated in Figure (b) [217].

In civil aviation, the stalls that exceed the attack angle limits are a more prominent danger, especially during take-off and landing [172, 175]. Therefore, the following flight situations trigger the stall effects by increasing the airplane's angle of attack without moving the active flow controls. Hence, for this more relevant flight condition, the flaps are extended to a position close to their maximal angle of attack, e.g., landing position. Then, the pilot decelerates the aircraft and increases its angle of attack until the flow detaches at the flap. The time-series in Figure 5.33 illustrates the three subsequent stall events detected and monitored by the measurement system. The time-series shows that the flow becomes very turbulent at the trailing edge, but turbulent flows do not affect the measurement locations at shorter chord-wise lengths. More clear than the time-series information is the spectrogram in Figure 5.33, which contains frequent high peaks induced by detaching wake effects for just

5. Experimental Aerodynamic Validation of the Measurement System

a few seconds.

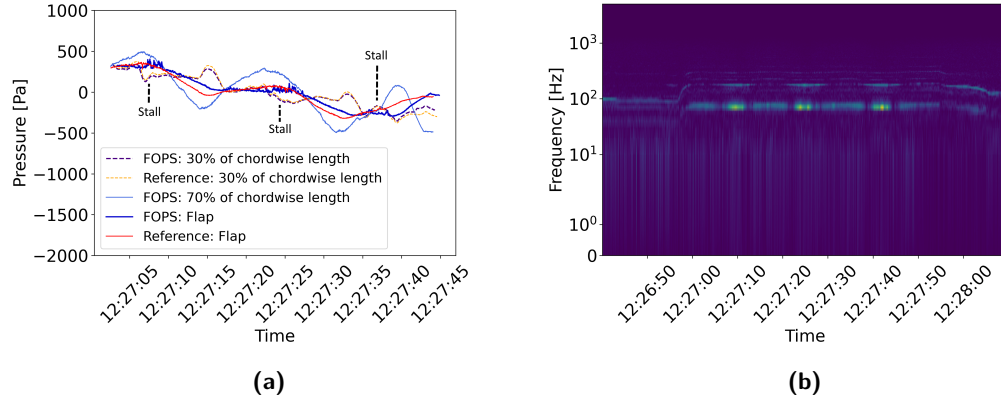


Figure 5.33.: Time-series and spectrogram of three subsequent stall events. Time-series reveals three subsequent stall events, which can be seen in the sensor’s pressure signals at different chord-wise lengths. The noisy signals at the trailing edge indicate a detached flow condition. The subsequent stall events are also observable as high-frequency components in the spectrogram for a few seconds [217].

A fundamental benefit of the sensors is the surface-neutral integration of the membrane with the aerodynamic flow of the airfoil, which will not blur dynamic pressure responses due to tubing-induced latencies [132]. During the maneuver at low air-speed, the chords, which indicate the airflow’s direction, tilt up to almost 90° locally at the trailing edge. The turbulent flow typically reverses in the boundary layer. On top of this typical stall behavior, flow separation bubbles and other parasitic vortexes from the engine or gears influence the flow direction and speed. With the time differences of arrival at each sensor’s location, their positioning information, the primary pressure field propagation, and its speed are estimated [159, 239]. The turbulence propagates across a field of sensors and results in a set of signals with almost similar shapes but includes a phase difference. Assuming a planar wavefront propagates over a field of multiple sensors at a close distance, its propagation speed u is decomposed in a x - and y - component; therefore, its velocities to u_x and u_y respectively. Figure 5.34 sketches the propagation of such wavefront in a cruise flight configuration.

5. Experimental Aerodynamic Validation of the Measurement System

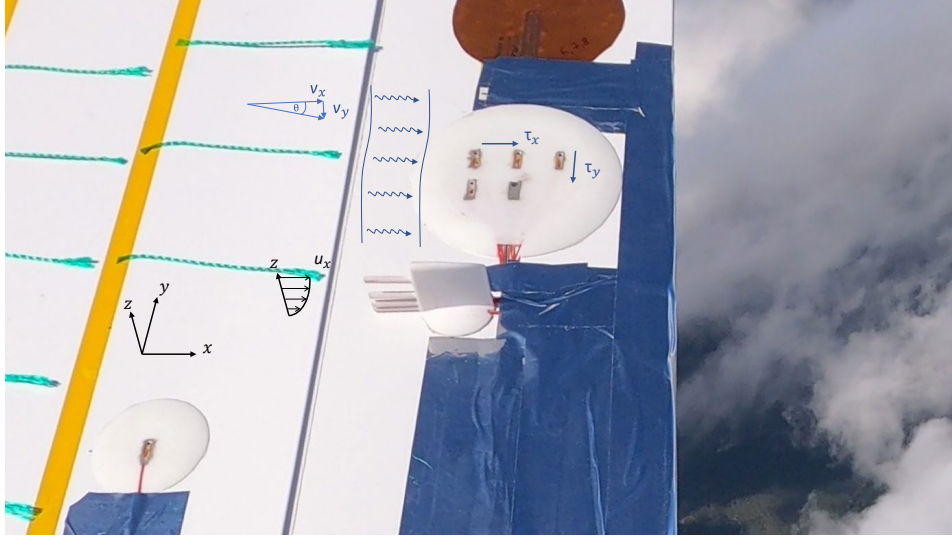


Figure 5.34.: Sensor patch with four sensors and boundary layer rake are instrumented on the flap. The boundary layer rake measures the airflow's velocity at different distances to the blade surface. The airflow's velocity closely over the surface is slowed down due to skin friction. Increasing distance, the airflow's velocity increases exponentially to the maximal flow velocity. A sketch of a wavefront propagating across the sensor patch is depicted. By measuring the time difference of arrival at different sensor locations, the flow's propagation is monitored [217].

By deriving the time delay τ , representing the time difference of the pressure wave's arrival and decomposed in a x - and y - component, a trigonometric function results in the angle of arrival θ . Assuming the sensors to be located in a triangular and orthogonal position with the same distance Δz to each other, and referring to the sketch included in Figure 5.34 equation 5.3 is derived. Nevertheless, because the trigonometric function has only an image from excluding -90° to 90° , reversing airflow has to be addressed by additional case differentiation. Here, the sign of the time delay τ_x indicates reversed airflow.

$$\theta = \frac{180}{\pi} \arctan\left(\frac{u_y}{u_x}\right) = \frac{180}{\pi} \arctan\left(\frac{\tau_x}{\tau_y}\right) \quad (5.3)$$

With the set of Pythagoras, the velocity of the wavefront v is derived by equation 5.4.

$$u = \sqrt{u_x^2 + v_u^2} = \sqrt{\frac{\Delta z_x^2}{\tau_x} + \frac{\Delta z_y^2}{\tau_y}} \quad (5.4)$$

In order to measure the time difference of arrival, the set of three pressure sensor signals must be correlated to each other. Any fluctuation of the planar wavefront alters the time delays τ , depending on the velocity and propagation direction of the flow. In general, this calculation is either done by calculating the coherence via cross-

5. Experimental Aerodynamic Validation of the Measurement System

spectral density between the signals or by the direct correlation of time-series directly to extract the time delay. Both theoretical principles have been discussed in chapter 2.1.4.2 and 2.1.4.3 and their application to measurement recording investigated in wind tunnel tests as preparation for this flight test. In this example, the time-series are windowed by 2.0s, which corresponds to 20000 data points, considering the sampling frequency of 10 kHz. The number of data points used in each block for the transform is set to be 4096 points.

First, the application of the coherence approach for this flight test is discussed. Figure 5.35 illustrates a snippet of a coherence calculation. The first graph illustrates the time-series of all four pressure sensors. The second plot demonstrates that the peak of each cross-spectral density picks the same frequency of the idling engine as the primary signal. This peak determines the frequency selection in the following. In the last plot, the phase is derived. Here the phase information at the selected frequency is of interest. This case corresponds to a neglectable phase shift because the flow is attached, not tilted, and mainly the downwash from the engine propagates over the sensor array. The calculated phase information of frequencies other than those marked with a red dot is questionable because neither the coherence function nor the cross-spectral density indicates a harmonic signal. Here, the calculated phase information is the result of the measurement noise.

Second, the application of the cross-correlation approach for this flight test is discussed. The maximal correlation coefficient estimates the probable time difference τ or shift in data point m , which is then considered to calculate velocity v and direction θ . The developed cross-correlation algorithm relies on feature extraction. Therefore, transient events such as a stall or detaching bubble are monitored. The algorithms find correlation even with a windowing functions as short as 0.1s. The drawback of this algorithm is its modest performance for non-transient events. If the algorithm does not capture characteristic features, it does not show enough dominant correlations, making the calculation noisy. The minimal resolvable time delay τ_{min} between two sensor signals calculates to $\tau_{min} = \frac{1}{f_s}$. Still, the angular resolution is limited by the spacing between the sensors, the measurement noise, and the sampling frequency. On the one side, tighter spacing supports the correlation because alternations of the traveling wavefront are locally avoided. On the other side, the sampling frequency and signal quality requirement increase.

Considering this flight experiment, in which the events are relatively short and unstable, the direct correlation approach has been preferred, regardless of the frequency information. This flight experiment has been sampled with 10 kHz, and the sensors are spaced with 20 mm distance to each other at the flap. Still, determining the direction of sounds traveling at 343 m/s across the sensor network with this setup and algorithmic approach is not achievable because of too small a temporal resolution necessary. Nevertheless, the setup can estimate the general direction of airflow and turbulence, traveling at lower speeds than 100 m/s. Additionally, characteristic features in the time-series are missing in the case of the attached flow, which is less turbulent, so the algorithm is more likely to output implausible information. The result of such an algorithm for a flow separation is depicted in Figure

5. Experimental Aerodynamic Validation of the Measurement System

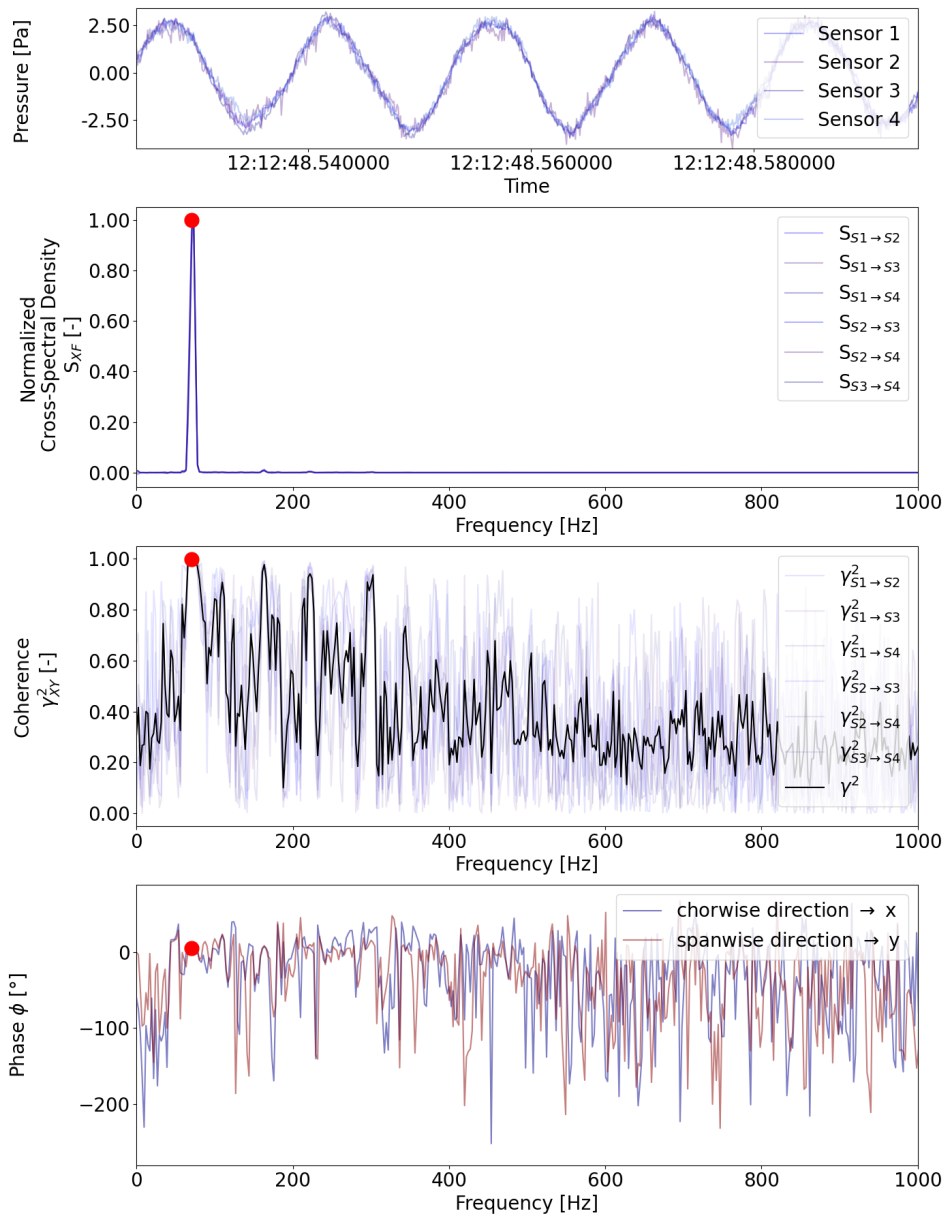


Figure 5.35.: Coherence function of the measurement. The measurement shows the pressure sensing signal of 4x sensors.

5. Experimental Aerodynamic Validation of the Measurement System

5.36. The propagation direction changes substantially during flow separation, which agrees with the chord direction on the trailing edge, monitored by the video camera in Figure 5.31 [239]. While direct cross-correlation is better for monitoring transient events, the approach via the coherence function is suited for settling for non-transient events. Nevertheless, the flow direction and propagation velocity can be resolved sufficiently.

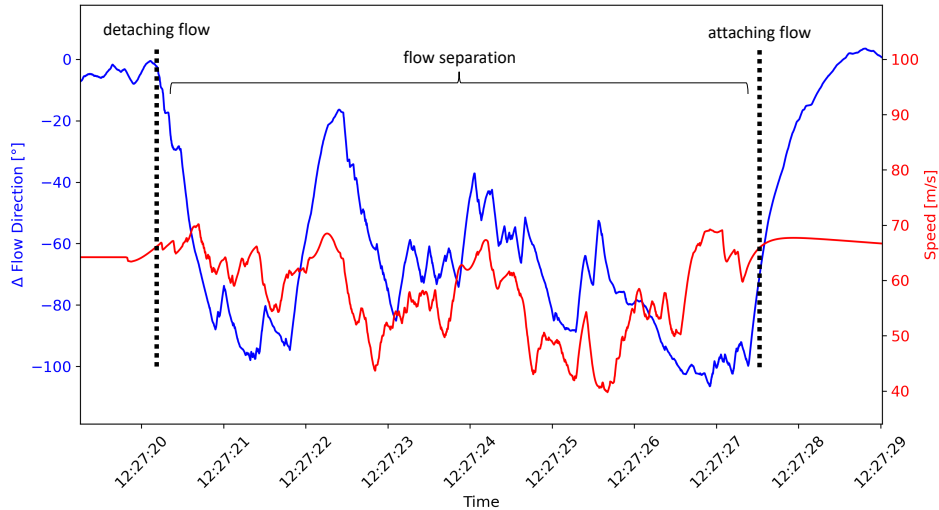


Figure 5.36.: The direction of pressure field propagation and its speed during a low-speed maneuver. The direction of pressure field propagation and its speed during a low-speed maneuver changes significantly due to flow separation at the trailing edge. The direction is derived by correlating a fiber-optic pressure sensing array. The sensor array is mounted on the movable flap. [217].

5.3.2.3. Fiber-Optic Boundary Layer Rake

In addition to the surface-mounted pressure sensors, which measure perpendicular to the fiber direction, four cylindrical pressure sensors have been installed on the flap. The instrumentation aims to measure the boundary layer's flow speed at different distances y to the surface to derive the boundary layer thickness $\sigma(x)$. The boundary layer thickness is defined as the nominal distance from the surface to a point where the flow velocity has essentially reached 99% of the free flow velocity u_∞ [167].

For this instrumentation, a rake has been manufactured as a printed part, made in polyamide plastic, which encloses the cylindrical pressure sensors at distances $y = 1.5$ mm; 5.0 mm; 10.0 mm; 20.0 mm from the surface. The airfoil has a chordwise length of approximately $c = 1.08$ m. The rake's location on the airfoil is at $x = 0.95$ m, closely in front of the trailing edge and mounted on the movable flap. Figure 5.34 displays the rake at the bottom and also sketches the theoretical expected relative non-linear velocity profile.

One main challenge of this experiment is varying flow speeds depending on the

5. Experimental Aerodynamic Validation of the Measurement System

flight situation, which affects the Reynolds number significantly. Based on the recordings of GPS position and electrical flight information system (EFIS), in this experiment, the flow speed u ranges from 0 m/s to 60 m/s and as temperature and air density drops with altitude, the Reynolds number grows up to approximately 5.0 mio. Nevertheless, the additional downwash from the propeller in front of the instrumentation has to be considered. In theory, with increasing Reynolds number, the boundary layer thickness decreases. Assuming a maximal flow speed of $u = 60$ m/s, a chordwise location of $x = 0.95$ m and a Reynolds number of $Re = 4.5$ mio, the boundary layer thickness for turbulent flow equals theoretically $\sigma = 16.4$ mm, which is smaller than the elevation of rake. Therefore, one good approach is to derive the flow velocity from the measured dynamic pressure. Another challenge is the temperature cross-sensitivity of the pressure sensor in this experiment, which could falsify the derived flow speeds. However, the measured dynamic pressure loads are relatively low, and because the temperature varies, only small chunks of measurement data shall be compared.

In the following flight experiment, a turbulent boundary flow is expected. Figure 5.37 illustrates a short flight experiment, which includes two longer sections of driving tests of the aircraft on the ground and a short flight within the aerodrome traffic circuit. The grey curve illustrates the barometric pressure. In the section where the barometric pressure drops, the aircraft is airborne. The integrated pressure sensors, facing the incoming flow, measure the dynamic pressure. The pressure sensors are not temperature compensated because their temperature cross-sensitivity is unknown. Although the temperature varies between 14 °C and 24 °C, only a minor drift is observed at the end of the measurement data.

Figure 5.38 displays different pressure sensor locations, free flow velocities, and dynamic pressure loads. Both figures demonstrate that a pressure sensor mounted closer to the airfoil's surface affects a smaller dynamic pressure load, corresponding to lower speeds. This measurement agrees with the exceptions, but the measured flow velocity is larger than the flow speeds induced by the air stream. Presumably, the propeller's downwash in front induces additional flow to the structure so that higher dynamic pressure loads are observed.

Based on the measured flow velocity u in addition to the pressure sensor's elevation y , which is well known by design, a curve fit of the velocity profile 2.7 is computed. Then the boundary thickness σ and free stream velocity u_∞ for each given time in the measurement is approximated. Figure 5.39 illustrates the measurement results and compares them to the theoretical assumptions. While the theory considers simply the Reynolds number, the actual measurement results consider the flow speed at different levels, derived from the dynamic pressure measurement, map those to the assumed velocity profile, and derive the free flow velocity and boundary layer thickness. The measured boundary layer thickness is slightly thicker than the theoretical assumption, presumably due to surface imperfections and the added cabling for the instrumentation of the flush-mounted sensors. Additionally, a gap between the main airfoil and the movable flap is located in front and close to the fence. Moreover, the measurement shows that the boundary layer thickness increases and

5. Experimental Aerodynamic Validation of the Measurement System

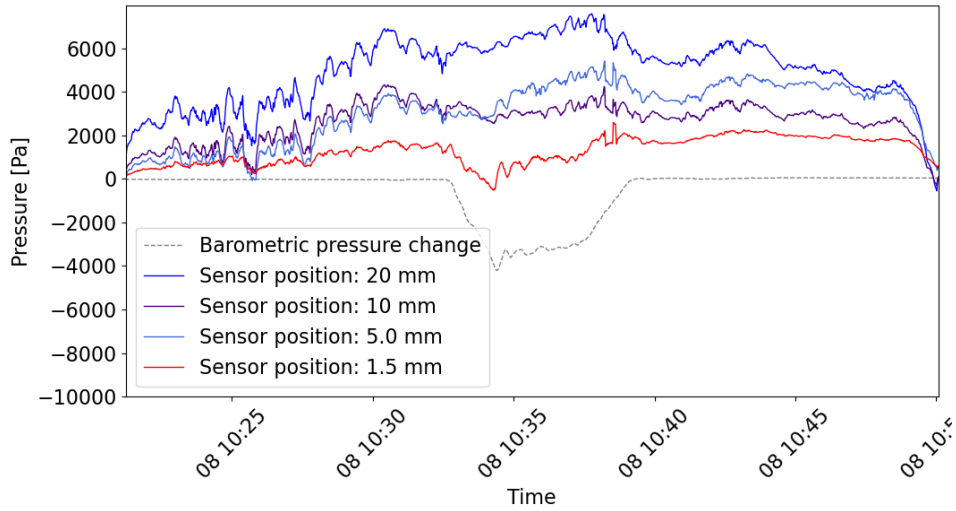


Figure 5.37.: Time-series of the pressure sensor mounted in a rake to measure different velocity profiles. The test includes two longer sections of driving tests of the aircraft on the ground and a short flight within the aerodrome traffic circuit. The grey curve illustrates the barometric pressure change. The pressure sensors are not temperature compensated, although the temperature varies between 14°C and 24°C . Therefore, a minor drift is observed at the end of the measurement data.

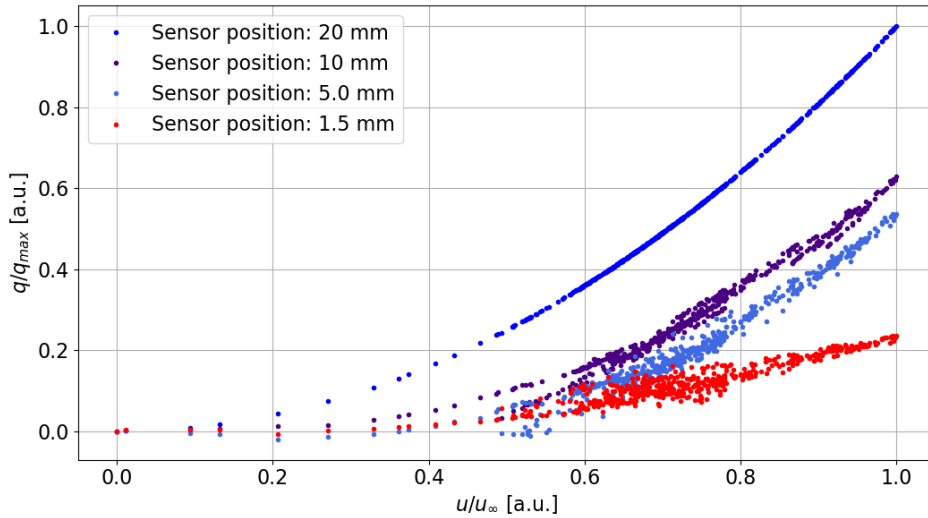


Figure 5.38.: Flow velocity over dynamic pressure for pressure sensors at different elevations from the surface. The dynamic pressure increases quadratically with the free stream velocity. Due to skin friction, the flow velocity is lower for sensors close to the surface. With increasing distance from the airfoil's surface, the flow speed increases. By measuring the flow speed at different levels and assuming a known velocity profile, the boundary layer thickness can be derived at each given time.

5. Experimental Aerodynamic Validation of the Measurement System

deviates from the theoretical assumption, especially at lower speeds and Reynolds numbers. In this interesting case, surface imperfections might also significantly affect the aerodynamic profile. In this example, Figure 5.39 illustrates only a smaller chunk of data of about 8 min at ground level in order to counter drifts, temperature cross sensitivities and barometric pressure changes. Unfortunately, no reference rake measurement at that location has been instrumented, so measurement deviations are difficult to quantify, and only the reference to theoretical expectation remains an option.

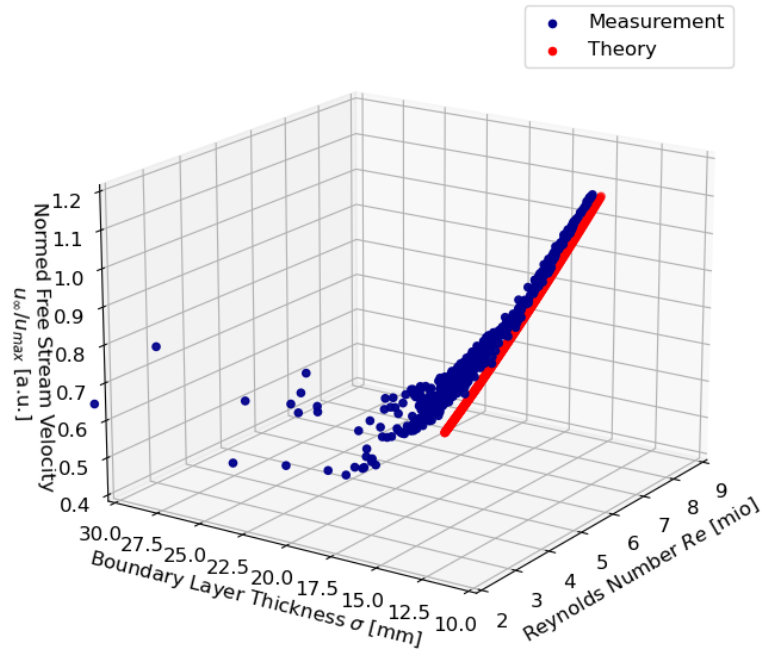


Figure 5.39.: Boundary layer thickness measurement on an aircraft with fiber-optic pressure sensors. While the theory considers the Reynolds number, the measurement results consider the flow speed at different levels. The results are derived from the dynamic pressure measurement, are mapped to the assumed velocity profile, which derives the free flow velocity and boundary layer thickness. The downwash of the propeller in the rake direction adds induced airflow. The measurement shows that the boundary layer thickness is presumably slightly thicker due to surface imperfections and the added cable routing.

Mounting the sensor at the tip of the rake allows dynamic sensing flow effects in the boundary layer in flight. Figure 5.40 illustrates power spectral densities at different flight situations. In the first case, the aircraft is in cruise flight configuration, and the flaps are retracted. While the chords near the rake indicate attached flow, the chords at the flap are tilted slightly, indicating some turbulence effects. The shown power spectral density at normal flight conditions demonstrates that the turbulence

5. Experimental Aerodynamic Validation of the Measurement System

intensity is very similar across the layer. Noticeable is again the noise peak, which originates from the engine. Figure 5.40 also depicts the flow phenomena at a stall. The picture illustrates the chords in front of the rake tilt. Nevertheless, the chords at the flap are shown in various directions. Presumably, the flow is completely detached at the flap. The power spectral density measurement shows very similar results to the measurement performed with surface-mounted pressure sensors. Noticeable is a slightly lower turbulence intensity for the sensor in the rake, mounted closest to the flap's surface.

5.3.3. Summary of the Results

The experiments on a light sports aircraft in relevant flight conditions prove the measurement setup's flight capabilities. The measurement results have been compared to their electrical references and demonstrate the competitive performance of the fiber-optic setup. All fiber-optic pressure sensors have survived four consequent flight tests without damage. Due to the fiber-optic design, the sensors are well-suited for harsh-condition in-flight tests. This benefit has been the first demonstration of fiber-optic Fabry-Pérot pressure sensors combined with edge-filter interrogators in-flight applications. Unlike the wind tunnel test, this flight test also reveals the difficulty of allowing a wide measurement range and acceptable pressure resolution. Therefore, a high dynamic range of the measurement systems is required. This experiment demonstrates that the reference sensing technology is of lower noise, although electromagnetic interference is coupled to the electrical supply. Moreover, the fiber-optic system would also benefit from better precision if residual temperature dependencies could be narrowed down further.

Nevertheless, integrating the sensor almost surface neutral to the airfoil benefits the dynamic sensing characteristics. As in the wind tunnel tests, the frequency components indicate the detached and attached flow conditions very well. Moreover, as time responses of the sensor are neglectable, airflow speed and directions can be monitored.

In addition, the fiber-optic pressure sensor has been instrumented in a boundary layer rake. As a result, the boundary layer thickness has been successfully measured, and the dynamic pressure difference in flight has been investigated. This rake instrumentation is the first of its kind, using fiber-optic means in an actual flight test. Nevertheless, in this case, the main challenge is the temperature cross-sensitivity of the sensors for adequate static pressure sensing.

5. Experimental Aerodynamic Validation of the Measurement System

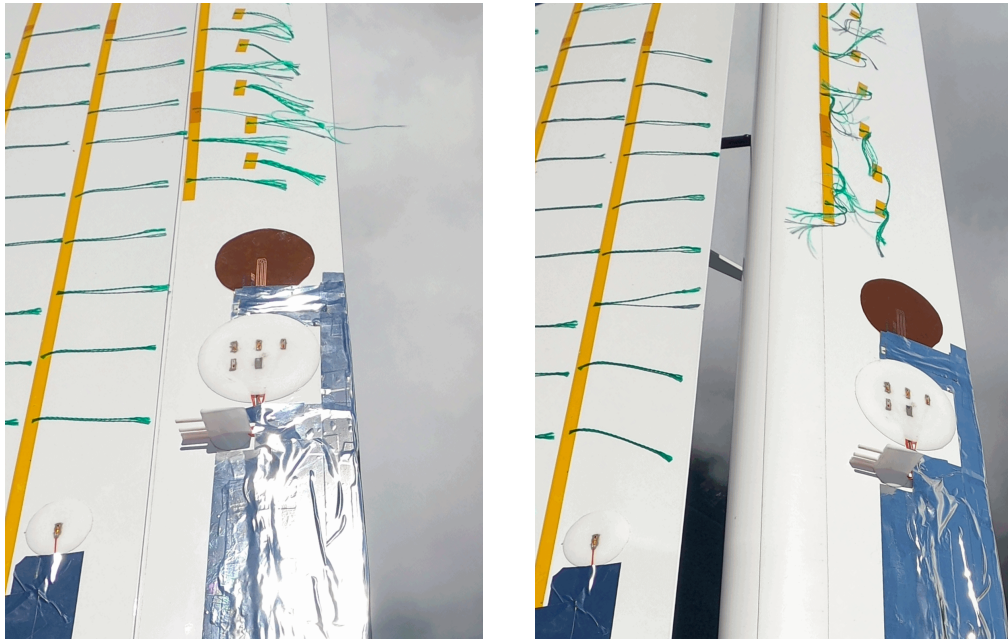
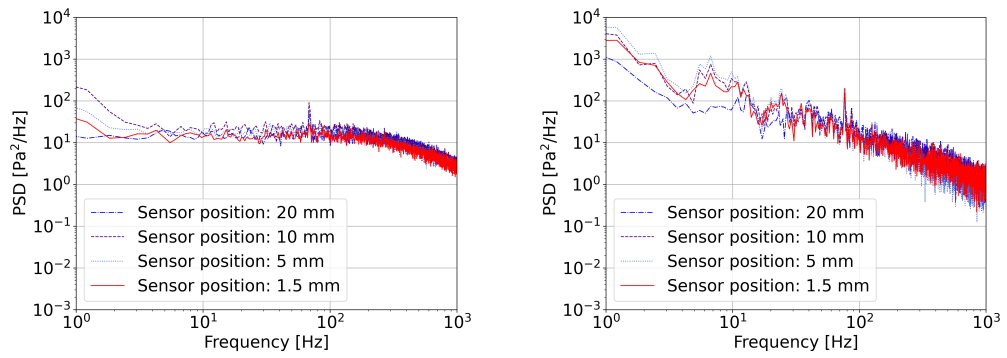


Figure 5.40.: Power spectral density measurement of cylindrical sensors in a rake at normal and stalling flight conditions. The power spectral density function of multiple cylindrical sensors at attached flow conditions is shown in Figure (a). The turbulence intensities are shown in the attached flow conditions. The flaps are completely retracted at times. Here, all pressure sensor measures similar turbulence fluctuations across the distance from the surface. The surface imperfections, e.g., of the taped cabling, trigger a turbulent flow. The power spectral density function of multiple cylindrical sensors at detached flow conditions is shown in Figure (b). Here the flow fluctuations also indicate turbulent flow conditions at all levels [217].

5.4. Integration of Fiber-Optic Pressure Sensors into a Multi-hole Pressure Probe to Monitor Unsteady Inflow

Flow directions and their velocity are fundamental properties of interest in aerodynamic experiments, especially considering unsteady pressures [168]. For aerodynamic measurements of flow field propagation, measurement techniques are grouped into non-intrusive and intrusive techniques. The prominent representatives for non-intrusive measurements, which are used to examine the velocity field but require high calibration efforts and high costs, are optical particle image velocimetry and laser Doppler anemometry [212, 213]. The main drawback is the need for undisturbed optical access to the test object. Unfortunately, this rules out non-intrusive measurement techniques in most experiments. Hot-wire and multi-hole pressure probes are most commonly used for intrusive measuring methods. Hot-wire anemometry allows high temporal resolution but lacks mechanical robustness for field tests in harsh environments. Multi-hole pressure probes are a more common cost-efficient tool because of their more straightforward setup. Nevertheless, each application differs in temperatures, pressure ranges, or spatial restrictions of the installation space and requires different design, assemblies, and calibration processes. [148, 149, 212–214].

Conventionally, a typical Pitot tube measures pressure on two sides. Here, a pressure tap measures the static pressure at one side and perpendicular to the incoming flow, and a pressure tap facing the inflow measures the dynamic pressure. Typically, a differential pressure transducer relates the pressures obtained, and according to Bernoulli's principle, the velocity is determined [4, 96].

Like the well-known Pitot probe, where the stagnation pressure is measured at a probe's tip with a single pressure port, multi-hole probes measure the pressure distribution at different locations on the probe's tip. The working principle of a Pitot probe relies on the stagnation of the flow around the probe [96, 212–214].

At the stagnation point, the maximal pressure equals the static and dynamic pressure sum. The flow properties at the probe's tip are derived by measuring all pressures and setting these measurements in relation to each other. Nevertheless, a spatial calibration for each probe is necessary [65, 212–214].

A challenge is to record unsteady pressure changes with conventional multi-hole probes because of delays and distortions of the pressure signal, which reduces the accuracy of high-frequency measurements [4]. In contrast to steady measurements for unsteady evaluations, long pressure taps, which conventionally connect the probe holes to the sensors, attenuate and phase-shift the time-dependent pressure fluctuations. Therefore, the dynamic system inside the pressure channels significantly influences the measurement of unsteady flow phenomena. Resonance and attenuation dominate the dynamic system, but filtering techniques can be used to reconstruct the original pressure signal [103]. Therefore, in addition to the spatial calibration, the dynamic characteristics of the multi-hole probe are necessary for insight into high fluctuating pressure effects. The theoretical dynamic behavior of these pneumatic line-cavity systems is complex but can be analytically described [66, 73, 149].

5. Experimental Aerodynamic Validation of the Measurement System

Nonetheless, experiments have shown that due to manufacturing tolerances, the analytic solutions serve only as a first guess, and the need for more accurate transfer functions leads to the experimental verification of the acoustic behavior [73, 212–214]. In the dynamic calibration, sinusoidal waves are emitted and recorded at specified frequency steps. Hence, the amplitude ratio and the phase shift between the emitter and the integrated sensor are obtained [179, 212, 214]. The research illustrates the experimental transfer function $H(f)$ with fiber-optic sensors. It stresses the motivation for placing the sensor close to the tip of the probe [148, 151]. Figure 5.41 illustrates a transfer function $H(f)$ of an exemplary pressure tap with length 20 mm and diameter 1.5 mm. The graph illustrates that the pressure reading $P_{sensor}(f)$ is very different from the actual pressure P_{tip} at the tip. The transfer function is characterized by repeating attenuation effects and the frequency band, which are the consequence of the resonance and attenuation effects of the flow. Presumably, the fiber-optic sensor has been compressed due to the surrounding silicone tubing, which might have caused a change in the calibration coefficient [212, 214] and explaining the deviation of the amplitude in Figure 5.41.

Nevertheless, this experiment focuses on the relative frequency response rather than the correct static amplitude characteristic. The results demonstrate that the withdrawn sensor position and prolonged pressure tubing dampen the frequency response of the overall sensing system. Therefore, carefully dynamic acoustic calibration or a more suitable sensor placement close to the tip must be considered to monitor unsteady pressure fluctuations.

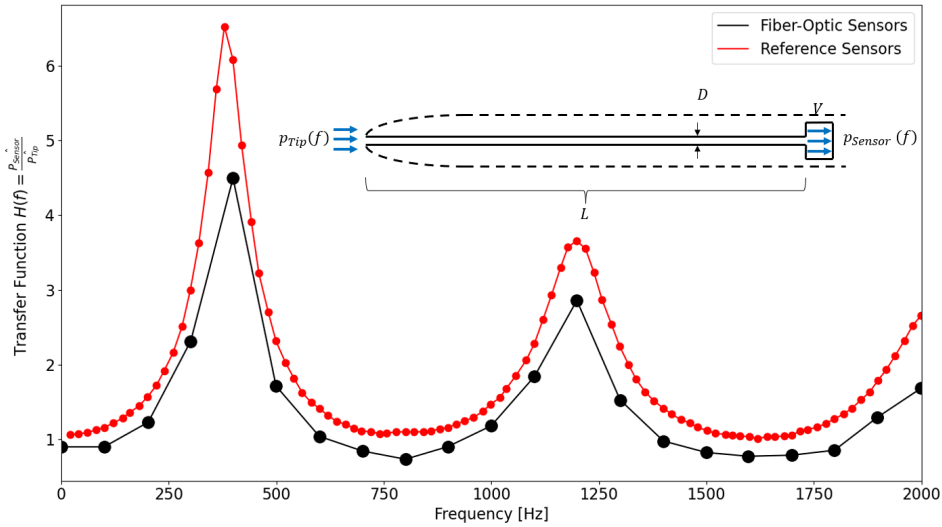


Figure 5.41.: Comparison of a single-hole probe transfer characteristic between fiber-optic and conventional electrical sensors. Both sensors are mounted at the end of the probe. Due to the tight tubing, attenuation and distortion effects between the tip and the end of a pressure tubing occur. Experiments are conducted in a frequency test rig, which emits a sound wave at different frequencies. For each frequency, the amplitudes, measured at the tip and the end of the channel, are related to each other [149, 212–214].

5. Experimental Aerodynamic Validation of the Measurement System

To avoid dynamic calibration and allow the measurement of rapid unsteady pressure fluctuation and operation in harsh environments, the surface-neutral integration of fiber-optic pressure transducers at the probe tip is the focus of research. Especially in the field of research on aerodynamic turbomachinery application, interferometric fiber-optic sensors have been recognized as a robust means to measure pressure profiles with high spatial and temporal resolution [89, 129, 201, 202]. While the main objective in the field of research on aerodynamic turbomachinery applications is to measure shock dynamics, another merging motivation is the measurement of inflow condition is uncontrolled and prone to lightning environments as on wind turbines [11, 19, 62, 112, 191].

Together with the partner Vectoflow, the research institute Fraunhofer IWES and the Chair of Aerodynamics and Fluid Mechanics, Department of Mechanical Engineering, Technical University of Munich, the combination of differential fiber-optic pressure sensors and multi-hole probes have been studied. The results have been published in conference and journal papers [212–214].

5.4.1. Description of Experiment

The aerodynamic calibration determines the correlation between the mean free-stream flow conditions and the measured pressures with the probe. The probes in this experiment have been instrumented with five fiber-optic pressure sensors at each tip. Moreover, a fiber-optic temperature sensor has been integrated for temperature compensation. The left Figure 5.42 displays the wind tunnel. Within this static spatial calibration, different flow velocities at various inflow angles α and β towards the probe affect pressure distributions at the tip. In later experiments, angle combinations at specific velocities are precisely calibrated depending on the expected angle and velocity range. Finally, the recorded correlation between the mean free-stream flow conditions and the measured pressures at the probe is determined and used as input data for interpolation. Table 5.3 summarizes the specifications of the calibration facility.

Table 5.3.: Aerodynamic key parameters of the wind tunnel experiment for fiber-optic probe [212, 214].

Parameter	Unit	Value
P	kW	90
Ma	–	0.16 ... 0.22
Ma non-uniformity	%	± 0.25 at 0.1 Ma
α	–	-42.0° ... 42.0°
β	–	-42.0° ... 42.0°

5. Experimental Aerodynamic Validation of the Measurement System

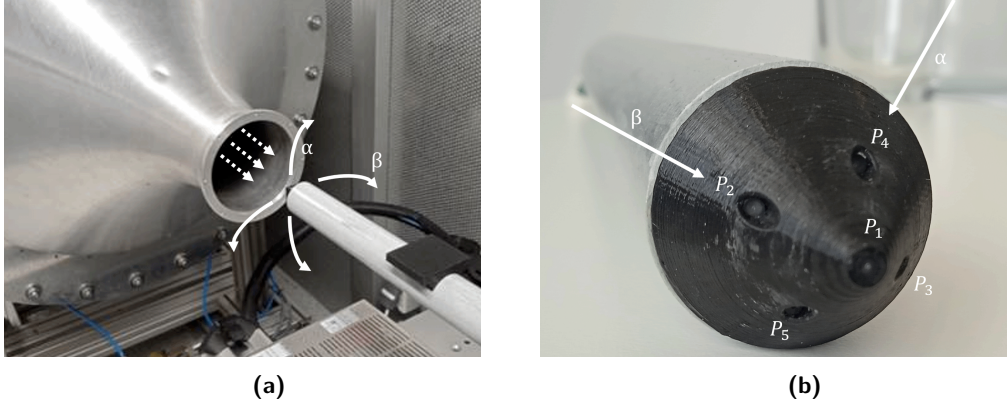


Figure 5.42.: Calibration of fiber-optic probe with flush mounted sensors. In the wind tunnel, spatial calibration is performed. Therefore, at different velocities and angles α and β , pressure signals are recorded and used as calibration input. Sensors are located close to the tip, so dynamic unsteady pressure fluctuations can be monitored without the need for frequency calibration. The five pressure sensors are distributed around the tip, so that flow direction-induced pressure distribution is monitored and flow direction, and speed can be processed [212, 214].

5.4.2. Experimental Results - Spatial Calibration of a Fiber-Optic Pressure Probe

During the spatial calibration process, the probe is exposed to a steady flow with general conditions, and pitch α and yaw angles β change to 1451 positions at two velocity settings. The acquired data is post-processed and later used in field experiments to determine the flow conditions at the probe tip. There are multiple methods of how the calibration data is used to reconstruct the unknown flow-field properties. An interpolation scheme to calculate the flow properties at the probe tip is most commonly used. For each pressure sensor, a point cloud is obtained. Figure 5.43 illustrates the point clouds for the middle sensor at $Ma = 0,22$. The shape of the point cloud fits a multidimensional Gaussian bell. As the temperature increases within the duration of the experiment and as the setup tilts, optic polarization and temperature cross dependencies of the fiber-optic sensor might cause slight deviations. The standard deviation between measurement and fit results to 71 Pa and 68 Pa respectively and are in the same range as the lab results in respect to polarization in section 4.3.2 on page 66. A two-dimensional Gaussian function 5.5 can be fitted to the data well. The data shows for this sensor a great match to the function, in which \hat{p} represents the maximal dynamic pressure, p_{off} the static pressure offset, α and β the angle of incident, α_0 and β_0 the offsets and the variables σ_α and σ_β control the width the fitted Gaussian bell.

$$p_{Sensor} = \hat{p} e^{-\frac{(\alpha-\alpha_0)^2}{2\sigma_\alpha^2} - \frac{(\beta-\beta_0)^2}{2\sigma_\beta^2}} + p_{off} \quad (5.5)$$

Nevertheless, the point cloud is more difficult to describe analytically for non-

5. Experimental Aerodynamic Validation of the Measurement System

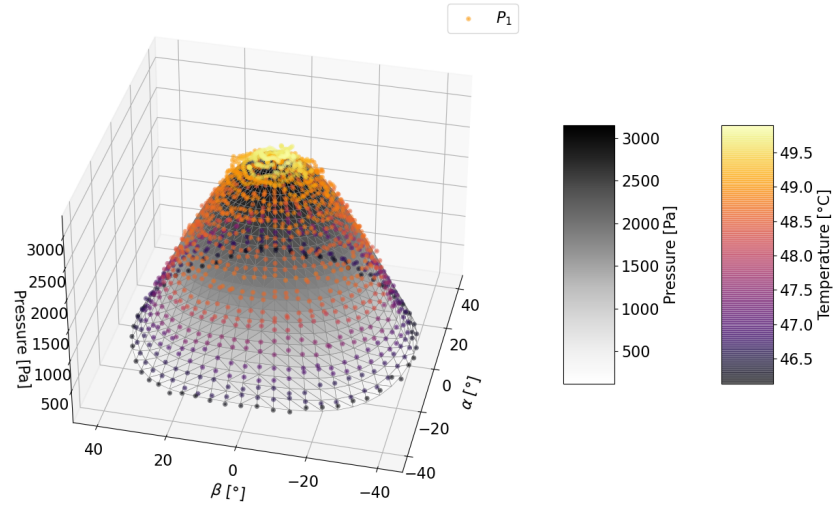


Figure 5.43.: Point cloud of pressure sensor centered at the tip for velocity $Ma = 0,22$. At this velocity level, induced dynamic pressure due to stagnation increases up to 3000 Pa. Measurement deviations are less dominant due to the larger excitation.

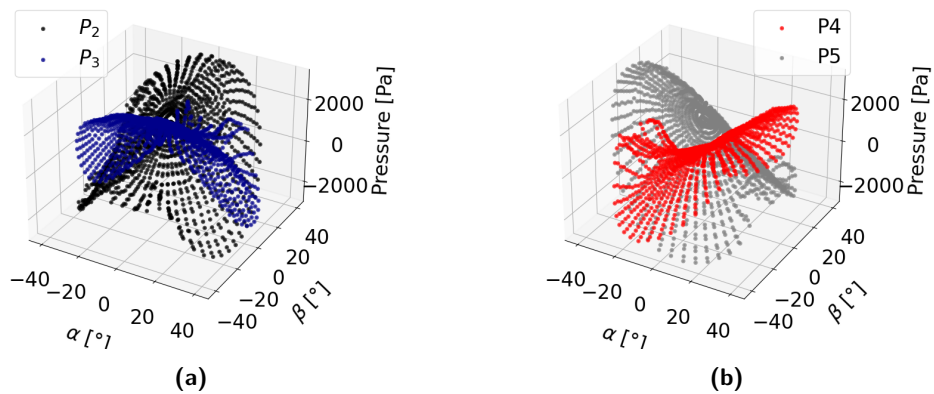


Figure 5.44.: Point cloud of pressure sensors P_2, P_3, P_4 and P_5 for for velocity $Ma = 0,22$. The point clouds of the opposing sensor are mirroring. The shape of the surface cannot be expressed easily anymore. Additionally, at extreme angles α or β , vortex flows result in a non-steady slope of the calibration surface.

5. Experimental Aerodynamic Validation of the Measurement System

centered sensors, as illustrated in Figure 5.44. Here, the point clouds of the opposing sensor mirror each other. Moreover, at extreme angles α or β , vortex flow results in a non-steady slope of the calibration surface. Nonetheless, the repeatable point clouds of all five sensors and the additional temperature sensor allow interpolation. The fiber-optic probes have been used in a subsequent research project, in which, based on the data recorded, the incident inflow angles and velocity of a wind turbine are derived. This experiment is discussed in the following section 5.5.

5.5. Measurement of Aerodynamics of a Wind Turbine with Fiber-Optic Sensors

An ongoing research question is now to increase inflow awareness and aerodynamic performance of wind turbine generators. The developed sensor technology opens up a toolkit for subsequent research activities to investigate aerodynamics in harsh and prone-to-lightning environments. Moreover, the technology might deliver valuable input for advanced control strategies for next-generation wind turbines. The motivation for these applications has been introduced in chapter 1.

The field test validation of aerodynamic profiles of wind turbines is very similar to the evaluation of an aircraft's airfoil. The validation of a wind turbine's aerodynamics includes pressure distribution, noise emissions, and the measurements of lift coefficient. The previously discussed applications have already characterized the sensors' static and dynamic measurement performance. Additionally, reference sensors are difficult to integrate into this specific application for long-term monitoring due to the harshness and prone to the lightning environment. Therefore, this section concentrates on mentionable observations of exemplary projects involving wind turbine generators.

5.5.1. Description of Experiment

Prior to this work, as part of an initial development project between the companies fos4X and Enercon, the aerodynamic performance of wind turbine generators has been studied with fiber-optic means [131, 132]. For field validation of a turbine, approximately about 150 x sensors have been instrumented on a rotor blade along three blade sections [178, 215]. To ensure that the sensor's frequency response is not affected by the distance between the surface pressure and the location of the transducers, the sensors have been flush-mounted to the blade's surface [4, 215]. Nevertheless, the flush surface integration of the sensors and cables into the blade structure requires time-consuming fine machining in the blade factory.

Within this work, the matured pressure sensing technology has been introduced in two additional projects on an onshore and offshore wind turbine. In the first project, in cooperation with the company Vectoflow and the institute, the Fraunhofer IWES 72 x pressure sensors have been installed on an offshore turbine in a retrofit operation [88]. Next to a set of pressure sensors distributed on the airfoil in two sections, the previously presented fiber-optic 5-hole probes have been instrumented. The challenging retrofit installation of a pressure-sensing solution on an erected turbine is challenging. Therefore, to ease the installation procedure and minimize downtime, four aerodynamic shells have been prepared in which the fiber-optic pressure sensors have been integrated neutral to the shell's surface. The fiber-optic cables have been routed at the trailing edge with a flat ribbon cable and fed into the blade's root area, where cabinets include the measurement devices. Figure 5.45 illustrates the turbine and displays an aerodynamic shell, which includes distributed pressure sensors and

5. Experimental Aerodynamic Validation of the Measurement System

the probe from chapter 5.4. In a second project, the 24 x fiber-optic pressure sensors will be installed on an offshore turbine. The scope of this second project is the aerodynamic validation of different interchangeable split blades [1].

5.5.2. Experimental Results

Prior to this work, the first project with the initial generation sensors, see sensor version V1-2-X in chapter 4.2 on page 51, has demonstrated that the executed field measurements are beneficial to optimize computational fluid dynamics simulation as seen in Figure 5.46 [215]. This experiment's measured pressure coefficient distribution is compared to a two-dimensional simulation with the software Xfoil [125]. The aerodynamic profile as input for the simulation is based on a laser scan of the actual instrumented blade. Figure 5.46 illustrates the difference between the simulation and measurement for the instrumentation at spanwise location $y/b = 90\%$. The maximal simulated pressure coefficient normalizes the pressure coefficients. Excluding sensors at the stagnation point, the measurements are within 5% deviation from simulation. More significant deviations might be due to insufficient surface quality at some locations since each sensor has been manually integrated into the blade's laminate.

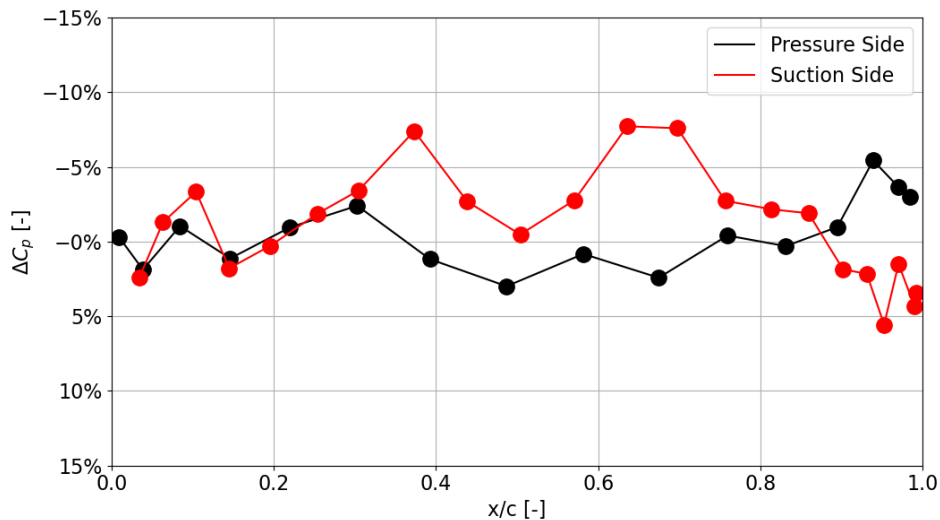


Figure 5.46.: Difference between measured pressure coefficient distribution of the rotor blade to simulation. The graph illustrates the difference between the simulation and measurement for the instrumentation at the spanwise location $y/b = 90\%$. The maximal simulated pressure coefficient normalizes the pressure coefficients. Excluding sensors at the stagnation point, the measurements are within 5% deviation from simulation. [22, 215].

Additionally, the inflow velocity is only approximated and might cause normalization deviation. Altogether, the agreement between the static pressure distribution

5. Experimental Aerodynamic Validation of the Measurement System

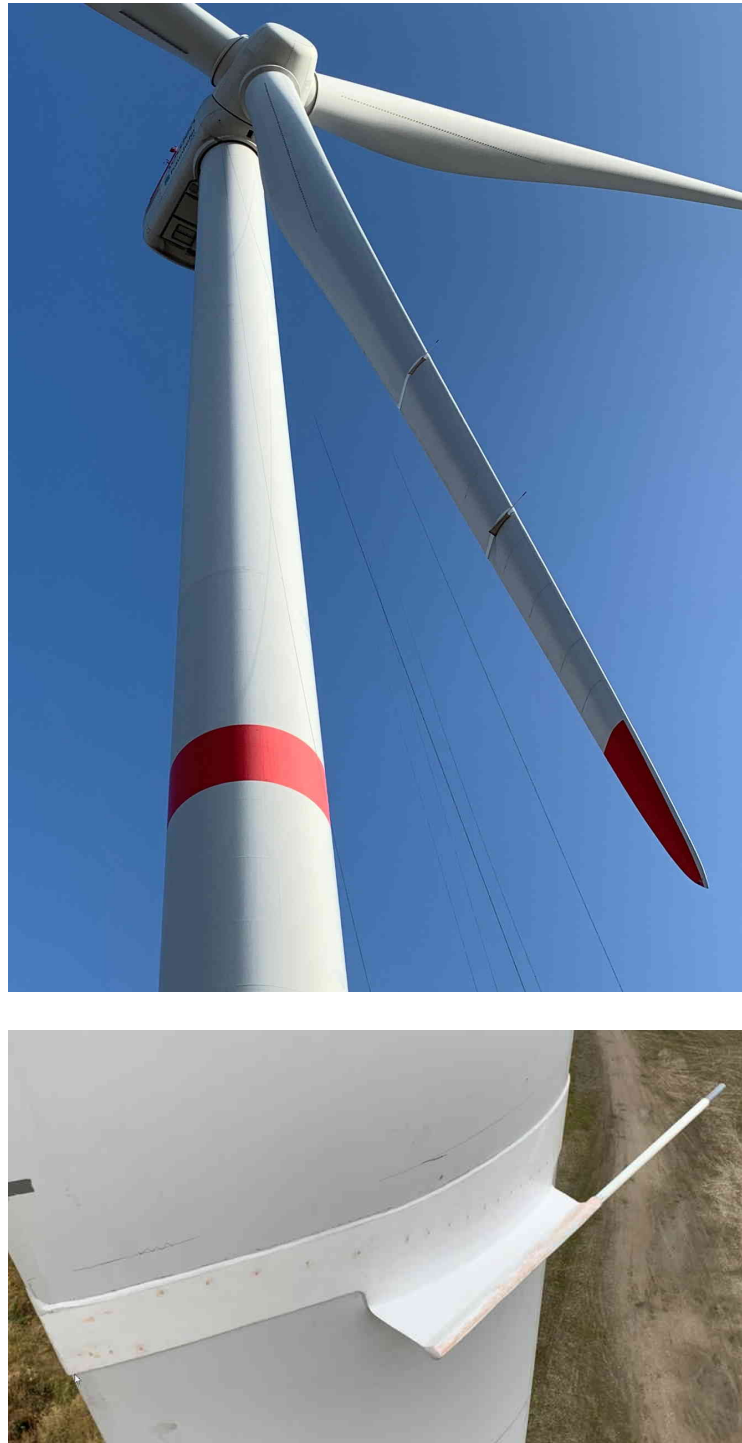


Figure 5.45.: Wind turbine instrumented with two aerodynamic shells, including distributed pressure sensor and probes. Aerodynamic shells include distributed pressure sensor and a probe and are bonded to a single blade of an offshore wind turbine, which is erected onshore for research purposes. The fiber-optic cables are routed along the trailing edge.

5. Experimental Aerodynamic Validation of the Measurement System

has been considered good, especially at the most outwards measurement section. There, the observed pressure amplitudes are the highest, and in relation to those amplitudes, parasitic measurement effects are most negligible [22, 215].

Further, the fiber-optic instrumentation revealed that the extrapolated measured trailing-edge noise results in a good qualitative agreement to the conventionally measured far-field noise emission [7, 22, 142, 215]. While for the low-frequency range, the deviation in measured sound power level has been reported to be within 3 dB(A), measurements at higher frequencies deviate up to 6 dB(A) due to frequency depending attenuating emission [7].

The main shortcoming is the degrading measurement quality towards the end of the campaign. Poorer signal-to-noise ratio and sensor drifts have been observed. After disassembling the blade from the turbine, the airfoil with sensors has been manually inspected utilizing a spectrometer. A large number of the sensors have formed a parasitic optical resonator. The aging effects have been simulated in the lab environment and are discussed in section 4.2.3 on page 61. This successful project concluded that the optical deflection unit inside the pressure sensor had to be adhesive-free in the optical path. The feedback initiated the second generation of pressure sensors at that time [131, 132, 178, 215].

Within this work, two subsequent projects have been initiated. Considering the results of the first generation of the sensor, the main aim of the current sensor is a more drift-stable version. These projects have been instrumented with updated sensor design that has proven to be less affected by aging in the lab environment, as discussed in section 4.2. Additionally, the sensor installation routine has changed as sensors are no longer embedded into the blade. This paragraph concentrates on the main findings so far.

Even though temperature effects on wind turbines are relatively slow and less impactful, temperature cross-sensitivity remains a fundamental sensing property for long-term static measurement tasks. It is crucial to be minimal or well-known. Fortunately, the static barometric altitude during slow rotation changes is sufficient for wind turbines to test the plausibility of sensitivity and offset of installed pressure sensors. During this maneuver, the wind turbine rotates slowly at low wind speed so that aerodynamic loads can be neglected. The altitude change of the sensors, especially at the blade's tip, continuously measures the static barometric air pressure. The recorded measurement signal forms a sinusoidal function with an offset. This signal shape is used for a sensitivity plausibility check and an offset correction by knowing the radial position of the sensors and applying the barometric formula [2]. The temperature cross-sensitivity is estimated by mapping the mean pressure offset of slow roll maneuver and at low wind speed for each sensor with temperature information. Figure 5.47 shows the temperature cross-sensitivity differs from the lab results.

5. Experimental Aerodynamic Validation of the Measurement System

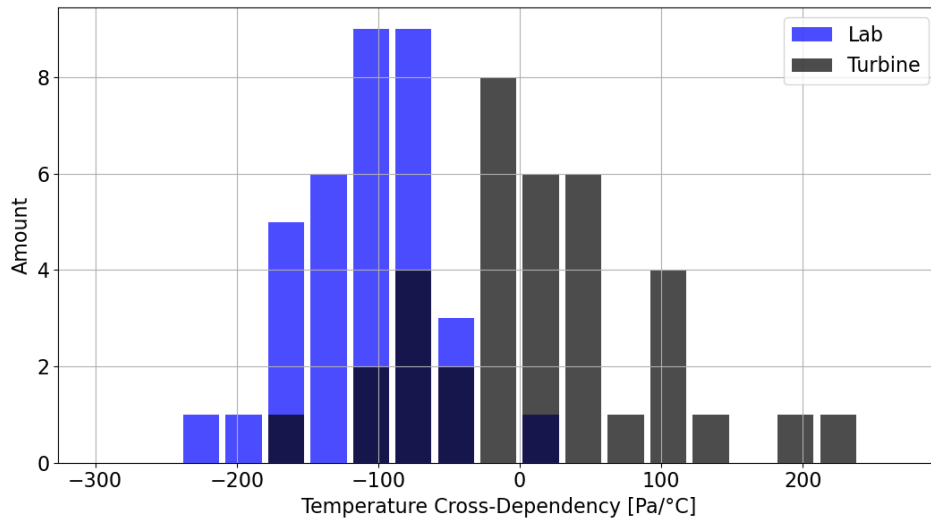


Figure 5.47.: Histogram of the temperature cross-sensitivity in the lab and on the turbine. By mapping the mean pressure offset of slow roll maneuver at low wind speed for each sensor with temperature information, the temperature cross-sensitivity is estimated as long as no aerodynamic forces act on the airfoil.

The mean temperature cross-sensitivity on the turbine results $14.07 \text{ Pa}/^\circ\text{C}$, which is better than the mean value $-116.30 \text{ Pa}/^\circ\text{C}$ of the same sensors, observed in a lab experiment. Nevertheless, the standard deviation is increased with $77.96 \text{ Pa}/^\circ\text{C}$ to $57.79 \text{ Pa}/^\circ\text{C}$ respectively.

This deviation is still an ongoing discussion. The integration and installation of the sensors affected the sensor's offset. In addition, the mechanical coupling between the aerodynamic shells and the sensor might add parasitic mechanical cross-sensitivities. The deviating temperature sensitivity is accompanied by observing short-term offset changes, which could depend on the turbine's operation and have exceeded the expected measurement uncertainty.

As a recommended step, pressure and temperature recalibration of the instrumented sensor, including the aerodynamic shell, is the next intended step. Additionally, the possible unexpected mechanical coupling due to the novel retrofit installation needs to be investigated on the ground.

These campaigns have yet to be finished when this thesis has been finalized but represent opportunities for further research.

6. Conclusion and Outlook

This work introduces fundamental challenges in testing innovative and noise-reduced rotor blades on modern wind turbines and next-generation transport aircraft aerodynamics. Conventional electrical pressure sensors strongly degrade in performance in harsh environments during flight or wind turbine monitoring applications. Therefore, a novel and durable sensing technology is required to generate validation data on full-scale structures under realistic environmental conditions over a long-term measurement.

Pressure-sensing fiber-optic sensors have shown a considerable potential to fulfill advanced requirements in test & measurement, and control applications within aviation and wind turbines and could open up many new aerodynamic application possibilities. In the research cooperation with Polytech Wind Power Technology Germany GmbH (formerly fos4X GmbH), a former spin-off of the Chair of Measurement Systems and Sensor Technology, the suitability of fiber-optic pressure sensor technology for measuring the aerodynamics of airfoils has been investigated. As a result, the developed and evaluated Fabry–Pérot measurement system measures aerostatic, aerodynamic, and acoustic events. Furthermore, the sensors are well-suited for harsh environments due to the fiber-optic design.

Next to an intense qualification in lab environments, various extensive field tests have raised the technology's readiness. Three wind tunnel tests and numerous flights have been carried out as part of the Cleansky 2 project SKOPA (Skin friction and fiber-optics-based surface pressure measurements for aircraft applications). While the wind tunnel tests aim to provide complex aerodynamic situations, which have been studied with fiber-optic means, the flight tests are a feasibility study for fiber-optic pressure sensors. The proposed fiber-optic measurement setup successfully demonstrates its capability to measure the static pressure distributions along the airfoil. Furthermore, the wind tunnel experiments, combined with active flow controls, demonstrate that the measurement system could evaluate the lift performance of actuators and act as control input in future applications. Due to the high-frequency capabilities of the fiber-optic sensors, the dynamic behavior of the boundary layer separation and vortex generation can be captured in the frequency domain. The dynamic measurements of complex turbulent flows in wind tunnel tests prove the system's performance in monitoring complex aerodynamic events, which reveals aerodynamic phenomena such as flow separation. Furthermore, it has enabled the measurement of noisy boundary layers with minimal aerodynamic and aeroacoustics disturbance. Additionally, due to the sensor's flush surface membrane, pressure field propagation and direction measurements have been performed successfully in controlled environments and flight tests. A fiber-optic stall indicator, integrated into the trailing edge and monitoring the turbulence intensity, is a

6. Conclusion and Outlook

possible commercial attractive option for monitoring trailing edge noise emission.

In cooperation with the aerodynamic chair at the TU Berlin, this work finishes with the first demonstration of fiber-optical Fabry–Pérot pressure sensors in combination with edge-filter interrogators in-flight applications with relevant aerodynamic results. The flight experiments in relevant flight conditions have proven the measurement setup’s flight capabilities. Fluctuating pressure intensities, pressure field propagation, and lift effect at prone-to-flow separation areas on the aircraft have been monitored in flight successfully. Moreover, a fiber-optic rake based on the developed pressure sensor to measure the boundary layer thickness has been instrumented and evaluated as the first of its kind on an actual flight test. In cooperation with the aerodynamic chair at TU Munich, the company Vectoflow, and the IWES Fraunhofer, a fiber-optic multi-probe sensor has been developed and evaluated and later instrumented to wind turbine. Additionally, two sets of fiber-pressure sensors monitor the blades’ aerodynamics in an ongoing research effort.

One of the main challenges investigated and improved is the reduction of temperature cross-sensitivity. Still, the most challenging application is to utilize the sensors to measure quasi-static lift coefficients because it requires measuring the remaining temperature cross-sensitivity for each combination of sensor and measurement channel. Therefore, active temperature compensation needs to be introduced in the measurement data post-processing for accurate static pressure measurements. Reducing this cross-sensitivity further is a task of ongoing research activities. Another challenge is reducing the noise floor and expanding the measurement range. Even though a fiber-optic sensor is noise-free, the interrogator’s electronics induce a higher noise level than a conventional electrical reference sensor. This measurement approach’s limitation relies on the interrogator’s electronics and the demodulation principle. Either the interrogator’s dynamic range needs to maximize without losing sensitivity, or the system design must prioritize either to optimize static or dynamic measurement capabilities. Next to measurement challenges, the sensor’s manufacturing requires another industrialization step for commercialization. Although the selective laser etching technology of fused silica structures as a novel micromachining technology for fiber-optic sensors has been well utilized, vacuum packaging remains challenging. The sensors require tight tolerances on the cavity length to match the interrogator’s operating point. Bonding the fiber assembly to the glass chip is manual and difficult to scale in production. Additionally, the evacuation process’s quality slows production and dominates the cross-sensitivity towards sensitivity.

Nevertheless, the field tests prove that such measurement systems can resolve complex aerodynamic measurements in the static and dynamic domains. Furthermore, the sensors demonstrate their inherent advantages as they can measure in harsh environments due to the increased overload robustness. Therefore, the developed measurement system becomes an enabler for ongoing research activities, including distributed pressure measurement on a multi-megawatt wind power turbine and novel condition monitoring applications.

Appendix

Dynamic Characteristics of the Pressure Taps

The following equations support the understanding of section 5.4 on page 120.

Measurement of fluctuating pressure with a pressure tap, which connects the model with a remote pressure transducer, is a common technique in aerodynamic experiments. Nevertheless, every pressure tap with considerable length and narrow diameter introduces amplitude and phase distortion effects, which are result of resonance and viscous damping inside the pressure tap.

Bergh and Tijdeman developed the following theoretical model for the introduced distortion. The model represents the tubing system as a linear, time-invariant system and characterized by a frequency depending transfer function. Still, theoretical dynamic behavior of these pneumatic line-cavity systems is complex . Thus the variable J_i denotes a Bessel function of i th order, κ_h describes the specific heat ratio, the Prandtl number Pr , the mean velocity of sound c_s , the density ρ_{air} and dynamic viscosity μ of the fluid [66, 73, 149].

$$H(f) = \frac{p_{Sensor}(f)}{p_{Tip}(f)} = \left(\cosh(\psi L) + \frac{V \eta \psi}{\kappa_h \pi r^2} \sinh(\psi L) \right)^{-1} \quad (.1)$$

$$\psi = \frac{2\pi f}{c_s} \sqrt{\frac{\kappa_h J_0(\gamma)}{\eta J_2(\gamma)}} \quad (.2)$$

$$\eta = \left(1 + \frac{\kappa - 1}{\kappa_h} \frac{J_2(\gamma \sqrt{Pr})}{J_0(\gamma \sqrt{Pr})} \right)^{-1} \quad (.3)$$

$$\gamma = i^{3/2} r \sqrt{\frac{2\pi f \rho_{air}}{\mu}} \quad (.4)$$

Power Spectral Density of Winglet with Active Flow Control

The following Figures from A1 to A6 illustrate all power spectral density measurement on the suction side and are discussed in 5.2.2.2 on page 92. The Figures A7 and A8 show the results of the sensors mounted on the pressure side. The following table summarizes the sensor position in the experiment.

Table .1.: Sensor positions in experiment.

Sensor number	x/c [-]	side
1	0.000	stagnation point
2	0.005	suction side
3	0.019	suction side
4	0.031	suction side
5	0.042	suction side
6	0.053	suction side
7	0.109	suction side
8	0.128	suction side
9	0.145	suction side
10	0.165	suction side
11	0.184	suction side
12	0.216	suction side
13	0.259	suction side
14	0.323	suction side
15	0.408	suction side
16	0.515	suction side
17	0.630	suction side
18	0.737	suction side
19	0.844	suction side
20	0.406	pressure side
21	0.739	pressure side
22	0.630	pressure side
23	0.530	pressure side
24	1.000	trailing edge

Appendix

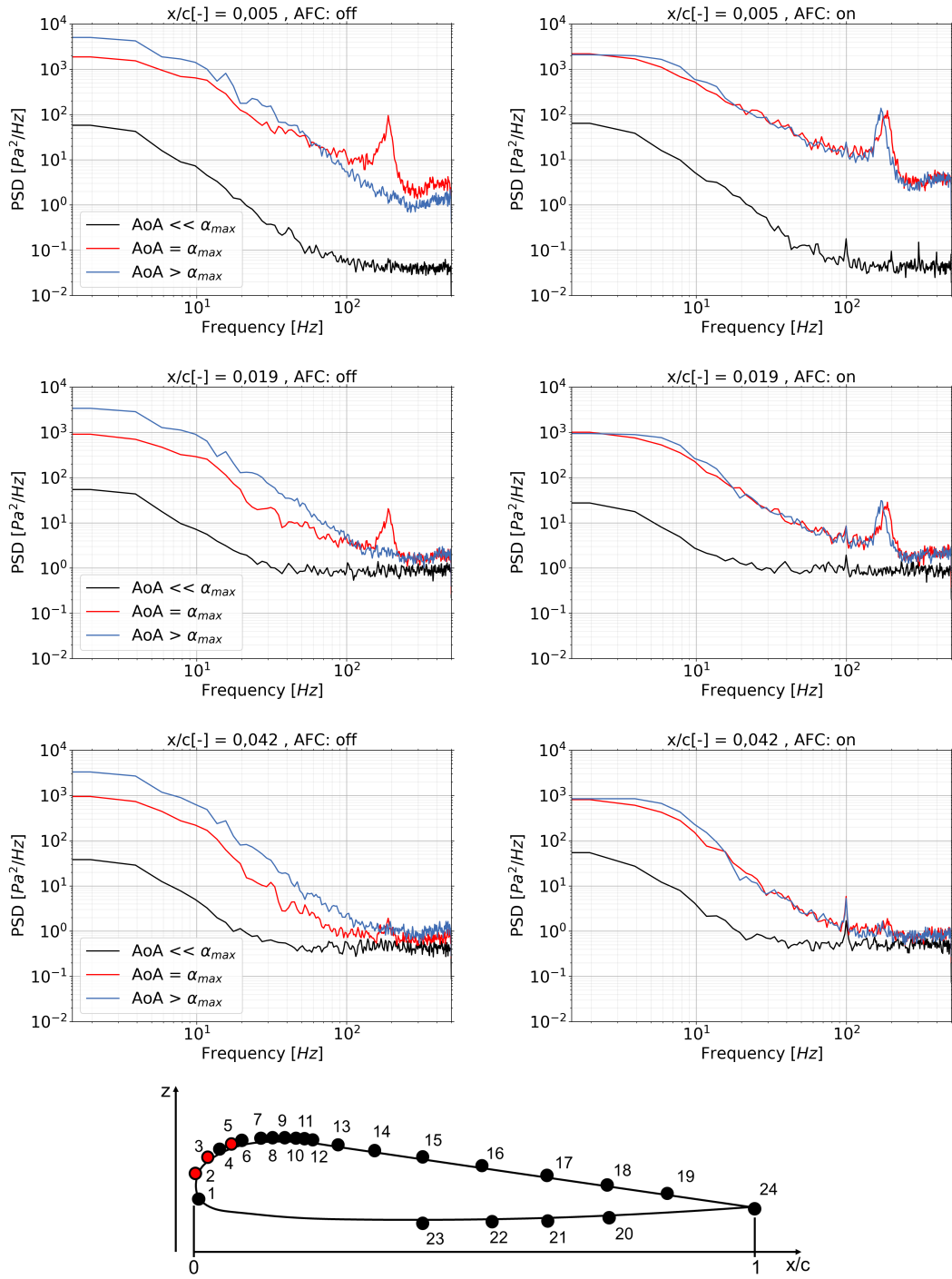


Figure A1.: Power spectral densities of a pressure sensors on the suction side for sensors at $x/c = 0,005$ to $0,042$ at the leading edge.

Appendix

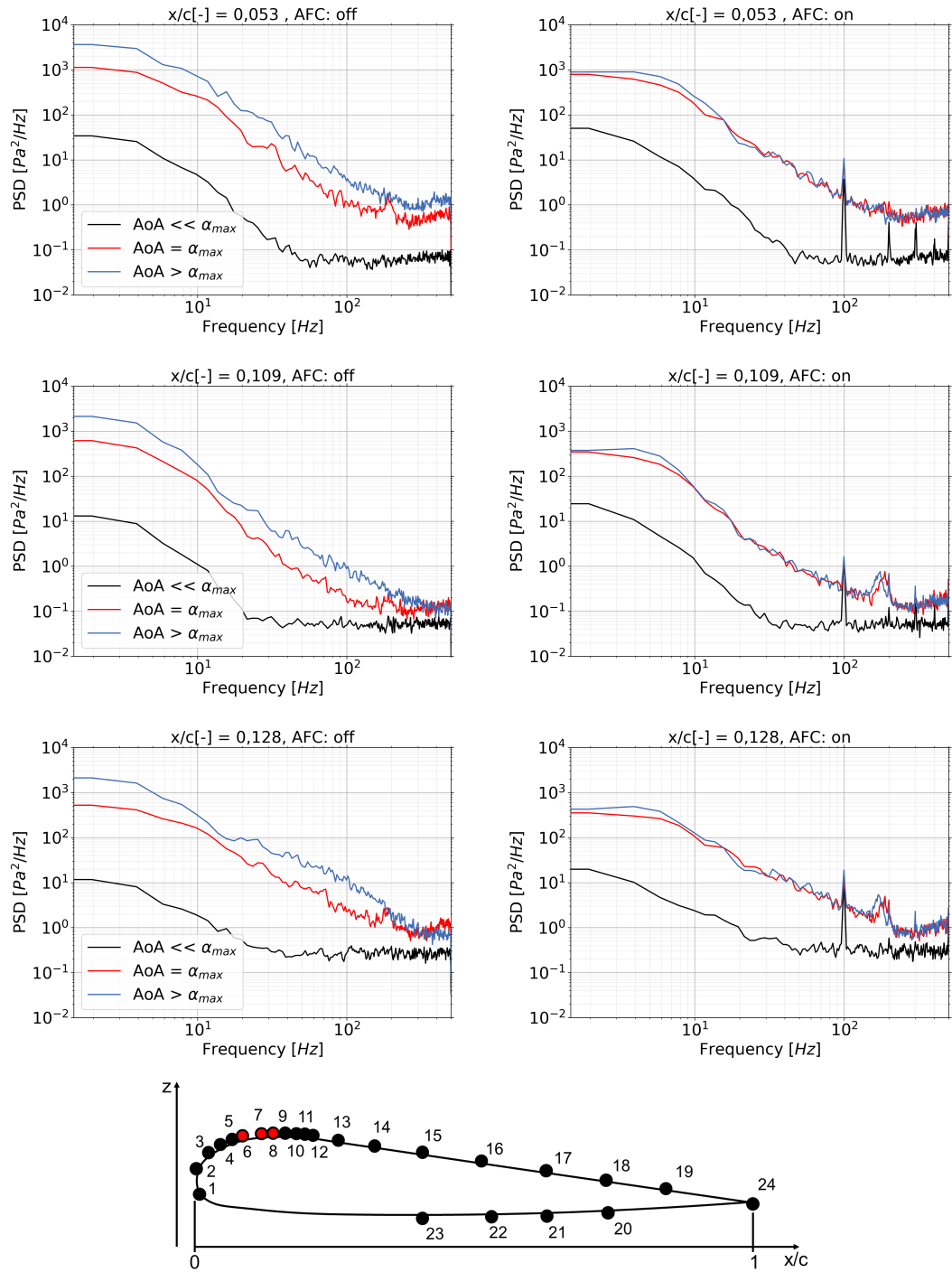


Figure A2.: Power spectral densities of a pressure sensors on the suction side for sensors at $x/c = 0,053$ to $0,128$.

Appendix

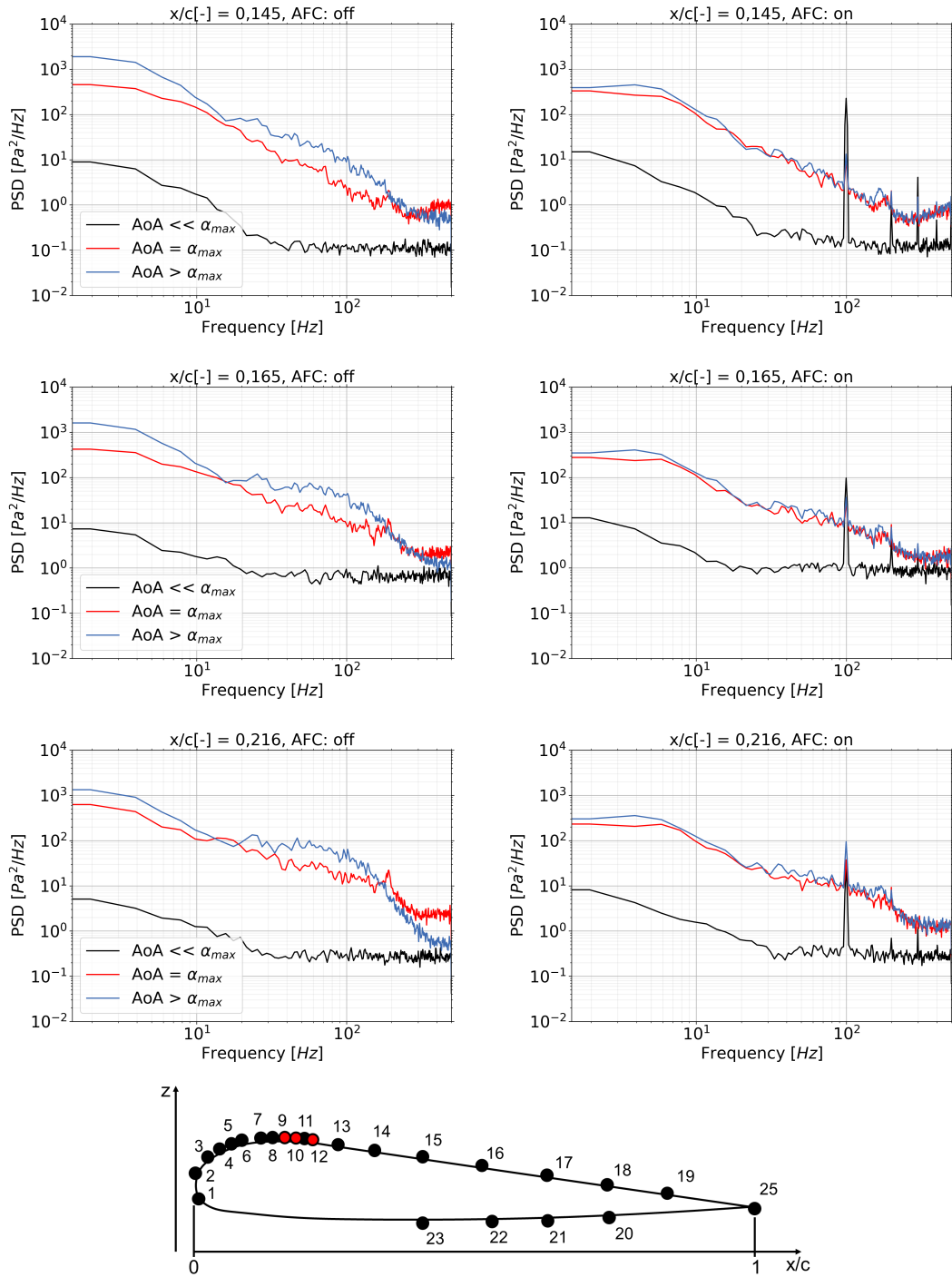


Figure A3.: Power spectral densities of a pressure sensors on the suction side for sensors at $x/c = 0,145$ to $0,216$.

Appendix

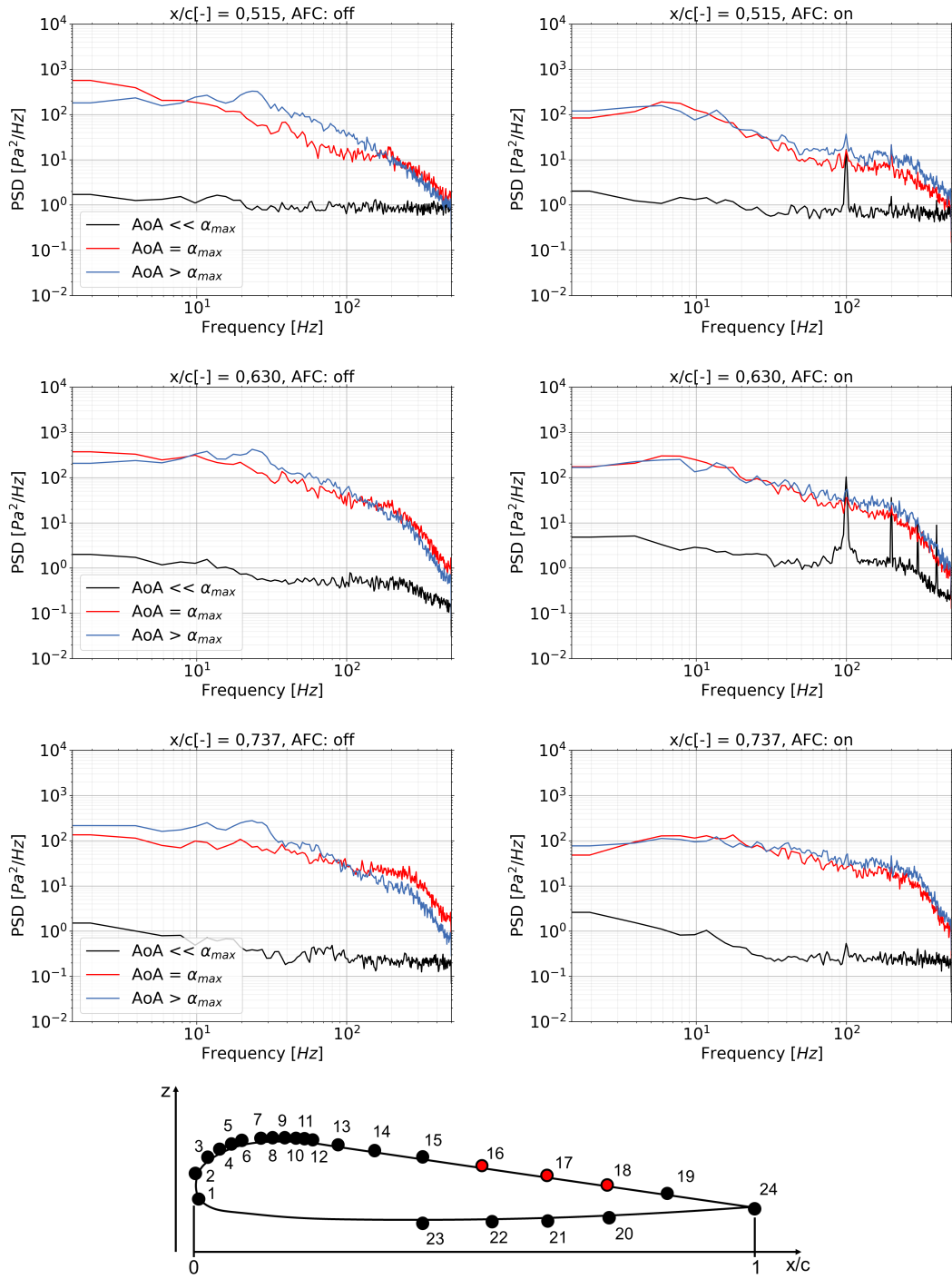


Figure A5.: Power spectral densities of a pressure sensors on the suction side for sensors at $x/c = 0,515$ to $0,737$.

Appendix

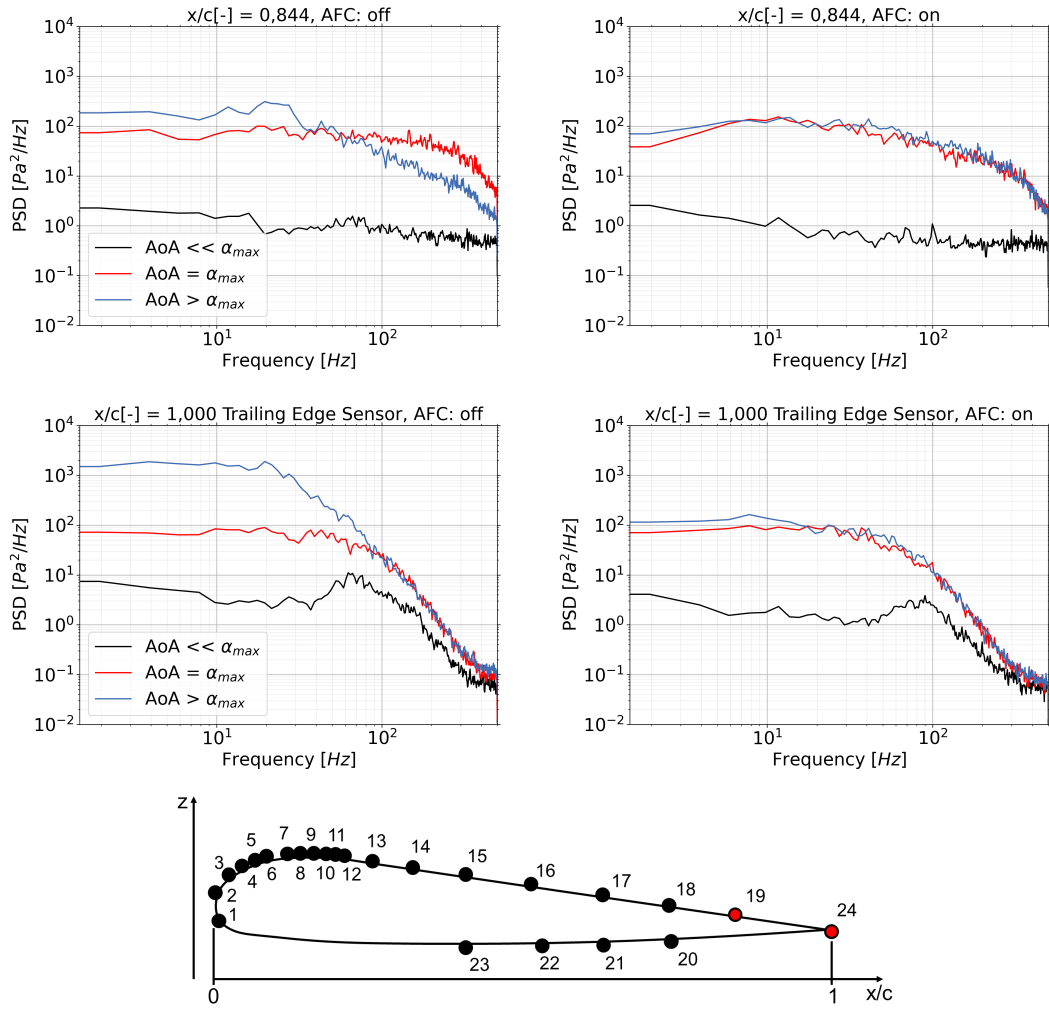


Figure A6.: Power spectral densities of a pressure sensors on the suction side for sensors at $x/c = 0,844$ and $1,000$.

Appendix

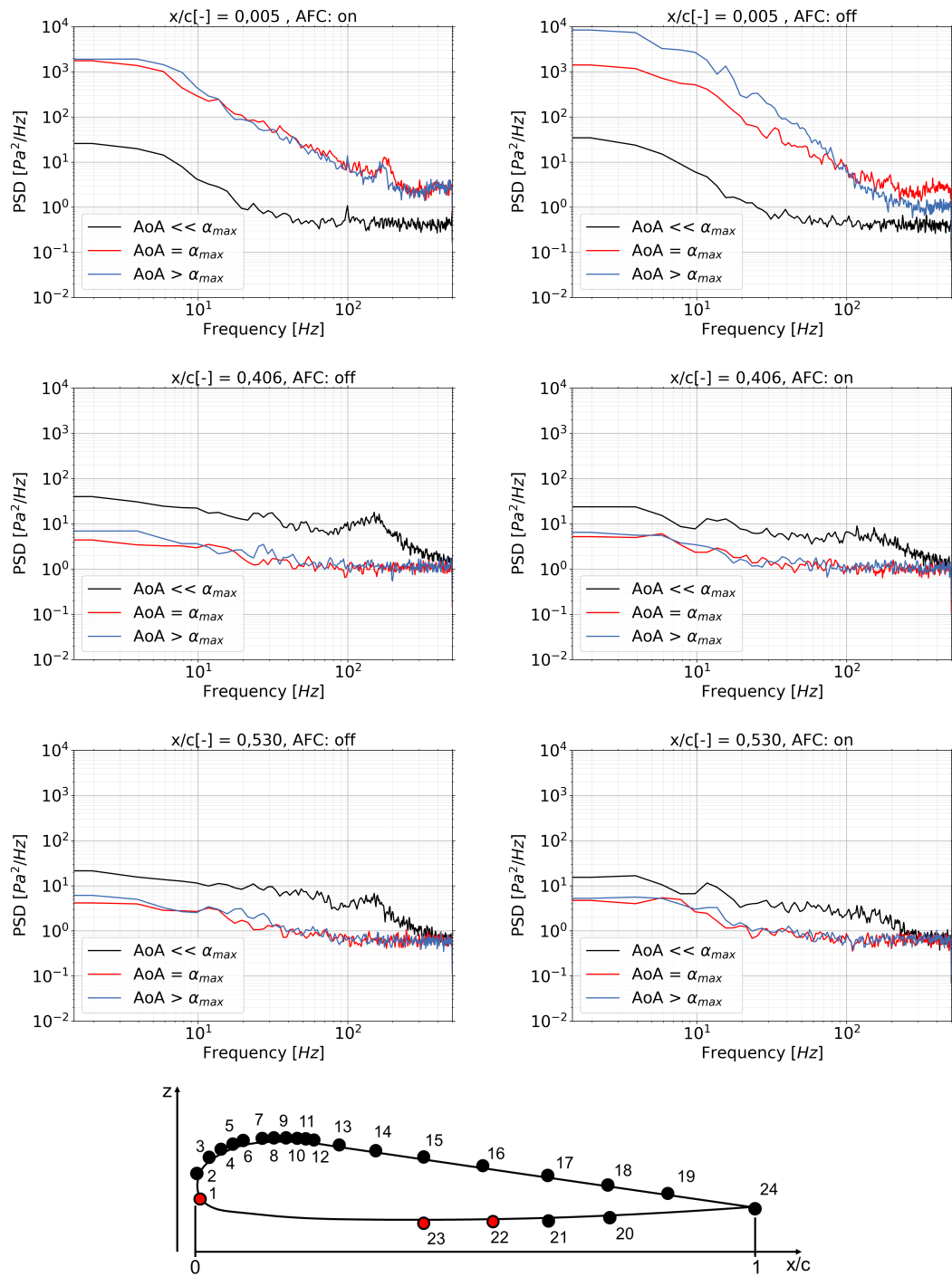


Figure A7.: Power spectral densities of a pressure sensors on the pressure side for sensors at $x/c = 0,005$ to $0,530$.

Appendix

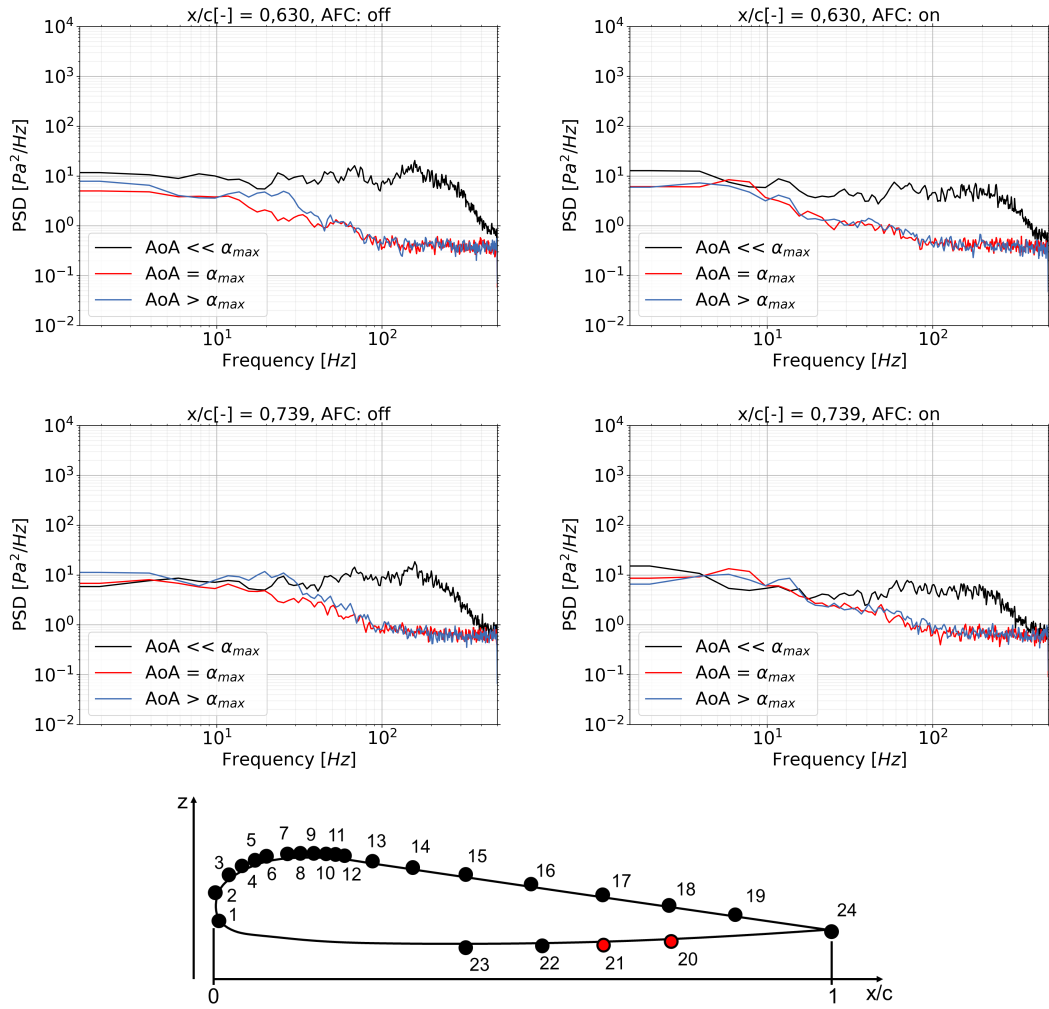


Figure A8.: Power spectral densities of a pressure sensors on the pressure side for sensors at $x/c = 0,630$ and $0,739$.

List of Figures

2.1.	Aerodynamic forces on an airfoil.	15
2.2.	Light as an electromagnetic waveform.	21
2.3.	Wave vector of the incident, refracted and reflected wave at the planer interface between two media.	23
2.4.	An ideal single-mode glass fiber with step index refractive index profile and its radiation characteristic.	26
2.5.	Illustration for the description of the Fabry-Pérot resonator	28
2.6.	Schematic structure of an edge filter based fiber-optic measurement device for Fabry-Pérot sensors	33
2.7.	Transfer curve of Fabry-Pérot sensor in combination with an edge filter interrogator.	35
2.8.	Section drawing of a membrane.	38
2.9.	Typical simulated Bode-Diagram of the membrane.	42
3.1.	Schematic drawing of the cylindrical fiber-optic pressure sensor.	45
3.2.	Schematic drawing of the flat fiber-optic pressure sensor.	45
3.3.	Cylindrical sensor head with single-mode fiber before bonding	46
3.4.	Cylindrical-shaped fiber-optic pressure sensor.	48
3.5.	Flat fiber-optic pressure sensor.	48
4.1.	Calibration procedure of the fiber-optic sensors.	50
4.2.	Dynamic calibration of a pressure sensor with a pistophone.	51
4.3.	Fabry-Pérot spectrum of a cylindrical pressure transducer.	52
4.4.	Measured spectral shift of a fiber-optic sensor shifts depending on the applied pressure level.	54
4.5.	Cavity length in relation to the applied pressure.	54
4.6.	Calibration set up to evaluate temperature cross sensitivities of the fiber-optic pressure sensors.	57
4.7.	Typical spectral shift of a fiber-optic pressure sensor due to temperature changes.	58
4.8.	Center wavelength shift of a fiber-optic pressure sensor over temperature.	58
4.9.	Histogram of the temperature cross-sensitivity of a cylindrical and flat fiber-optic pressure sensor of the same batch each.	59
4.10.	Center wavelength shift of a differential fiber-optic pressure sensor over temperature.	60
4.11.	Aged spectrum of a fiber-optic pressure sensors.	62

List of Figures

4.12. Fit of measurement data with simulation, linear deviation, a relative and absolute measurement deviation of the transfer curve of Fabry–Pérot sensor in the combination of an edge filter interrogator.	65
4.13. Measurement deviations due to polarization and a non-uniform light density increase.	68
5.1. Test setup of the low-speed and high-speed wind tunnel test.	72
5.2. Filtered time-series of eight pressure sensors illustrate the propagation of a pressure field.	73
5.3. Filtered time-series of eight fiber-optic pressure sensors and an electrical sensor integrated into the AFC illustrate the propagation of the pulsed air stream from the AFC.	74
5.4. Time-series and cross-correlation of a windowed turbulent flow.	75
5.5. Coherence of the measurement signals.	76
5.6. Coherence length of the turbulent airflow on a flat plate.	77
5.7. Time-series of the pressure signals in the high-speed wind tunnel test.	78
5.8. Typical power spectral density of measurement demonstrating the effect of the active flow control in the low and high-frequency region.	79
5.9. Spectrogram of a sensor in the high-speed wind tunnel.	80
5.10. Outer Winglet Model installed in the wind tunnel.	83
5.11. Drawing of the outer winglet model.	85
5.12. Absolute fiber-optic pressure sensors in a PEEK housing.	86
5.13. C_p distribution of suction side based on fiber-optic sensors with disabled active flow control.	89
5.14. C_p distribution of suction side based on fiber-optic sensors with enabled active flow control.	89
5.15. Normalized lift coefficient based on the force and pressure sensors.	90
5.16. C_p distribution of the outer winglet model has been recorded with the electrical reference and fiber-optic pressure sensors.	91
5.17. Temperature response of the pressure sensors.	92
5.18. Power spectral densities of a pressure sensor near the leading edge.	93
5.20. Power spectral densities of pressure sensors located on the pressure side.	94
5.19. Power spectral densities of pressure sensors on the suction side for sensors across the blade in the chordwise direction.	95
5.21. Power spectral densities of the pressure sensors located in the trailing edge.	96
5.22. Turbulence intensity of the trailing edge sensors over the angle of attack.	97
5.23. Test aircraft in flight.	99
5.24. Location of the fiber-optic pressure sensors in-flight tests.	101
5.25. Cockpit view on instrumentation.	102
5.26. Static pressure reading of a fiber-optic pressure sensor and a reference sensor at the flap in flight tests.	104
5.27. The quasi-static pressure readings of the reference sensor.	106

List of Figures

5.28. Pressure Coefficient distribution of the airfoil SM701 shortly after take-off.	106
5.29. A static pressure reading of a fiber-optic pressure sensor during flow separation at the flap.	107
5.30. Power spectral density in cruise flight conditions.	108
5.31. Power spectral density in flight conditions with the separated flow.	108
5.32. The noise floor measurement of the system under test and the reference system.	109
5.33. Time-series and spectrogram of three subsequent stall events.	110
5.34. Sensor patch with four sensors and boundary layer rake are instrumented on the flap.	111
5.35. Coherence function of the measurement.	113
5.36. The direction of pressure field propagation and speed during a low-speed maneuver.	114
5.37. Time-series of the pressure sensor mounted in a rake to measure different velocity profiles.	116
5.38. Flow velocity over dynamic pressure for pressure sensors at different elevations from the surface.	116
5.39. Boundary layer thickness measurement on an aircraft with fiber-optic pressure sensors.	117
5.40. Power spectral density measurement of cylindrical sensors in a rake at normal and stalling flight conditions.	119
5.41. Comparison of single-hole probe transfer characteristic between fiber-optic and conventional electrical sensors.	121
5.42. Calibration of fiber-optic probe with flush mounted sensors.	123
5.43. Point cloud of pressure sensor centered at the tip for velocity $Ma = 0,22$	124
5.44. Point cloud of pressure sensors P_2 , P_3 , P_4 and P_5 for velocity $Ma = 0,22$	124
5.46. Difference between measured pressure coefficient distribution of the rotor blade to simulation.	127
5.45. Wind turbine instrumented with two aerodynamic shells, including distributed pressure sensor and probes.	128
5.47. Histogram of the temperature cross-sensitivity in the lab and on the turbine.	130
A1. Power spectral densities of a pressure sensors on the suction side for sensors at $x/c = 0,005$ to $0,042$ at the leading edge.	135
A2. Power spectral densities of a pressure sensors on the suction side for sensors at $x/c = 0,053$ to $0,128$	136
A3. Power spectral densities of a pressure sensors on the suction side for sensors at $x/c = 0,145$ to $0,216$	137
A4. Power spectral densities of a pressure sensors on the suction side for sensors at $x/c = 0,259$ to $0,408$	138
A5. Power spectral densities of a pressure sensors on the suction side for sensors at $x/c = 0,515$ to $0,737$	139

List of Figures

A6.	Power spectral densities of a pressure sensors on the suction side for sensors at $x/c = 0,844$ and $1,000$	140
A7.	Power spectral densities of a pressure sensors on the pressure side for sensors at $x/c = 0,005$ to $0,530$	141
A8.	Power spectral densities of a pressure sensors on the pressure side for sensors at $x/c = 0,630$ and $0,739$	142

List of Tables

2.1. Eigenvalues of the frequency equation 2.86 [37, 144, 200].	43
4.1. Specifications of different fiber-optic pressure sensors. The table summarizes the fundamental mechanical and optical properties of each sensor version. Whereas, the variable $\Delta p/\Delta\lambda$ describes the pressure sensitivity of the transducer, $\Delta L/\Delta p$	55
4.2. Model of the residual temperature cross-sensitivity $\Delta\lambda/\Delta T$	61
4.3. Experimental evaluation of the burst pressure p_{max}	64
4.4. Measurement ranges of the final cylindrical fiber-optic pressure sensing setup.	66
5.1. Aerodynamic key parameters of the experiment [219].	84
5.2. Aerodynamic key parameters of the flight experiment [217].	103
5.3. Aerodynamic key parameters of the wind tunnel experiment for fiber-optic probe [212, 214].	122
.1. Sensor positions in experiment.	134

List of Abbreviations

Abbreviation	Expression
a.u.	Arbitrary unit
ADC	Analog digital converter
AFC	Active flow control
AoA	Angle of attack
<i>BFSL</i>	Best fit straight line
CO ₂	Carbon dioxide
C-band	wavelength range 1530 – 1565 nm
FP	Fabry–Pérot
FBG	Fiber-Bragg-grating
FOPS	Fiber-optic pressure sensing
<i>FSR</i>	Free-Spectral-Range
<i>FWHM</i>	Full-Width-Half-Maximum
GPS	Global positioning system
GroWiKa	”großer Windkanal” (big wind-tunnel)
IWES	Fraunhofer Institute for Wind Energy Systems
LiPo	Lithium polymer battery
MEMS	Micro-Electro-Mechanical system
MST	Institute for Measurement Systems and Sensor Technology
NTP	Network time protocol
PEEK	Polyether ether ketone
PSD	Power-spectral-density
<i>Q</i> -point	Quadrature point
RMS	Root-mean-square
SKOPA	Skin friction and fiber-optics-based surface pressure measurements
SNR	Signal-noise-ratio
TIADE	Turbine Improvements for Additional Energy

List of Symbols

Symbol	Expression
\hat{A}	amplitude
A	area
A_{ref}	reference surface area of the airfoil
a	fiber's radius
a_{acc}	acceleration
\mathcal{A}	absorption
α	angle of attack
α_0	offset of inflow angle
α_{min}	minimal angle of attack
α_{max}	maximal angle of attack
B	photodiode frequency bandwidth
b	spanwise length
β	inflow angle
β_0	offset of inflow angle
β_m	propagation constant for mode m
c	speed of light in a vacuum
C_P	pressure coefficient
C_L	lift coefficient
c_L	sectional lift coefficient
C_D	drag coefficient
$c(x)$	chord section
$C_{1..4}$	unknown constant
c_s	mean velocity of sound
d_{drop}	diameter of a raindrop
δ	decay rate constant
e	exponent
E	Young's module
E	electric field
\hat{E}	amplitude of the electric field
\hat{E}_0	initial amplitude of the electric field
\hat{E}_R	amplitude of the electric field in reflection
\hat{E}_T	amplitude of the electric field in transmission
$\vec{E}(\varphi)$	electric field distribution
E_m	electric field for mode m
E_F	filtering photodetector sensitivity

List of Symbols

E_R	referencing photodetector sensitivity
\mathcal{E}	expectation
ϵ_0	electric constant
f	frequency
f_s	sampling frequency
Δf	frequency resolution
f_0	undamped natural frequency
f_ζ	damped frequency
F_L	lift force
F_D	drag force
F_S	restoring force of a spring
F_{acc}	acceleration force
\mathcal{F}	Fourier operator
FS	Full-Scale
F_{abs}	absolute measurement deviation
F_{rel}	relative measurement deviation
F	finesse coefficient
F	finesse
g	unit[9.81] m/s^2
$G(s)$	transfer function
γ_{XY}	coherence
H	magnetic field
\hat{H}	amplitude of the magnetic field
h	membrane thickness
$H(f)$	transfer function of a probe
I	intensity
\hat{I}_0	initial intensity
\hat{I}_R	intensity in reflection
\hat{I}_T	intensity in transmission
i	unit imaginary number
i_c	photocurrent
J_i	Bessel function of i -th order
k	wavenumber
K	plate stiffness
k_s	spring constant
k_x	sensitivity factor
k_{spring}	spring constant
κ	specific phase displacement
κ_h	specific heat ratio
L	length
L_0	initial resonator length
ΔL	membrane deflection
$\Delta L/\Delta p$	displacement sensitivity

List of Symbols

l	lift force per unit span of the wing
l_c	characteristic length of an airfoil
λ	wavelength
λ_x	eigenvalues
$\Delta\lambda$	Free-Spectral-Range
$\delta\lambda$	Full-Width-Half-Maximum
Λ_0	optical path length
Λ_p	coherence length scale of turbulent structures
M	total amount of samples, size
m	sample, index
M_{FP}	modulation coefficient of the Fabry–Pérot interferometer
Ma	Mach number
m_a	mass of membrane
$m_{\phi\phi,h}$	bending moment
$\dot{m} =$	maximum mass-flow rate through each actuator segment
μ	dynamic viscosity
μ_0	magnetic constant
μ_r	relative magnetic permeability
N	operating order of the Fabry–Pérot interferometer
n	refractive index
ν	Poisson number
NA	numerical aperture
n_{eff}	effective refractive index of a mode
P	polarized direction, perpendicular to the reflecting surface
$P(s)$	Laplace pressure excitation
p	pressure
Δp	pressure difference
$p(t)$	time-variant pressure signal
p_∞	barometric pressure
p_{max}	burst pressure
p_{drop}	pressure of a raindrop
p_{cal}	pressure reference level
$p_{\text{sensor}}(f)$	frequency-depending pressure reading at sensor
$p_{\text{tip}}(f)$	frequency-depending pressure at probe's tip
$\Delta p / \Delta\lambda$	pressure sensitivity
P	power
Pr	Prandtl number
φ	polar angle
ε	relative dielectric permittivity
ϕ	phase of the signal, angle
Φ_c	critical angle for total reflection
Φ_F	illumination intensity of the filtering photodiode
Φ_R	illumination intensity of the referencing photodiode

List of Symbols

q	dynamic pressure
q_r	shear force
r	radius, reflection
r_a	radius of membrane
r_r	regular reflection coefficient
r_d	diffuse reflection coefficient
r_s	reflection coefficient in S -polarized direction
r_p	reflection coefficient in P -polarized direction
$r_T(t)$	rectangular window
$R_{xy}(\tau)$	cross-correlation
$R_{xy}[m]$	discrete cross-correlation
\mathcal{R}	reflection
\mathcal{R}_{FP}	Fabry–Pérot interferometer in reflection
ρ	scalar measurement value
ρ_0	offset of scalar measurement value
ρ_D	membrane material's density
ρ_{RMS}	signal's root-mean-square
ρ_{air}	density of the air
S	polarized direction, parallel to the reflecting surface
S_{XX}	power spectral density
S_{XY}	cross-spectral density
s	Laplace index
σ	boundary layer thickness
σ_{short}	shot noise
σ_X	variance for x
σ_α	x -width of Gaussian bell
σ_β	y -width of Gaussian bell
T	period
t	time, transmission coefficient
t_r	regular transmission coefficient
t_d	diffuse transmission coefficient
t_s	transmission coefficient in S -polarized direction
t_p	transmission coefficient in P -polarized direction
$T.I.$	turbulence intensity
\mathcal{T}	transmission
\mathcal{T}_{FP}	Fabry–Pérot interferometer in transmission
Δt	sampling time
τ	phase delay
τ_m	discrete phase delay
$\Delta\tau$	discrete resolution of phase delay
θ_i	angle of the incident ray
θ_r	angle of the reflection ray
θ_t	angle of the transmitting ray
θ_D	angle of radiation, acceptance angle

List of Symbols

u	flow velocity
u_∞	free stream inflow velocity
u_{RMS}	root-mean-square of the turbulent velocity
V	normalized frequency parameter, so-called V -number
v_{tip}	tip speed
$w(r)$	deflection curve
$w_p(r)$	homogeneous solution for deflection curve
$w_h(r)$	particulate solution for deflection curve
w_G	Gaussian field radius
$w(z)$	field distribution
ω	angular frequency
x	x-coordinate
x/c	chordwise position
$X(s)$	Laplace sensor response
$x(t)$	time-series of signal x
$x[m]$	discrete data of signal x
X_T	Fourier transform of signal x
y	y-coordinate
$y(t)$	time-series of signal y
y/b	relative spanwise position
z	z-coordinate
Z_0	impedance of free space
Δz	separation distance between two sensors
Z_R	Rayleigh distance
ζ	damping

A. Bibliography

A.1. Bibliography

- [1] New research under project TIADE to be tested on prototype wind turbine: LM Wind Power. <https://www.lmwindpower.com/en/stories-and-press/stories/news-from-lm-places/new-research-under-project-TIADE-to-be-tested-on-prototype-wind-turbine>. Accessed: 2021-09-22.
- [2] A. Altmikus, M. Frauenlob, C. Scheit, C. Napierala and C. Frank. WO2019068606A1 - Method for calibrating a pressure sensor on a wind turbine plant and wind turbine plant having an apparatus for calibrating a pressure sensor, May 2017.
- [3] A. Altmikus, M. Kuhn, C. Napierala and J. Stoltenjohannes. WO2015185720 - Wind turbine with optical pressure sensors and method for operating a wind turbine, June 2015.
- [4] A. Cooperman and M. Martinez. Load monitoring for active control of wind turbines. *Renewable and Sustainable Energy Reviews*, 41:189–201, 09 2014.
- [5] A. E. Siegman. *Lasers*. University science books, 1986.
- [6] A. F. Molland and S. R. Turnock. 6 - Theoretical and Numerical Methods. In *Marine Rudders and Control Surfaces*, Seiten 233–311. Butterworth-Heinemann, Oxford, 2007.
- [7] A. Herrig. Validation and Application of a Hot-Wire based Method for Trailing-Edge Noise Measurements on Airfoils. Dissertation, University Stuttgart, 2012.
- [8] A. Herrig, W. Wuerzm, T. Lutz and E. Krämer. Trailing-Edge Noise Measurements Using a Hot-Wire Based Coherent Particle Velocity Method. In *Collection of Technical Papers - AIAA Applied Aerodynamics Conference*, volume 4, 06 2006.
- [9] A. Iele, M. Leone, M. Consales, Giovanni V. Persiano, A. Brindisi, S. Ameduri, A. Concilio, M. Ciminello, A. Apicella, F. Bocchetto and A. Cusano. A fiber optic sensors system for load monitoring on aircraft landing gears. In Kyriacos Kalli, Sinead O. O’Keeffe und Gilberto Brambilla, editors, *Seventh European Workshop on Optical Fibre Sensors*, volume 11199, Seiten 101 – 104. International Society for Optics and Photonics, SPIE, 2019.

A. Bibliography

- [10] A. Li and Y. Zhang. Design and implementation of dual-edge filter demodulation system based on the dual lpfg and embedded technology. In 2013 Third International Conference on Instrumentation, Measurement, Computer, Communication and Control, Seiten 1582–1587, 2013.
- [11] A. Moscardi and D. A. Johnson. A compact in-blade five hole pressure probe for local inflow study on a horizontal axis wind turbine. *Wind Engineering*, 40(4):360–378, 2016.
- [12] A. Ning and K. Dykes. Understanding the benefits and limitations of increasing maximum rotor tip speed for utility-scale wind turbines. In *Journal of Physics: Conference Series*, volume 524, Seite 012087. IOP Publishing, 2014.
- [13] A. Pätzold, I. Peltzer and W. Nitsche. *Sensors and Actuators for Laminar Flow Flight Experiments*, Seiten 331–340. Springer Berlin Heidelberg, Berlin, Heidelberg, 2013.
- [14] A. Sathe, J. Mann, T. Barlas, W. A. A. M. Bierbooms, and G. J. W. van Bussel. Influence of atmospheric stability on wind turbine loads. *Wind Energy*, 16(7):1013–1032, 2013.
- [15] A. Suryadi. Prediction of trailing-edge noise for separated turbulent boundary layers. In 21. DGLR-Fach-Symposium der STAB, Seiten 186–187, 11 2018.
- [16] B. Souza Heinzelmann. *Strömungsbeeinflussung bei Rotorblättern von Windenergieanlagen mit Schwerpunkt auf Grenzschichtabsaugung*. Doctoral thesis, Technische Universität Berlin, Fakultät V - Verkehrs- und Maschinensysteme, Berlin, 2011.
- [17] J. S. Bendat und A. G. Piersol. *Random Data: Analysis and Measurement Procedures*. Wiley Series in Probability and Statistics. Wiley, 2011.
- [18] T. Buck. *Untersuchungen zur Erfassung dynamischer Messgrößen mittels Faser-Bragg-Gitter-Messtechnik*. Dissertation, Technische Universität München, 2012.
- [19] C. Bak, H. A. Madsen, U. Schmidt Paulsen, G. Mac Gaunaa, P. Fuglsang, J. Romblad, N. A. Olesen, P. Enevoldsen, J. Laursen and L. Jensen. DAN-AERO MW: Detailed aerodynamic measurements on a full scale MW wind turbine. In *EWEC 2010 Proceedings online*. European Wind Energy Association (EWEA), 2010. 2010 European Wind Energy Conference and Exhibition, EWEC 2010; Conference date: 20-04-2010 Through 23-04-2010.
- [20] C. Doolan, D. Moreau and L. Brooks. Wind turbine noise mechanisms and some concepts for its control. *Acoustics Australia / Australian Acoustical Society*, 40:7–13, 04 2012.

A. Bibliography

- [21] C. Hansen and K. Hansen. Recent Advances in Wind Turbine Noise Research. *Acoustics*, 2(1):171–206, 2020.
- [22] C. Hornung, C. Scheit, C. Napierala, M. Arnold, D. Bekiropoulos, A. Altmikus and T. Lutz. Predicted and Measured Trailing-Edge Noise Emission for a 2.3 MW Wind Turbine. 7th International Conference on Wind Turbine Noise, 05 2017.
- [23] C. Lai, Y. Lo, J. Yur and C. Chuang. Application of Fiber Bragg Grating Level Sensor and Fabry-Pérot Pressure Sensor to Simultaneous Measurement of Liquid Level and Specific Gravity. *IEEE Sensors Journal*, 12(4):827–831, 2012.
- [24] C. P. Butterfield, M. D Jenks, D. A. Simms and W. P. Musial. Aerodynamic pressure measurements on a rotating wind turbine blade. Technical report, Solar Energy Research Inst.(SERI), Golden, CO (United States), 1990.
- [25] R. B. Bhat C. Rajalingham und G. D. Xistris. Vibration of circular membrane backed by cylindrical cavity. *International Journal of Mechanical Sciences*, 40(8):723–734, 1998.
- [26] C. Zhou, S. V. Letcher and A. Shukla . Fiber-optic Microphone based on a Combination of Fabry–Perot Interferometry and Intensity Modulation. *The Journal of the Acoustical Society of America*, 98(2):1042–1046, 1995.
- [27] P. E. Ciddor. Refractive index of air: New equations for the visible and near infrared. *Applied Optics*, 35(9):1566–1573, March 1996.
- [28] Clean Sky 2 JU. CleanSky 2 Joint Undertaking - Development Plan. <https://www.clean-aviation.eu/sites/default/files/2022-03/CS2DP-October-2021.pdf>. Accessed: 2022-12-06.
- [29] Corning Incorporated. Datasheet Corning ClearCurve ZBL Optical Fiber. Technical report, Corning Incorporated, One Riverfront Plaza, Corning, NY 14831 USA, 07 2014.
- [30] D. A. Krohn, T. MacDougall and A. Mendez. Fiber optic sensors: Fundamentals and applications: Fourth edition. 01 2015.
- [31] D. Castagnet, J. J. Wedel-Heinen , T. Kim, T. Buhl and N. Poulsen. Results from the First Full Scale Wind Turbine Equipped with Trailing Edge Flaps.
- [32] D. Homentcovschi and R. N. Miles. Modeling of viscous damping of perforated planar microstructures. Applications in acoustics. *The Journal of the Acoustical Society of America*, 116(5):2939–2947, 2004.
- [33] D. Schwab. Aerodynamische Grenzschichtuntersuchungen an einem Windturbinenblatt im Feldversuch. Doctoral thesis, Helmut-Schmidt-Universität / Universität der Bundeswehr Hamburg, Berlin, 2019.

A. Bibliography

- [34] D. Somers and M. Maughmer. The sm701 airfoil: An air foil for world class sailplanes. *Technical Soaring*, 16(3):70–77, 1992.
- [35] D. X. He and Y. Li. *Overview of Worldwide Wind Power Industry*, Seiten 29–60. Springer Singapore, Singapore, 2020.
- [36] E. A. Bossanyi. Individual blade pitch control for load reduction. *Wind Energy*, 6(2):119–128, 2003.
- [37] E. A. Witmer. *Elementary Bernoulli-Euler Beam Theory*. MIT Unified Engineering Course Notes, MIT, 1992:114–164, 1991.
- [38] E. Chehura, S. W. James, N. Lawson, K. P. Garry and R. P. Tatam. Pressure measurements on aircraft wing using phase-shifted fibre Bragg grating sensors. In Julian D. C. Jones, editor, *20th International Conference on Optical Fibre Sensors*, volume 7503, Seiten 454 – 457. International Society for Optics and Photonics, SPIE, 2009.
- [39] E. D. Palik, H. Boukari and R. W. Gammon. Experimental study of the effect of surface defects on the finesse and contrast of a fabry–perot interferometer. *Applied Optics*, 35(1):38–50, Jan 1996.
- [40] E. Hecht. *Optics*. Pearson, 2012.
- [41] E. Vorathin, Z.M. Hafizi, N. Ismail and M. Loman. Review of high sensitivity fibre-optic pressure sensors for low pressure sensing. *Optics & Laser Technology*, 121:105841, 2020.
- [42] Epoxy technology, Inc. Datasheet EPO-TEK 353ND. Technical report, Epoxy technology, Inc., 14 Fortune Drive, Billerica, MA 01821 USA , 02 2021.
- [43] F. Boden, N. Lawson, H. Jentink and J. Kompenhans. *Advanced In-Flight Measurement Techniques*. 01 2013.
- [44] F. Lechner. *Untersuchung zu Temperaturquerempfindlichkeiten und Drifteigenschaften eines Fabry-Pérot Drucksensors mit einem Kantenfiltermessgerät*. Master Thesis, 2021.
- [45] F. Puente León. *Messtechnik - Grundlagen, Methoden und Anwendungen*. Vieweg Verlag, 11. aufl. edition, 2019.
- [46] F. Stoliker. *Introduction to flight test engineering, flight test techniques series – volume 14*. Seite 455, 07 2005.
- [47] F. U. Mathiak. *Ebene Flächentragwerke 2 - Grundlagen der Plattentheorie*, 2008. Fachhochschule Neubrandenburg.
- [48] First Sensor. Datasheet Miniature Amplified Low Pressure Sensors HCLA - E / 11629 / G. Technical report, First Sensor.

A. Bibliography

- [49] Fläming Air GmbH. Flug- und Wartungshandbuch für das Ultraleichtflugzeug Peregrine SL. Technical report, Fläming Air GmbH, Am Flugplatz 2, 14913 Niedergörsdorf OT Zellendorf, 11 2019.
- [50] G. C. Hill, R. Melamud, F. E. Declercq, A. A. Davenport, I. H. Chan, P. G. Hartwell and B. L. Pruitt. SU-8 MEMS Fabry-Perot pressure sensor. *Sensors and Actuators A: Physical*, 138(1):52–62, 2007.
- [51] G. Duthé, I. Abdallah, S. Barber and E. Chatzi. Modeling and Monitoring Erosion of the Leading Edge of Wind Turbine Blades. *Energies*, 14(21), 2021.
- [52] G. E. Miller. Fiber Optic Sensors For Aircraft. In Ramon P. DePaula und Eric Udd, editors, *Fiber Optic and Laser Sensors VI*, volume 0985, Seiten 20 – 25. International Society for Optics and Photonics, SPIE, 1989.
- [53] G. Mac and P. B. Andersen. Load reduction using pressure difference on airfoil for control of trailing edge flaps. In *EWEC 2009 Proceedings online*. EWEC, 2009. 2009 European Wind Energy Conference and Exhibition, EWEC 2009 ; Conference date: 16-03-2009 Through 19-03-2009.
- [54] G. Rajan, Q. Wang, G. Farrell, Y. Semenova and P. Wang. Effect of SNR of input signal on the accuracy of a ratiometric wavelength measurement system. *Microwave and Optical Technology Letters*, 49(5):1022–1024, 2007.
- [55] G. Rajan, Q. Wang, Y. Semenova, G. Farrell and P. Wang. Effect of polarisation-dependent loss on the performance accuracy of a ratiometric wavelength measurement system. *IET Optoelectronics*, 2(2):63–68, 2008.
- [56] G. Wu, L. Zhang and K. Yang. Development and Validation of Aerodynamic Measurement on a Horizontal Axis Wind Turbine in the Field. *Applied Sciences*, 9(3), 2019.
- [57] G. Z. Xiao, A. Adnet, Z. Zhang, F. G. Sun and C. P. Grover. Monitoring changes in the refractive index of gases by means of a fiber optic fabry-perot interferometer sensor. *Sensors and Actuators A: Physical*, 118(2):177–182, 2005.
- [58] G. Zhang, Q. Yu and S. Song. An investigation of interference/intensity demodulated fiber-optic Fabry-Perot cavity sensor. *Sensors and Actuators A: Physical*, 116(1):33–38, 2004.
- [59] T. B. Gabrielson. Mechanical-thermal noise in micromachined acoustic and vibration sensors. *IEEE Transactions on Electron Devices*, 40(5):903–909, 1993.
- [60] K. Girkmann. Einführung in die Elastostatik der Scheiben, Platten, Schalen und Faltwerke, 1954.

A. Bibliography

- [61] GRAS Sound And Vibration. GRAS 42AG, Multifunction Sound Calibrator, Class 1. Technical report, GRAS Sound And Vibration, Skovlytoften 33, 2840 Holte, Denmark, 03 2022.
- [62] H. A. Madsen, C. Bak, P. Schmidt, M. Gaunaa, P. Fuglsang, J. Romblad, N. A. Olesen, P. Enevoldsen, J. Laursen and L. Jensen. The DAN-AERO MW experiments. Final report. Technical report, Technical University of Denmark, Risoe National Lab for Sustainable Energy, 09 2010.
- [63] H. A. Madsen, H. Bertagnolio, A. Fischer, C. Bak, U. Schmidt Paulsen. A novel full scale experimental characterization of wind turbine aero-acoustic noise sources - preliminary results. In Proceedings of the International Symposium on Transport Phenomena and Dynamics of Rotating Machinery, ISROMAC 2016, 04 2016. 16th International Symposium on Transport Phenomena and Dynamics of Rotating Machinery.
- [64] H. Altenbach, J. Altenbach and K. Naumenko. Ebene Flächentragwerke: Grundlagen der Modellierung und Berechnung von Scheiben und Platten, 2016.
- [65] H. Babinsky, U. Kuschel, H. P. Hodson, D. F. Moore and M. E. Welland. The aerodynamic design and use of multi-sensor pressure probes for MEMS applications. In XVth Bi-Annual Symposium on Measuring Techniques in Transonic and Supersonic Flows in Cascades and Turbomachines, 09 2000.
- [66] H. Bergh and H. Tijdeman. Theoretical and experimental results for the dynamic response of pressure measuring systems. F.: Nationaal Lucht- en Ruimtevaartlaboratorium. Nationaal lucht- en ruimtevaartlaboratorium, 1965.
- [67] H. E. Fiedler. Coherent structures in turbulent flows. Progress in Aerospace Sciences, 25(3):231–269, 1988.
- [68] H. J. Konle, C. O. Paschereit and I. Röhle. Application of Fiber-Optical Microphone for Thermo-Acoustic Measurements. Journal of Engineering for Gas Turbines and Power, 133(1), 09 2010. 011602.
- [69] H. J. T. Kooijman. Bending-torsion coupling of a wind turbine rotor blade, Dec 1996.
- [70] R. Mastel H. Jäger und Manfred M. Knaebel. Technische Schwingungslehre, volume 8. Springer, 2013.
- [71] H. M. Chan and A. R. Parker, A. Piazza and W. L. Richards. Fiber-optic sensing system: Overview, development and deployment in flight at NASA. In 2015 IEEE Avionics and Vehicle Fiber-Optics and Photonics Conference (AVFOP), Seiten 71–73, 2015.

A. Bibliography

- [72] H. M. Hashemian, C. L. Black and J. P. Farmer. Assessment of fiber optic pressure sensors, 1995.
- [73] H. P. A. H. Irwin, K.R. Cooper and R. Girard. Correction of distortion effects caused by tubing systems in measurements of fluctuating pressures. *Journal of Wind Engineering and Industrial Aerodynamics*, 5(1):93–107, 1979.
- [74] H. Rahimi, J. G. Schepers, W. Z. Shen, N. Ramos García, M. S. Schneider, D. Micallef, C. J. Simao Ferreira, E. Jost, L. Klein and I. Herráez. Evaluation of different methods for determining the angle of attack on wind turbine blades with cfd results under axial inflow conditions. *Renewable Energy*, 125:866–876, 2018.
- [75] H. Schlichting and E. Truckenbrodt. *Inkompressible reibungslose Strömungen (Hydrodynamik)*. In *Aerodynamik des Flugzeuges*, Seiten 22–142. Springer, 2001.
- [76] Halstrup-Walcher. Data sheet KAL 100/200 Series 3. Technical report, Halstrup-Walcher, One Riverfront Plaza, Corning, NY 14831 USA, 08 2022.
- [77] Hottinger Brüel and Kjaer GmbH. Datasheet HBM QuantumX MX1615B. Technical report, Hottinger Brüel and Kjaer GmbH, Im Tiefen See 45, 4293 Darmstadt, 08 2021.
- [78] I. Cotton. IEC 61400-24 Lightning Protection For Wind Turbines, May 2002. Lightning Protection Conference; Conference date: 01-01-1824.
- [79] I. Goold. Exclusive insight from the program leaders about Airbus’s innovative test campaign. *Aerospace Testing International*, Seiten 24 – 30, 2018.
- [80] I. Kressel, A. Handelman, Y. Botsev, J. Balter, P. Gud’s, M. Tur, S. Gali, A. C. R. Pillai, M. H. Prasad, A. K. Yadav, N. Gupta, S. Sathya and Sundaram, R. Health and Usage Monitoring of Unmanned Aerial Vehicles Using Fiber-Optic Sensors. In Jerzy Komorowski, editor, *ICAF 2011 Structural Integrity: Influence of Efficiency and Green Imperatives*, Seiten 465–471, Dordrecht, 2011. Springer Netherlands.
- [81] I. N. Bronstein, K. A. Semendjajew, and G. Musiol. *Taschenbuch der Mathematik*, m. CD-ROM. Deutsch (Harri), 2008.
- [82] ICP Deutschland GmbH. Datasheet DRPC-100-CV DRPC-120-BT. Technical report, ICP Deutschland GmbH, 08 2016.
- [83] imc Test and Measurement GmbH. imc CANSASflex-UNI8, Datenblatt Version 1.7 - 01.12.2020. Technical report, imc Test and Measurement GmbH, Max-Planck-Straße 22B, 61381 Friedrichsdorf.

A. Bibliography

- [84] IMV Corporation. Low Acoustic Noise and Compact Range Air Cooled Vibration Test Systems - m060 / MA1CE. Technical report, IMV Corporation, 11520 Blair St., Holland, MI 49424 USA, 02 2020.
- [85] LUNA Inc. SI155 Hyperion Optical Sensing Instrument, REV.2 02.15.19. Technical report, LUNA Inc., 2019.
- [86] IRENA. Future of wind: Deployment, investment, technology, grid integration and socio-economic aspects (a global energy transformation paper). Technical report, International Renewable Energy Agency, 2019.
- [87] Adhesives — Guide to the selection of standard laboratory ageing conditions for testing bonded joints. Standard, International Organization for Standardization, 03 2003.
- [88] Fraunhofer IWES. HighRe: Aerodynamik bei hohen Reynoldszahlen für große Offshore-Windenergieanlagen der Zukunft. <https://www.iwes.fraunhofer.de/de/forschungsprojekte/aktuelle-projekte/highre.html>, December 2022. Accessed: 2022-12-06.
- [89] J. Castracane, L. P. Clow Jr. and G. Seidler. Optical multichannel transducer array for wind tunnel applications. *Optical Engineering*, 35(9):2627 – 2633, 1996.
- [90] J. E. Alfonso, L. G. Cárdenas, C. A. Triana and M. V. Durán. Design of an optical sensing interrogator using an edge filter scheme. In 2013 SBMO/IEEE MTT-S International Microwave & Optoelectronics Conference (IMOC), Seiten 1–5, 2013.
- [91] J. Eom, C. Park, B. Ha Lee, J. Lee, I. Kwon and E. Chung. Fiber optic Fabry–Perot pressure sensor based on lensed fiber and polymeric diaphragm. *Sensors and Actuators A: Physical*, 225:25–32, 2015.
- [92] J. F. Kirkegaard. Very Large Offshore Blade Challenges. IWES Virtual Wind, IWES Virtual Wind, 2020.
- [93] J. G. Schepers and S. J. Schreck. Aerodynamic measurements on wind turbines. *WIREs Energy and Environment*, 8(1):e320, 2019.
- [94] S. Silva J. G. V. Teixeira, I. T. Leite und Orlando O. Frazão. Advanced fiber-optic Acoustic Sensors. *Photonic Sensors*, 4(3):198–208, 2014.
- [95] J. Gottmann, M. Hermans and J. Ortmann. Microcutting and hollow 3d microstructures in glasses by in-volume selective laser-induced etching (isle). *Journal of Laser Micro Nanoengineering*, 8(1):15, 2013.
- [96] J. J. Bertin and R. M. Cummings. *Aerodynamics for Engineers*. Cambridge University Press, 6 edition, 2021.

A. Bibliography

- [97] J. Kurelek, M. Kotsonis and S. Yarusevych. Transition in a separation bubble under tonal and broadband acoustic excitation. *Journal of Fluid Mechanics*, 853:1–36, 10 2018.
- [98] J. L. Elster, A. Trego, C. Catterall, J. Averett, M. E. Jones, M. K. Evans and B. Fielder. Flight demonstration of fiber optic sensors. In Daniele Inaudi und Eric Udd, editors, *Smart Structures and Materials 2003: Smart Sensor Technology and Measurement Systems*, volume 5050, Seiten 34 – 42. International Society for Optics and Photonics, SPIE, 2003.
- [99] J. L. Miller, E. Friedman, J. N. Sanders-Reed, K. Schwertz and B. McComas. *Photonics Rules of Thumb*. Number PUBDB-2021-03249. SPIE Press Bellingham, Washington, 2020.
- [100] J. Lee and F. Zhao. *Gwec | global wind report 2022*). Technical report, Global Wind Energy Council, 2022.
- [101] J. Li and X. Zhang. Active flow control for supersonic aircraft: A novel hybrid synthetic jet actuator. *Sensors and Actuators A: Physical*, 302:111770, 2020.
- [102] J. Li, P. Jia, G. Fang, J.n Wang, J. Qian, Q. Ren and J. Xiong. Batch-producible all-silica fiber-optic Fabry–Perot pressure sensor for high-temperature applications up to 800 °C. *Sensors and Actuators A: Physical*, 334:113363, 2022.
- [103] J. Strike, M. Hind, M. Saini, J. Naughton, M. Wilson and S. Whitmore. Unsteady Surface Pressure Reconstruction on an Oscillating Airfoil Using the Wiener Deconvolution Method.
- [104] J. W. Borinski, S. A. Meller, W. J. Pulliam, K. A. Murphy and J. Schetz. Aircraft health monitoring using optical fiber sensors. In 19th DASC. 19th Digital Avionics Systems Conference. Proceedings (Cat. No.00CH37126), volume 2, Seiten 6D1/1–6D1/8 vol.2, 2000.
- [105] J. Yin, T. Liu, J. Jiang, K. Liu, S. Wang, S. Zou and Z. Qin and Z. Ding. Self-Referenced Residual Pressure Measurement Method for Fiber-Optic Pressure Sensor Chip. *IEEE Photonics Technology Letters*, 26(10):957–960, 2014.
- [106] J. Zayas, C. Dam, R. Chow, J. Baker and E. Mayda. *Active Aerodynamic Load Control of Wind Turbine Blades*. volume 1, 01 2007.
- [107] K. Burg, H. Haf, F. Wille and A. Meister. *Höhere Mathematik für Ingenieure Band III: Gewöhnliche Differentialgleichungen, Distributionen, Integraltransformationen*. Springer-Verlag, 2010.
- [108] K. Chen, Z. Gong, M. Guo, S. Yu, C. Qu, X. Zhou and Q. Yu. Fiber-optic fabry-perot interferometer based high sensitive cantilever microphone. *Sensors and Actuators A: Physical*, 279:107–112, 2018.

A. Bibliography

- [109] K. H. Grote and E. K. Antonsson. Springer handbook of mechanical engineering, volume 10. Springer, 2009.
- [110] Kulite Semiconductor Products, Inc. Datasheet Thin Line Pressure Transducer LQ-080 Series, LQ-125 Series. Technical report, Kulite Semiconductor Products, Inc., One Willow Tree Road, Leonia, New Jersey 07605, USA.
- [111] Kulite Semiconductor Products, Inc. Datasheet Thin Line Pressure Transducer XT-140 Series, XT-140 Series. Technical report, Kulite Semiconductor Products, Inc., One Willow Tree Road, Leonia, New Jersey 07605, USA.
- [112] L. Fingersh and M. Robinson. Wind tunnel calibration of 5-hole pressure probes for application to wind turbines. In 35th aerospace sciences meeting and exhibit, Seite 854, 1998.
- [113] B. F. Skipper L. Glavind, I. S. Olesen und M. V. Kristensen. Fiber-optical grating sensors for wind turbine blades: A review. *Optical Engineering*, 52(3):1 – 10, 2013.
- [114] L. H. Hoffmann. Spektroskopische Instrumente zur Demodulation von Faser-Bragg-Gitter-Sensorsignalen. Dissertation, Technische Universität München, München, 2008.
- [115] L. Li, H. Jiang and Y. Hu. Feasibility study of fiber bragg grating sensor for strain measurement in flight test. In 2021 IEEE 15th International Conference on Electronic Measurement Instruments (ICEMI), Seiten 490–495, 2021.
- [116] L. Lohr. Simulation und Optimierung eines faseroptischen Fabry-Pérot-Sensors in Kombination mit einem kantenfilterbasiertem Interrogator. Master Thesis, 2020.
- [117] L. P. Melton, N. W. Schaeffler, C. Yao, and A. Seifert, Avi. Active control of flow separation from supercritical airfoil leading-edge flap shoulder. *Journal of Aircraft*, 42(5):1142–1149, 2005.
- [118] L. Papula. *Mathematik für Ingenieure und Naturwissenschaftler Band 2*. Springer, 2009.
- [119] M. Bauer. Design and application of a fluidic actuator system for high lift flow control. Doctoral Thesis, Technische Universität Berlin, Fakultät V - Verkehrs- und Maschinensysteme, Berlin, 2015.
- [120] M. Bauer, J. Lohse, F. Haucke and W. Nitsche. High-Lift Performance Investigation of a Two-Element Configuration with a Two-Stage Actuator System. *AIAA Journal*, 52(6):1307–1313, 2014.
- [121] M. Bauer, T. Grund and W. Nitsche. Experiments on Active Drag Reduction on a Complex Outer Wing Model. *AIAA Journal*, 53(7):1774–1783, 2015.

A. Bibliography

- [122] M. Bauer, T. Grund, W. Nitsche and V. Ciobaca. Wing Tip Drag Reduction at Nominal Take-Off Mach Number: An Approach to Local Active Flow Control with a Highly Robust Actuator System. *Aerospace*, 3(4), 2016.
- [123] M. Born and E. Wolf. *Principles of Optics*. sixth (corrected) edition, 1997.
- [124] M. DeSalvo, E. Whalen and A. Glezer. High-Lift Performance Enhancement Using Active Flow Control. *AIAA Journal*, 58(10):4228–4242, 2020.
- [125] M. Drela. XFOIL: An Analysis and Design System for Low Reynolds Number Airfoils. volume 54, 06 1989.
- [126] M. Girfoglio, C. Salvatore Greco, M. Chiatto and L. de Luca. Modelling of Efficiency of Synthetic Jet Actuators. *Sensors and Actuators A: Physical*, 233:512–521, 2015.
- [127] M. H. Tanielian. MEMS multisensor system for flight testing. In Henry Helvajian, Siegfried W. Janson und Franz Laermer, editors, *MEMS Components and Applications for Industry, Automobiles, Aerospace, and Communication*, volume 4559, Seiten 120 – 129. International Society for Optics and Photonics, SPIE, 2001.
- [128] M. Hermans, J. Gottmann and F. Riedel. Selective, laser-induced etching of fused silica at high scan-speeds using koh. *Journal of Laser Micro/Nanoengineering*, 9(2), 2014.
- [129] M. J. Gander, W. N. MacPherson, J. S. Barton, R.L. Reuben, J. D. C. Jones, R. Stevens, K. S. Chana, S. J. Anderson and T. V. Jones. Embedded micromachined fiber-optic Fabry-Perot pressure sensors in aerodynamics applications. *IEEE Sensors Journal*, 3(1):102–107, 2003.
- [130] M. J. Schmid. Untersuchungen zur industriellen faseroptischen Blattlastmessung an Windenergieanlagen. Dissertation, Technische Universität München, München, 2018.
- [131] M. J. Schmid, B. A. Kuhnle, M. S. Müller, C. F. Napierala, and A. Altmikus. Validation of highly dynamic fiber optic wall pressure sensors in wind tunnel experiments. In *EWEA 2016 - WindEurope Summit 2016 Conference*, 27.-29.09.2016, Hamburg, 09 2016.
- [132] M. J. Schmid, M. S. Müller, B. A. Kuhnle, M. W. Bauer, R. Pongratz, and A. Altmikus. Fiber optic acoustic pressure sensor with high dynamic range and low noise. In *ETC2016 - 36th European Telemetry and Test Conference*, 10.-12.05.2016, Nürnberg, May 2016.
- [133] M. Jeong, I. Lee, S. Yoo and K. Park. Torsional Stiffness Effects on the Dynamic Stability of a Horizontal Axis Wind Turbine Blade. *Energies*, 6(4):2242–2261, 2013.

A. Bibliography

- [134] M. Mai. Entwurf eines faseroptischen Drucksensors in Mikrochip-Technologie. Bachelor Thesis, 2014.
- [135] M. Maizi, R. Dizene, and M. Mohamed Cherif. Reducing Noise Generated from a Wind Turbine Blade by Pitch Angle Control using CFD and Acoustic Analogy. *Journal of Applied Fluid Mechanics*, 10:1201–1209, 07 2017.
- [136] M. P. Norton and D. G. Karczub. *Fundamentals of noise and vibration analysis for engineers*. Cambridge university press, 2003.
- [137] M. P. Sanders, L. D. de Santana, M. Azarpeyvand and C. H. Venner. Unsteady Surface Pressure Measurements on Trailing Edge Serrations Based on Digital MEMS Microphones. In *2018 AIAA/CEAS Aeroacoustics Conference*, 2018.
- [138] M. Staats and J. Weiss. Measuring wall shear stress in direction and magnitude. In *Aerospace Europe Conference*, 2020.
- [139] M. Staats, S. Löffler, C. Ebert, T. Grund and J. Weiss. A Fluidic Device for Active Flow Control: Simulation vs. Experiment with Emphasis on Application. In *2018 Applied Aerodynamics Conference*, 2018.
- [140] M. Staats, W. Nitsche, I. Peltzer. Active flow control on a highly loaded compressor cascade with non-steady boundary conditions. In R. King, editor, *Active Flow and Combustion Control 2014*, Seiten 23–37, Cham, 2015. Springer International Publishing.
- [141] M. Swoboda and W. Nitsche. *Strömungsmesstechnik*. Springer-Lehrbuch. Springer Berlin Heidelberg, 2013.
- [142] M.d Kamruzzaman, D. Bekiropoulos, A. Wolf, T. Lutz and E. Kraemer. Rnoise: A RANS Based Airfoil Trailing-edge Noise Prediction Model.
- [143] N. A. Hall, M. Okandan, R. Littrell, B. Bicen and F. L. Degertekin. Simulation of thin-film damping and thermal mechanical noise spectra for advanced micro-machined microphone structures. *Journal of Microelectromechanical Systems*, 17(3):688–697, 2008.
- [144] N. H. Asmar. *Partial differential equations with Fourier series and boundary value problems*. Courier Dover Publications, 2016.
- [145] N. J. Lawson, R. Correia, S. W. James, M. Partridge, S. E. Staines, J. E. Gautrey, K. P. Garry, J. C. Holt and R. P. Tatam. Development and application of optical fibre strain and pressure sensors for in-flight measurements. *Measurement Science and Technology*, 27(10):104001, sep 2016.
- [146] O. A. Bauchau and J. I. Craig. *Kirchhoff Plate Theory*, Seiten 819–914. Springer Netherlands, Dordrecht, 2009.

A. Bibliography

- [147] O. Şener, T. Farsadi, M. Ozan Gözcü and A. Kayran. Evaluation of the Effect of Spar Cap Fiber Angle of Bending–Torsion Coupled Blades on the Aero-Structural Performance of Wind Turbines. *Journal of Solar Energy Engineering*, 140(4), 03 2018. 041004.
- [148] O. Rediniotis, E. Johansen, T. Tsao, A. Seifert and L. Pack. MEMS-based probes for velocity and pressure measurements in unsteady and turbulent flow-fields.
- [149] O. Rediniotis, R. Allen, M. Zeiger and E. Johansen. Embedded-Sensor, Fast-Response Multi-Hole Probes.
- [150] P. Dees. A new airfoil optimized for light aircraft performance. Technical report, SAE Technical Paper, 2001.
- [151] P. Kupferschmied, P. Köppel, W. Gizzi, C. Roduner and G. Gyarmathy. Time-resolved flow measurements with fast-response aerodynamic probes in turbomachines. *Measurement Science and Technology*, 11:1036, 06 2000.
- [152] P. Medina, M. Singh, J. Johansen, A. R. A Rivera, E. Machefaux, L. J. Fingersh, and S. Schreck. Aerodynamic and Performance Measurements on a SWT-2.3-101 Wind Turbine. Technical report, National Renewable Energy Lab.(NREL), Golden, CO (United States), 2011.
- [153] P. Roriz, O. Frazão, A. B. Lobo-Ribeiro, J. L. Santos and J. A. Simoes. Review of fiber-optic pressure sensors for biomedical and biomechanical applications. *Journal of Biomedical Optics*, 18(5):050903, 2013.
- [154] P. Schloesser, V. Soudakov, M. Bauer and J. Wild. Active Separation Control at the Pylon-Wing Junction of a Real-Scale Model. *AIAA Journal*, 57(1):132–141, 2019.
- [155] C. A. Paget und C. Bockenheimer. Validation, verification and implementation of shm at airbus. 2014.
- [156] Polytech Wind Power Germany GmbH. Datasheet fos4Pressure, Sensor SEN0227. Technical report, Polytech Wind Power Germany GmbH, 2021.
- [157] Polytech Wind Power Germany GmbH. Datasheet fos4Pressure, Sensor SEN0571. Technical report, Polytech Wind Power Germany GmbH, 2021.
- [158] Polytech Wind Power Germany GmbH. Redhawk. Technical report, Polytech Wind Power Germany GmbH, 06 2021.
- [159] Q. Liu, Z. Jing, Y. Liu, A. Li, Z. Xia and W. Peng. Multiplexing fiber-optic Fabry–Pérot acoustic sensors using self-calibrating wavelength shifting interferometry. *Optical Express*, 27(26):38191–38203, Dec 2019.

A. Bibliography

- [160] Q. Yu and X. Zhou. Pressure sensor based on the fiber-optic extrinsic fabry-pérot interferometer. *Photonic Sensors*, 1(1):72–83, 2011.
- [161] R. Di Sante. Fibre Optic Sensors for Structural Health Monitoring of Aircraft Composite Structures: Recent Advances and Applications. *Sensors*, 15(8):18666–18713, 2015.
- [162] R. E. Bicking. Pressure sensor technology. *Sensors*, 1998.
- [163] R. Fischer, H. Mueller, T. Polonelli, L. Benini, and M. Magno. WindNode: A Long-Lasting And Long-Range Bluetooth Wireless Sensor Node for Pressure and Acoustic Monitoring on Wind Turbines. In 2021 4th IEEE International Conference on Industrial Cyber-Physical Systems (ICPS), Seiten 393–399, 2021.
- [164] R. Haindl, S. Preisser, M. Andreana, W. Rohringer, C. Sturtzel, M. Distel, Z. Chen, E. Rank, B. Fischer, W. Drexler and M. Liu. Dual modality reflection mode optical coherence and photoacoustic microscopy using an akinetic sensor. *Optical Letters*, 42(21):4319–4322, Nov 2017.
- [165] R. McKenna, P. Ostman v.d. Leye and W. Fichtner. Key challenges and prospects for large wind turbines. *Renewable and Sustainable Energy Reviews*, 53:1212–1221, 2016.
- [166] R. Sankaran and E.D. Jancauskas. Measurements of Cross-correlation in Separated Flows around bluff Cylinders. *Journal of Wind Engineering and Industrial Aerodynamics*, 49(1):279–288, 1993.
- [167] R. Schmit, C. McGaha, J. Tekell, J. Grove and M. Stanek. Performance Results for the Optical Turbulence Reduction Cavity.
- [168] R. W. Ainsworth and R. J. Miller and R. W. Moss and S. J. Thorpe. Unsteady pressure measurement. *Measurement Science and Technology*, 11(7):1055–1076, June 2000.
- [169] R. Williams. Fiber Optics - Advances in Fiber-optic Sensor Systems are offering test engineers the Opportunity to Measure and Record in new Ways and Environments. <https://www.aerospacetestinginternational.com/wp-content/uploads/archive-issues/march-2018.pdf>, 2018. Accessed: 2022-12-07.
- [170] C. Raab und K. Rohde-Brandenburger. In-Flight Testing of MEMS Pressure Sensors for Flight Loads Determination. *AIAA Scitech 2020 Forum*, Seite 512, 2020.
- [171] G. Rajan. *Optical Fiber Sensors: Advanced Techniques and Applications*. CRC Press, 2017.
- [172] S. B. Anderson. Historical Overview of Stall/Spin Characteristics of General Aviation Aircraft. *Journal of Aircraft*, 16(7):455–461, 1979.

A. Bibliography

- [173] S. Barber, J. Deparday, Y. Marykovskiy, E. Chatzi, I. Abdallah, G. Duthé, M. Magno, T. Polonelli, R. Fischer and H. Müller, . Development of a wireless, non-intrusive, MEMS-based pressure and acoustic measurement system for large-scale operating wind turbine blades. *Wind Energy Science Discussions*, 2022:1–25, 2022.
- [174] S. Ghildiyal, R. Balasubramaniam and J. John. Effect of flatness and parallelism errors on fiber optic fabry perot interferometer of low to moderate finesse and its experimental validation. *Optical Fiber Technology*, 60:102372, 2020.
- [175] S. J. Houston, R. O. Walton and B. A. Conway. Analysis of General Aviation Instructional Loss of Control Accidents. *Journal of Aviation/Aerospace Education and Research*, 22(1), 2012.
- [176] S. Pettinato, D. Baretin, V. Sedov, V. Ralchenko and S. Salvatori. Fabry-Perot Pressure Sensors Based on Polycrystalline Diamond Membranes. *Materials*, 14(7), 2021.
- [177] S. Timoshenko and S. Woinowsky-Krieger. *Theory of Plates and Shells*, volume 2. McGraw-hill New York, 1959.
- [178] S. U. Kienitz. Kennlinienoptimierung eines Fabry-Pérot Drucksensors. Master Thesis, 2017.
- [179] S. U. Kienitz. Entwicklung, Aufbau und Optimierung eines differentiellen, faseroptischen Drucksensors basierend auf dem Fabry-Pérot und dessen Einsatz in einer instationären Mehrlochsonde. Master Thesis, 2019.
- [180] S. Wang, L. Baldas, S. Colin, S. Orioux, N. Laurien, A. Kourta, N. Mazellier and S Loyer. Active flow control of ramp flow by fluidic oscillators. In 2nd MIGRATE International Workshop, number 154498, Sofia, Bulgaria, June 2017.
- [181] P. B. Ruffin S. Yin und T. S. Francis. *Fiber Optic Sensors*. CRC Press, 2017.
- [182] A. P. Schaffarczyk, D. Schwab, S. Ingwersen und M. Breuer. Pressure and Hot-Film Measurements on a Wind Turbine Blade Operating in the Atmosphere. *Journal of Physics: Conference Series*, 555:012092, dec 2014.
- [183] SIKA Dr. Siebert and Kühn GmbH and Co. KG. Technical datasheet Temperature calibrator TP 37200E.2 // TP 37200E.2i V1.2. Technical report, SIKA Dr. Siebert and Kühn GmbH and Co. KG, Struthweg 7-9, 34260 Kaufungen Germany, 08 2022.
- [184] S.M. Melle, K. Liu and R.M. Measures. A passive wavelength demodulation system for guided-wave bragg grating sensors. *IEEE Photonics Technology Letters*, 4(5):516–518, 1992.

A. Bibliography

- [185] Sr. R. W. Borek and A. Pool. Basic principles of flight test instrumentation engineering, Volume 1, Issue 2, March 1994.
- [186] T. Ahlefeldt. DLR specification for novel acoustic pressure sensors for measuring noise on arbitrary fuselage positions - Clean Sky 2 / ADEC FINCA. Technical report, German Aerospace Center, Institute of Aerodynamics and Flow Technology, 2016.
- [187] T. Ahlefeldt, S. Haxter, C. Spehr, D. Ernst and T. Kleindienst, Tobias. Road to Acquisition: Preparing a MEMS Microphone Array for Measurement of Fuselage Surface Pressure Fluctuations. *Micromachines*, 12(8), 2021.
- [188] T. J. Larsen, H. A. Madsen, and K. Thomsen. Active load reduction using individual pitch, based on local blade flow measurements. *Wind Energy*, 8(1):67–80, 2005.
- [189] T. J. Mueller, C. S. Allen, W. K. Blake, R. P. Dougherty, D. Lynch, P. T. Soderman and J. R. Underbrink. *Aeroacoustic Measurements*. Engineering online library. Springer, 2002.
- [190] T. Macquart and A. Maheri. A stall-regulated wind turbine design to reduce fatigue. *Renewable Energy*, 133:964–970, April 2019.
- [191] T. Maeda and H. Kawabuchi. Surface Pressure Measurement on a Rotating Blade of Field Horizontal Axis Wind Turbine in Yawed Condition. *JSME International Journal Series B Fluids and Thermal Engineering*, 48(1):156–163, 2005.
- [192] T. Reichstein, A. P. Schaffarczyk, C. Dollinger, N. Balaesque, E. Schülein, C. Jauch and A. Fischer. Investigation of Laminar–Turbulent Transition on a Rotating Wind-Turbine Blade of Multimegawatt Class with Thermography and Microphone Array. *Energies*, 12(11), 2019.
- [193] T. Wah. Vibration of Circular Plates. *The Journal of the Acoustical Society of America*, 34(3):275–281, 1962.
- [194] T. Yoshino, K. Kurosawa, K. Itoh and T. Ose. Fiber-Optic Fabry-Perot Interferometer and its Sensor Applications. *IEEE Transactions on Microwave Theory and Techniques*, 30(10):1612–1621, 1982.
- [195] V. Ciobaca and J. W. Wild. Active Flow Control for an Outer Wing Model of a Take-off Transport Aircraft Configuration - A Numerical Study. June 2014.
- [196] W. Demtröder. *Elektrizität und Optik*, volume 2. Springer, 2009.
- [197] W. J. Pulliam, P. M. Russler and R. S. Fielder. High-temperature high-bandwidth fiber optic MEMS pressure-sensor technology for turbine-engine component testing. In M. A. Marcus and B. Culshaw, editor, *Fiber Optic*

A. Bibliography

- Sensor Technology and Applications 2001, volume 4578, Seiten 229 – 238. International Society for Optics and Photonics, SPIE, 2002.
- [198] W. J. Wang, R. M. Lin, D. G. Guo and T. T. Sun. Development of a novel Fabry–Pérot Pressure Microsensor. *Sensors and Actuators A: Physical*, 116(1):59–65, 2004.
- [199] W. L. Richards, A. Parker, W. Ko, William, A. Piazza and H. Chan. Application of Fiber Optic Instrumentation, Flight Test Instrumentation Series – Volume 22. 07 2012.
- [200] W. Mader. Dreieckiges, konformes Kirchhoff-Plattenelement nach Hsieh, Clough und Tocher. Diplomarbeit, 2013.
- [201] W. N. MacPherson and M. J. Gander and J. S. Barton and J. D. C. Jones and C. L. Owen and A. J. Watson and R. M. Allen. Blast-pressure measurement with a high-bandwidth fibre optic pressure sensor. *Measurement Science and Technology*, 11(2):95–102, January 2000.
- [202] W. N. MacPherson, J. M. Kilpatrick, J. S. Barton and J. D. C. Jones. Miniature fiber optic pressure sensor for turbomachinery applications. *Review of Scientific Instruments*, 70(3):1868–1874, 1999.
- [203] W. van der Velden, A. Zuijlen, A. Jong and H. Bijl. On the estimation of spanwise pressure coherence of a turbulent boundary layer over a flat plate. July 2014.
- [204] W. Zhang, Q. Chen, L. Zhang and H. Zhao. Fiber Optic Fabry–Pérot Sensor with Stabilization Technology for Acoustic Emission Detection of Partial Discharge. In 2018 IEEE International Conference on High Voltage Engineering and Application (ICHVE), Seiten 1–4, 2018.
- [205] R. E. Wagner und W. J. Tomlinson. Coupling Efficiency of Optics in Single-mode Fiber Components. *Applied Optics*, 21(15):2671–2688, 1982.
- [206] A. Wang, H. Xiao, J. Wang, Z. Wang, W. Zhao und R.G. May. Self-calibrated interferometric-intensity-based optical fiber sensors. *Journal of Lightwave Technology*, 19(10):1495–1501, 2001.
- [207] Y. Javed, M. Mansoor and I. A. Shah. A Review of Principles of MEMS Pressure Sensing with its Aerospace Applications. *Sensor Review*, 2019.
- [208] Y. Zhang, Z. Zhou, K. Wang and X. Li. Aerodynamic Characteristics of Different Airfoils under Varied Turbulence Intensities at Low Reynolds Numbers. *Applied Sciences*, 10(5), 2020.
- [209] Z. Fang, K. Chin, R. Qu and H. Cai. Fundamentals of optical Fiber Sensors, volume 226. John Wiley & Sons, 2012.

A. Bibliography

- [210] Z. Qu, P. Lu, Y. Li, X. Fu, W. Zhang, D. Liu and J. Zhang. Low-frequency acoustic fabry-pérot fiber sensor based on a micromachined silicon nitride membrane. *Chinese Optical Letters*, 18(10):101201, Oct 2020.

A.2. Own Publications

- [211] A. H. Fallahpour, S. U. Kienitz and P. Lugli. Origin of dark current and detailed description of organic photodiode operation under different illumination intensities. *IEEE Transactions on Electron Devices*, 64(6):2649–2654, 2017.
- [212] F. M. Heckmeier, D. Iglesias, S. Kreft, S. U. Kienitz and C. Breitsamter. Development of unsteady multi-hole pressure probes based on fiber-optic pressure sensors. *Engineering Research Express*, 1(2):025023, oct 2019.
- [213] F. M. Heckmeier, K. Meusel, S. U. Kienitz, D. Iglesias, C. Breitsamter. Development of Fiber-Optic Pressure Sensors for the Usage in Unsteady Multi-Hole Probes. In *Proceedings der 27. GALA-Fachtagung "Experimentelle Strömungsmechanik"*, Erlangen, 2019.
- [214] F. M. Heckmeier, M. D. Iglesias, S. U. Kienitz and C. Breitsamter. An Innovative Development of a Five-Hole Pressure Probe for Highly Unsteady Flow Phenomena. In *Volume 6: Ceramics; Controls, Diagnostics, and Instrumentation; Education; Manufacturing Materials and Metallurgy*, volume Volume 6 of *Turbo Expo: Power for Land, Sea, and Air*, 06 2019. V006T05A001.
- [215] M. J. Schmid, S. U. Kienitz, B. A. Kuhnle, C. F. Napierala, C. Scheit, A. Altmikus, M. S. Müller and A. W. Koch. A fiber-optic sensor for measuring quasi-static and unsteady pressure on wind energy converters. In *Smarte Strukturen und Systeme – 4SMARTS Konferenz Proceedings*. Shaker Verlag, 2017.
- [216] H. Eigner M. Raith, S. U. Kienitz und S. Kreft. Ein Schallemissionssensor auf Basis eines Fabry-Pérot Interferometers - Möglichkeiten und Randbedingungen - Einleitung und Stand der Technik. In *22. Kolloquium Schallemission, März 2019, Karlsruhe, Germany (DGZfP AE-2019)*, Karlsruhe, 2019.
- [217] S. U. Kienitz, L. Lohr, M. J. Schmid, A. W. Koch. Static and Dynamic Pressure Measurement in Flight Test Application With Optical Fabry-Pérot Sensors. *IEEE Transactions on Instrumentation and Measurement*, 70:1–11, 2021.
- [218] S. U. Kienitz, M. J. Schmid, M. Jakobi and A. W. Koch. Forschung auf dem gebiet der angewandten faseroptischen drucksensorik. *Annual Magazine Engineering Sciences Germany 2021/22, Measurement and Sensor Technology*, November 2021.

A. Bibliography

- [219] S. U. Kienitz, M. Staats, L. Lohr, J. Irsperger, M. J. Schmid, A. W. Koch and J. Weiss. Fiber optic pressure measurement on a complex outer winglet model with active flow control actuators. *Sensors and Actuators A: Physical*, 332:113140, 2021.
- [220] S. U. Kienitz, S. Kreft, M. J. Schmid, M. Staats and A. W. Koch. Miniature Airworthy Fiber-Optic Pressure Sensor for Measuring Static Pressure and Acoustics. In *Aerospace Europe Conference 2020, Bordeaux, France*, 2020.

A.3. Patents

- [221] S. U. Kienitz A. J. Kitzman und J. H. Rud. Thermowell with infrared sensor. Patentschrift, WO2017003648, 01 2017.
- [222] A. J. Kitzman J. H. Rud und S. U. Kienitz. Improved explosive-proof thermal imaging system. Patentschrift, WO2017003707, 01 2017.
- [223] S. U. Kienitz. Bestimmung des Torsionswinkels und Pitchwinkelbestimmung mittels mindestens zwei Beschleunigungssensoren. Patentschrift, DE102018119733A1, 02 2020.
- [224] S. U. Kienitz und S. Kreft. Fabry-Pérot-Temperatursensor. Patentschrift, DE102019132522A1, 06 2021.
- [225] S. U. Kienitz und M. J. Schmid. Faseroptischer Sensor und Verfahren. Patentschrift, DE102019101630A1, 07 2020.
- [226] S. U. Kienitz und M. J. Schmid. Temperaturkompensierter faseroptischer Sensor und Verfahren zur Druckmessung. Patentschrift, DE102018124753A1, 04 2020.
- [227] M. J. Schmid M. Müller und S. U. Kienitz. Acoustic emission sensor having at least two mechanical coupling elements. Patentschrift, WO2018122327, 07 2018.
- [228] T. Möller und S. U. Kienitz. Securing method, securing device, use of a securing device and temperature sensor. Patentschrift, WO2019042747, 03 2019.
- [229] T. Möller und S. U. Kienitz. Temperature Sensor. Patentschrift, WO2019180161, 09 2019.
- [230] L. Lohr S. U. Kienitz und M. J. Schmid. Fibre-optic accelerometer. Patentschrift, WO2021185667, 09 2021.
- [231] M. J. Schmid S. U. Kienitz und M. Mai. Fiber-optic acceleration sensor having lever arm. Patentschrift, WO2018115486, 06 2018.

A.4. Supervised Student-based Seminar Papers and Theses

- [232] Optimierung und Validierung eines Faser-Bragg-Gitter-Beschleunigungssensors. Bachelor Thesis, 2017.
- [233] Entwicklung von Elektronik für die Integration von RTK-Korrekturdaten in ein hochpräzises GNSS-Navigationssystem zur Verwendung in einer fliegenden Messplattform. Research Practice, 2019.
- [234] Evaluierung von Kantenfiltermesstechnik für faseroptische Sensoren. Engineering Practice, 2019.
- [235] Konzeptionierung und Evaluierung einer statischen Druckkammer zur Justierung eines faseroptischen Drucksensors. Bachelor Thesis, 2019.
- [236] Optimierung der dynamischen Eigenschaften eines gyrostabilisierten Neigungssensors durch gezielte Erkennung typischer Bewegungsprofile. Bachelor Thesis, 2019.
- [237] Analyse eines Kantenfilter-Messsystems für die Automatisierung des Herstellungsprozesses. Bachelor Thesis, 2020.
- [238] Build Verification Tests for Edge Filtering Measuring Devices by Electrical Mocking of Optic Components. Engineering Practice, 2020.
- [239] Detection of Air Flow Direction with an Array of Fiber-Optic Fabry-Pérot Pressure Sensors. Bachelor Thesis, 2020.
- [240] Erweiterung eines faseroptischen Messgeräts zu einem intelligenten IIoT-Sensor im Anwendungsbereich Windkraft. Master Thesis, 2020.
- [241] Evaluation of Single-Point Temperature Calibration of Fibre Bragg Temperature Sensors. Bachelor Thesis, 2020.
- [242] Optimierung des Analog-Front-Ends eines Messsystems für faseroptische Sensorik. Research Practice, 2020.
- [243] Scalability and Optimization of a Fiber-optic Measurement Production. Master Thesis, 2020.
- [244] Automatische Bilderkennung in der Produktion faseroptischer Messsysteme im Sinne einer Smart Factory. Bachelor Thesis, 2021.
- [245] Evaluating Aerodynamic Characteristics of an Airfoil in a Wind Tunnel Using Fiber-optic Fabry-Pérot Pressure Sensors . Bachelor Thesis, 2021.
- [246] Optimierung und Validierung von dynamischen Neigungssensoren. Research Practice, 2021.

A. Bibliography

- [247] Characterization and Optimization of an Optical-Electrical Converter Chip to Measure Fiber Bragg Gratings. Master Thesis, 2022.
- [248] Evaluierung von Fabry-Pérot Beschleunigungssensoren zur Zustandsüberwachung von Windkraftanlagen. Bachelor Thesis, 2022.
- [249] Overview of Fiber-optic Fabry-Pérot based Pressure Sensors and their Resulting Cross-Sensitivity. Advanced Seminar Theses, 2022.